



Title	Controlled Synthesis of Two-Dimensional Transition Metal Disulfide Monolayers for SolarDriven Hydrogen Production
Author(s)	海, 曉
Citation	北海道大学. 博士(理学) 甲第12919号
Issue Date	2017-09-25
DOI	10.14943/doctoral.k12919
Doc URL	http://hdl.handle.net/2115/67432
Type	theses (doctoral)
File Information	Xiao_Hai.pdf



[Instructions for use](#)

Controlled Synthesis of Two-Dimensional Transition Metal Disulfide

Monolayers for Solar-Driven Hydrogen Production

(二次元遷移金属硫化物単層の制御合成と光照射下における水素生成助触媒特性)

Xiao Hai

Functional Materials Chemistry Unit

Graduate School of Chemical Sciences and Engineering

Hokkaido University

2017

CONTENTS

Contents	1
Abstract	1
Chapter 1 Introduction	4
1.1 General introduction of photocatalytic H ₂ evolution	4
1.2 Concept of cocatalysts for photocatalytic H ₂ evolution	7
1.2.1 Fundamental principles of cocatalysts	7
1.2.2 Opportunities of non-precious metal cocatalysts	9
1.3 Transition metal disulfides	10
1.3.1 Structure and properties	10
1.3.2 Theoretical feasibility for H ₂ evolution reaction	13
1.4 Modification of transition metal disulfides	16
1.4.1 Structure match	16
1.4.2 Phase transformation	19
1.4.3 Energy band engineering	22
1.5 Research motivation and thesis organization	28
References	30
Chapter 2 Targeted synthesis of 2H- and 1T-phase MoS₂ monolayers for catalytic hydrogen evolution	
2.1 Introduction	37
2.2 Experimental section	38

Contents

2.2.1 Synthesis of 2H-MoS ₂ monolayers	39
2.2.2 Synthesis of 1T-MoS ₂ monolayers	39
2.2.3 Reaction process of (NH ₄) ₂ MoS ₄ and LiOH	39
2.2.4 Characterization	40
2.2.5 Electrode preparation	41
2.2.6 Photocatalysts preparation	41
2.2.7 Photocatalytic H ₂ evolution	41
2.3 Results and discussion	42
2.3.1 The synthesis mechanism	42
2.3.2 Characterization of obtained 2H- and 1T-phase MoS ₂ monolayers	47
2.3.3 Photocatalytic H ₂ evolution	60
2.4 Conclusion	66
References	67

Chapter 3 Engineering the edges of transition metal disulfides for direct exfoliation into monolayers in polar micromolecular solvents and their cocatalytic performances

3.1 Introduction	72
3.2 Experimental section	74
3.2.1 Synthesis of monolayer transition metal disulfide (MoS ₂ and WS ₂) nanosheets	74
3.2.2 Preparation of transition metal disulfide monolayers decorated CdS photocatalysts	74
3.2.3 Characterization	74
3.2.4 Photocatalytic H ₂ evolution	75
3.3 Results and discussions	76
3.3.1 Characterization of as-synthesized transition metal disulfide bulk crystals	76
3.3.2 The exfoliation mechanism	79

Contents

3.3.3 Characterization of exfoliated MoS ₂ and WS ₂ monolayers	85
3.3.4 Cocatalytic performance of exfoliated MoS ₂ and WS ₂ monolayers	91
3.4 Conclusion	99
References	100

Chapter 4 Engineering crystallinity of MoS₂ monolayers for enhanced cocatalytic activity

4.1 Introduction	104
4.2 Experimental section	105
4.2.1 Synthesis of differently crystalline MoS ₂ monolayers	105
4.2.2 Preparation of differently crystalline MoS ₂ decorated CdS photocatalysts	106
4.2.3 Characterization	106
4.2.4 Photocatalytic H ₂ evolution	106
4.2.5 DFT calculations	107
4.3 Results and discussion	107
4.3.1 Characterization of crystallinity-dependent MoS ₂ crystals	107
4.3.2 Characterization of crystallinity-dependent MoS ₂ monolayers	113
4.3.3 Evaluation of cocatalytic performances of crystallinity-dependent MoS ₂ monolayers	120
4.3.4 The role of crystallinity for enhanced cocatalytic performance	125
4.4 Conclusion	128
References	128

Chapter 5 Maximizing synergistic cocatalytic activity of MoS₂ monolayers combining crystallinity engineering and cobalt substitution

5.1 Introduction	132
5.2 Experimental section	134

Contents

5.2.1 Synthesis of MoS ₂ precursors with crystallinity engineering and cobalt substitution	134
5.2.2 Exfoliation of bulk precursors to monolayers	134
5.2.3 Characterization	135
5.2.4 Electrode preparation and electrochemical measurements	135
5.2.5 Preparation of MoS ₂ /CdS photocatalysts	136
5.2.6 Photocatalytic H ₂ evolution	136
5.2.7 DFT calculations	137
5.3 Results and discussion	138
5.3.1 Characterization of rational designed MoS ₂ precursors	138
5.3.2 Characterization of rational designed MoS ₂ monolayers	140
5.3.3 Theoretical study of the rational designed MoS ₂ monolayers for H ₂ evolution	144
5.3.4 Electrochemical H ₂ evolution	146
5.3.5 Photocatalytic H ₂ evolution	153
5.4 Conclusion	156
References	156
Chapter 6 General conclusion and future prospects	
6.1 General conclusion	161
6.2 Future prospects	162
Acknowledgement	164

Abstract

The production of hydrogen fuels by using sunlight is an attractive and sustainable solution to the global energy and environmental problems. Although platinum (Pt) is known as the most efficient cocatalyst in hydrogen evolution reaction (HER), its high-cost and limited-reserve urge to seek for the alternative non-precious cocatalysts with low-cost and high efficiency. Monolayer transition metal disulfides (TMDs) including molybdenum disulfide (MoS_2) and tungsten disulfide (WS_2) are regarded as promising HER candidates to replace Pt due to their highly active edge sites for hydrogen adsorption ($\Delta G_{\text{H}} \sim 0.08$ eV) and large in-plane electron mobilities (>200 $\text{cm}^2 \text{V}^{-1} \text{s}^{-1}$). However, until now, facile and efficient preparation of TMDs monolayers has faced with great challenges. Furthermore, the inert but thermodynamically favorable basal planes significantly limit their efficiency in photocatalytic HER. Thus, this thesis focused on targeted synthesis of TMDs monolayers with various phases, lateral sizes, crystallinities, and atomic structures to create more exposed active sites, in particular reactivate the inert basal plane towards superior cocatalytic performance for photocatalytic HER.

In chapter 1, a general background of photocatalytic H_2 evolution, cocatalyst, and transition metal disulfides is introduced. Then, the current strategies to modify transition metal disulfides as efficient cocatalysts are summarized.

In chapter 2, targeted synthesis of semiconductor phase (2H) and metal phase (1T) MoS_2 monolayers was investigated. A facile and effective lithium molten salt assisted method was first developed to synthesize a series of MoS_2 precursors by simply controlling the calcination temperature. These precursors can be easily and accurately exfoliated into 2H- and 1T-phase MoS_2 monolayers by subsequent hydrolysis process. During the synthesis process, lithium molten salt not only acts as the fluxing medium, but also controls the MoS_2 phases switching between 1T and 2H. Due to metallic characteristic, the 1T-

Abstract

MoS₂ monolayers show significantly higher activities than the semiconducting 2H-MoS₂ monolayers over TiO₂ for photocatalytic H₂ evolution.

In chapter 3, a novel strategy through engineering lateral size of TMDs (MoS₂ and WS₂) was explored for direct exfoliation in polar micromolecular solvents to produce monolayer MoS₂ and WS₂ nanosheets in high yield. The exfoliation yield of monolayers was measured to be as high as 21% for MoS₂ and 18% for WS₂ in ethanol. Even in pure water, a monolayer yield of 6% for MoS₂ and 5% for WS₂ can be achieved. The successful exfoliation of the as-prepared crystals was attributed to the significantly improved ratio of hydrodynamic forces to interlayer van der Waals forces, allowing for ready exfoliation in polar micromolecular solvents. These exfoliated monolayer TMDs nanosheets exhibit superior catalytic H₂ activity when loaded on CdS for photocatalytic HER with optimized sacrificial agents, PH values, and loading amount.

In chapter 4, to further create more active sites in MoS₂ monolayers for triggering a higher HER activity, crystallinity engineering was adopted to enhance its catalytic H₂ activity. It was found that the cocatalytic performance of the monolayer MoS₂ is gradually enhanced with reduced crystallinity, and an apparent quantum efficiency as high as 71.6% can be achieved for the lowest crystalline monolayer MoS₂ over CdS under visible light irradiation at 420 nm. As compared to the highly crystalline monolayer MoS₂, the increased catalytic H₂ activity for the poorly crystalline monolayers is attributed to the low-crystallization induced structural disorder, which contains abundant unsaturated sulfur atoms as additional active sites for HER.

In chapter 5, to effectively reactivate the inert basal plane of MoS₂ monolayers, elemental (like cobalt) doping combining with crystallinity engineering was systematically investigated. The density functional theory calculations and experimental results show that the combination of crystallinity engineering with cobalt substitution can activate and reuse of the inert basal plane of MoS₂ monolayers for HER, leading to the significantly enhanced catalytic H₂ activity with an apparent quantum efficiency of 80.2% over CdS under visible light irradiation at 420 nm.

Abstract

In chapter 6, an overall summary of this dissertation work was provided. This thesis carried out a systematic study on controllable synthesis of monolayer TMDs and rational design of their active sites for efficient photocatalytic H₂ evolution. By lithium molten salt assisted and edge engineering methods, direct exfoliation and targeted synthesis of 2H-, 1T-phase MoS₂ monolayers can be achieved. By crystallinity engineering, abundant unsaturated sulfur atoms as additional active sites were introduced as an effective way for improving the cocatalytic performance of MoS₂ monolayers. By cobalt doping, the inert basal plane was activated, further enhancing the cocatalytic performance of crystallinity engineered MoS₂ monolayers for photocatalytic HER. This study potentially provides new avenues for facile synthesis and design of more efficient monolayer TMDs cocatalysts for photocatalytic H₂ evolution in the future research.

Chapter 1 Introduction

1.1 General introduction of photocatalytic H₂ evolution

Technological needs for realizing a sustainable society has led to the surge in renewable energy research in the 21st century. Hydrogen exhibits the highest specific energy of combustion of all chemical fuels and produces only water as a combustion product; therefore, it is regarded as one possible contender for meeting future fuel needs. The production of hydrogen fuels by using sunlight is an attractive and sustainable solution to global energy and environmental problems.^[1, 2] Since the 1970s, the discovery of photo-electrochemical (PEC) water splitting system for hydrogen evolution by Fujishima and Honda, splitting water using solar energy has attracted a significant attention as a possible means for converting solar energy to chemical energy in the form of clean and renewable hydrogen fuel.^[3] During the past decades, water splitting for hydrogen evolution by using semiconductors has been extensively studied.^[4-12]

Currently, there are mainly three types of reaction systems of photocatalytic water splitting for H₂ evolution as shown in Figure 1.1. PEC system as the earliest route for water splitting has been studied extensively, from the initial half reaction to the final full reactions. Figure 1.1a shows that the complete PEC cell should be composed of two sides: n-type semiconductor as photo-anode and p-type semiconductor as photo-cathode.^[13, 14] Under the light irradiation, the electrons and holes are generated by both sides. For n-type semiconductor side, the photo-excited holes transfer to the surface of semiconductor to oxidize water (H₂O) to molecular oxygen (O₂), whereas the electrons transfer to the photo-cathode side. In the case of photo-cathode side, H₂O is reduced to H₂ on the surface of p-type semiconductor by photo-excited electrons, whereas the holes are consumed by electrons from n-type semiconductor side. However, a large external bias using a power supply is required; therefore, it is undesirable in terms of the energy consumption. To overcome this shortcoming, semiconductor powder systems have been designed by self-generated photovoltage to simulate the “micro-PEC” system to fulfill

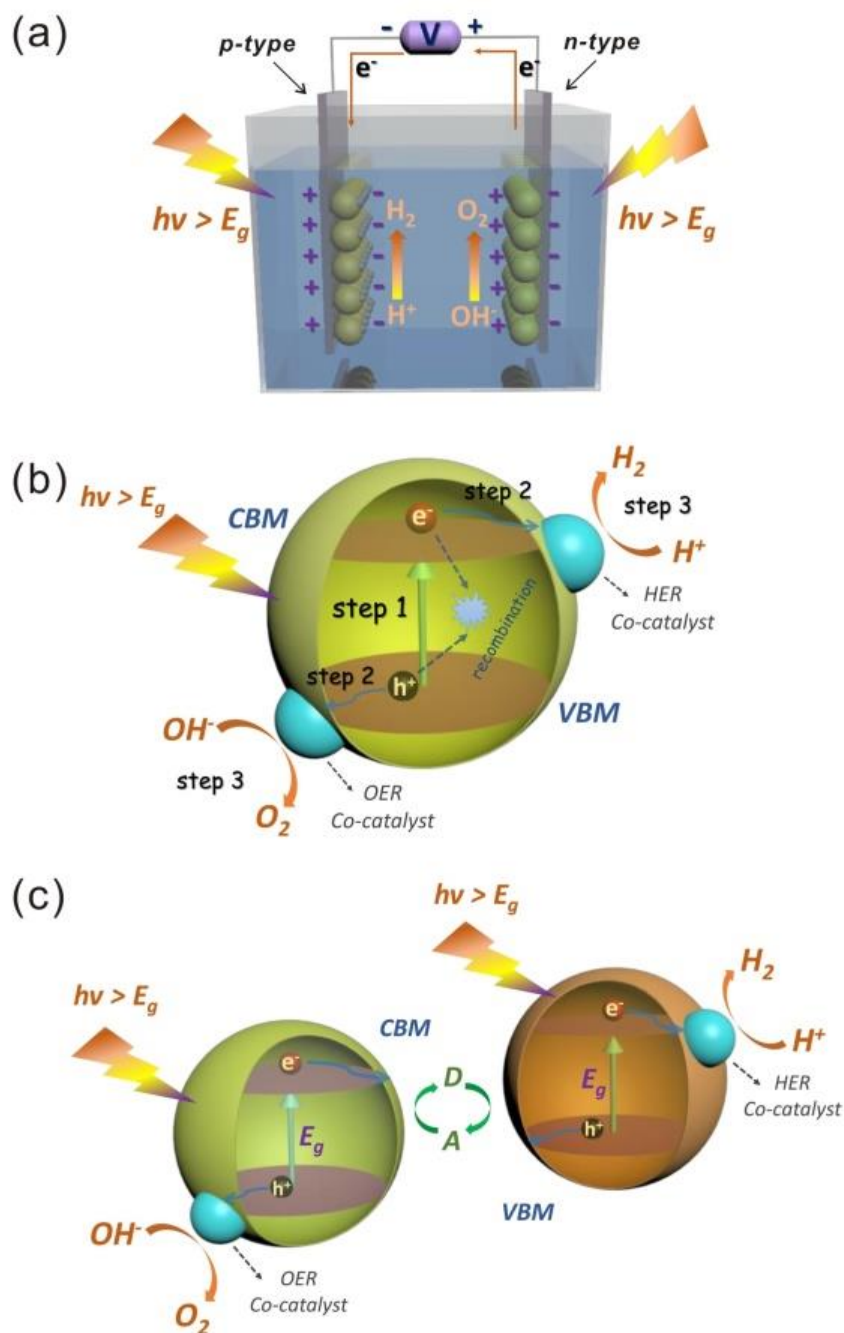


Figure 1.1 Typical systems for photocatalytic overall water splitting: (a) photo-electrochemical water splitting system, (b) processes involved in one-step photocatalytic overall water splitting system, and (c) Z-scheme water splitting system. E_g indicates the bandgap energy of the semiconductor.

the water splitting. Figure 1.1b illustrates the typical one-step water splitting process involving three major stages: (1) light absorption by photocatalyst to generate photo-excited electron-hole pairs in the bulk, (2) the photo-excited carriers separation and migration to the surface without recombination, and (3) surface reaction for hydrogen reduction or water oxidation by photo-excited electrons and holes to produce H_2 and O_2 , respectively. It is well known that process of water splitting is a typical “uphill reaction”, involving a large positive change in the Gibbs energy ($\Delta G^0 = 237.13 \text{ kJ mol}^{-1}$), corresponding to a photon energy of 1.23 eV. However, due to an activation barrier in the charge transfer process between the photocatalyst and H_2O molecules, the photon energy higher than the bandgap of the semiconductor is usually necessary to drive the water splitting reaction.^[15] Moreover, the serious backward reaction, *i.e.*, H_2O formation from H_2 and O_2 , also decreases the water splitting efficiency.

Z-scheme water splitting system was developed in the past years, and it was inspired by natural photosynthesis in green plants.^[16, 17] It is composed of two half reactions: hydrogen reduction and oxygen oxidation, as well as an appropriate shuttle redox mediator (Figure 1.1c). For this system, in a sense, the backward reactions could be avoided in the presence of the shuttle redox mediator. However, the decrease of photon utilization and the limitation of selection of oxidation-reduction reaction restrict its improvement of water splitting activity. For example, the hydrogen reduction photocatalyst can not only reduce H^+ ions to form H_2 but also can reduce the shuttle redox mediator (A, the electron acceptor); the oxygen oxidation photocatalyst can not only oxidize OH^- ions to form O_2 , but also oxidize the shuttle redox mediator (D, the electron donor).

To overcome this disadvantage, co-catalysts are often used to improve the abilities of H_2 and O_2 evolution during the system. In general, to promote the development of photocatalytic water splitting, co-catalysts are often employed to be modified on the surface of semiconductors, in particular, for hydrogen reduction sites. Most semiconductors cannot deliver a high hydrogen evolution reaction (HER) rate without a co-catalyst even in the presence of sacrificial electron donor,^[18] thus, the enhancement factor for HER co-catalyst would be higher than that of oxygen evolution reaction (OER) co-catalyst. Therefore,

except for exploring new visible-light-harvesting semiconductors, the most important objective is to develop highly efficient co-catalysts to activate the semiconductor surface site and reduce the activation energy for surface chemical reactions.

1.2 Concept of cocatalysts for photocatalytic H₂ evolution

1.2.1 Fundamental principles of cocatalyst

During the photocatalytic HER, most semiconductor photocatalysts cannot offer an active site for catalytic hydrogen evolution on the surface, leading to the facile recombination of photo-excited electron-hole pairs before migrating to the surface for reactions. Loading co-catalyst can retard the recombination of photo-generated electron-hole pairs in a big sense. Traditionally, metal, in particular, noble metals such as Pt and ruthenium, as co-catalyst, are often used to support the surface of semiconductors. This is attributed to the fact that these noble metals have the larger work function, *i.e.*, lower Fermi level, which can more easily trap the photo-excited electrons to retard the recombination of electron-hole pairs. Among the noble metals, Pt has the lowest Fermi level, and thus possesses the best abilities for trapping electrons and the highest hydrogen evolution activities. However, unlike the electrocatalytic reaction, a Schottky barrier is formed at the interface between co-catalyst and semiconductor. Thus, the photocatalytic hydrogen evolution activity is not only dependent on the properties of semiconductors themselves but also dependent on the selection of the proposed and structure-matched co-catalysts. Figure 1.2 demonstrates that following the light absorption, photo-excited electrons generated from the interior of semiconductor can be migrated to the surface and then have to overcome the Schottky barrier to participate in the subsequent reactions. Exploring structure-matched co-catalysts with semiconductor and optimizing the synthesis conditions of the composites can decrease the Schottky barrier at the interface, facilitating the transfer of photo-generated electrons to the co-catalysts.

The subsequent HERs occurring on the co-catalyst can be divided into two steps: hydrogen adsorption and desorption. First, co-catalyst provides catalytic sites to adsorb the protons from the solution. Then the photo-excited electrons which crossed the Schottky barrier combine with the protons to form hydrogen atoms. Two hydrogen atoms are further combined to form a hydrogen molecule and then desorbed from the active sites of co-catalyst (Figure 1.2). In general, for many noble metals, desorption of molecular hydrogen is the rate determining step because of its uphill Gibbs free energy. However, for the non-precious metal materials, the rate determining step is usually the adsorption step. Therefore, highly active co-catalysts with the zero-approaching free energy of hydrogen adsorption/desorption are primarily proposed for hydrogen evolution.

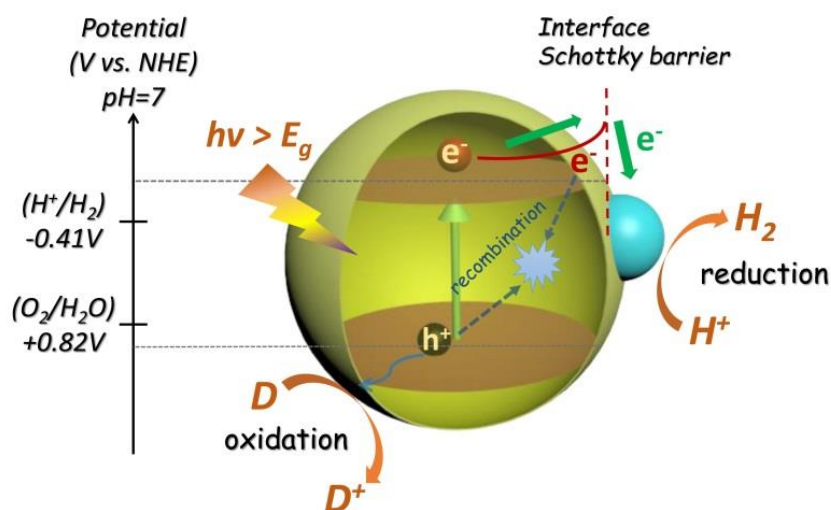


Figure 1.2 Description of band diagram for photocatalytic hydrogen evolution reaction.

Furthermore, another important aspect of co-catalyst that needs consideration is the particle size control and loading amount. In general, the present research on Pt or other noble metals loaded semiconductor involves the utilization of the *in-situ* photo-deposition to synthesize small and uniform nanoparticles on the surface of semiconductors. The loading amount of co-catalyst is usually controlled at less than 3 wt.% because presence of excessive dark-color co-catalysts on the surface of semiconductor

blocks the light transmission. Moreover, the smaller particle size of co-catalyst can produce more active sites and reduce the activation energy for surface chemical reaction. Therefore, three aspects for designing the highly efficient co-catalysts are worth to be considered: (1) the smaller Gibbs free energy of both hydrogen adsorption and desorption; (2) the smaller particle size; and (3) the lower Schottky barrier after combining with semiconductors.

1.2.2 Opportunities of non-precious metal cocatalysts

Although noble metals such as Pt, exhibit the state-of-the-art activities for HER, due to the serious drawbacks of noble metals themselves, seeking for alternative co-catalysts based on non-precious metals and metal-free materials are urged. The drawbacks of noble metal co-catalysts are mainly reflected in two aspects. First is the serious backward reaction during the overall water splitting, i.e., the oxygen reduction reaction (ORR). Noble metals have the lower Fermi level and good electron trapping abilities; therefore, it is easier to reduce the as-generated oxygen. Thus, during the overall photocatalytic water splitting system, the co-catalysts for HER sites are usually employing non-Pt metals or metal oxides, such as nickel (Ni), rhodium (Rh), and nickel oxide (NiO or NiO_x) et al.,^[19-23] as well as utilizing non-cocatalyst photo-harvesters such as CuInZnS.^[24] Moreover, noble metals due to their high-cost and limited-reserve in the earth, in particular, Pt for which the abundance is about 3.7×10^{-6} %, are orders of magnitude smaller than that of other non-precious metals.^[25] Given this, it is valuable to develop highly efficient and low-cost noble-metal-free co-catalysts to further facilitate the development of HER.

During the past decades, a large number of noble-metal-free co-catalysts for hydrogen evolution have been successfully developed in photocatalytic hydrogen evolution half reaction, including non-precious metals (cobalt (Co), Ni, copper (Cu))^[26, 27] and their oxides,^[28, 29] hydroxides^[30, 31] and sulfide compounds,^[32, 33] and carbon-based materials^[34, 35]. Although some of them have been successfully used for the enhancement of photocatalytic hydrogen evolution activity compared to bare semiconductors without loaded co-catalysts, they still exhibit a big gap if compared to Pt loaded semiconductors. As the

typical layered transition metal disulfides (TMDs), MS_2 (M = molybdenum (Mo), tungsten (W)), with the structure composed of three stacked atom layers (S-M-S) held together by van der Waals forces, have attracted remarkable attentions toward HER.^[25] They not only have the most zero-approaching Gibbs free energy of hydrogen adsorption, but also possess the unique structural and electrical properties for two-dimensional (2D) layered materials, as discussed in the following sections.

1.3 Transition metal disulfides

1.3.1 Structure and properties

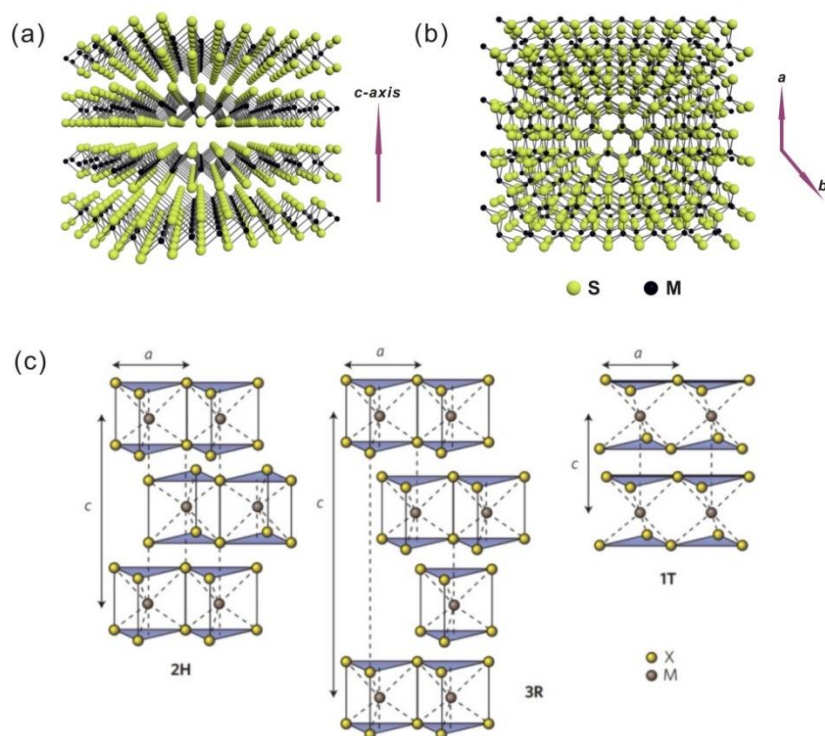


Figure 1.3 Schematic illustrations of natural MS_2 ($M=Mo, W$), (a) side view, and (b) top view. Structural representation of 1T, 2H, and 3R transition metal dichalcogenides and their corresponding metal atoms coordination.^[36]

MoS₂ and WS₂ are 2D materials that belong to the class of transition metal dichalcogenides with the layered structures. Figure 1.3a and 1.3b exhibits that the layers of S and M atoms are hexagonal in structure and each M atom is located at the center of a trigonal prism created by six S atoms.^[36] The S-M-S sandwich-like structure is considered as a monolayer of MS₂, which is stacked by weak van der Waals interactions. TMDs show the graphite-like layered structure that leads to strong anisotropy in their electrical, chemical, mechanical and thermal properties.^[37, 38] In general, there are three types of structures for TMDs, 1T, 2H, and 3R, respectively, where the letters stand for trigonal, hexagonal and rhombohedral (Figure 1.3c). The 1T-phase MoS₂ is a metastable structure discovered in the 1990s, which has octahedral coordination with tetragonal symmetry and only one S-Mo-S layer as a repeat cell.^[39, 40] Under the specific conditions, the metastable 1T phase can change into the stable 2H phase.^[41-43] Generally, 2H-MoS₂ has trigonal prismatic arrangement of Mo and S atoms, with the S atoms in the lower layer lying directly below those of the upper layer, as shown in Figure 1.4^[44]

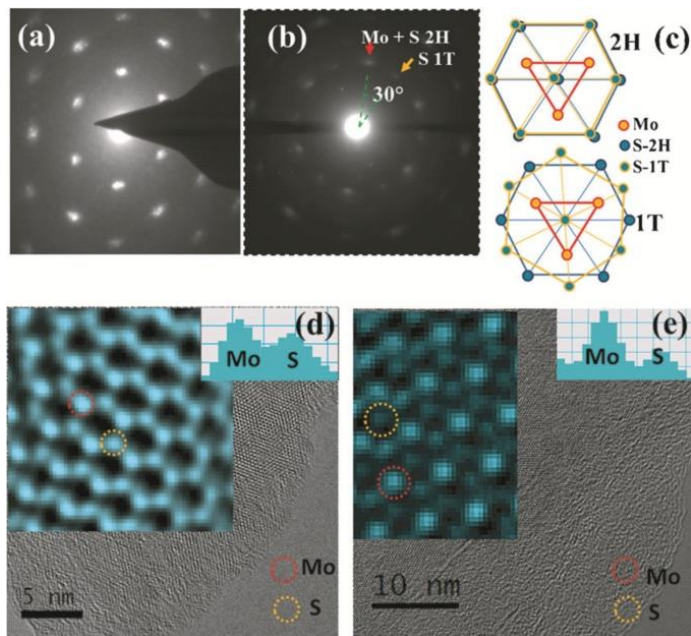


Figure 1.4 The comparison of 2H and 1T-phase MoS₂ structures. Electron diffraction patterns from single-layer MoS₂ with (a) the 2H and (b) 1T structures. (c) Their corresponding structural models. HRTEM images of the (d) 2H and (e) 1T structures.^[44]

For 1T-MoS₂, the S atoms in the upper and lower planes are off-set from each other by 30° such that the Mo atoms lie in the octahedral holes of the S layers (Figure 1.4c). Thus, the electron diffraction pattern of 1T-MoS₂ often shows an extra hexagonal spot at 30° angular in between the hexagonal spots of the 2H structure (Figure 1.4a and 1.4b). To compare with the HRTEM images of 2H and 1T-phase structures (Figure 1.4d and 1.4e), it is found that in case of 2H-MoS₂ three S atoms surrounds one Mo atom whereas for the 1T structure six S atoms surrounds one Mo atom. Although this distorted 1T-phase structure is a metastable state, the discovery of metallic properties of 1T-phase TMDs provides a new perspective to the understanding of TMDs and their properties; thus extensive research efforts have been devoted to these 1T-phase TMDs in recent years.^[40, 44-51] By using this character, the conductivity of TMDs has been significantly improved.

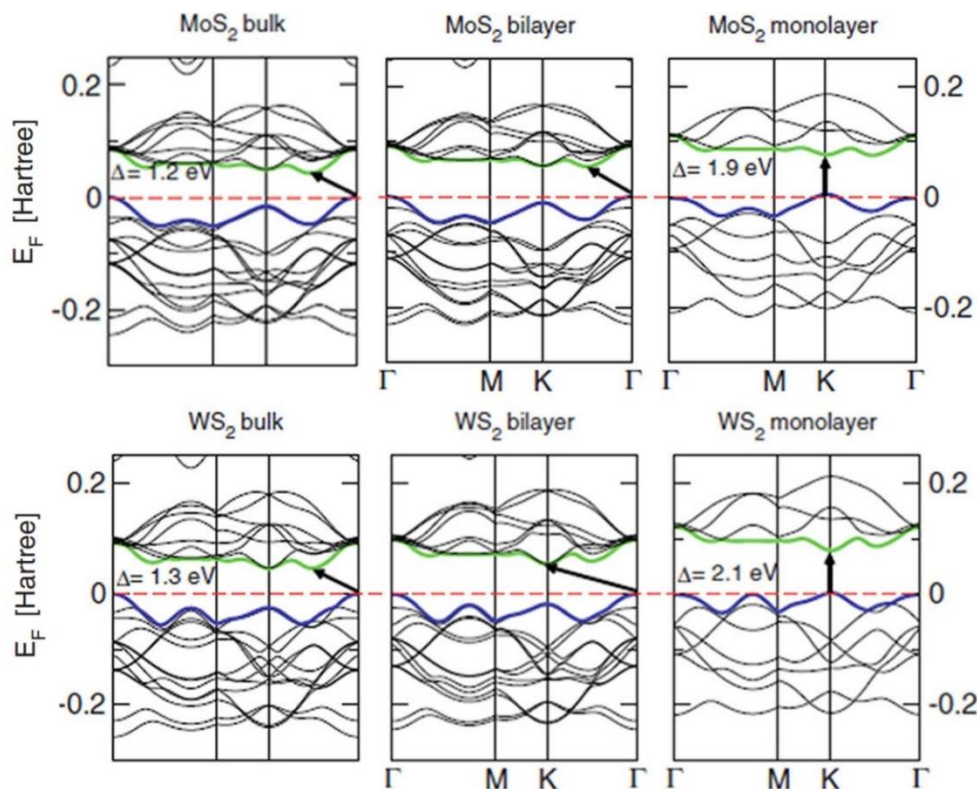


Figure 1.5 Band structure of MoS₂ bulk, MoS₂ bilayer, and MoS₂ monolayer; WS₂ bulk, WS₂ bilayer, and WS₂ monolayer calculated at the DFT/PBE level.^[54]

For 2H phase TMDs, many theoretical reports have indicated that these semiconducting phases could be changed from indirect band gap to direct band gap by tuning layer numbers.^[52, 53] For example, natural bulk MoS₂ is an indirect band gap semiconductor with a band gap of 1.2 eV, which originates from the top of the valence band situated at the Γ point to the bottom of the conduction band halfway between the Γ and K points (Figure 1.5).^[54] With the decrease in layer numbers, the fundamental indirect band gap increases because of the quantum confinement effect. In the case of monolayer MoS₂, the band gap becomes larger than the direct band gap located at the K-point, in which the band gap has been changed to 1.9 eV. The same phenomenon is also observed in the WS₂ material. Figure 1.5 exhibits that the indirect band gap of bulk WS₂ (1.3 eV) is supplanted by the direct band gap (2.1 eV) at the monolayer WS₂ K-point. With this layer-dependent characteristics, 2D ultrathin mono- or few-layer TMDs exhibit unique electronic and optical properties, and therefore have attracted significant attention in recent years.

1.3.2 Theoretical feasibility for H₂ evolution reaction

Generally speaking, a good catalyst for HER needs to fulfill the requirement when the free energy of adsorbed atomic hydrogen is close to thermoneutral, i.e., $\Delta G_{H^*} \rightarrow 0$, where ΔG_{H^*} is the adsorption free energy of hydrogen, which is a good descriptor for hydrogen evolution.^[55, 56] This is attributed to the fact that if the hydrogen does not efficiently bind to the catalyst or if it forms too strong bond with the catalyst, then the proton/electron-transfer step and hydrogen release become inefficient, thus decreasing the catalytic activities. Moreover, until now as we know, Pt is the unbeatable catalyst for hydrogen evolution. It not only has the super-high conductivity and good stability, but also the zero-approaching adsorption free energy of hydrogen. To explore the real Pt-alternative catalysts for hydrogen evolution, it is necessary to start from the theoretical calculation of the adsorption free energy for hydrogen.

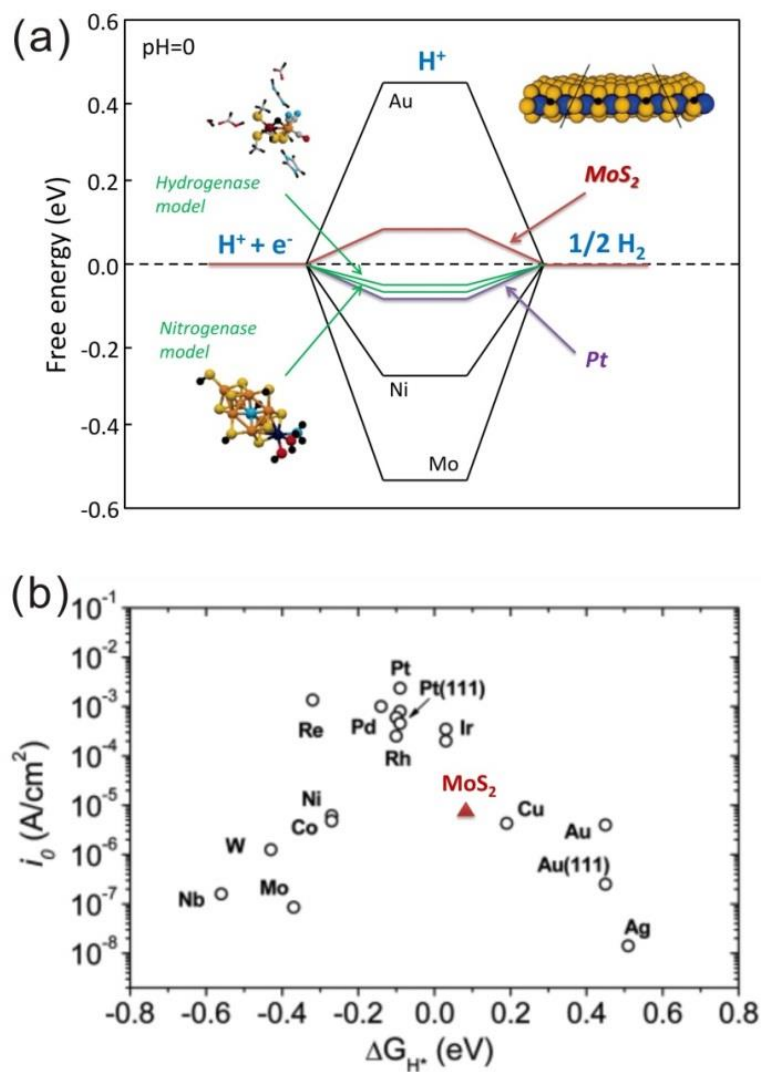


Figure 1.6 (a) The free energy diagram of hydrogen evolution at zero potential and zero pH for platinum, gold, nickel, molybdenum, MoS₂ exposed edge, and the active centers in hydrogenase and nitrogenase. (b) Volcano plot of the exchange current density as a function of the DFT-calculated Gibbs free energy of adsorbed atomic hydrogen for MoS₂ nanoparticles and some pure metals.^[57]

Since 2005, Norskov and co-workers performed the density functional theory (DFT) calculations and found that the computational free energy of atomic hydrogen bonding to the MoS₂ edge was close to that of the Pt, and both of them approached to zero (Figure 1.6a).^[57] However, different from that of Pt, the rate determining step of MoS₂ is the adsorption step for HER. Moreover, Norskov and coworkers also found that the MoS₂ edge structure had a close resemblance to that of the nitrogenase active site. In both the structures, the sulfur atom bounded to hydrogen, was 2-fold coordinated to other metal atoms. The HER activity of various catalysts can be summarized in the “volcano plot”, where the exchange current density for catalysts is plotted as a function of the DFT calculated Gibbs free energy of hydrogen adsorption, as shown in Figure 1.6b. The HER activity reaches a peak value near the zero-approach free energy for several noble metals including Pt, Rh, Ir, and Pb. Chorkendorff and co-workers prepared different sized MoS₂ and measured their HER activities. Finally, they found that the nanoparticulate MoS₂ with more exposed edges showed the highest catalytic hydrogen activities and calculated its free energy of adsorption of hydrogen by DFT method as shown in Figure 1.6b.^[58] The result showed that hydrogen binding energy of MoS₂ edges was the closest to the top of the volcano plot compared to those of common metals. During the following researches, extensive study indicated that only the edges of MoS₂ had the high catalytic activity for hydrogen evolution; however, inactive catalytic activity at the basal plane of MoS₂ was observed.^[25, 59-61] These results provided the possibility of MoS₂ as a promising Pt-alternative catalyst for the hydrogen evolution.

Both MoS₂ and WS₂ belong to the same group; therefore they possess similar electronic and crystal structures. Thus, in recent years, WS₂ has also been studied as a good HER catalyst. Recently, Voiry and co-workers used Li intercalation chemical method to exfoliate 1T-phase WS₂ monolayers and explored its electrocatalytic properties for HER.^[46] They found that the HER characteristics are strongly linked to both the 1T phase concentration and strain as indicated by a gradual decrease in the exchange current density with increasing 2H fraction and decreasing strain. The results of DFT calculation indicated that strain could significantly influence the free energy of atomic hydrogen adsorption on the surface of distorted 1T WS₂, and the free energy equal to zero could be extrapolated for a strain value of 2.7%. However, for 2H

WS₂, effect of strain was not observed on the catalytic hydrogen activity. Therefore, they indicated that the presence of strain and metallic 1T sites are important factors in enhancing catalytic activity of WS₂ nanosheets. This study guides us that metallic 1T-phase WS₂ also can be the noble-metal-alternative catalyst for hydrogen production.

The above mentioned discussion indicates that the TMDs have the most zero-approach Gibbs free energy of hydrogen adsorption, which is the closest to the top of the volcano plot except for the well-established noble metals. Theoretically, TMDs have the most possibilities to replace Pt for hydrogen production, and might be the noble-metal-alternative catalysts for HER. This is mainly because of active sulfide atoms on the exposed edges, with high activity as the active sites for catalytic hydrogen. In other words, it is a smart way to employ appropriate molecular catalysts to imitate these active sites. For example, Karunadasa and co-workers reported a synthesis of a well-defined Mo(IV)-disulfide inorganic compound [(PY₅Me₂)MoS₂]²⁺, which mimics the disulfide-terminated exposed edges of MoS₂ for the high-efficient catalytic hydrogen generation.^[62] However, as I discussed before, a good co-catalyst not only needs the good catalytic hydrogen activities, but also requires the matched junction with semiconductors, as well as the good stabilities under the light irradiation.

1.4 Modification of transition metal disulfides

1.4.1 Structure match

The TMDs have been regarded as the promising Pt-alternative catalysts for HER; therefore, Zong and co-workers first reported MoS₂ and WS₂ loaded on cadmium sulfide (CdS) by chemical method for photocatalytic HER (Figure 1.7).^[63, 64] The loaded MoS₂ or WS₂, which acted as the co-catalysts, significantly enhanced the photocatalytic H₂ evolution activities of CdS, which even exceeded the photocatalytic activities of Pt and other noble metals loaded on CdS in the lactic acid solution. The following studies showed that MoS₂ or WS₂ deposited chemically on CdS exhibited remarkably higher

activity than the mechanical mixture of MoS₂ (WS₂) and CdS, indicating that the intimate contact between co-catalysts and CdS is crucial for the charge transport between each other. They also indicated that because the two components have the common S²⁻ anions, the junctions between MoS₂ or WS₂ and CdS could be readily formed.^[18] Although this speculation has not been confirmed exactly, a large number of experiments on MoS₂ as co-catalyst indirectly concluded that the “outer atomic match” structure has a big possibility. Chen and co-workers used ball-milling combined calcination method to synthesize few-layered MoS₂/CdS composites. This intimate-contact composite exhibited a high H₂ evolution rate of 1.3 mmol h⁻¹ after optimization, exceeding Pt/CdS catalyst with 0.48 mmol h⁻¹ rate, thus this result further confirmed the importance of the interfacial charge transport between co-catalyst and semiconductor for the enhancement of photocatalytic H₂ evolution activity. However, notably, the above mentioned experiment was performed in the presence of lactic acid solution as the hole scavenger, and Pt/CdS photocatalyst showed a low activity for the H₂ evolution. When the photocatalytic activity of Pt/CdS was performed in the Na₂S-Na₂SO₃ solution, it not only exhibited a very high H₂ evolution activity (4.8 mmol h⁻¹ of H₂ evolution rate with a QE of 51% at 420 nm)^[65] but also could be protected by S²⁻ anions in the solution to avoid photocorrosion during the long-term light irradiation.^[66-69] Thus the selection of sacrificial agent plays a key role in the catalytic oxidation in photocatalytic H₂ evolution system. Chang et al. attributed the factor to poisoning phenomenon of Pt by the -CO group from the degradation of lactic acid.^[70] In such a case, using MoS₂ as a co-catalyst could further avoid this disadvantage.

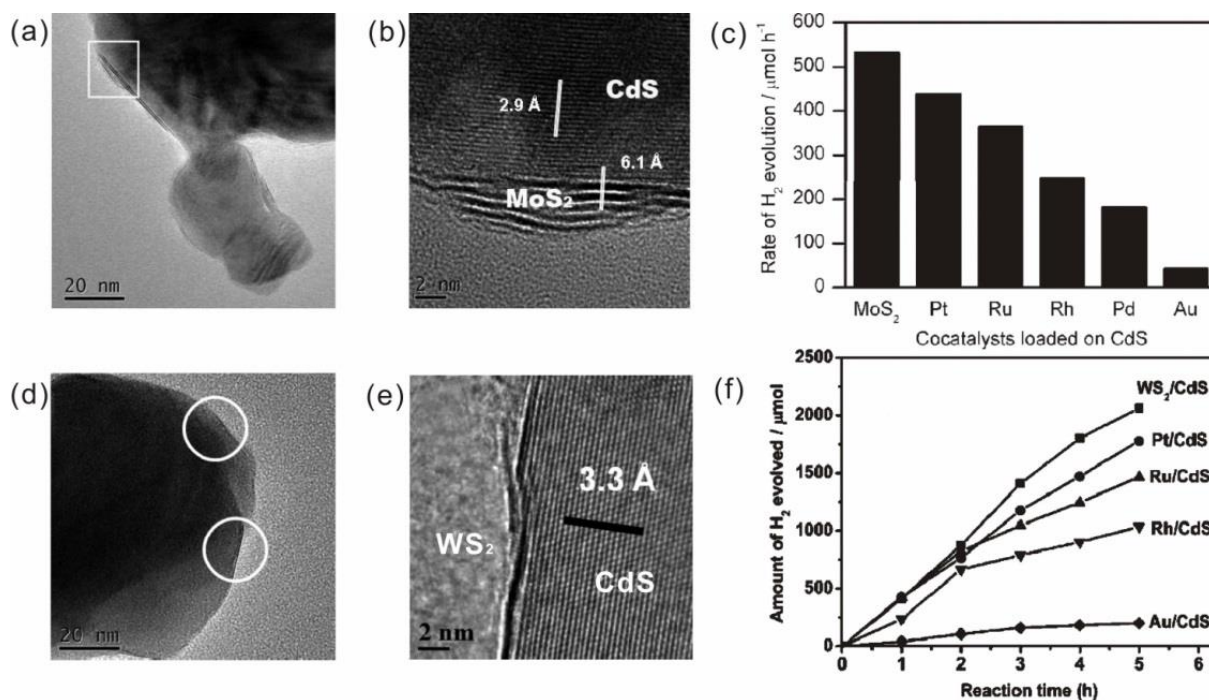


Figure 1.7 (a) TEM image of MoS₂/CdS composite, (b) the magnified HRTEM image of selected frame from image (a), (c) rate of H₂ evolution on CdS loaded with 0.2 wt% of different co-catalysts (0.1 g) under visible light ($\lambda > 420$ nm). (d) TEM image of WS₂/CdS composite, (e) the magnified HRTEM image of selected frame from image (d), and (f) time courses of photocatalytic H₂ evolution on CdS loaded with different co-catalysts under visible light ($\lambda > 420$ nm).^[63, 64]

For photocatalytic H₂ evolution, loading co-catalysts of course plays an essential role in constructing active sites for the separation of electron-hole pairs. It is well known that a high-efficient co-catalyst is usually designed as smaller sized, which can produce more active sites and reduce the activation energy for surface chemical reactions. For traditional noble metals as co-catalysts, they are typically loaded onto the photocatalyst surface as dispersed nanoparticles within the range 1 to 50 nm in size. Moreover, the high conductivity of noble metals could significantly decrease the Schottky barrier, facilitating the transport of photo-excited electrons to the co-catalysts. In general, Schottky barrier is regarded as a junction at the interface between co-catalysts and semiconductors. The presence of Schottky barrier can facilitate the charge separation. A high Schottky barrier; however, blocks the transport of photo-excited

electrons to the surface of co-catalysts. Often, in most cases, the Schottky barrier for noble metals loaded semiconductors is not considered; however, it is definitely taken into account for the design of high-efficient non-precious metal co-catalysts. Undeniably, a lot more systematic explorations are seriously demanded in order to increase the intimate contact with semiconductors and to create more active sites.

1.4.2 Phase transformation

As mentioned before, three types of phases of TMDs exist in nature, namely, 1T, 2H, and 3R. 2H phase has the semiconducting properties and 1T phase shows the metallic properties. Several studies have confirmed that 1T phase TMDs show higher HER activities than 2H phase due to their high conductivity which is beneficial for the rapid charge transport.^[2, 71] Recently, Ding and co-workers reported chemical exfoliated 1T-MoS₂ monolayers as a good co-catalyst in a silicon-based PEC cell for hydrogen evolution.^[72] They indicated that heterostructures of chemical exfoliated 1T-MoS₂ on planar p-Si behave as efficient and robust photocathodes, exhibiting an excellent onset of photocurrent and a high current density at 0 V vs. reversible hydrogen electrode (RHE). Lukowski et al. reported that the chemical exfoliated 1T phase MoS₂ showed a drastic enhancement in the catalytic activity for HER with an electrocatalytic current density of 10 mA cm⁻² at a low overpotential of -187 mV vs RHE and a Tafel slope of 43 mV/decade.^[2] In General, the intercalation with alkali metals induces phase changes. The most common method is lithium intercalation in 2H phase TMDs, which results in the transformation to 1T phase.^[73-75] Destabilization of the original phase may be attributed to the effective change in the *d*-electron count – through transfer of an electron from the valence *s* electron orbital of the lithium metal to the *d* electron orbital of the transition metal center.^[37] The battery testing system is the most convenient route for the lithium intercalation, which can monitor and control the lithiation process at room temperature within only several hours, as shown in Figure 1.8a.^[76] Normally, the discharge curve in this system represents the lithiation process, where the electronic structure of MoS₂ could be tuned. The voltage of MoS₂ vs. Li⁺/Li is decreased monotonically from 2.1 to 1.2 V, corresponding to the formation

of Li_xMoS_2 . The following lithiation process between 1.2 and 1.1 V underwent a 2H to 1T MoS_2 first-order phase transition.^[75, 77, 78]

Recently, Kang et al. found that plasmonic gold (Au) hot electrons could induce the structure phase transition in MoS_2 monolayer from 2H to 1T phase, as shown in Figure 1.8b.^[43] The Au nanoparticles were deposited on the MoS_2 monolayer. When excited by laser resonance, the hot electrons generated from plasmon decay effectively transfer into the d electron orbital of MoS_2 layer. The 2H phase first leads to the destabilization of the lattice, and then through the population of the Mo $4d$ orbitals into a structural transition to the 1T phase. Through the Raman spectra, the additional three new peaks at 156, 226, and 323 cm^{-1} provided the evidence for the presence of 1T phase. It should be highlighted that this phase transformation is a reversible process, and it can only be induced under the light irradiation. Based on this phenomenon, Shi et al. reported that the hot electrons generated from plasmonic Au nanorods activated the HER abilities of MoS_2 nanosheets.^[79] The plasmonic Au- MoS_2 hybrids dramatically improved the HER activities, leading to a ~3-fold increase in current under excitation of Au localized surface plasmon resonance, and also resulting in a decrease in the overpotential of HER at MoS_2 to ~120 mV.

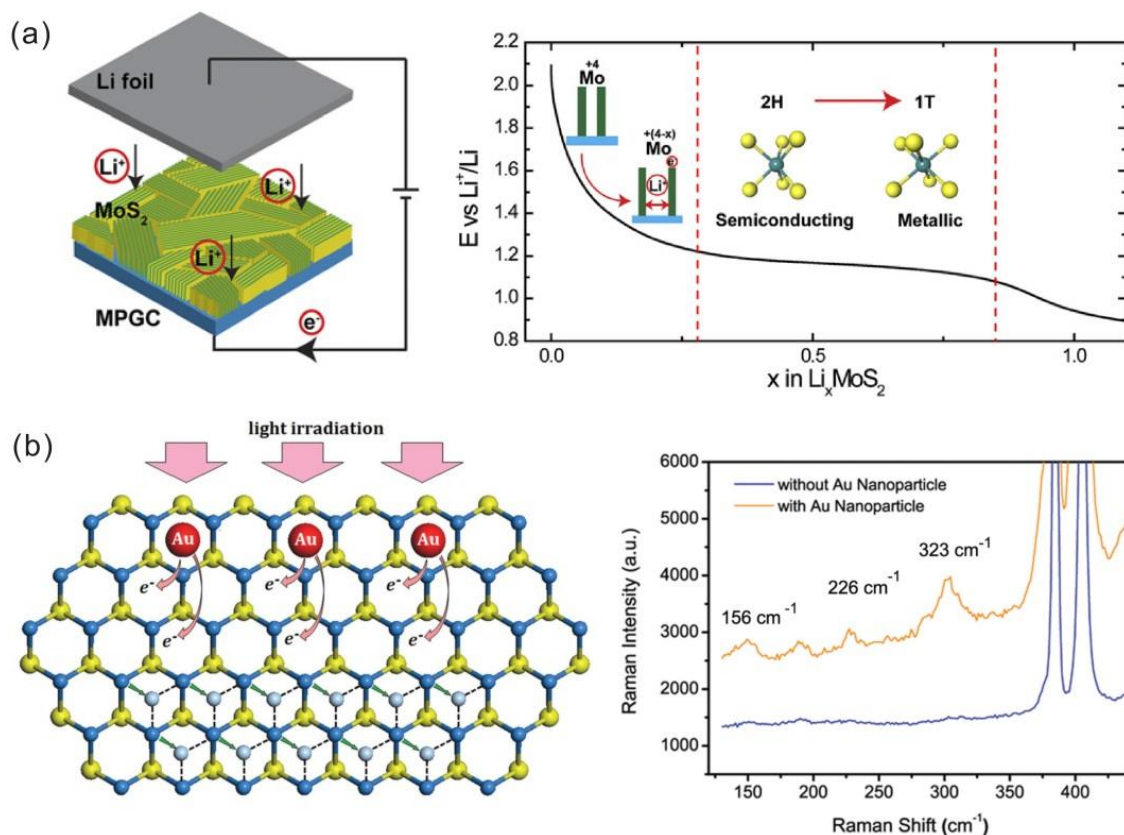


Figure 1.8 (a) Schematic of the lithium ion battery testing system and the galvanostatic discharge curve of the lithiation process inducing the phase conversion from 2H to 1T.^[76] (b) Illustration of plasmonic hot electron induced 2H to 1T phase transition for MoS₂ monolayer, and the Raman spectra of MoS₂ monolayer with and without Au nanoparticles.^[43]

Chemical synthesis of 1T phase TMDs is a recent popular and effective method compared to those traditional low-yield procedures, such as the above-mentioned chemical exfoliation method and chemical vapor deposition (CVD) method.^[42, 80] Liu et al. employed bottom-up hydrothermal synthetic strategy to successfully synthesize a highly stable 1T-phase WS₂ nanoribbon with an unusual zigzag-chain type superlattice structure.^[81] By confirming with synchrotron radiation-based X-ray absorption, this structure exhibited W-W reconstruction and W-S distorted octahedral coordination. Mahler and co-workers described a novel colloidal synthesis method to successfully prepare distorted 1T-WS₂ and regular 2H-WS₂, respectively, and investigated their co-catalytic H₂ evolution activities over TiO₂ (P25)

photoharvester.^[49] Similar case was also presented in Xiong group's study.^[82] They employed chemical exfoliated 1T and 2H phases MoS₂ as the co-catalysts over TiO₂ and investigated their photocatalytic performance. The photocatalytic H₂ evolution activities were in the following order: 1T-MoS₂/TiO₂ > TiO₂ > 2H-MoS₂/TiO₂. They believed that 2H-phase MoS₂ did not provide any reaction sites on the basal plane and the photo-excited electrons had to transfer to the active sites on exposed edges; however, 1T-phase MoS₂ not only acted as electron delivery channels with higher mobility, but also offered additional reaction sites for H₂ evolution on their basal plane. Thus, from the above mentioned experimental results, we can conclude that as the photo-co-catalysts, TMDs with metallic 1T-phase exhibit better abilities for the separation of photo-excited electron-hole pairs from the semiconductors, where they play the role of electronic conductor for the photo-excited electrons transport to the active sites.

1.4.3 Energy band engineering

As the typical layered structural TMDs, the layer-dependent properties have recently attracted a significant attention. It is well known that for the 2H-phase semiconducting MoS₂ and WS₂, there is a transition from an indirect band-gap in the bulk to a direct gap for monolayer, corresponding to their band gap tunable from ~1.2 to ~1.9 eV.^[52, 53] This discovery led to an increase in the research interest in layer-dependent band structure variation in TMDs, in particular, in their optical and optoelectronic properties.^[42, 83, 84] Coleman and co-workers discovered the liquid exfoliation method which can produce mono- and few-layer nanosheets of TMDs in common solvents, since then this method, insensitive to air and water, can be scaled up to produce high quantities of exfoliated TMD materials.^[85] Based on this method, the layer-dependent TMD materials could be obtained by combination of ultrasonication and gradient centrifugation method.^[86-88] Lately, Coleman's group through the optical extinction spectrum of liquid dispersion of MoS₂ nanosheets determined the mean values of physical properties MoS₂, including its nanosheet size, thickness, and concentration, as shown in Figure 1.9.^[89] MoS₂ band sedimentation used centrifugation technique, which led to the spreading of the material through the vial such that nanosheet mass increased from top to bottom. The extinction spectrum of these fractions indicated that the ratio of

Ext_B/Ext_{345} and position of A-exciton increased from thin and small sized nanosheets to large and thick nanosheets. Through the atomic force microscopy (AFM), photoluminescence (PL), and Raman techniques, the quantification gave access to the determination of mean flake length and thickness in one single extinction measurement. Noteworthy, the extinction coefficient at 345 nm is widely independent on nanosheet thickness and length, allowing the extinction spectrum to be used to measure concentration of liquid exfoliated TMD nanosheets. Moreover, with the increase in the layer numbers, λ_A (approximately corresponding to the band gap of MoS_2) increased, indicating that the band gap of MoS_2 could be tuned through the layer numbers.

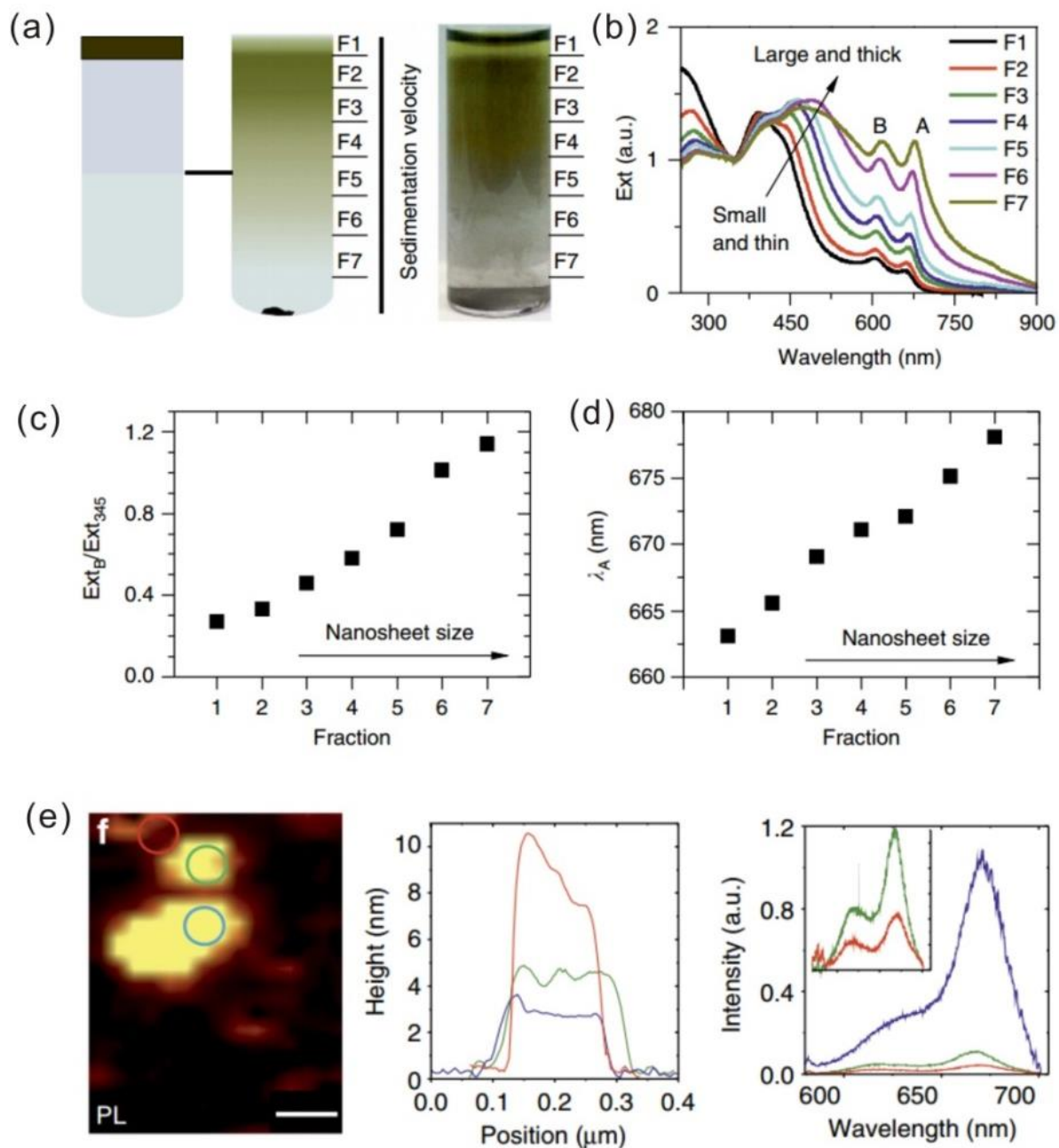


Figure 1.9 (a) MoS₂ band sedimentation centrifugation involving layering a nanomaterial stock dispersion on top of a race layer, (b) extinction spectrum of the fractions normalized to the local minimum at 345 nm, (c) ratio of extinction at B-exciton to that at 345 nm, Ext_B/Ext_{345} plotted versus fraction number, (d) Peak position (wavelength) of the A-exciton with different fractions, (e) PL mapping of different layered MoS₂ and corresponding thickness and PL intensities.^[89]

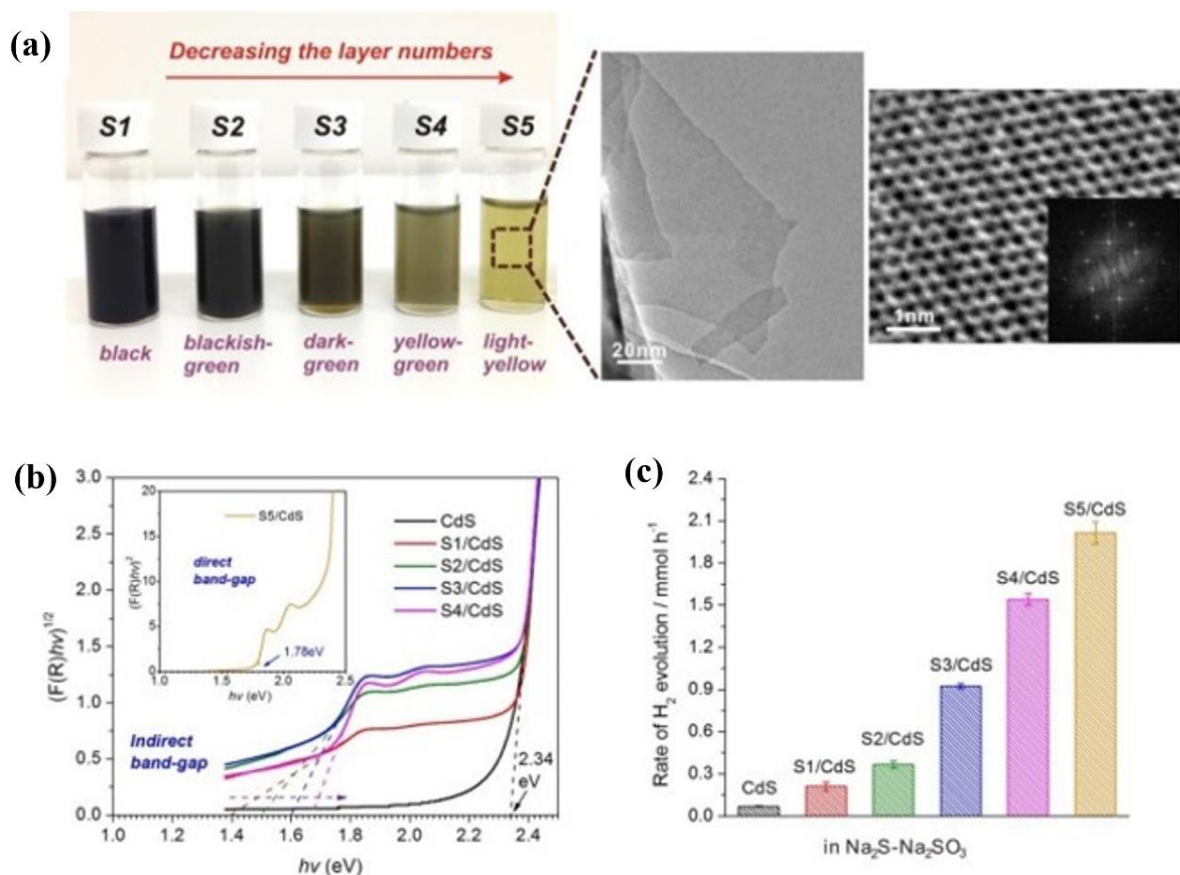


Figure 1.10 (a) Photograph of different MoS₂ samples with the decreasing layer numbers from S1 to S5, and TEM, HRTEM images of corresponding S5, (b) plots of $(F(R)hv)^{1/2}$ vs. (hv) for estimation of the optical band gaps of MoS₂ samples from S1/CdS to S4/CdS according to the indirect band gap of MoS₂, the insert shows plots of $(F(R)hv)^2$ vs. (hv) for estimation of the optical band gaps of SL-MoS₂ according to the direct band gap of MoS₂, (c) photocatalytic H₂ production activities of different samples in 300 mL of 0.35 mol L⁻¹ of Na₂S-Na₂SO₃ aqueous solution, in which the amount of co-catalyst is 2.0 wt%.^[90]

It is well known that by tuning layer numbers of MoS₂ from bulk to single-layer, its bandgap increases from 1.3 to 1.8 eV, arising from quantum confinement effects (Figure 1.10).^[90] During the photocatalytic H₂ evolution activity experiments, the drastic H₂ evolution catalytic activities could be observed with the decrease in MoS₂ layer numbers, in particular, the single-layer/CdS showed the highest catalytic activity toward HER, corresponding to an AQE of 30.2% in Na₂S-Na₂SO₃ solution and 38.4% in lactic acid solution at 420 nm. The UV-vis diffuse reflectance spectrum of single-layer/CdS along with the AQE of H₂ evolution as a function of incident light wavelength demonstrated that pure MoS₂ even with single-layer had negligible contribution to the H₂ evolution in the composites. The main effect of MoS₂ is to provide a suitable CB position for the photo-excited electrons from CdS injection to participate in hydrogen reduction reaction. The improvement in H₂ evolution activities due to the influence of nanostructure is attributed to the presence of more exposed edges for single-layer MoS₂. Nevertheless, from the energy band structure influence, it is known that single-layer MoS₂ showed the more negative CBM energy level than the H⁺/H₂ potential compared to the commercial MoS₂, and thereby exhibited good hydrogen reduction ability.

The single-layer WS₂ exhibits structure and properties similar to those of MoS₂; thus it can also be a good co-catalyst for HER. Chen and co-workers reported a facile one-pot wet-chemical method to synthesize single-layer MoS₂ and WS₂ selectively grown on the Cd-rich (0001) surface of wurtzite CdS nanocrystals (Figure 1.11), respectively.^[91] These single-layer MS₂/CdS (M = Mo, W) nanocomposites possess a large number of edge sites in the MS₂ layers, which are active sites for catalytic H₂ evolution. During the photocatalytic H₂ production activity test in lactic acid solution, both the single-layer MS₂/CdS nanocomposites exhibited H₂ production rate several times than that of pure CdS (Figure 18d). Comparison of their activities indicated that the single-layer WS₂/CdS showed a higher catalytic H₂ production activity than single-layer MoS₂/CdS.

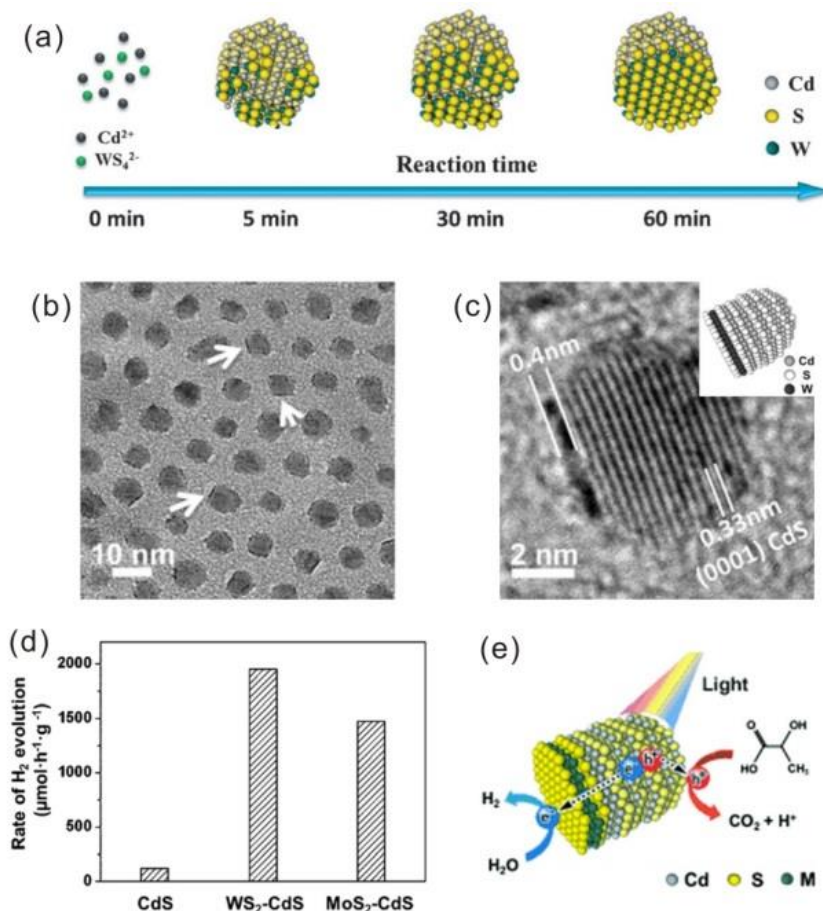


Figure 1.11 (a) Schematic illustration of the shape evolution of WS₂-CdS nanohybrids, (b) TEM image of WS₂ monolayer grown on the Cd-rich (0001) surface of CdS nanocrystals, (c) HRTEM image of WS₂-CdS nanohybrids, (d) comparison of photocatalytic H₂ evolution rate for CdS, WS₂-CdS and MoS₂-CdS, and (e) schematic illustration of the photocatalytic process of MS₂-CdS nanohybrids in the lactic acid solution.^[91]

The 1T-phase metallic TMDs exhibit promising potential catalytic H₂ evolution activities; however, they are metastable structures. For 2H-phase TMDs with semiconducting properties, the layer numbers and active edge sites determine their catalytic H₂ activities, in which the single-layer TMDs with smaller sheet size exhibit the excellent catalytic activities toward HER. However, they only can be as the co-catalysts over the photo-harvesters which show the more negative CB position than themselves, such as

CdS, C₃N₄ etc, but mismatched with TiO₂ which shows the more positive CB position than that of 2H phase single-layer TMDs.

1.5 Research Motivation and thesis organization

The production of hydrogen fuels by using sunlight is an attractive and sustainable solution to the global energy and environmental problems. Pt is known as the most efficient co-catalyst in HER. However, due to its high-cost and limited-reserve, it is highly demanded to explore the alternative non-precious metal co-catalysts with low-cost and high efficiency. In recent years, monolayer TMDs including MoS₂ and WS₂ are regarded as promising HER candidates to replace Pt due to their highly active edge sites for hydrogen adsorption ($\Delta G_H \sim 0.08$ eV) and large in-plane electron mobilities (>200 cm² V⁻¹ s⁻¹). Their unique structural and electronic properties allow them to have many opportunities to be designed as the highly efficient co-catalysts over various photo harvesting semiconductors. However, so far facile and efficient preparation of TMDs monolayers has faced with great challenges. Furthermore, the inert but thermodynamic favorable basal planes significantly limit their efficiency in photocatalytic HER. Thus, this thesis focused on targeted synthesis of TMDs monolayers with various phases, lateral sizes, crystallinities, and atomic structures to create more active sites, in particular reactivate the inert basal plane towards superior cocatalytic performance for photocatalytic HER.

The dissertation is divided into six chapters. A summary of the remaining five chapters follows:

Chapter 2 Targeted synthesis of 2H- and 1T-phase MoS₂ monolayers for catalytic hydrogen evolution

Previous studies show that both 2H and 1T phased MoS₂ monolayers bear great promising in non-previous catalysts for HER. However, the low yield production and the complication strategy for preparing metallic 1T- phase MoS₂ monolayers strictly restrict its further development and application. In this chapter, a facile and effective lithium molten salt assisted method was developed to synthesize a

series of MoS₂ precursors by simply controlling the calcination temperature. These precursors can be easily and accurately exfoliated into 2H- and 1T-phase MoS₂ monolayers by subsequent hydrolysis process. During the synthesis process, lithium molten salt not only acts as the fluxing medium, but also controls the MoS₂ phases switching between 1T and 2H. After loading on different semiconducting photo-harvesters, the catalytic H₂ performance of different phased MoS₂ monolayers were comprehensively studied.

Chapter 3 Engineering the edges of transition metal disulfides for direct exfoliation into monolayers in polar micromolecular solvents and their cocatalytic performances

Direct exfoliation of layered TMDs into monolayer nanosheets in polar micromolecular solvents, such as ethanol and water, is a challenge and of great interest. In this chapter, I present a novel strategy of engineering the lateral size of MoS₂ and WS₂ crystals in the nanoscale to increase the fraction of edges. The increased edges can significantly improve the ratio of hydrodynamic forces to interlayer van der Waals forces, which is expected to allow for ready exfoliation of TMDs in polar micromolecular solvents to produce monolayer nanosheets in high yield. Their cocatalytic performance was systematically investigated by optimizing sacrificial agents, PH values, and loading amount on CdS for photocatalytic HER.

Chapter 4 Engineering crystallinity of MoS₂ monolayers for enhanced cocatalytic activity

Although the edge site of MoS₂ monolayers is highly active for catalytic HER, thermodynamics favors the formation of inactive basal planes that restricts the presence of active edge sites. In the previous studies of electrocatalysis, crystallinity engineering considers as an efficient way to introduce structural disorder and unsaturated atoms as active sites for catalytic reactions. This chapter investigated the crystallinity-dependent MoS₂ monolayers through liquid exfoliation of the corresponding crystallinity-controllable bulk precursors. The crystallinity engineering is expected to introduce unsaturated sulfur atoms as additional active sites, leading to an enhanced cocatalytic performance of MoS₂ monolayers.

Chapter 5 Maximizing synergistic cocatalytic activity of MoS₂ monolayers combining crystallinity engineering and cobalt substitution

In the last chapter, in order to maximizing the synergistic cocatalytic performance of MoS₂ monolayers, an attempt study for reactivating the inert basal plane for HER was carried out by combining crystallinity engineering and cobalt doping. Chemical doping is usually utilized to improve the intrinsic properties of the material and recent works suggest that either cation or anion doping can decrease the ΔG_H of MoS₂ basal plane. The combination of crystallinity engineering and cobalt doping is expected to not only create more active sites, but also reactivate the inert basal planes, leading to a maximized synergistic cocatalytic activity. The density functional theory (DFT) calculations was carried out to examine the active sties by absorption ability of H*.

Chapter 6 General conclusion and future prospects

This chapter makes an overall summary and conclusions of the results in this dissertation work. The prospects for further work were also presented in this chapter.

Reference

- [1] J. F. Xie, J. J. Zhang, S. Li, F. Grote, X. D. Zhang, H. Zhang, R. X. Wang, Y. Lei, B. C. Pan, Y. Xie, *J. Am. Chem. Soc.* 2013, *135*, 17881.
- [2] M. A. Lukowski, A. S. Daniel, F. Meng, A. Forticaux, L. S. Li, S. Jin, *J. Am. Chem. Soc.* 2013, *135*, 10274.
- [3] A. Fujishima, K. Honda, *Nature* 1972, *238*, 37.
- [4] Z. G. Zou, J. H. Ye, K. Sayama, H. Arakawa, *Nature* 2001, *414*, 625.
- [5] H. Tong, S. X. Ouyang, Y. P. Bi, N. Umezawa, M. Oshikiri, J. H. Ye, *Adv. Mater.* 2012, *24*, 229.
- [6] Q. Yu, X. G. Meng, T. Wang, P. Li, J. H. Ye, *Adv. Funct. Mater.* 2015, *25*, 2686.

- [7] Z. B. Jiao, Y. Zhang, S. X. Ouyang, H. C. Yu, G. X. Lu, J. H. Ye, Y. P. Bi, *ACS Appl. Mater. Interfaces* 2014, 6, 19488.
- [8] P. Li, H. Abe, J. H. Ye, *International Journal of Photoenergy* 2014.
- [9] J. W. Shi, J. H. Ye, L. J. Ma, S. X. Ouyang, D. W. Jing, L. J. Guo, *Chemistry-a European Journal* 2012, 18, 7543.
- [10] H. Xu, X. Q. Chen, S. X. Ouyang, T. Kako, J. H. Ye, *J. Phys. Chem. C* 2012, 116, 3833.
- [11] J. Y. Cao, Y. J. Zhang, H. Tong, P. Li, T. Kako, J. H. Ye, *Chem. Commun.* 2012, 48, 8649.
- [12] J. W. Shi, J. H. Ye, Z. H. Zhou, M. T. Li, L. J. Guo, *Chemistry-a European Journal* 2011, 17, 7858.
- [13] Q. Yu, X. G. Meng, T. Wang, P. Li, L. Q. Liu, K. Chang, G. G. Liu, J. H. Ye, *Chem. Commun.* 2015, 51, 3630.
- [14] Q. Kang, J. Y. Cao, Y. J. Zhang, L. Q. Liu, H. Xu, J. H. Ye, *Journal of Materials Chemistry A* 2013, 1, 5766.
- [15] A. Kudo, Y. Miseki, *Chem. Soc. Rev.* 2009, 38, 253.
- [16] A. J. Bard, *J Photochem* 1979, 10, 59.
- [17] K. Maeda, *Acs Catalysis* 2013, 3, 1486.
- [18] J. H. Yang, D. G. Wang, H. X. Han, C. Li, *Acc. Chem. Res.* 2013, 46, 1900.
- [19] T. K. Townsend, N. D. Browning, F. E. Osterloh, *Energy & Environmental Science* 2012, 5, 9543.
- [20] K. Sayama, H. Arakawa, K. Domen, *Catal. Today* 1996, 28, 175.
- [21] H. Kato, A. Kudo, *Chem. Phys. Lett.* 1998, 295, 487.
- [22] K. Yamaguti, S. Sato, *J Chem Soc Farad T 1* 1985, 81, 1237.
- [23] H. Kato, A. Kudo, *Catal. Lett.* 1999, 58, 153.
- [24] X. S. Tang, Q. L. Tay, Z. Chen, Y. Chen, G. K. L. Goh, J. M. Xue, *Journal of Materials Chemistry A* 2013, 1, 6359.
- [25] X. X. Zou, Y. Zhang, *Chem. Soc. Rev.* 2015, 44, 5148.

- [26] P. D. Tran, L. F. Xi, S. K. Batabyal, L. H. Wong, J. Barber, J. S. C. Loo, *Phys. Chem. Chem. Phys.* 2012, *14*, 11596.
- [27] W. J. Foo, C. Zhang, G. W. Ho, *Nanoscale* 2013, *5*, 759.
- [28] J. G. Yu, Y. Hai, M. Jaroniec, *J. Colloid Interface Sci.* 2011, *357*, 223.
- [29] S. P. Xu, D. D. Sun, *Int. J. Hydrogen Energy* 2009, *34*, 6096.
- [30] J. G. Yu, Y. Hai, B. Cheng, *J. Phys. Chem. C* 2011, *115*, 4953.
- [31] J. G. Yu, J. R. Ran, *Energy & Environmental Science* 2011, *4*, 1364.
- [32] M. Tabata, K. Maeda, T. Ishihara, T. Minegishi, T. Takata, K. Domen, *J. Phys. Chem. C* 2010, *114*, 11215.
- [33] J. Wang, B. Li, J. Z. Chen, N. Li, J. F. Zheng, J. H. Zhao, Z. P. Zhu, *Appl. Surf. Sci.* 2012, *259*, 118..
- [34] A. H. Ye, W. Q. Fan, Q. H. Zhang, W. P. Deng, Y. Wang, *Catalysis Science & Technology* 2012, *2*, 969.
- [35] T. Y. Peng, K. Li, P. Zeng, Q. G. Zhang, X. G. Zhang, *J. Phys. Chem. C* 2012, *116*, 22720.
- [36] R. G. Dickinson, L. Pauling, *J. Am. Chem. Soc.* 1923, *45*, 1466.
- [37] M. Chhowalla, H. S. Shin, G. Eda, L. J. Li, K. P. Loh, H. Zhang, *Nat Chem* 2013, *5*, 263.
- [38] J. A. Wilson, F. J. Disalvo, S. Mahajan, *Adv Phys* 1975, *24*, 117.
- [39] X. R. Qin, D. Yang, R. F. Frindt, J. C. Irwin, *Physical Review B* 1991, *44*, 3490.
- [40] F. Wypych, R. Schollhorn, *J Chem Soc Chem Comm* 1992, 1386.
- [41] A. N. Enyashin, L. Yadgarov, L. Houben, I. Popov, M. Weidenbach, R. Tenne, M. Bar-Sadan, G. Seifert, *J. Phys. Chem. C* 2011, *115*, 24586.
- [42] G. Eda, H. Yamaguchi, D. Voiry, T. Fujita, M. W. Chen, M. Chhowalla, *Nano Lett* 2011, *11*, 5111.
- [43] Y. M. Kang, S. Najmaei, Z. Liu, Y. J. Bao, Y. M. Wang, X. Zhu, N. J. Halas, P. Nordlander, P. M. Ajayan, J. Lou, Z. Y. Fang, *Adv. Mater.* 2014, *26*, 6467.

- [44] U. Maitra, U. Gupta, M. De, R. Datta, A. Govindaraj, C. N. R. Rao, *Angewandte Chemie-International Edition* 2013, 52, 13057.
- [45] F. Wypych, R. Schollhorn, *Quim. Nova* 1996, 19, 5.
- [46] D. Voiry, H. Yamaguchi, J. W. Li, R. Silva, D. C. B. Alves, T. Fujita, M. W. Chen, T. Asefa, V. B. Shenoy, G. Eda, M. Chhowalla, *Nat. Mater.* 2013, 12, 850.
- [47] U. Gupta, B. S. Naidu, U. Maitra, A. Singh, S. N. Shirodkar, U. V. Waghmare, C. N. R. Rao, *Apl Mater* 2014, 2.
- [48] R. Kappera, D. Voiry, S. E. Yalcin, W. Jen, M. Acerce, S. Torrel, B. Branch, S. D. Lei, W. B. Chen, S. Najmaei, J. Lou, P. M. Ajayan, G. Gupta, A. D. Mohite, M. Chhowalla, *Apl Mater* 2014, 2.
- [49] B. Mahler, V. Hoepfner, K. Liao, G. A. Ozin, *J. Am. Chem. Soc.* 2014, 136, 14121.
- [50] D. B. Putungan, J. L. Kuo, *Integr Ferroelectr* 2014, 156, 93.
- [51] R. Raja, P. Sudhagar, A. Devadoss, C. Terashima, L. K. Shrestha, K. Nakata, R. Jayavel, K. Ariga, A. Fujishima, *Chem. Commun.* 2015, 51, 522.
- [52] K. F. Mak, C. Lee, J. Hone, J. Shan, T. F. Heinz, *Phys. Rev. Lett.* 2010, 105.
- [53] Q. H. Wang, K. Kalantar-Zadeh, A. Kis, J. N. Coleman, M. S. Strano, *Nat. Nanotechnol.* 2012, 7, 699.
- [54] A. Kuc, N. Zibouche, T. Heine, *Physical Review B* 2011, 83, 245213.
- [55] J. K. Nørskov, T. Bligaard, J. Rossmeisl, C. H. Christensen, *Nature Chem.* 2009, 1, 37.
- [56] S. Trasatti, *J. Electroanal. Chem.* 1972, 39, 163.
- [57] B. Hinnemann, P. G. Moses, J. Bonde, K. P. Jørgensen, J. H. Nielsen, S. Horch, I. Chorkendorff, J. K. Nørskov, *J. Am. Chem. Soc.* 2005, 127, 5308.
- [58] T. F. Jaramillo, K. P. Jørgensen, J. Bonde, J. H. Nielsen, S. Horch, I. Chorkendorff, *Science* 2007, 317, 100.
- [59] Y. G. Li, H. L. Wang, L. M. Xie, Y. Y. Liang, G. S. Hong, H. J. Dai, *J. Am. Chem. Soc.* 2011, 133, 7296.
- [60] S. X. Min, G. X. Lu, *J. Phys. Chem. C* 2012, 116, 25415.

- [61] Z. Y. Lu, W. Zhu, X. Y. Yu, H. C. Zhang, Y. J. Li, X. M. Sun, X. W. Wang, H. Wang, J. M. Wang, J. Luo, X. D. Lei, L. Jiang, *Adv. Mater.* 2014, 26, 2683.
- [62] H. I. Karunadasa, E. Montalvo, Y. J. Sun, M. Majda, J. R. Long, C. J. Chang, *Science* 2012, 335, 698.
- [63] X. Zong, H. J. Yan, G. P. Wu, G. J. Ma, F. Y. Wen, L. Wang, C. Li, *J. Am. Chem. Soc.* 2008, 130, 7176.
- [64] X. Zong, J. F. Han, G. J. Ma, H. J. Yan, G. P. Wu, C. Li, *J. Phys. Chem. C* 2011, 115, 12202.
- [65] H. J. Yan, J. H. Yang, G. J. Ma, G. P. Wu, X. Zong, Z. B. Lei, J. Y. Shi, C. Li, *J. Catal.* 2009, 266, 165.
- [66] I. Tsuji, H. Kato, H. Kobayashi, A. Kudo, *J. Am. Chem. Soc.* 2004, 126, 13406.
- [67] K. Hara, K. Sayama, H. Arakawa, *Applied Catalysis a-General* 1999, 189, 127.
- [68] K. Hara, K. Sayama, H. Arakawa, *J Photoch Photobio A* 1999, 128, 27.
- [69] M. A. Fox, T. L. Pettit, *Langmuir* 1989, 5, 1056.
- [70] K. Chang, Z. W. Mei, T. Wang, Q. Kang, S. X. Ouyang, J. H. Ye, *Acs Nano* 2014, 8, 7078.
- [71] D. Voiry, M. Salehi, R. Silva, T. Fujita, M. W. Chen, T. Asefa, V. B. Shenoy, G. Eda, M. Chhowalla, *Nano Lett.* 2013, 13, 6222.
- [72] Q. Ding, F. Meng, C. R. English, M. Caban-Acevedo, M. J. Shearer, D. Liang, A. S. Daniel, R. J. Hamers, S. Jin, *J. Am. Chem. Soc.* 2014, 136, 8504.
- [73] J. A. Wilson, A. D. Yoffe, *Adv Phys* 1969, 18, 193.
- [74] R. Bissessur, M. G. Kanatzidis, J. L. Schindler, C. R. Kannewurf, *J Chem Soc Chem Comm* 1993, 1582.
- [75] M. A. Py, R. R. Haering, *Canadian Journal of Physics* 1983, 61, 76.
- [76] H. T. Wang, Z. Y. Lu, S. C. Xu, D. S. Kong, J. J. Cha, G. Y. Zheng, P. C. Hsu, K. Yan, D. Bradshaw, F. B. Prinz, Y. Cui, *P Natl Acad Sci USA* 2013, 110, 19701.
- [77] N. Imanishi, M. Toyoda, Y. Takeda, O. Yamamoto, *Solid State Ionics* 1992, 58, 333.

- [78] Z. Y. Zeng, T. Sun, J. X. Zhu, X. Huang, Z. Y. Yin, G. Lu, Z. X. Fan, Q. Y. Yan, H. H. Hng, H. Zhang, *Angewandte Chemie-International Edition* 2012, *51*, 9052.
- [79] Y. Shi, J. Wang, C. Wang, T. T. Zhai, W. J. Bao, J. J. Xu, X. H. Xia, H. Y. Chen, *J. Am. Chem. Soc.* 2015, *137*, 7365.
- [80] R. Kappera, D. Voiry, S. E. Yalcin, B. Branch, G. Gupta, A. D. Mohite, M. Chhowalla, *Nat. Mater.* 2014, *13*, 1128.
- [81] Q. Liu, X. L. Li, Z. R. Xiao, Y. Zhou, H. P. Chen, A. Khalil, T. Xiang, J. Q. Xu, W. S. Chu, X. J. Wu, J. L. Yang, C. M. Wang, Y. J. Xiong, C. H. Jin, P. M. Ajayan, L. Song, *Adv. Mater.* 2015, *27*, 4837.
- [82] S. Bai, L. M. Wang, X. Y. Chen, J. T. Du, Y. J. Xiong, *Nano Res* 2015, *8*, 175.
- [83] A. Splendiani, L. Sun, Y. B. Zhang, T. S. Li, J. Kim, C. Y. Chim, G. Galli, F. Wang, *Nano Lett.* 2010, *10*, 1271.
- [84] R. S. Sundaram, M. Engel, A. Lombardo, R. Krupke, A. C. Ferrari, P. Avouris, M. Steiner, *Nano Lett.* 2013, *13*, 1416.
- [85] J. N. Coleman, M. Lotya, A. O'Neill, S. D. Bergin, P. J. King, U. Khan, K. Young, A. Gaucher, S. De, R. J. Smith, I. V. Shvets, S. K. Arora, G. Stanton, H. Y. Kim, K. Lee, G. T. Kim, G. S. Duesberg, T. Hallam, J. J. Boland, J. J. Wang, J. F. Donegan, J. C. Grunlan, G. Moriarty, A. Shmeliov, R. J. Nicholls, J. M. Perkins, E. M. Grievson, K. Theuwissen, D. W. McComb, P. D. Nellist, V. Nicolosi, *Science* 2011, *331*, 568.
- [86] K. Chang, M. Li, T. Wang, S. X. Ouyang, P. Li, L. Q. Liu, J. H. Ye, *Advanced Energy Materials* 2015, *5*, DOI: 10.1002/aenm.201402279.
- [87] T. Y. Wang, D. L. Gao, J. Q. Zhuo, Z. W. Zhu, P. Papakonstantinou, Y. Li, M. X. Li, *Chemistry-a European Journal* 2013, *19*, 11939.
- [88] C. Backes, R. J. Smith, N. McEvoy, N. C. Berner, D. McCloskey, H. C. Nerl, A. O'Neill, P. J. King, T. Higgins, D. Hanlon, N. Scheuschner, J. Maultzsch, L. Houben, G. S. Duesberg, J. F. Donegan, V. Nicolosi, J. N. Coleman, *Nature Communications* 2014, *5*, 4576.

- [89] C. Backes, R. J. Smith, N. McEvoy, N. C. Berner, D. McCloskey, H. C. Nerl, A. O'Neill, P. J. King, T. Higgins, D. Hanlon, N. Scheuschner, J. Maultzsch, L. Houben, G. S. Duesberg, J. F. Donegan, V. Nicolosi, J. N. Coleman, *Nature Communications* 2014, 5.
- [90] T. R. Thurston, J. P. Wilcoxon, *J. Phys. Chem. B* 1999, 103, 11.
- [91] J. Z. Chen, X. J. Wu, L. S. Yin, B. Li, X. Hong, Z. X. Fan, B. Chen, C. Xue, H. Zhang, *Angewandte Chemie-International Edition* 2015, 54, 1210.

Chapter 2 Targeted synthesis of 2H- and 1T-phase MoS₂ monolayers for catalytic hydrogen evolution reaction

2.1 Introduction

Since the discovery of graphene, a state-of-the-art one-atom-thick monolayer exfoliated from graphite,^[1, 2] a lot of attention has been devoted to study various types of monolayer materials.^[3, 4] Transition metal dichalcogenides (TMDCs) in which a monolayer is comprised of two close-packed chalcogenide planes sandwiching a transition-metal layer have the analogue layered structure of graphite and therefore also can be exfoliated into monolayers by chemical and physical methods.^[5] Pioneering work have showed monolayer TMDCs bear great promise in two-dimensional materials because of their multiple transformable properties, ranging from insulators to semiconductors to metals,^[6] which could find applications in diverse fields such as transistors,^[7] photodetectors,^[8] optoelectronics,^[9] secondary batteries,^[10] and catalysis.^[11, 12]

As the most representative family member of TMDCs, MoS₂, in particular the monolayer structure, has been extensively investigated because of its large in-plane electron mobility ($> 200 \text{ cm}^2 \text{ V}^{-1} \text{ s}^{-1}$), high current on/off ratios, remarkable mechanical and optical properties, as well as high catalytic activity for hydrogen evolution reaction (HER).^[13-16] Natural MoS₂ is commonly found in the 2H (hexagonal) phase, showing semiconducting properties with a tunable bandgap of 1.3~1.9 eV, whereas chemical lithium intercalation could induce the phase change of MoS₂ from 2H to 1T (trigonal) which shows the metallic properties.^[17, 18] Previous studies show that both 2H and 1T phased MoS₂ monolayers are found very efficient catalytic hydrogen activities, whereas the former are based on its active exposed edges^[19, 20] and the latter is reported to exhibit the higher activities of HER due to its more active sites on both of the basal plane and edges.^[21, 22]

In general, three kinds of strategy for fabricating monolayer MoS₂ with different phase were well used: (i) physical exfoliation – “tape” method (for 2H phase);^[1, 7] (ii) chemical assisted method – liquid phase exfoliation (LPE) employed the substitute solvent such as NMP (for 2H phase),^[23] and chemical lithium intercalation/extraction exfoliation (for 1T phase);^[18, 24] (iii) Chemical vapor deposition (CVD) (for 2H phase).^[25] Up to now, although people have explored numerous strategies for preparing monolayer MoS₂, there are still two critical issues restricting its further application and development: (1) low yield production for monolayers in pure water. Although LPE is considered to be the most promising route for exfoliating monolayer MoS₂ on a large scale, the dependence on rigorous solvent has narrowed its applicability, in which directly exfoliation of monolayer MoS₂ in polar micromolecular solvents such as water and ethanol would be a great challenge;^[26] (2) complication of strategy for preparing metallic 1T phase. At present, chemical lithium intercalation/extraction exfoliation is still the most effective route to obtain the 1T-phase MoS₂ monolayer with high crystallinity in contrast with colloidal synthesis method in recent reports. However, the rigmarole process and high risk of using metallic lithium reagent allow us to blaze another trail for the 1T-phase MoS₂.

In this chapter, a novel method by employing lithium molten salts to accurately control the different phases of MoS₂ precursor at different calcination temperature was developed. Then with the subsequent hydrolysis reaction of lithium salts, the precursors can be rapidly exfoliated into 2H or 1T phased monolayer MoS₂, which depends on the annealing temperature of the precursors. Our proposed method not only can provide a high yield production of monolayer MoS₂ with high crystallinity, but also can selectively synthesize various phased MoS₂ as I expected, significantly broadening its usability. Finally, I also systematically investigated their catalytic hydrogen activities over electro- and photo-catalytic reactions. Through matching with different photo-harvesters, I comprehensively evaluated the values of different phased MoS₂.

2.2 Experimental section

2.2.1 Synthesis of 2H-MoS₂ monolayers

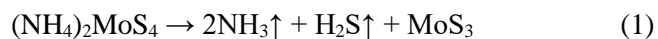
First, 4 mmol LiOH·H₂O (99.95%, Aldrich) was dissolved into 5 ml deionized (DI) water. Then, 2 mmol (NH₄)₂MoS₄ (99.97%, Aldrich) was dissolved into above solution. Afterward, the mixed solution was transferred into alumina crucible which was placed at the center of tube furnace. Under the protection of Ar atmosphere, the temperature was first raised to 80 °C and kept for 5 hours to dry the water in the precursors. Subsequently, the temperature was increased to the proposed values (in the range from 400 to 900 °C) with the rate of 5 °C per minutes and kept for 4 hours, and then allowed to cool down to the room temperature naturally. After that, 50 mg of the annealed samples were added into DI water with stirring and after being sonicated for several minutes. For the samples at 400, 500, and 600 °C, when added into water, the colorless solution immediately change into yellow green. The obtained suspension was centrifuged at 4000 rpm for 45 min to remove the precipitates. The supernatant was centrifuged, collected and wash by DI water and ethanol at 18000 rpm. Then the products were re-dispersed into 50 ml ethanol for later use.

2.2.2 Synthesis of 1T-MoS₂ monolayers

To be similar with above procedures, the exfoliated 1T-MoS₂ could be obtained when annealed temperature of precursor was increased to 1000 and 1100 °C. When added the annealed precursor into water, the colorless solution immediately change into black brown. After sonicated for several minutes, the obtained suspension was centrifuged at 1000 rpm for 45 min to remove the precipitated. The supernatant was centrifuged, collected and wash by DI water and ethanol at 18000 rpm. Then the products were re-dispersed into 50 ml ethanol for later use. The pure samples obtained at 400, 500, 600, 700, 800, 900, 1000, 1100 °C were marked with MoS₂-400, MoS₂-500, MoS₂-600, MoS₂-700, MoS₂-800, MoS₂-900, MoS₂-1000, MoS₂-1100, respectively.

2.2.3 Reaction process of (NH₄)₂MoS₄ and LiOH

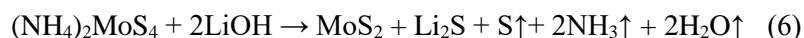
It is known that MoS₂ can be generated by thermal decomposition of (NH₄)₂MoS₄, which the salt decomposes in two distinct steps as following equations:



The first step (equation, eq. 1) involves the decomposition to the MoS₃ and the released NH₃ and H₂S gas, and the second step (eq. 2) the decomposition of the MoS₃ to the MoS₂ and elemental sulfur. Given this, the stoichiometric LiOH was induced into the first step to form Li₂MoS₄ and it is expected to precede the following reactions:



The whole reaction would be:



The first step (eq. 3) is the formation of Li₂MoS₄ and the following decomposition to MoS₃ and Li₂S (eq. 4) and then decomposition of MoS₃ to the MoS₂ (eq. 5). Thus, according to the whole reaction of this process (eq. 6), the generated elemental S, NH₃ and H₂O gas will be released under the high temperature, where the crystalline MoS₂ with around *in-situ* formed Li₂S is left. On the basis of the common knowledge concerning easily hydrolysis of Li₂S to LiOH and H₂S which is an exothermic reaction, the MoS₂ is therefore easily exfoliated after putting the products into the water. Also, it is known that the decomposition temperature of MoS₃ is over 335 °C. I carried out this method and calcined the precursors at the different temperature in the range of 400 to 1100 °C since that MoS₂ is easy sublimated at the high temperature.

2.2.4 Characterization

The samples were characterized by X-ray diffraction (XRD, RINT-2000; Rigaku Corp., Japan) with Cu $K\alpha_1$ radiation, field emission scanning electron microscope (FESEM, Hitachi S-4800), transmission electron microscope (TEM, TECNAI G2 F30, Japan), atomic force mode (AFM, Nanoscope H, Japan), and Raman spectra (Horiba-Jobin-Yvon, T64000, Japan). UV-vis diffuse reflectance spectra were measured using the diffuse reflection method with a Shimadzu UV-2500 spectrophotometer. XPS data were collected using a PHI Quantera SXM (ULVAC-PHI, Japan). Zeta potential data were measured using Beckman/Coulter Delsa Nano analyzer (Japan).

2.2.5 Electrode preparation

Three-electrode cell on a CH Instruments Model 650A electrochemical workstation was used to evaluate the electrochemical activities of various catalysts. Linear sweep voltammetry with a 5 mV s^{-1} scan rate was carried out from 0 to -0.6 V (vs Ag/AgCl) in electrolyte solution under continuous purging with Ar. For the preparation of the working electrode, 1 ml of 0.20 mg ml^{-1} as-synthesized suspensions were mixed with 20 μL Nafion solution (5.0% Nafion in ethanol). The mixture was sonicated and the suspension was spin-coating onto a fluorine doped tin oxide (FTO) substrates with a $1 \text{ cm} \times 1 \text{ cm}$ of area and then fully dried. All electrodes were prepared by depositing the same mass loading of catalysts on FTO using identical method.

2.2.6 Photocatalysts preparation

0.5 g commercial photo-harvesters (P25, CdS) and with 1 wt.% MoS_2 suspension in ethanol are mixed and stirred in ethanol solution at the room temperature until dry. The composite products were transferred into vacuum drying oven to dry overnight at the room temperature.

2.2.7 Photocatalytic H_2 Evolution

The photocatalytic H_2 evolution was carried out with 50 mg photocatalyst suspending in 300 mL solution in a Pyrex glass reaction cell. The reaction cell was connected to a gas-closed system with a

gas-circulated pump. Ultraviolet light was produced by a 300 W Xe lamp and visible light ($\lambda > 420$ nm) was generated by a 300 W Xe lamp combined with a UV-cut-off filter (L42, Hoya Co., Japan). The evolved H_2 was analyzed using an on-line gas chromatograph (GC-8A, Shimadzu Co., Japan) equipped with a thermal conductivity detector (TCD.) The apparent quantum efficiency (AQE) was measured by applying a Xe lamp (300 W) with a 365 nm and 420 nm band-pass filter (MIF-W, Optical Coatings Japan Co., Japan). The number of incident photons was measured using a radiant power energy meter (Ushio Spectroradiometer, USR-40).

2.3 Results and discussion

2.3.1 The synthesis mechanism

During the whole experiments, $(NH_4)_2MoS_4$ and LiOH were employed as the starting materials and calcined in Ar atmosphere under different temperature. The detailed experimental method and chemical reactions of calcining process and relative statements can be referred in Supplementary Information. Figure 2.1 shows the XRD patterns of products calcined from the precursors of $(NH_4)_2MoS_4$ and LiOH in the range of 400 to 1100 °C with intervals of 100 °C. As shown in the analysis results, MoS_2 is the main products for each sample. A few parts of impurities including Li_2MoO_4 , Li_4MoO_5 and $Li_{12}Mo_5O_{17}$ might be caused by the reactions of molybdenum sulfides and lithium oxides generated from the thermal decomposition of LiOH, which can be easily removed in the following washing procedure. Noticeably, the calcined products deliver 2H phased MoS_2 below 600 °C but 3R-type MoS_2 over 700 °C. Generally, both 2H and 3R phase are belonging to the natural layered MoS_2 polymorphs. As the most commonly encountered structure, 2H-phase MoS_2 with the two duplicate unit cells of S-Mo-S layer are stacked along the *c*-axis orientation, while the 3R (rhombohedral) phased MoS_2 exhibits triplicate unit cells of S-Mo-S layer which are stacked together along the *c*-axis^[6]. From the XRD patterns, the notable changes between 2H (PDF 01-073-1508) and 3R (PDF 01-086-2308) MoS_2 polymorphs are that the 002 peak for 2H- MoS_2

at $2\theta = 14.4^\circ$ changes into 003 peak for 3R-MoS₂, and the 103 peak for 2H-MoS₂ at $2\theta = 39.6^\circ$ splits into 104 and 015 two peaks for 3R-MoS₂ at $2\theta = 38.3^\circ$ and 41.1° , respectively. However, the weak 103 peaks are still can be observed in the samples which obtained from 600 to 900 °C, indicating that a small amount of unconverted 2H-MoS₂ exists in the 3R phase. The factor of phase conversion from 2H to 3R might be induced by molten lithium salt which can play a role of fluxing medium.^[27, 28] By contrast, even if the precursor without lithium salt is calcined at 1100 °C, the product still exhibits the 2H structure.

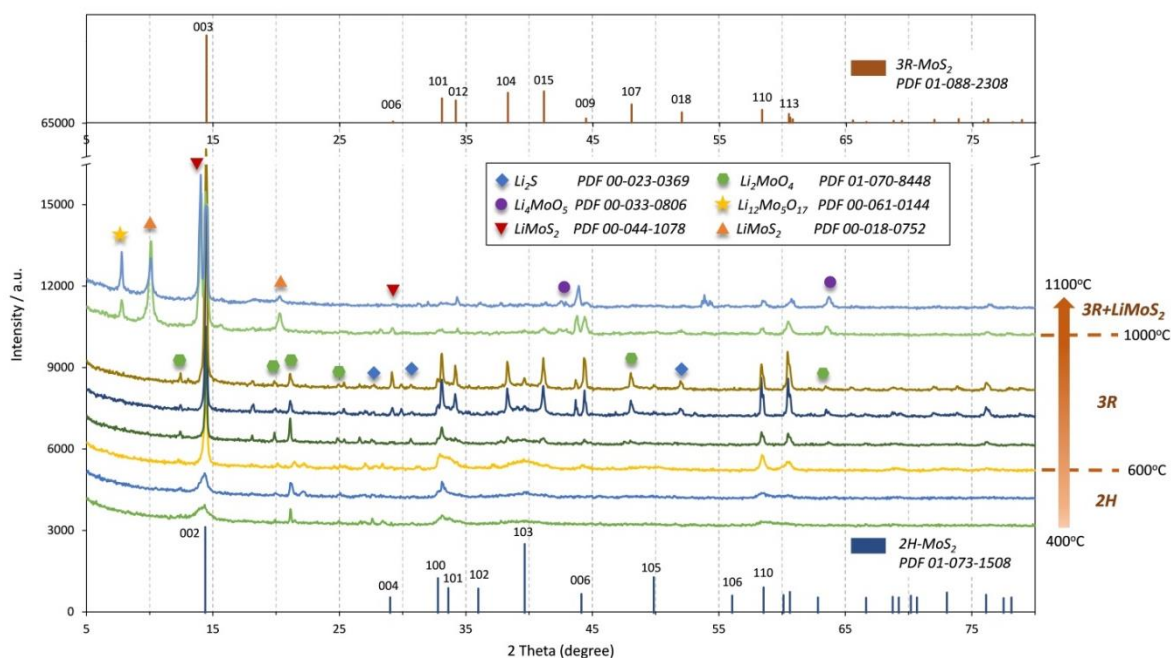


Figure 2.1 XRD patterns of products calcined from the precursors of (NH₄)₂MoS₄ and LiOH in the range of 400 to 1100 °C with per 100 °C. The standard diffraction peak position of 2H-MoS₂ and 3R-MoS₂ are displayed at the bottom and top of the diagram, respectively. The characteristic peaks for each component are marked with different colored symbols.

When the temperature rose over 1000 °C, interesting is that a new compound of LiMoS₂ was generated as shown in Figure 2.1. According to the PDF Card index, the diffraction at $2\theta = 10^\circ$ (PDF 000-018-0752) and 14° (PDF 00-044-1078) belong to two different types of LiMoS₂ peaks, respectively. Figure 2.2 clearly shows the split of LiMoS₂ and 3R-MoS₂ main diffraction peak. To compare with the

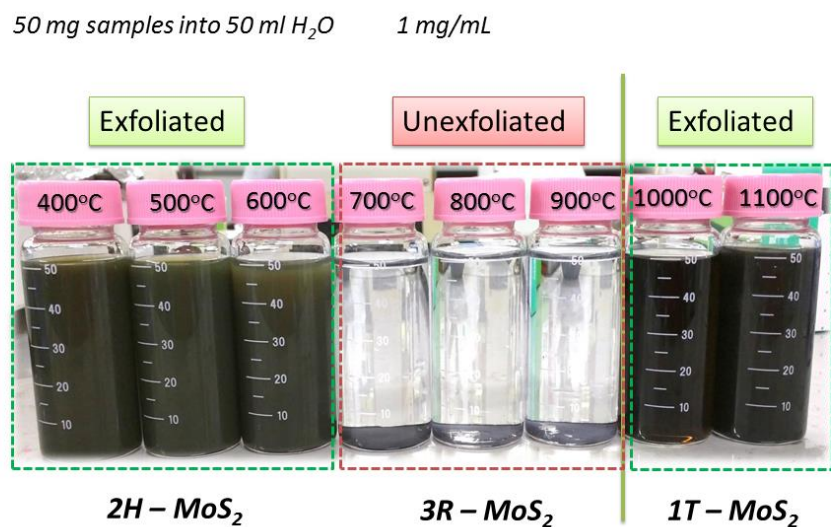


Figure 2.3 Photograph of 50 mg of products calcined at different temperature after reacting with water. The exfoliated suspensions of 2H-MoS₂ show the dark yellow-green color, while the suspensions of 1T-MoS₂ show the dark brown color. 3R-type MoS₂ cannot be exfoliated after reacting with water.

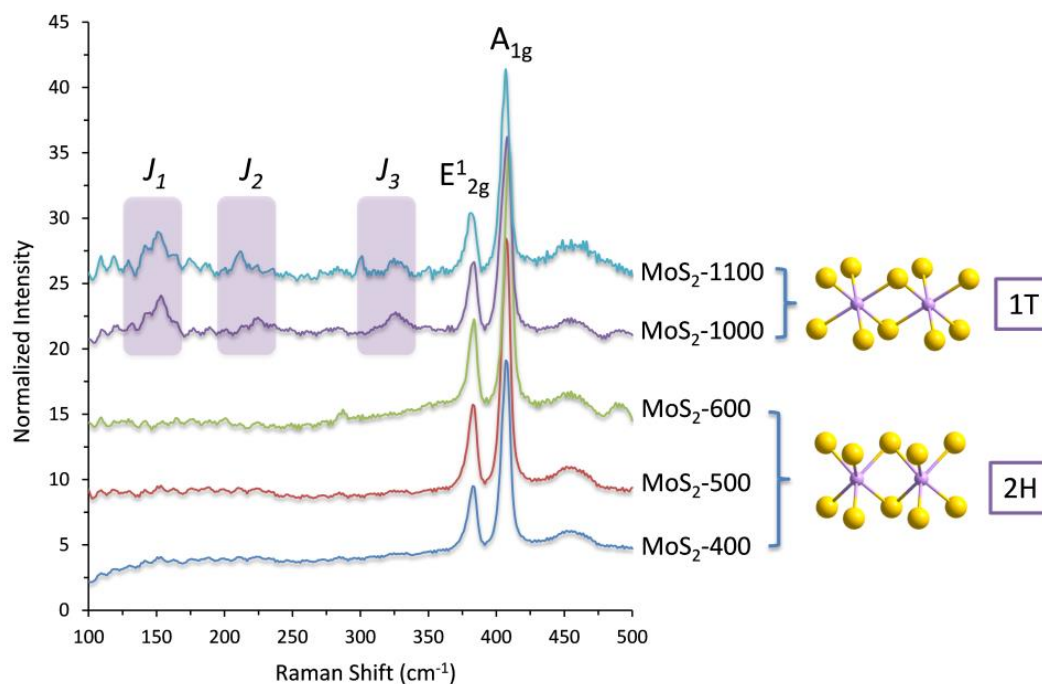


Figure 2.4 Raman spectrum of exfoliated MoS₂ samples and their corresponding schematic illustration of 2H and 1T phase molecular structures.

From the analysis of XRD patterns, it is known that Li_2S existed in the products calcined in the range of 400 ~ 900 °C and LiMoS_2 generated when calcined temperature raised over 1000 °C. Both of the two lithium salts are easily to be hydrolyzed. Simultaneously, these exothermic reactions are facilitating the rapid exfoliation of bulk MoS_2 precursor into monolayer structure. Figure 2.3 give a photograph of products calcined at different temperature after reacting with water. It is seen that the 2H-phase MoS_2 with calcined temperature range of 400 to 600 °C can be easily exfoliated to the yellow-green suspensions, while the 3R-phase MoS_2 with calcination temperature range of 700 to 900 °C cannot be exfoliated. However, when the temperature raised over 1000 °C, the exfoliated black-brown suspensions might indicate the generation of 1T-phase MoS_2 from the Raman spectra (Figure 2.4), which is consistent with the results of XRD analysis. Generally, Raman spectra analysis is the idiomatic and powerful method to determine the MoS_2 phase. Two prominent peaks corresponding to the in-plane E_{2g}^1 and out-of-plane A_{1g} modes of MoS_2 can be clearly seen in all samples. The MoS_2 -1000 and MoS_2 -1100 samples exhibit additional weak peaks in the lower frequency region which marked by shaded regions with J_1 , J_2 and J_3 , respectively. These peaks correspond to modes that are active in 1T-phase MoS_2 but not allowed in 2H- MoS_2 according to previous reports. Our results further confirm that the MoS_2 samples obtained below 600 °C show the 2H-phase trigonal prismatic structures and those MoS_2 samples obtained over 1000 °C exhibit the 1T-phase octahedral prismatic structures.

After washing and redispersing the pure MoS_2 samples into ethanol by the proposed method, the exfoliation degree of each MoS_2 sample could be roughly estimated to 28.2 wt%, 15.0 wt%, 3.0 wt%, 9.8 wt%, and 8.2 wt% for MoS_2 -400, MoS_2 -500, MoS_2 -600, MoS_2 -1000, MoS_2 -1100, respectively. The MoS_2 -400 shows the highest exfoliated production yield among the 2H-phase MoS_2 samples, which might be related with the crystallization of the products. For 1T phase, MoS_2 -1000 shows the approximately equivalent exfoliation degree with MoS_2 -1100, indicating the equivalent amount of generated LiMoS_2 phase at the two different temperatures.

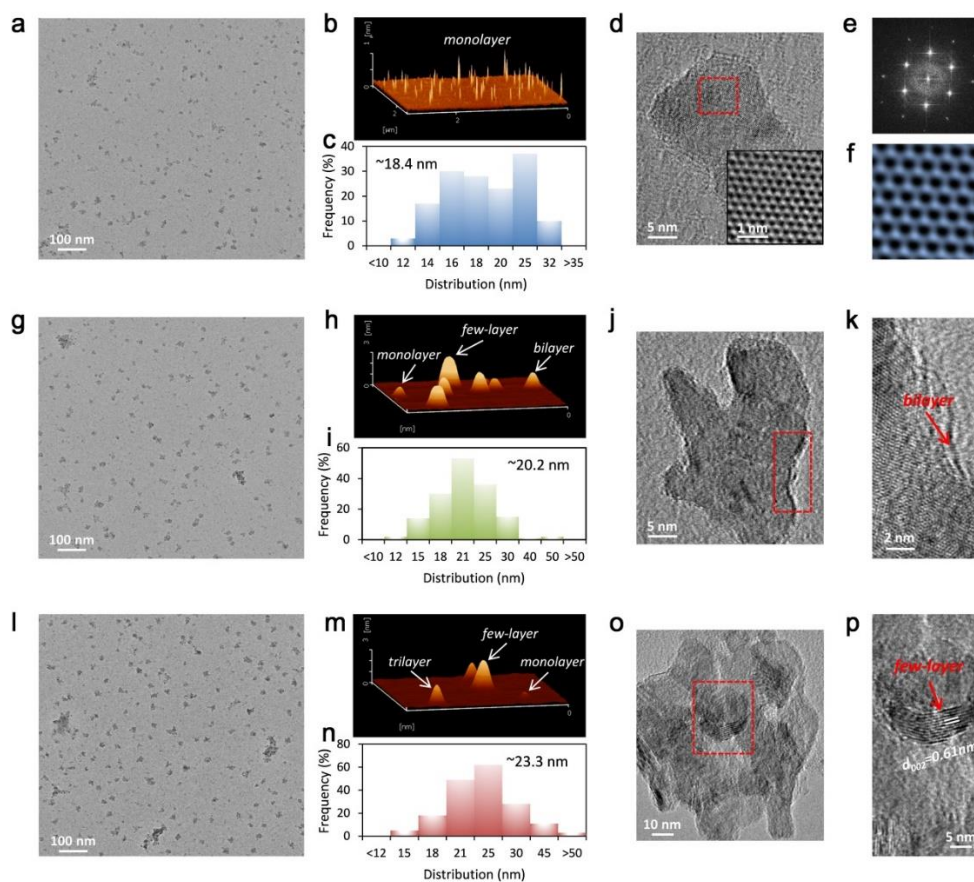
2.3.2 Characterization of obtained 2H- and 1T-phase MoS₂ monolayers

Figure 2.5 Characterizations of size, thickness, and crystal structures of 2H-phase MoS₂ nanosheets obtained at different temperature. (a) TEM image of MoS₂-400, and corresponding (b) 3D mode of AFM image of MoS₂-400, indicating only monolayers of distribution, (c) distribution of diameters with the average value of ~25.1 nm, (d) TEM image of one piece of MoS₂-400 monolayer, the insert shows the HRTEM image of selected region, (e) FFT pattern of selected region of (d), and (f) FFT-filtered atomic resolution selected area in (d). (g) TEM image of MoS₂-500, and corresponding (h) 3D mode of AFM image, indicating co-existence of single or few layers in MoS₂-500, (i) distribution of diameters with the average value of ~25.6 nm, (j) TEM image of MoS₂-500 nanosheet, and (k) HRTEM image of selected region of (j). (l) TEM image of MoS₂-600, and corresponding (m) 3D mode of AFM image, indicating co-existence of single or few layers in MoS₂-600, (n) distribution of diameters with the average value of ~24.2 nm, (o) TEM image of MoS₂-600 nanosheet, and (p) HRTEM image of selected region of (o).

Figure 2.5 gives general information of morphologies, sizes, and crystal structures of exfoliated MoS₂-400, MoS₂-500, and MoS₂-600 samples. The TEM images in Figure 2.5a, 2.5g, and 2.5l show that three samples are distributed uniformly without obvious aggregation. From the nanosheets size statistics in Figure 2.5c, 2.5i, and 2.5n, all the three samples exhibit approximately similar particle size in the range of 20 to 30 nm and the average size of ~25 nm. However, the AFM characterizations demonstrate that only MoS₂-400 samples show the single-layer structure, and co-existence of mono or few layers are presented in MoS₂-500 and MoS₂-600 samples (as seen in Figure 2.5b, 2.5h, and 2.5m). This interesting phenomenon indicates that in this proposed condition, only the sample synthesized at 400 °C can be exfoliated to the single-layer nanostructure. To further reveal the possible mechanism, the structure and morphologies of the precursors before exfoliation were examined by XRD and SEM analysis. As shown in Figure 2.6a, the intensity of 002 diffraction peaks along *c* axis for different samples increases with the increase of the annealing temperature, but the FWHM value decreases. This fact reveals that with the increase of annealing temperature, the stacking degree of MoS₂ layers along *c* axis increases, which also can be reflected in the observation of SEM images in Figure 2.6b to 2.6d. The thickness of MoS₂ layers increases with the raising of the annealing temperature. Moreover, XRD pattern in Figure 2.6a shows that with the increase of annealing temperature, the 002 peak position for the samples shift to the high angle from 14.2° to 14.45°. According to the Bragg equation, it is calculated that the interlayer distance of samples decreases from 0.623 nm to 0.612 nm with the temperature raising from 400 to 600°C. Thus, it is known that the higher temperature could increase the crystallinity and the interlayer stack degree. It might be the reason of difficulty to obtain the pure MoS₂ monolayers for MoS₂-500 and MoS₂-600 samples. To further raise the annealing temperature, as shown in Figure 2.7, the MoS₂ samples can be changed from 2H into 3R phase, in which the large and thick bulk materials are completely unable to be exfoliated. We could examine these objects in more detail using TEM and HRTEM (Figure 2.5d, 2.5j, 2.5k, 2.5o, and 2.5p). For the MoS₂-500 and MoS₂-600 samples, we could find the bilayer and few-layer non-exfoliated MoS₂ nanoparticles with the interlayer distance of ~0.6 nm. The HRTEM image inserted in Figure 2.5d and the associated Fourier transforms (Figure 2.5e) illustrate the hexagonal symmetry of MoS₂-400

sample. After Fast Fourier Transform (FFT) filtering, Figure 2.5f reveals MoS₂ prepared under this temperature exhibiting hexagon widths of 3.8Å, confirming that no distortions were introduced by lithium exfoliation. It is noteworthy that HRTEM image in Figure 2.5d shows that MoS₂-400 sample has exhibited good crystallinity, which might attribute to the role of fluxing medium by molten lithium salt.

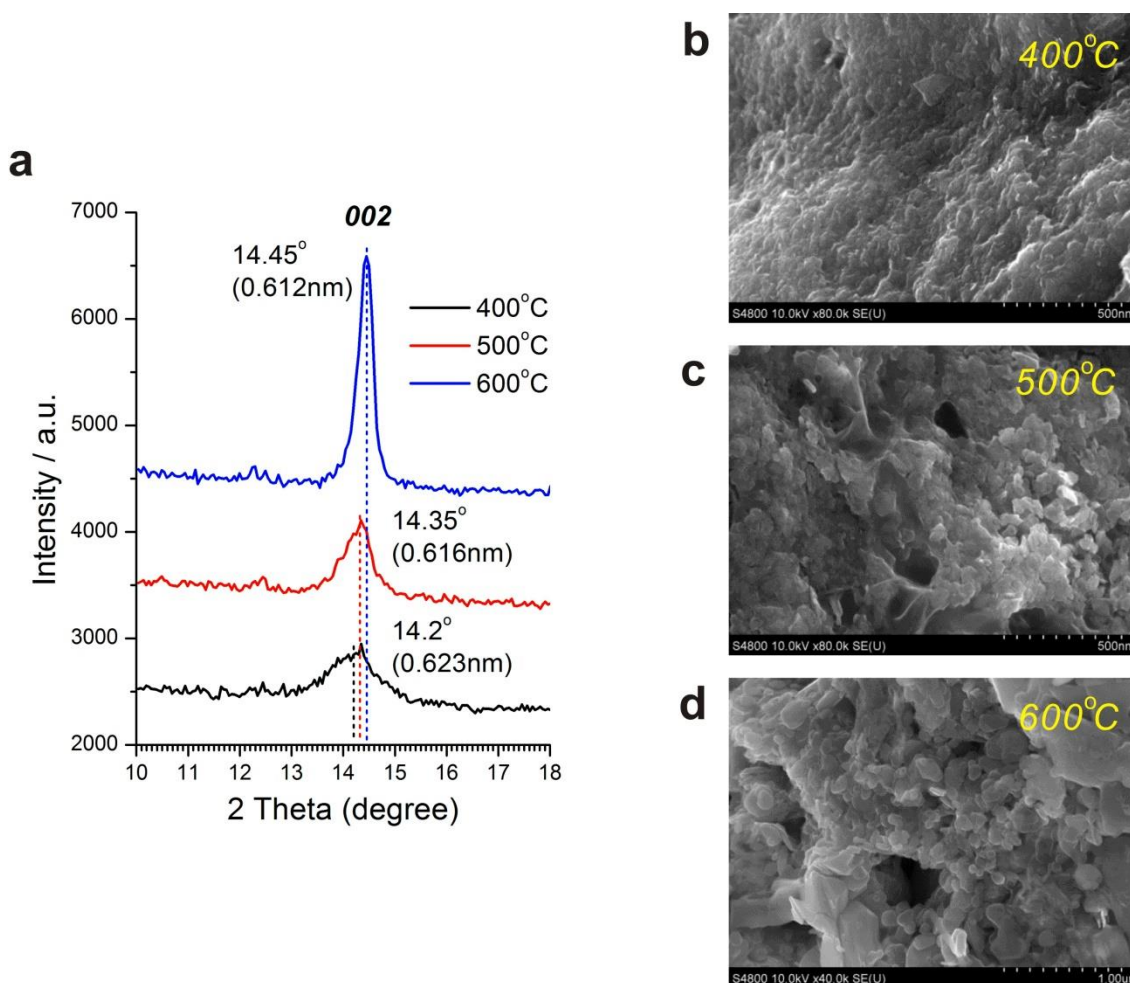


Figure 2.6 (a) XRD patterns of 002 diffraction peaks of products calcined from the precursors of (NH₄)₂MoS₄ and LiOH at the different temperature: 400°C, 500°C, 600°C, and (b, c, d), their corresponding SEM images.

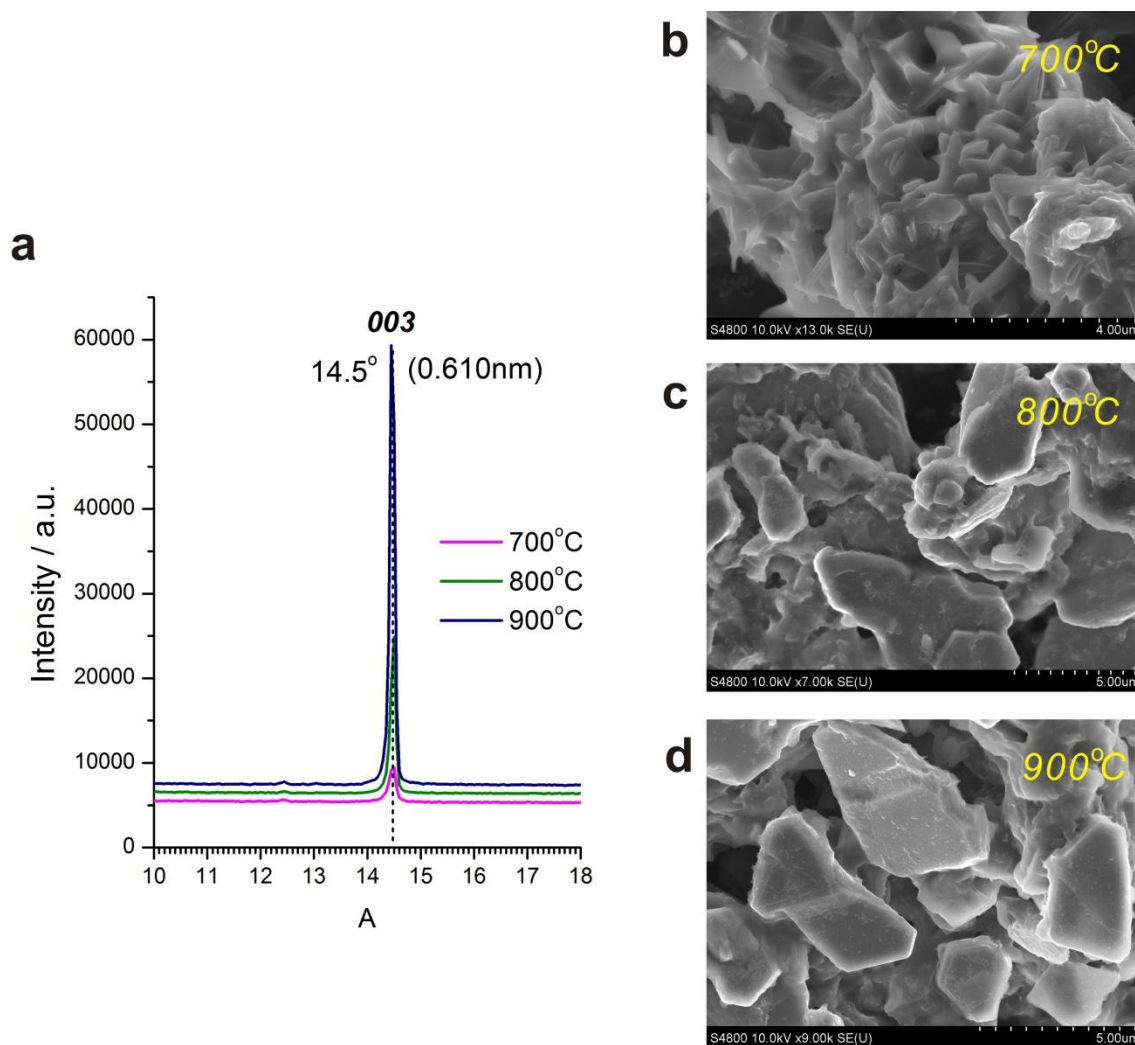


Figure 2.7 (a) XRD patterns of 003 diffraction peaks of products calcined from the precursors of $(\text{NH}_4)_2\text{MoS}_4$ and LiOH at the different temperature: 700°C, 800°C, 900°C, and (b, c, d), their corresponding SEM images.

Figure 2.8 gives the general view of photographs of three MoS₂ sample suspensions in ethanol with different concentration. Gradient color change from dark green to light yellow with decrease of concentration indicates that three MoS₂ samples show the representative semiconducting characteristics of 2H phase.^[33-35] Optical absorption spectroscopy was usually employed to characterize the size and thickness of semiconducting MoS₂ sheet suspensions.^[23, 35]

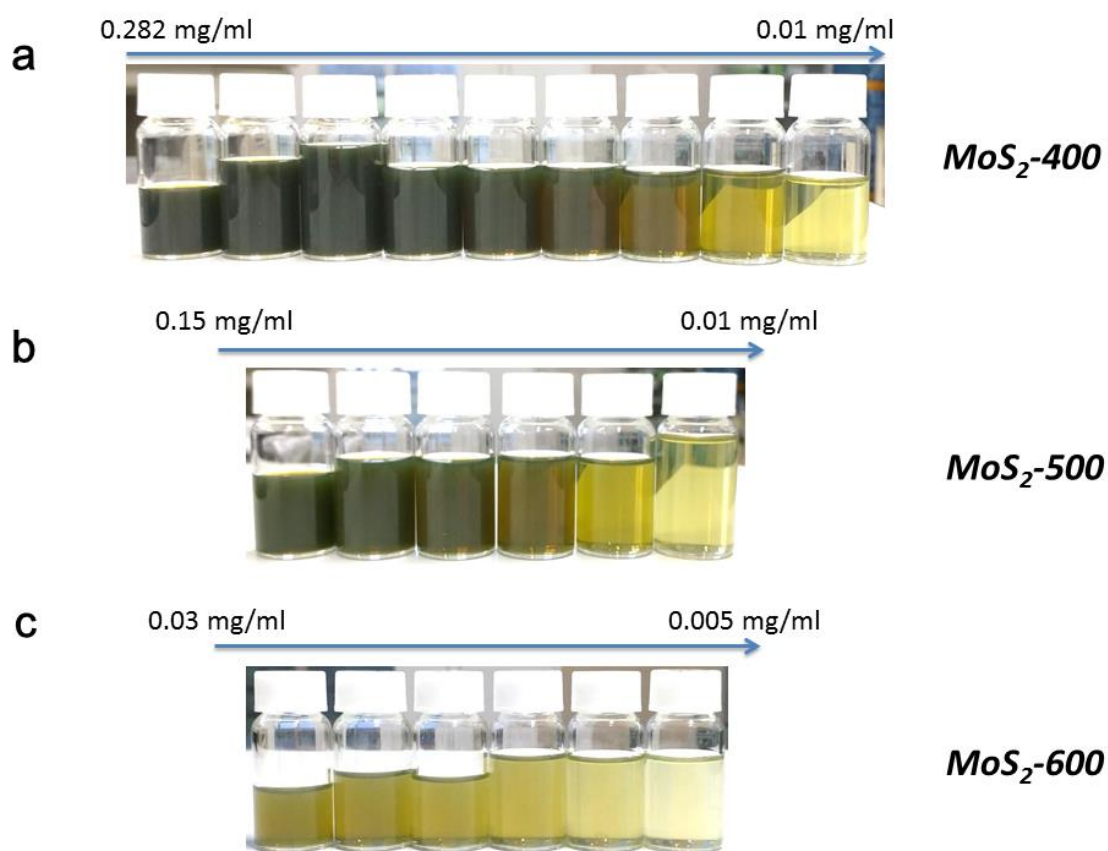


Figure 2.8 Photographs of MoS₂ nanosheet suspensions in ethanol with different concentration, (a) MoS₂-400, (b) MoS₂-500, (c) MoS₂-600. All the sample suspensions show the gradient color change from dark green to light yellow with the decrease of concentration, indicating the representative semiconducting characteristics of 2H-phase MoS₂ nanosheets.

Figure 2.9 elucidate that three 2H-MoS₂ samples all deliver the small lateral dimensions where MoS₂-400 shows the smallest, being consistent with the observation in Figure 2.5. In Figure 2.9, there are two distinct peaks for 2H-MoS₂ located at around 617 (B-exciton) and 670 nm (A-exciton) which are assigned to the direct excitonic transitions of MoS₂ at the K point of Brillouin zone.^[14, 36] In order to simplify the tedious weighting process for determining nanosheets concentration, it can be simply estimated by means of optical absorption spectrum using the Lambert-Beer law that relates the measured absorbance at a given wavelength to the concentration of the dispersion by the formula $A/l = \alpha C$, where A is the absorbance, l is the optical path length, α is the absorption coefficient, and C is the concentration.^[23] A/l scaled linearly with C (Figure 2.9a to 2.9c) for all the dispersions, allowing calculation of α value. The obtained absorption coefficients of monolayer MoS₂ nanosheets range from 900 to 1300 ml mg⁻¹m⁻¹ (Figure 2f), which are much smaller than published data (~ 3000 ml mg⁻¹m⁻¹).^[23] According to the analysis by TEM and AFM (Figure 2.5), it strongly suggests that in our experiment the slope of Abs. A value is directly proportional to MoS₂ sheet thickness. The normalized extinction spectra of a typical set of suspensions (Figure 2.9d) display the excitonic transitions typical of MoS₂.^[35, 37] The distinct and clear changes are found comparing with three samples, which reflect the different size distributions of the MoS₂ nanosheets in the dispersion. To further clearly observe these changes, the second derivative of the absorbance spectra of A and B peaks is shown in Figure 2.9e. It is clearly that the position of A-exciton, λ_A , and B-exciton, λ_B , varied with red-shifting from MoS₂-400 to MoS₂-600, as well as the increase of ratio of absorbance to that at the local minimum at 345 nm. These similar changes of slopes of Abs_A and Abs_B/Abs₃₄₅ of each MoS₂ sample are plotted in Figure 2.9f, showing a clear trend versus MoS₂ sheet thickness from monolayer to few layer, which can be attributed to the confinement effects of TMDCs.^{[14,}

18, 35]

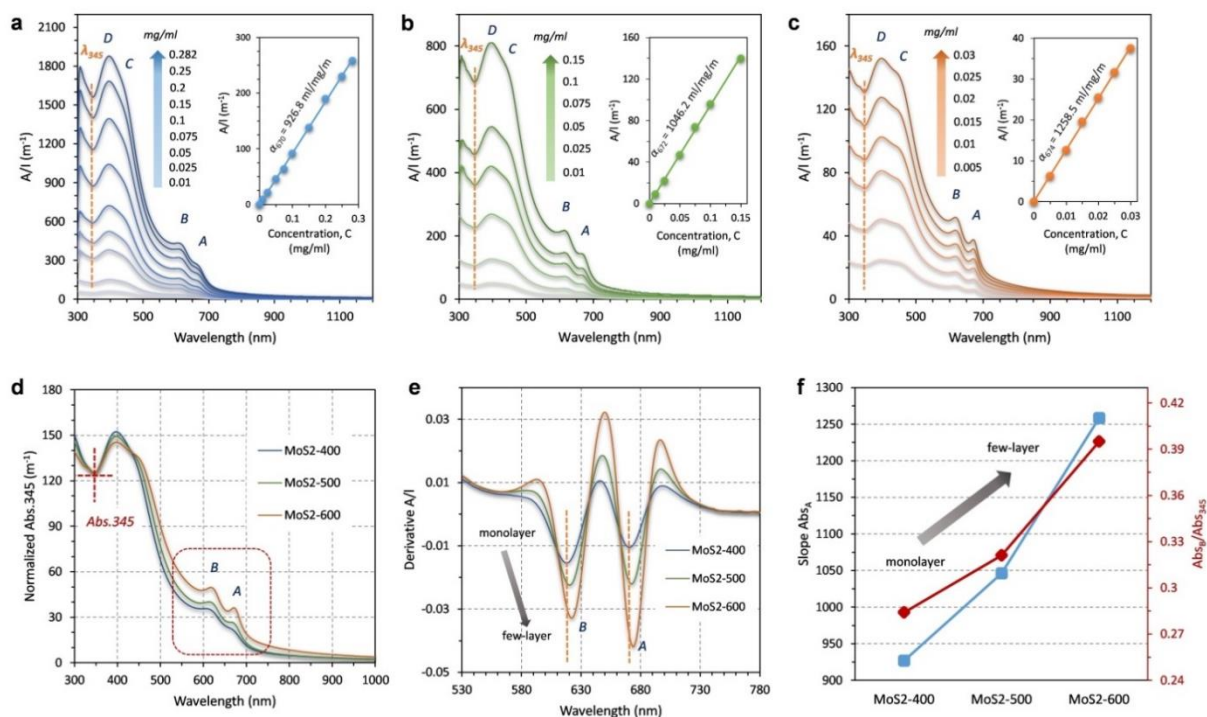


Figure 2.9 Absorbance spectra information for different sample suspensions in ethanol. The positions of the A-, B-, C- and D-excitations are marked. (a) Absorbance spectra of MoS₂-400 suspensions with different concentration, the insert shows Lambert-Beer plots of absorbance A (Abs_A) for MoS₂-400. (b) Absorbance spectra of MoS₂-500 suspensions with different concentration, the insert shows Lambert-Beer plots of absorbance A for MoS₂-500. (c) Absorbance spectra of MoS₂-600 suspensions with different concentration, the insert shows Lambert-Beer plots of absorbance A for MoS₂-600. (d) Absorbance spectra of three sample suspensions normalized to the local minimum at 345 nm. (e) Example spectra of the second derivative of the selected region in (d). (f) Slope of absorbance A calculated from Lambert-Beer plots and ratio of absorbance at B-exciton to that at 345 nm, Abs_B/Abs₃₄₅ plotted versus samples, respectively.

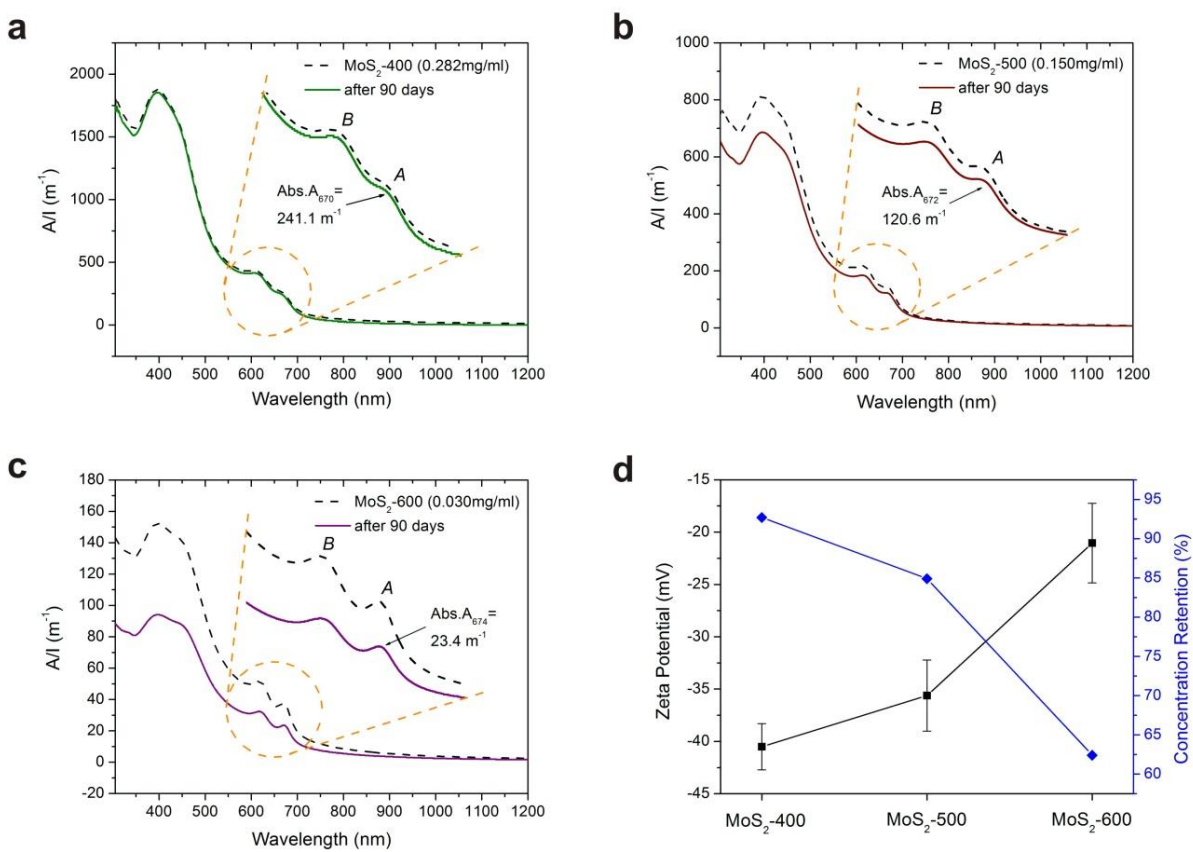


Figure 2.10 Absorbance spectra of each sample suspensions after standing 90 days, (a) MoS₂-400, (b) MoS₂-500, (c) MoS₂-600. (d) Zeta potential of sample suspensions in ethanol and their corresponding concentration retention calculated from Abs.A value before and after standing. It can be calculated from the change of Abs.A that the concentration retention of MoS₂-400, MoS₂-400, and MoS₂-400 after standing 90 days is 92.7%, 84.9%, and 62.4%, respectively.

To further evaluate the stability of each sample in the ethanol solution, zeta potential for each sample suspensions in ethanol and their absorbance spectra after standing 90 days were measured and shown in Figure 2.10. 92.7% of concentration retention for MoS₂-400 sample suspension in ethanol solution after standing 90 days suggests that it is most stable in all of the suspensions. It also can be reflected in zeta potential results (Figure 2.10d), in which among all the samples, MoS₂-400 delivers the most negative charge of ~-40.5 mV and therefore exhibits the highest stability and concentration retention.

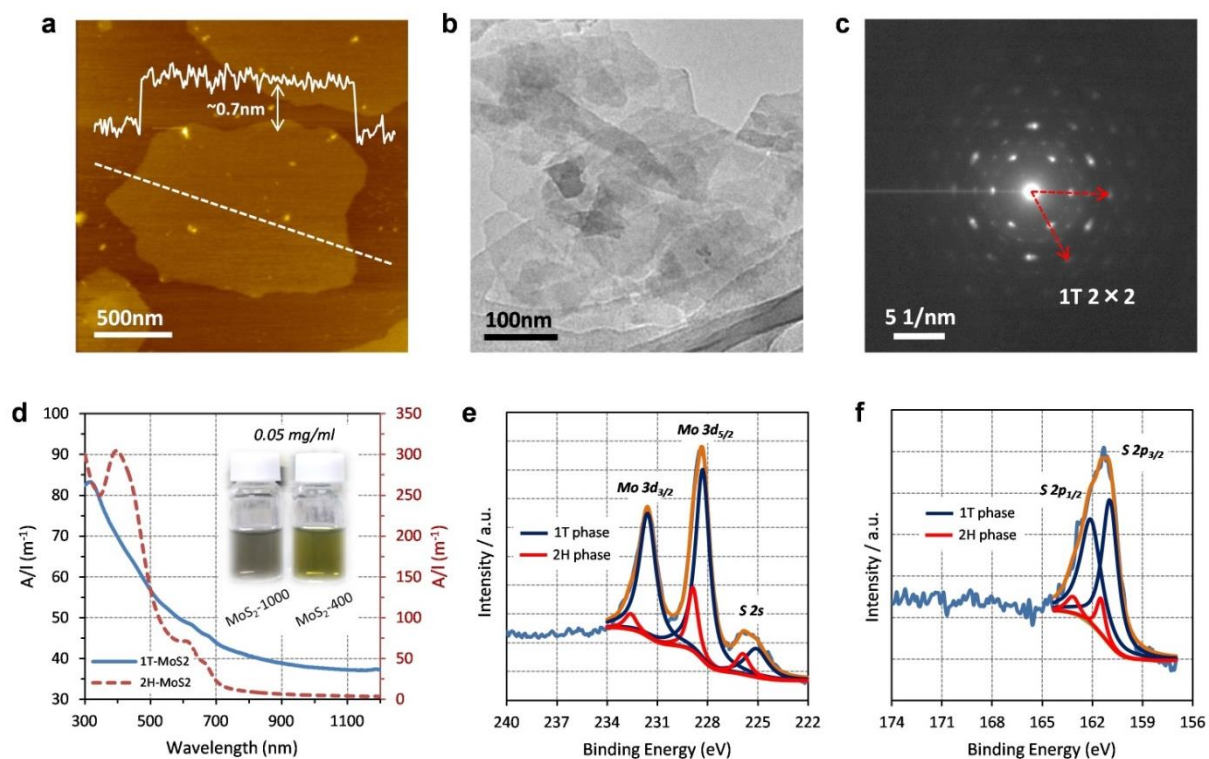


Figure 2.11 Characterizations of 1T-phase MoS₂ nanosheets. (a) AFM image of individual exfoliated 1T-phase MoS₂ monolayer. Height profile along the dash line is overlaid on the image. (b) TEM image of 1T-phase MoS₂ monolayers. (c) SAED pattern from the MoS₂ sheets in (b). (d) Absorbance spectra of 1T-phase MoS₂-1000 suspensions (blue line) compared with 2H-phase MoS₂-400 (red line). The insert show the photograph of two suspensions with 0.05 mg ml⁻¹ in ethanol solution. (e, f) High-resolution XPS spectra of Mo 3d, S 2s and S 2p core level peaks of 1T-phase MoS₂. After Shirley background subtraction, the Mo 3d, S 2s and S 2p peaks were deconvoluted to show 1T and 2H contribution.

As characterized by Raman spectra in Figure 2.4, it has been known that the 1T-phase MoS₂ could be obtained when the synthesized temperature rose up over 1000 °C. However, MoS₂ is easy to be sublimated at the high temperature (> 1000 °C) and annealed products at 1100 °C are relatively less. Here, MoS₂-1000 obtained at 1000 °C as the representative sample is characterized and investigated. It is well known that intercalation with some alkali metals such as Li, Na, et al. can induce phase changes in MoS₂ from 2H to 1T. As a result, a colloidal suspension of highly monodisperse monolayer MoS₂ sheets was prepared from bulk LiMoS₂ precursor through lithium hydrolysis followed by extensive purification. A majority of the exfoliated MoS₂ sheets were found to be 300 nm ~ 2 μm in lateral dimensions and exhibited typical thickness of ~0.7 nm (Figure 2.11a, 2.11b), approaching the theoretical value of monolayer MoS₂ (0.68 nm).^[38] The selected area electron diffraction (SAED) pattern in Figure 2.11c clearly shows that $2a \times 2a$ superstructure with additional dark spots is corresponding to the typical 1T-phase MoS₂.^[39, 40] The properties for 2H-MoS₂ and 1T-MoS₂ monolayers are very different, of which the former are semiconducting with a direct band gap of about 1.9 eV,^[5] whereas the latter possesses a metallic character. Optical absorbance spectra could easily highlight the difference between two phase samples, as shown in Figure 2.11d. After diluting to 0.05 mg ml⁻¹, the 1T-MoS₂ sample appears gray, while the 2H-MoS₂ sample (MoS₂-400) is yellow-green (Figure 2.11d, inset). More precisely, compared with 2H-phase MoS₂ sample (red line), the 1T-phase MoS₂ dispersion efficiently absorbs light in the full spectral range from 300 to 1200 nm, with a monotonic decrease of the absorbance with increasing wavelength (blue line), indicating the characteristic of a nonplasmonic metallic nanostructure. Additionally, under the same concentration of 0.05 mg ml⁻¹, 1T-phase MoS₂ dispersion shows the narrower light absorbance intensity range of ~35 – 85 m⁻¹ than 2H-phase MoS₂ dispersion with the light absorbance intensity range of ~0-300 m⁻¹. To compare with the traditional n-butyllithium insertion and exfoliation route, our proposed method put forward a facile and efficient strategy for preparing monolayer 1T-MoS₂ with a high yield production and quality.

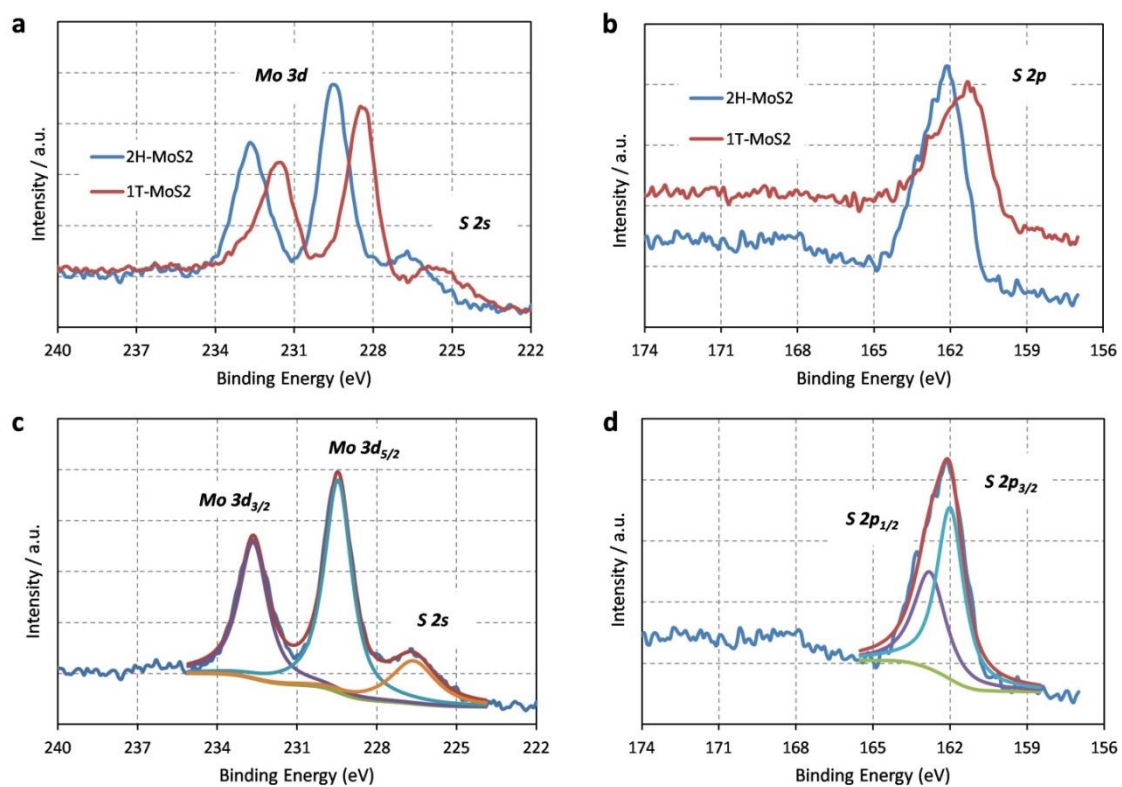


Figure 2.12 XPS spectra of 1T-phase and 2H-phase MoS₂. (a, b) comparison of XPS spectra of 1T-MoS₂ (MoS₂-1000) and 2H-MoS₂ (MoS₂-400) for Mo 3d and S 2p peaks, respectively. (c, d) XPS spectra of Mo 3d and S 2p regions of 2H-MoS₂ (MoS₂-400).

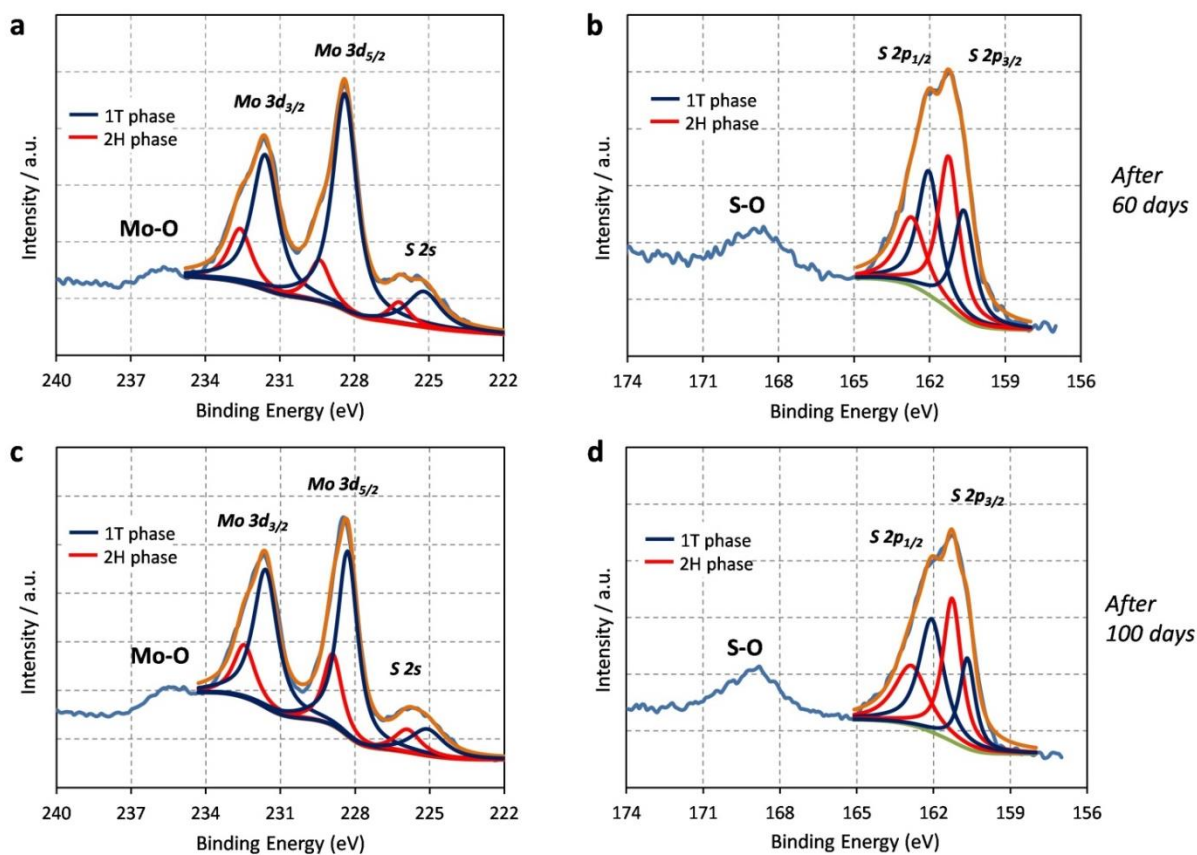


Figure 2.13 Stabilities of proposed 1T-phase MoS₂ suspensions in ethanol. (a, b) XPS spectra of Mo and S elements of the suspensions in ethanol solution after 60 days. (c, d) XPS spectra of Mo and S elements of the suspensions in ethanol solution after 100 days. The exposed unsaturated Mo and S would be oxidized in the air. (e) Schematic illustration of phase transformation energy barrier between 1T metastable state and 2H stable state.

To further accurately distinguish the phases of proposed MoS₂, XPS spectra were employed to analyze the phase compositions of 1T and 2H. In our case, compared with 2H-MoS₂ sample (MoS₂-400), all the core level peaks of Mo 3d and S 2s and 2p regions in 1T-MoS₂ are blue-shifted (Figure 2.12a and 2.12b). According to the analysis of XPS spectra for MoS₂-400 (Figure 2.12c), it is known that the Mo 3d spectra consist of peaks at around 229.5 and 232.7 eV which correspond to Mo⁴⁺ 3d_{5/2} and Mo⁴⁺ 3d_{3/2} components of 2H-phase, respectively. In addition, in the S 2p region of the spectra (Figure 2.12d), two peaks at around 162 and 162.8 eV which correspond to S²⁻ 2p_{3/2} and S²⁻ 2p_{1/2} components, respectively. By contrast, as shown in Figure 3e, for the proposed 1T-phase MoS₂ sample, deconvolution of known peaks reveals additional peaks that are shifted to lower binding energy by ~1.0 eV with respect to the position of the 2H-phase MoS₂. Similarly, in the S 2p region (Figure 2.11f), additional peaks are found besides the known doublet peaks of 2H-MoS₂, S 2p_{3/2} and S 2p_{1/2}, which appear at 161 and 162.1 eV, respectively. The parallel shift of these additional peaks to the lower binding energy suggests the formation of 1T phase.^[18, 41] The signal peaks of 2H phase in 1T-MoS₂ can be detected, which is attributed to the partial phase transformation between 1T and 2H according other reports.^[6, 18, 42] It is known that 1T phase MoS₂ is metastable, which could be changed into 2H-phase stable state under the certain conditions.^[18, 26] Here, I still employed XPS technique to characterize the stabilities of 1T-phase MoS₂ dispersion displayed at different days. As shown in Figure 2.13, it can be seen that even displayed 100 days, the proposed MoS₂ dispersion still mainly exhibits 1T phase. The new peaks appeared at around 235.5 eV for Mo 3d and 169 eV for S 2p regions can attributed to the partial oxidation of unsaturated Mo and S atoms in the air. According to previous report,^[43] although the transformation from 1T metastable state to 2H stable state is down-hill reaction, there is an energy barrier for phase relaxation. It is suggested that our proposed 1T-phase MoS₂ sample remains constant in laboratory store for over 100 days.

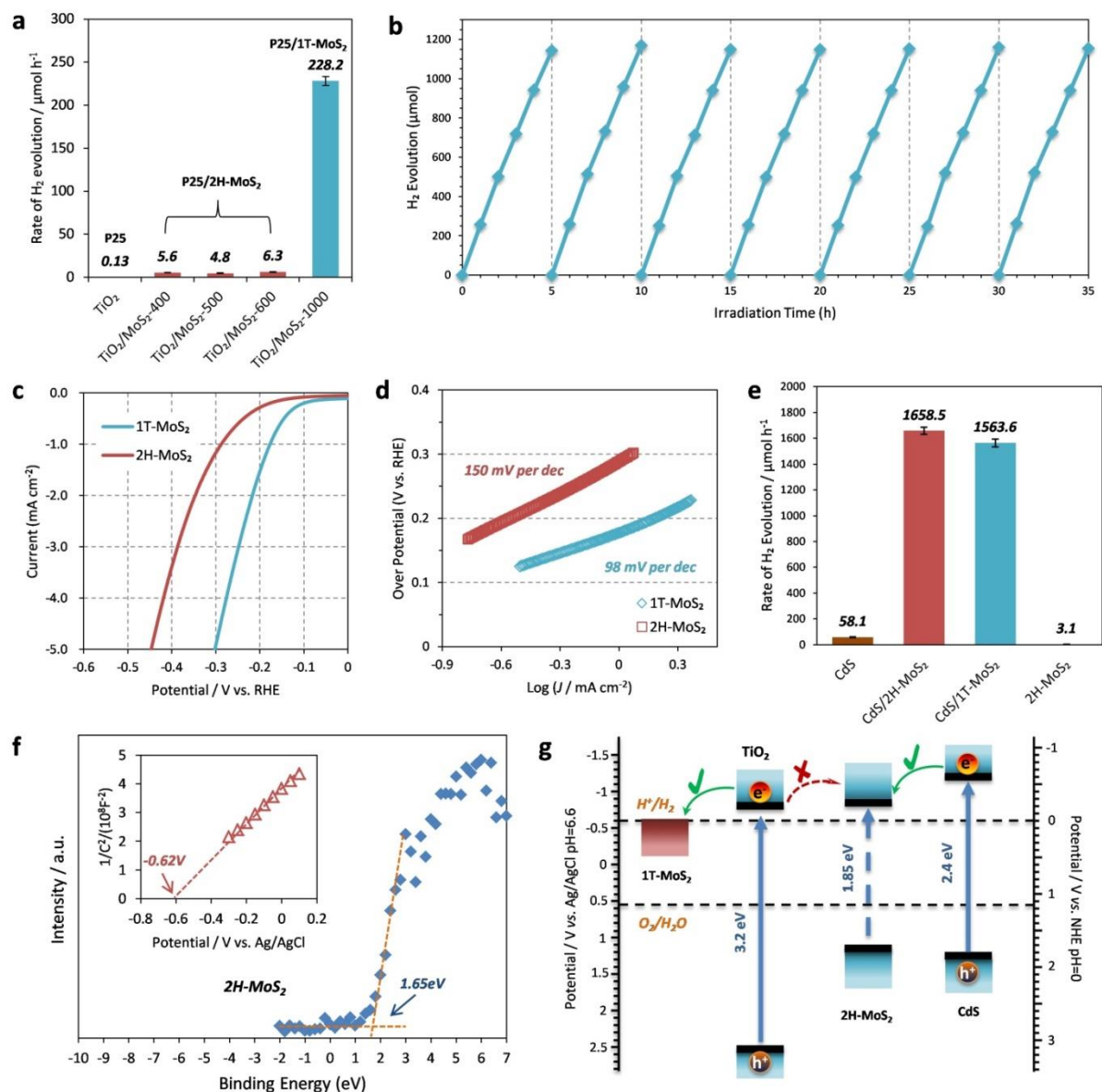
2.3.3 Photocatalytic H₂ evolution

Figure 2.14 Evaluation of catalytic hydrogen activities of 1T- and 2H-phase MoS₂. (a) Photocatalytic H₂ evolution activities of 1T- and 2H-MoS₂ over TiO₂ (P25), (b) stabilities of H₂ evolution for P25/1T-MoS₂ in seven runs. Light source: 300 W Xe lamp, $\lambda > 350$ nm; Reaction solution: 300 ml methanol aqueous solution (20%); Cat. 0.1 g, co-cat. 1.0 wt.%. (c) Linear sweep voltammograms (LSV) (5 mV s^{-1}) for MoS₂ films on fluorine doped tin oxide (FTO) substrates, comparing the electrocatalytic response towards HER. Measured potentials were subjected to iR correction, and supporting electrolyte was 0.5 M H₂SO₄

aqueous solution. (d) Over potential versus current density plots showing Tafel slopes expressed as mV per decade (mV per dec). (e) Photocatalytic H₂ evolution activities of 1T- (MoS₂-1000) and 2H-phase MoS₂ (MoS₂-400) over commercial CdS. Light source: 300 W Xe lamp with a L42 cut-off, $\lambda > 420$ nm; Reaction solution: 300 ml sodium lactate solution (20% lactic acid adjusted by NaOH, pH ~ 6.4); Cat. 0.1 g, co-cat. 1.0 wt.%. (f) Valence-band XPS (VB-XPS) spectrum of 2H-MoS₂. Insert shows its corresponding Mott-Schottky plots in 0.5 M Na₂SO₄ aqueous solution. (g) Schematic energy level diagrams of 1T-, 2H-MoS₂, TiO₂, and CdS in comparison with the potentials for water reduction and oxidation.

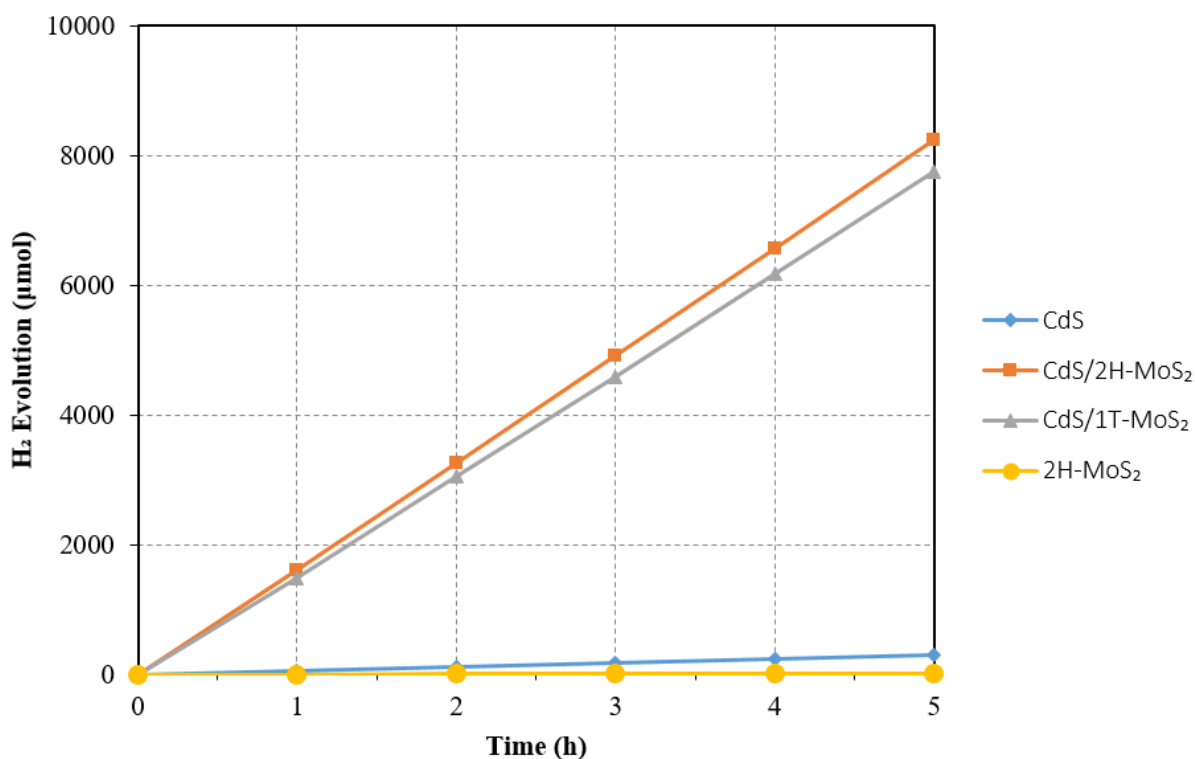


Figure 2.15 Photocatalytic H₂ evolution activities of CdS, CdS/2H-MoS₂, CdS/1T-MoS₂, and 2H-MoS₂ catalysts under visible light irradiation. Light source: 300 W Xe lamp with a L42 cut-off, $\lambda > 420$ nm; Reaction solution: 300 ml sodium lactate solution (20% lactic acid adjusted by NaOH, pH ~ 6.4); Cat. 0.1 g, co-cat. 1.0 wt.%.

In addition to the synthesis and characterization, I aim to compare the catalytic hydrogen evolution activity of the semiconducting and metallic MoS₂ nanostructures. As 1T- and 2H-MoS₂ are reported to function as an efficient electro-catalyst.^[21, 44, 45] it is expected that these nanosheets can also act as the hydrogen evolution cocatalysts when associated with a suitable photo-harvester. The most representative photo-harvesting semiconductors are TiO₂ with a 3.2 eV and CdS with a 2.4 eV of bandgap,^[46, 47] the latter of which is particularly effective in visible-light-region response. Here, I use P25-TiO₂ and commercial CdS as the photo-harvesters to create nanocomposite TiO₂/MoS₂ and CdS/MoS₂ as a model water splitting photosystem. To equally compare the catalytic hydrogen abilities of each sample, all the photocatalytic hydrogen evolution test were performed in neutral aqueous solutions (pH value around ~7).

I first compared the catalytic hydrogen activities for bare P25, P25/2H-MoS₂, and P25/1T-MoS₂ samples in Figure 2.14a. Bare P25-TiO₂ due to its high crystallinity cannot offer an active site for catalytic hydrogen evolution on the surface, leading to the facile recombination of photo-excited electron-hole pairs before migrating to the surface for reactions, and therefore shows inactive catalytic hydrogen evolution (0.13 $\mu\text{mol h}^{-1}$). Although three kinds of 2H-phase MoS₂ (MoS₂-400, MoS₂-500, MoS₂-600) as cocatalysts were loaded on the surface of TiO₂, respectively, the improvement of catalytic hydrogen activities are not obvious which only show around 5 $\mu\text{mol h}^{-1}$. By contrast, TiO₂/1T-MoS₂ nanocomposite exhibits drastic activity enhancement in photocatalytic hydrogen evolution with 228.2 $\mu\text{mol h}^{-1}$, corresponding to an apparent quantum yield (AQY) of 14.5% at 365 nm. This activity could last over 35 hours without significant decay (Figure 2.14b), indicating the robust structure of nanocomposite and stable phase of 1T-MoS₂ structure. This might be attributed to the good metallic conductivity and catalytic hydrogen activity of 1T-phase MoS₂. Electrocatalytic HER experiments were carried out on FTO glass electrode. Similar results can be found from previous reports,^[21, 48] 1T-MoS₂ not only be characterized by lower over potential and Tafel slope but also exhibit higher current density for HER in comparison with 2H-MoS₂ in our case (Figure 2.14c and 2.14d). It is well known that for 2H-MoS₂, only exposed edges could provide active sites for catalytic hydrogen evolution and inactive activity at the basal plane were observed.^[11, 12] However, for 1T-MoS₂, due to its distorted crystal structure, the active sites for

catalytic hydrogen evolution in the basal plane were comprehensively activated,^[43, 47, 49] and thereby delivers the good catalytic hydrogen performance. While the explanation is quite reasonable in the field of electrocatalytic HER, when as a cocatalyst in photocatalysis, the effect of incident light on the relationship between electronic levels of semiconductors is of equal importance.

Figure 2.14e and Figure 2.15 illustrate the photocatalytic hydrogen production activities of kinds of catalysts by using CdS as photoharvester. Similar with the results of bare TiO₂, the bare CdS also shows the poor catalytic hydrogen activity with ~58.1 μmol h⁻¹, in which it needs cocatalyst to provide active site on its surface. 1T-MoS₂ due to its excellent catalytic hydrogen activity drastically enhanced the hydrogen reduction abilities of CdS, showing 1563.6 μmol h⁻¹ of hydrogen evolution rate, corresponding to the AQY of 24.1% at 420 nm. However, more interestingly, loading 2H-MoS₂ on the surface of CdS also can significantly improve the catalytic hydrogen activities – 1658.5 μmol h⁻¹ of hydrogen evolution rate which is even higher than that of CdS/1T-MoS₂. This fact is attributed to the smaller particle size of as-synthesized 2H-MoS₂, which is more easily adsorbed on the surface of CdS. The good contact between co-catalyst and photoharvester semiconductors is facilitating the photo-excited electrons transport. It is worth noting that all the photocatalyst composites were not annealed at high temperature due to the transformation of MoS₂ from 1T to 2H phase.^[18] Through heat treatment, CdS/2H-MoS₂ composites can exhibit much higher photocatalytic hydrogen activities (62.1% of AQY at 420 nm, Figure 2.16). It can be seen that after annealed at high temperature, CdS/2H-MoS₂ exhibits ultrahigh hydrogen evolution rate of 4842.1 μmol h⁻¹, corresponding to the AQY of 62.1% at 420 nm, which is much higher than the case before annealing. That is attributed to the tight contact between MoS₂ and CdS during the heat treatment, decreasing the interface Schottky barrier and facilitating the photo-excited electrons migrating from CdS to MoS₂ for reactions. However, for TiO₂/2H-MoS₂ nanocomposite, the photocatalytic H₂ activity does not show significant improvement after annealing process. It might be attributed to the relationship of electronic level for each semiconductor.

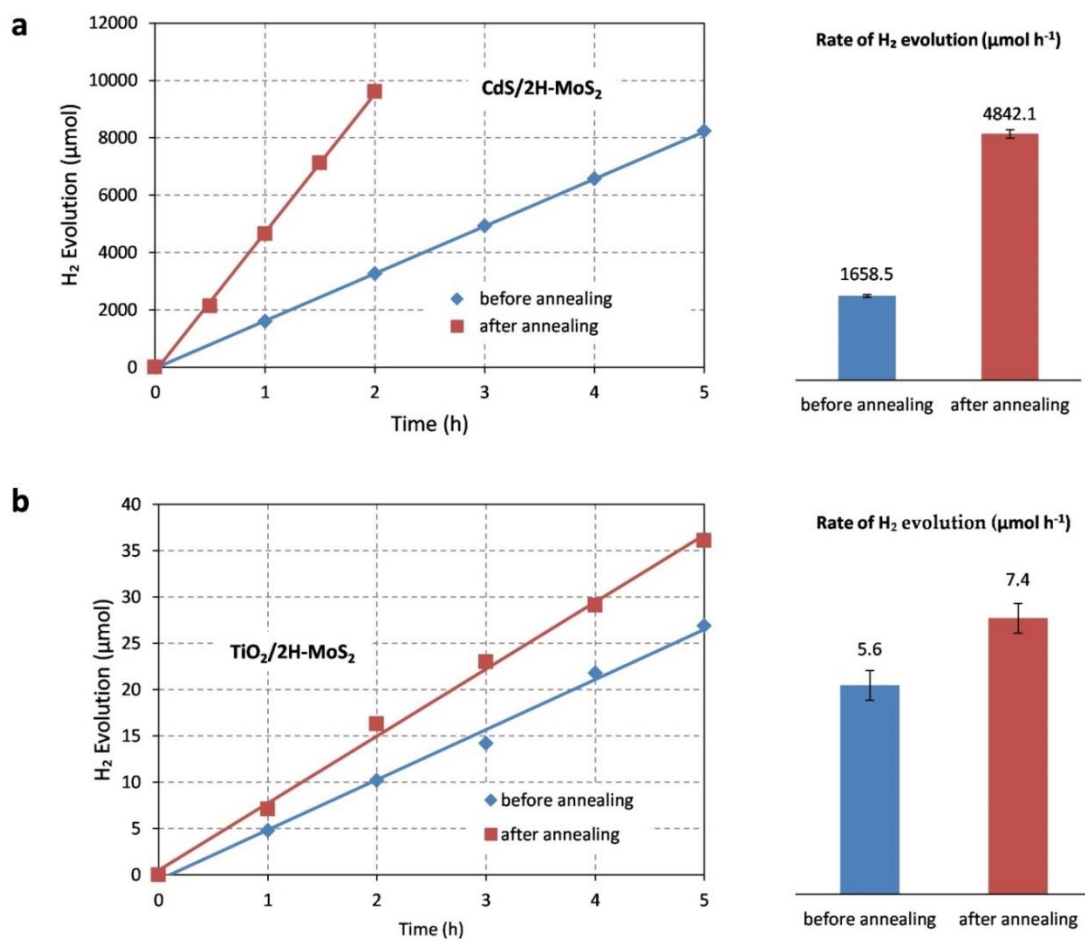


Figure 2.16 Comparison of photocatalytic H₂ evolution activities 2H-MoS₂ based composites before and after annealing. The annealing temperature is 400 °C in Ar for 2 hours.

In addition to the effect of MoS₂ sheet size, the matchability of electronic energy level between photoharvester semiconductors and 2H-MoS₂ was even more important, considering 2H-MoS₂ monolayer as a semiconductor with the direct bandgap of 1.9 eV.^[14] Valence band (VB)-XPS and Mott-Schottky plots analysis are powerful methods to determine the VB position of semiconductor and then the conduction band (CB) position can be obtained according to the band gap.^[16] According to the λ_{670} of peak A of MoS₂-400 in Figure 2.9e, it is estimated that the optical band gap of 2H-MoS₂ is around 1.85 eV considering its direct band gap property.^[23] Additionally, according to the VB-XPS and Mott-Schottky plots in Figure 2.14f, the CB and VB position of 2H-MoS₂ can be accurately determined. Combining with additional measurements in Figure 2.17, a sketch of the experimentally determined electronic band alignment between 1T-MoS₂, 2H-MoS₂, TiO₂, and CdS is displayed in Figure 2.14g. Monolayer 2H-MoS₂ due to its quantum-confinement effect exhibits a larger bandgap than the bulk one (1.3 eV),^[14] where the conduction band minimum (CBM) position shows even more negative than that of TiO₂. Theoretically, the photo-excited electrons from TiO₂ are difficult to inject into the CB of monolayer 2H-MoS₂ for the hydrogen reduction. Moreover, the low photocatalytic H₂ activity of bare 2H-MoS₂ monolayer (Figure 2.14e) indicates its poor mobility of photo-excited electron-holes. By contrast, metallic 1T-MoS₂ due to its lower energy level is easily to capture photo-excited electrons, facilitating the catalytic HER activities. By contrast, for CdS with more negative CB position, the photo-excited electrons can be easily injected into 1T or 2H-MoS₂ for reactions. This sketch could decipher the reason of gap phenomenon between 1T- and 2H-MoS₂ loading on TiO₂ and CdS photo-harvesters for their catalytic hydrogen activities.

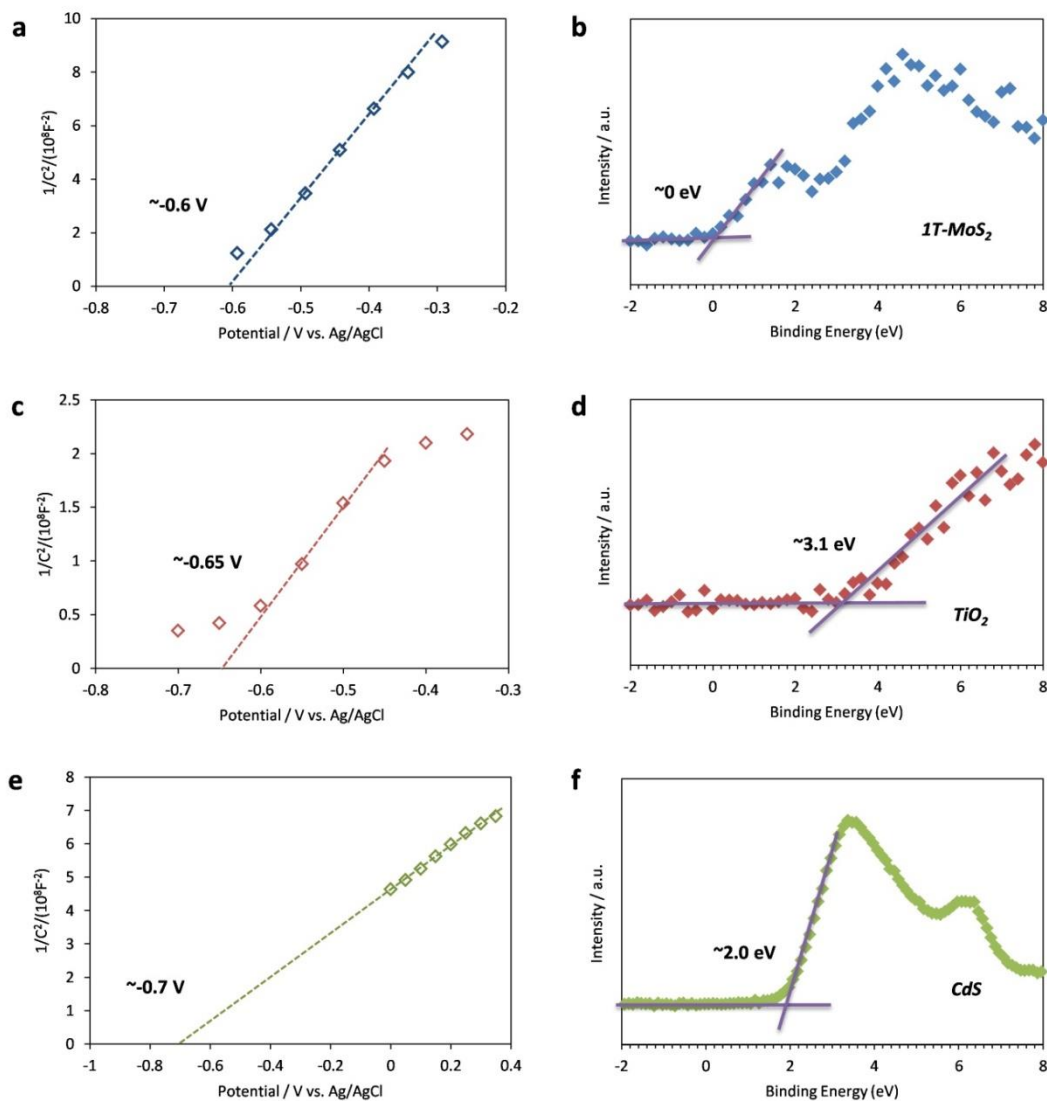


Figure 2.17 (a, c, e) Mott-Schottky plots of 1T-MoS₂, P25-TiO₂, CdS in 0.5M Na₂SO₄ solution, (b, d, f) their corresponding VB-XPS spectra.

2.4 Conclusion

In conclusion, a facile and effective lithium molten salt method to synthesize a series of MoS₂ precursors by controlling the calcination temperature, where the precursors can be accurately exfoliated into 2H- and 1T-phase MoS₂ monolayers with a high yield production was developed. During the

synthesis process, lithium molten salt plays not only the role of fluxing medium, but more importantly is controlling the MoS₂ phases – 1T, 2H, and 3R. The critical point is that when the temperature is up to 1000 °C, a new phase of LiMoS₂ is obtained, leading to a phase change from 2H to 1T by the lithium intercalation. The proposed semiconducting 2H- and metallic 1T-phase MoS₂ monolayers all exhibit the good stabilities. In addition, compared with present liquid phase exfoliation for 2H-TMDCs and lithium insertion/extraction exfoliation for 1T-TMDCs, our proposed method is more efficient, convenient and secure. It is expected to extend our proposed method to synthesize other TMDCs like WS₂ with different phase. I also systematically investigated the catalytic hydrogen evolution activities for different-phased MoS₂. The results show that similar with common reported, the 1T-MoS₂ exhibited higher electrocatalytic hydrogen activities than 2H-MoS₂. However, to be as a co-catalyst in photocatalysis, the characteristic of semiconducting 2H-MoS₂ monolayer is determined not suitable for matching with some metal oxide semiconductors such as TiO₂ with lower CB position. By contrast, the photoharvester semiconductors like CdS with higher CB position would be beneficial for the photo-excited electrons transport into 2H-MoS₂ monolayer, facilitating the hydrogen reduction reaction.

Reference

- [1] K. S. Novoselov, A. K. Geim, S. V. Morozov, D. Jiang, Y. Zhang, S. V. Dubonos, I. V. Grigorieva, A. A. Firsov, *Science* 2004, 306, 666.
- [2] Y. Hernandez, V. Nicolosi, M. Lotya, F. M. Blighe, Z. Y. Sun, S. De, I. T. McGovern, B. Holland, M. Byrne, Y. K. Gun'ko, J. J. Boland, P. Niraj, G. Duesberg, S. Krishnamurthy, R. Goodhue, J. Hutchison, V. Scardaci, A. C. Ferrari, J. N. Coleman, *Nat Nanotechnol* 2008, 3, 563.
- [3] M. S. Xu, T. Liang, M. M. Shi, H. Z. Chen, *Chem Rev* 2013, 113, 3766.

- [4] V. Nicolosi, M. Chhowalla, M. G. Kanatzidis, M. S. Strano, J. N. Coleman, *Science* 2013, 340, 1226419.
- [5] Q. H. Wang, K. Kalantar-Zadeh, A. Kis, J. N. Coleman, M. S. Strano, *Nat Nanotechnol* 2012, 7, 699.
- [6] M. Chhowalla, H. S. Shin, G. Eda, L. J. Li, K. P. Loh, H. Zhang, *Nature Chemistry* 2013, 5, 263.
- [7] B. Radisavljevic, A. Radenovic, J. Brivio, V. Giacometti, A. Kis, *Nat Nanotechnol* 2011, 6, 147.
- [8] O. Lopez-Sanchez, D. Lembke, M. Kayci, A. Radenovic, A. Kis, *Nat Nanotechnol* 2013, 8, 497.
- [9] Z. Y. Yin, H. Li, H. Li, L. Jiang, Y. M. Shi, Y. H. Sun, G. Lu, Q. Zhang, X. D. Chen, H. Zhang, *ACS Nano* 2012, 6, 74.
- [10] K. Chang, W. X. Chen, *Acs Nano* 2011, 5, 4720.
- [11] B. Hinnemann, P. G. Moses, J. Bonde, K. P. Jorgensen, J. H. Nielsen, S. Horch, I. Chorkendorff, J. K. Nørskov, *Journal of the American Chemical Society* 2005, 127, 5308.
- [12] T. F. Jaramillo, K. P. Jorgensen, J. Bonde, J. H. Nielsen, S. Horch, I. Chorkendorff, *Science* 2007, 317, 100.
- [13] A. Splendiani, L. Sun, Y. B. Zhang, T. S. Li, J. Kim, C. Y. Chim, G. Galli, F. Wang, *Nano Lett* 2010, 10, 1271.
- [14] K. F. Mak, C. Lee, J. Hone, J. Shan, T. F. Heinz, *Physical Review Letters* 2010, 105.
- [15] J. Kibsgaard, Z. B. Chen, B. N. Reinecke, T. F. Jaramillo, *Nat Mater* 2012, 11, 963.
- [16] K. Chang, M. Li, T. Wang, S. X. Ouyang, P. Li, L. Q. Liu, J. H. Ye, *Advanced Energy Materials* 2015, 5, 1402279.
- [17] P. Joensen, R. F. Frindt, S. R. Morrison, *Mater Res Bull* 1986, 21, 457.
- [18] G. Eda, H. Yamaguchi, D. Voiry, T. Fujita, M. W. Chen, M. Chhowalla, *Nano Letters* 2011, 11, 5111.
- [19] J. F. Xie, H. Zhang, S. Li, R. X. Wang, X. Sun, M. Zhou, J. F. Zhou, X. W. Lou, Y. Xie, *Advanced Materials* 2013, 25, 5807.

- [20] J. F. Xie, J. J. Zhang, S. Li, F. Grote, X. D. Zhang, H. Zhang, R. X. Wang, Y. Lei, B. C. Pan, Y. Xie, *Journal of the American Chemical Society* 2013, 135, 17881.
- [21] M. A. Lukowski, A. S. Daniel, F. Meng, A. Forticaux, L. S. Li, S. Jin, *Journal of the American Chemical Society* 2013, 135, 10274.
- [22] D. Voiry, M. Salehi, R. Silva, T. Fujita, M. W. Chen, T. Asefa, V. B. Shenoy, G. Eda, M. Chhowalla, *Nano Lett* 2013, 13, 6222.
- [23] J. N. Coleman, M. Lotya, A. O'Neill, S. D. Bergin, P. J. King, U. Khan, K. Young, A. Gaucher, S. De, R. J. Smith, I. V. Shvets, S. K. Arora, G. Stanton, H. Y. Kim, K. Lee, G. T. Kim, G. S. Duesberg, T. Hallam, J. J. Boland, J. J. Wang, J. F. Donegan, J. C. Grunlan, G. Moriarty, A. Shmeliov, R. J. Nicholls, J. M. Perkins, E. M. Grieveson, K. Theuwissen, D. W. McComb, P. D. Nellist, V. Nicolosi, *Science* 2011, 331, 568.
- [24] Z. Y. Zeng, T. Sun, J. X. Zhu, X. Huang, Z. Y. Yin, G. Lu, Z. X. Fan, Q. Y. Yan, H. H. Hng, H. Zhang, *Angewandte Chemie-International Edition* 2012, 51, 9052.
- [25] Y. H. Lee, X. Q. Zhang, W. J. Zhang, M. T. Chang, C. T. Lin, K. D. Chang, Y. C. Yu, J. T. W. Wang, C. S. Chang, L. J. Li, T. W. Lin, *Advanced Materials* 2012, 24, 2320.
- [26] K. Chang, X. Hai, J. Ye, *Advanced Energy Materials* 2016, DOI: 10.1002/aenm.201502555.
- [27] M. Zeuner, S. Pagano, S. Hug, P. Pust, S. Schmiechen, C. Scheu, W. Schnick, *European Journal of Inorganic Chemistry* 2010, 4945.
- [28] I. W. Donald, B. L. Metcalfe, A. E. P. Morris, *Journal of Materials Science* 1992, 27, 2979.
- [29] M. A. Py, R. R. Haering, *Canadian Journal of Physics* 1983, 61, 76.
- [30] J. A. Wilson, A. D. Yoffe, *Advances in Physics* 1969, 18, 193.
- [31] R. Bissessur, M. G. Kanatzidis, J. L. Schindler, C. R. Kannewurf, *Journal of the Chemical Society-Chemical Communications* 1993, 1582.
- [32] H. T. Wang, Z. Y. Lu, S. C. Xu, D. S. Kong, J. J. Cha, G. Y. Zheng, P. C. Hsu, K. Yan, D. Bradshaw, F. B. Prinz, Y. Cui, *Proceedings of the National Academy of Sciences of the United States of America* 2013, 110, 19701.

- [33] D. B. Velusamy, R. H. Kim, S. Cha, J. Huh, R. Khazaeinezhad, S. H. Kassani, G. Song, S. M. Cho, S. H. Cho, I. Hwang, J. Lee, K. Oh, H. Choi, C. Park, *Nature Communications* 2015, 6.
- [34] J. Kim, S. Kwon, D. H. Cho, B. Kang, H. Kwon, Y. Kim, S. O. Park, G. Y. Jung, E. Shin, W. G. Kim, H. Lee, G. H. Ryu, M. Choi, T. H. Kim, J. Oh, S. Park, S. K. Kwak, S. W. Yoon, D. Byun, Z. Lee, C. Lee, *Nature Communications* 2015, 6.
- [35] C. Backes, R. J. Smith, N. McEvoy, N. C. Berner, D. McCloskey, H. C. Nerl, A. O'Neill, P. J. King, T. Higgins, D. Hanlon, N. Scheuschner, J. Maultzsch, L. Houben, G. S. Duesberg, J. F. Donegan, V. Nicolosi, J. N. Coleman, *Nature Communications* 2014, 5, 4576.
- [36] G. J. Guan, S. Y. Zhang, S. H. Liu, Y. Q. Cai, M. Low, C. P. Teng, I. Y. Phang, Y. Cheng, K. L. Duei, B. M. Srinivasan, Y. G. Zheng, Y. W. Zhang, M. Y. Han, *Journal of the American Chemical Society* 2015, 137, 6152.
- [37] J. A. Wilson, A. D. Yoffe, *Advances in Physics* 1969, 18, 193.
- [38] J. Li, G. Zhan, Y. Yu, L. Zhang, *Nat Commun* 2016, 7.
- [39] F. Wypych, C. Solenthaler, R. Prins, T. Weber, *J Solid State Chem* 1999, 144, 430.
- [40] L. F. Wang, Z. Xu, W. L. Wang, X. D. Bai, *J Am Chem Soc* 2014, 136, 6693.
- [41] C. A. Papageorgopoulos, W. Jaegermann, *Surf Sci* 1995, 338, 83.
- [42] G. Eda, T. Fujita, H. Yamaguchi, D. Voiry, M. W. Chen, M. Chhowalla, *ACS Nano* 2012, 6, 7311.
- [43] D. Voiry, H. Yamaguchi, J. W. Li, R. Silva, D. C. B. Alves, T. Fujita, M. W. Chen, T. Asefa, V. B. Shenoy, G. Eda, M. Chhowalla, *Nature Materials* 2013, 12, 850.
- [44] Z. Y. Lu, W. Zhu, X. Y. Yu, H. C. Zhang, Y. J. Li, X. M. Sun, X. W. Wang, H. Wang, J. M. Wang, J. Luo, X. D. Lei, L. Jiang, *Adv Mater* 2014, 26, 2683.
- [45] X. X. Zou, Y. Zhang, *Chemical Society Reviews* 2015, 44, 5148.
- [46] J. H. Yang, H. J. Yan, X. L. Wang, F. Y. Wen, Z. J. Wang, D. Y. Fan, J. Y. Shi, C. Li, *J Catal* 2012, 290, 151.

Chapter 2

- [47] B. Mahler, V. Hoepfner, K. Liao, G. A. Ozin, *Journal of the American Chemical Society* 2014, 136, 14121.
- [48] J. D. Benck, T. R. Hellstern, J. Kibsgaard, P. Chakthranont, T. F. Jaramillo, *Acs Catalysis* 2014, 4, 3957.
- [49] S. Bai, L. M. Wang, X. Y. Chen, J. T. Du, Y. J. Xiong, *Nano Research* 2015, 8, 175.

Chapter 3 Engineering the edges of transition metal disulfides for direct exfoliation into monolayers in polar micromolecular solvents and their cocatalytic performances

3.1 Introduction

Pioneering works have shown that monolayer transition metal dichalcogenides (TMDCs) bear great promise as two-dimensional materials because of their intrinsic semiconducting characteristics compared with the gapless nature of graphene.^[1-5] Among them, monolayer molybdenum disulfide (MoS₂) and tungsten disulfide (WS₂) are notable due to having direct bandgaps, large in-plane electron mobilities (>200 cm² V⁻¹ s⁻¹), high current on/off ratios, remarkable mechanical and optical properties, and high catalytic activity in the hydrogen evolution reaction (HER).^[6-11] In general, large lateral size, high crystallinity and defect-free morphologies are required in physical applications such as transistors, photodetectors and electroluminescent devices.^[5,12,13] Alternatively, in the catalysis of HER, possessing large specific surface areas and a larger number of exposed active sites are beneficial.^[14,15] Density function theory (DFT) calculation and corresponding experiments have revealed that the activity of MoS₂ (WS₂) in HER can be attributed to the edge-site S atoms, which have a free energy of hydrogen adsorption (ΔG_{H^*}) close to zero when catalyzing H₂ evolution.^[14,16] Despite the fact that monolayer MoS₂ and WS₂ can be good candidates for HER owing to their relatively low cost, natural abundance, high catalytic activity and good stability, large-scale production of monolayer MoS₂ and WS₂ is still a challenge.^[17,18]

Over the past years, tremendous effort has been made toward the reliable and scaled-up production of atomically thin TMDC nanosheets.^[13] Among the methods, liquid phase exfoliation, first utilized by Coleman and colleagues, is considered to be the most promising route toward the large-scale production

of mono- and few-layer MoS₂ (WS₂).^[19-22] Currently, there are two major issues restricting further application and development of this method. First and foremost is the low yield in monolayer production, where most of the products are few-layer nanosheets.^[13,23] Second, this method is highly dependent on the solvent. Thus far, N-methyl-2-pyrrolidone and other pyrrolidone-based solvents have been found to be the most compatible solvents for MoS₂ (WS₂) exfoliation.^[20] Generally, pyrrolidone-based solvents can sufficiently intercalate into the inner layers of the crystals due to the compatible surface tension between the liquid solvents and the bulk MoS₂ (WS₂) crystals. Then, the generated cavitation bubbles inside of the crystals can delaminate the layered crystallites to produce exfoliated ultrathin nanosheets. However, these pyrrolidone-based solvents are generally toxic and have high-boiling points, which poses a significant environmental risk at the industrial scale. Even though many attempts have been made to exfoliate bulk MoS₂ (WS₂) crystals in low boiling point polar micromolecular solvents, such as water, via probing surface tension components or through temperature control, neither the concentration of dispersions nor the monolayer yield were satisfactory.^[23,24] Owing to the mismatch in surface tension between polar micromolecular solvents (water, ethanol and methanol) and bulk crystals, hydrodynamic force from the collapse of cavitation bubbles can only appear on the crystals edges, which is insufficient to overcome the strong van der Waals attraction between microscale adjacent layers of commercial MoS₂ (WS₂).^[23] Overcoming these disadvantages and achieving the highly efficient exfoliation of bulk MoS₂ (WS₂) crystals into monolayers in low boiling point polar micromolecular solvents, such as water and ethanol, is a challenge and of great interest.

In this chapter, inspired by the unique layered structural properties of MoS₂ (WS₂), I tailor their lateral size to the nanoscale to increase the fraction of edges. As expected, the obtained MoS₂ (WS₂) crystals can be efficiently exfoliated to monolayer MoS₂ (WS₂) nanosheets in low boiling point polar micromolecular solvents, even in pure water, without the use of any surfactant. Our strategy for preparing MoS₂ (WS₂) monolayers improves not only the monolayer yield but also the stability of the monolayer nanosheets in polar micromolecular solvents with low boiling points, making them highly useful.

3.2 Experimental section

3.2.1 Synthesis of monolayer transition metal disulfides (MoS₂ and WS₂) nanosheets

Bulk MoS₂ and WS₂ precursors were synthesized by thermal decomposition of (NH₄)₂MoS₄ (Purity 99.5%, Wako) and (NH₄)₂WS₄ (Purity 99.97, Aldrich) in an Ar atmosphere. The temperature was raised to 800°C with the rate of 5°C per minute and maintained for 5 hours, then the material was cooled to room temperature naturally. Typically, 100 mg of the as-prepared bulk MoS₂ (WS₂) precursor was added into a 100 ml glass vial. Then, 50 mL of polar micromolecular solvent was added as the exfoliation and dispersion solvent. The mixture was bath sonicated for 48 hours using an FU-260-C at a frequency of 28 kHz. The resulting suspensions were first centrifuged using a TOMY LC-200 centrifuge at 2000 rpm (RCF: 760 g) for 1 hour, then the top 2/3 portions of the supernatants were carefully collected by pipette. The obtained supernatants were added into a new glass vial and sonicated again for another 4 hours. Then, the monolayer MoS₂ (WS₂) dispersions were collected by pipette, followed by another centrifugation of the supernatant at 4000 rpm (RCF: 3020 g) for 1 hour.

3.2.2 Preparation of transition metal disulfide monolayers decorated CdS photocatalysts

Monolayer MoS₂ (WS₂) suspensions were mixed with commercial CdS (99%, Aldrich) in different stoichiometric ratios, sonicated and stirred overnight until dry, then the composites were collected and annealed in an Ar atmosphere at 400°C for 4 hours.

3.2.3 Characterization

The bulk material structures were determined using an X-ray diffractometer (X'pert powder, PANalytical B.V., Netherlands) with Cu-K α radiation. SEM was performed on a JEOL 6701F field-emission scanning electron microscope. TEM was performed on an FEI Tecnai G2 F30 microscope with a 300 kV accelerating voltage. AFM was carried out in tapping mode (Nanoscope H, Japan). XPS data were collected using a PHI Quantera SXM (ULVAC-PHI, Japan). Raman spectroscopy was performed using a

Horiba Jobin Yvon LabRAM system with a 532 nm excitation laser. UV-vis absorption spectra were measured using a Shimadzu UV-2500 spectrophotometer in quartz cuvettes with a pathlength of 2 mm. The zeta potential was tested using a Zeta-potential & Particle size Analyzer ELSZ-2000 series.

3.2.4 Photocatalytic H₂ evolution

The photocatalytic H₂ evolution was carried out with 0.2 g of the photocatalyst hybrid in 300 mL of solution in a Pyrex glass reaction cell. The optimized reaction solution is 30 vol.% lactic acid adjusted by NaOH to achieve a pH ~5.0. The reaction cell was connected to a closed gas system with a gas circulation pump. A 300 W Xenon lamp equipped with L42 cut-off filter was used as the visible light source ($\lambda > 420$ nm). H₂ evolution was measured with an on-line gas chromatograph (GC-8A, Shimadzu) equipped with a thermal conductivity detector according to the standard curve. The AQEs with various monochromatic lights were obtained by using a series of band-pass filters (Optical Coatings Japan). The light intensity was measured using a radiant power energy meter (Ushio spectroradiometer, USR-40, Japan). The AQE was calculated using the following equation:

$$\begin{aligned} \text{AQE} &= \frac{\text{Number of reacted electrons}}{\text{Number of incident photons}} = \frac{\text{Number of evolved H}_2 \text{ molecules} \times 2}{\text{Number of incident photons}} \\ &= \frac{M \times N_A \times 2}{\frac{I \times A \times t}{E_g \times J}} \end{aligned}$$

where M represents the amount of H₂ generation, N_A represents Avogadro's constant, I is the light intensity, A is the light incident area, t is the light incident time, and E_g and J are fixed constants.

3.3 Results and discussion

3.3.1 Characterization of as-synthesized transition metal disulfide bulk crystals

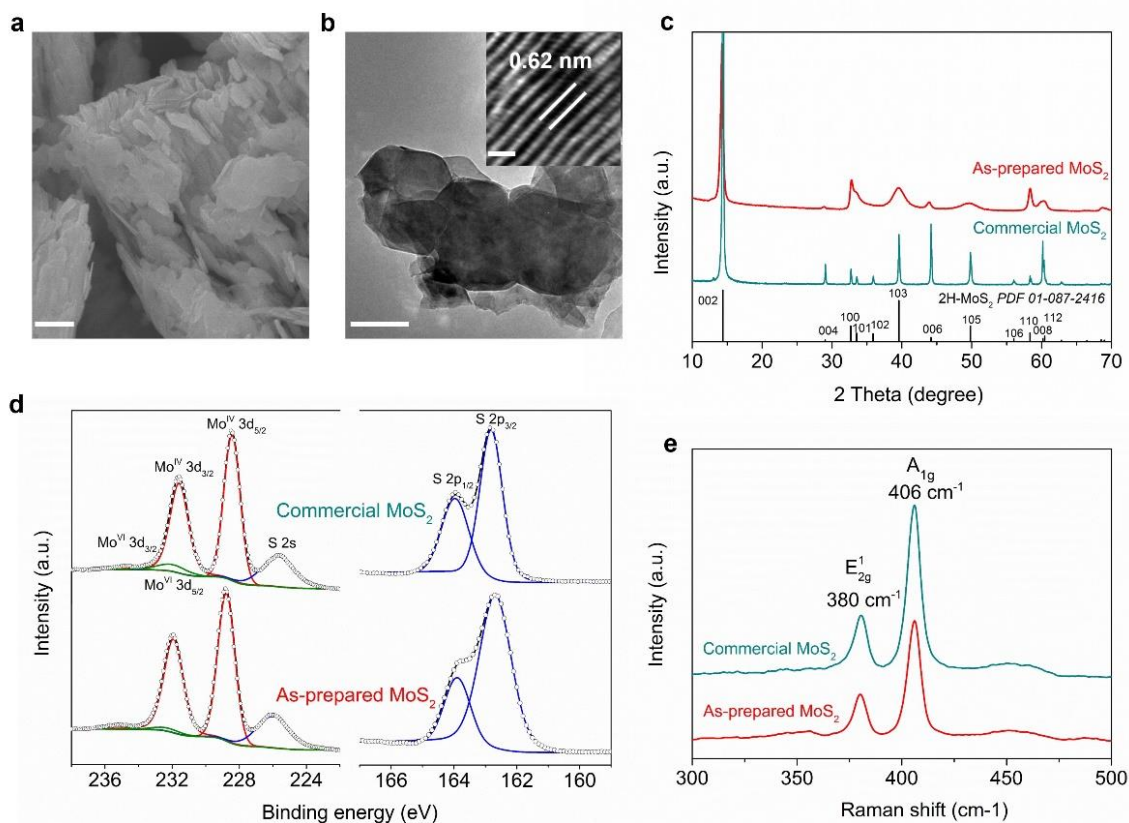
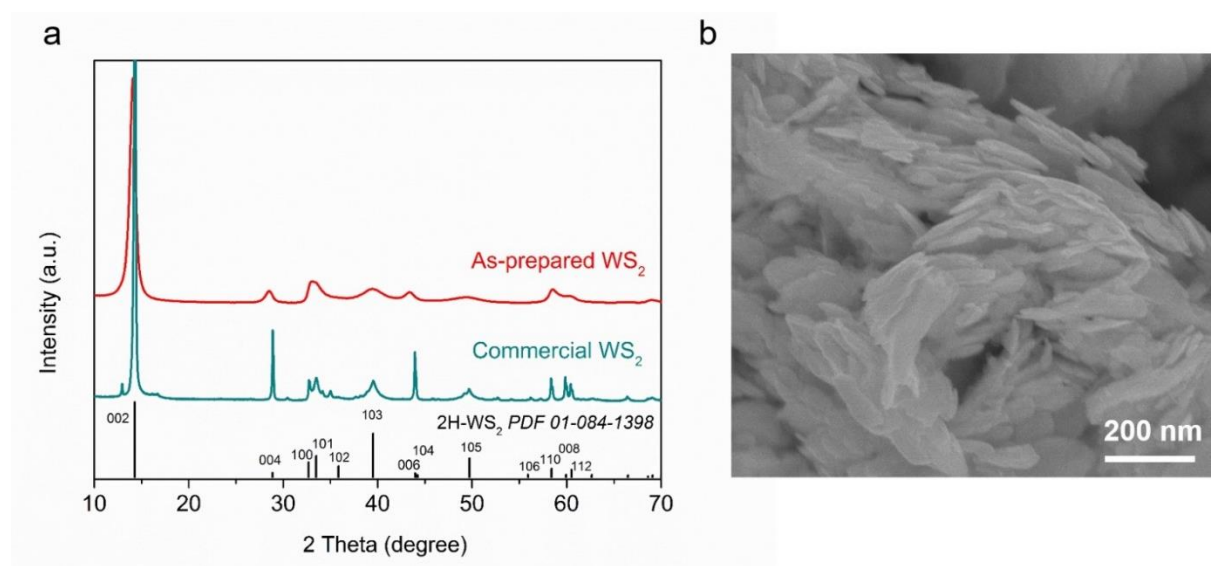


Figure 3.1 (a) SEM image of the as-prepared MoS₂ crystals. Scale bar = 200 nm. (b) TEM image of the as-prepared MoS₂ crystals. Scale bar = 100 nm. Inset is the high-resolution TEM image. Scale bar = 1 nm. (c) XRD patterns of the as-prepared and commercial MoS₂. The standard diffraction peak position of 2H-MoS₂ is displayed at the bottom of the diagram. (d) Fitted XPS Mo 3d, S 2s and S 2p core-level spectra of the as-prepared and commercial MoS₂. (e) Raman spectra of the as-prepared and commercial MoS₂.

The morphologies, structure and chemical states of the as-prepared MoS₂ (WS₂) precursors were examined by scanning electron microscopy (SEM), transmission electron microscopy (TEM), X-ray diffraction (XRD), X-ray photoelectron spectroscopy (XPS) and Raman spectroscopy. Compared with commercial MoS₂, the lateral size of the as-prepared MoS₂ precursor was drastically decreased from the microscale to the nanoscale, as shown in the SEM (Figure 3.1a) and TEM (Figure 3.1b) images. An estimation of the lateral size from the full-width at half-maximum of the (110) reflection in the XRD pattern (Figure 3.1c) is approximately 160 nm. Furthermore, the (002) peak is characterized by a shift to a lower angle compared with commercial MoS₂ and the 2H-MoS₂ crystal (PDF 01-087-2416). This shift in the (002) peak indicates an enlarged interlayer distance of the as-prepared MoS₂ precursor.^[25,26] According to the Bragg equation, the interlayer distance is calculated to be 0.62 nm, which is in agreement with the observed result in high-resolution TEM (inset of Figure 3.1b). It is worth noting that despite the significantly decreased lateral size, the as-prepared MoS₂ precursor still maintains high crystallinity, as shown by the sharp (002) peak observed in the XRD pattern and the uniform lattice arrangement in the high-resolution TEM image.

The chemical states of Mo and S in the as-prepared MoS₂ precursor were investigated by XPS (Figure 3.1d). The Mo 3d, S 2s and S 2p spectra of the as-prepared MoS₂ precursor are similar to that of commercial MoS₂. According to the analysis of the Mo 3d spectra, most of the Mo signals arise from the 3d_{3/2} peak at 232.0 eV and the 3d_{5/2} peak at 229.2 eV, indicating the characteristic +4 oxidation state.^[15] For both as-prepared and commercial MoS₂, deconvolution of the Mo 3d peaks revealed a weak Mo⁶⁺ 3d doublet with the 3d_{5/2} peak at 232.5 eV and 3d_{3/2} peak at 235.5 eV, likely due to slight surface oxidation upon exposure to air. In the S 2p core-level spectra, only a single doublet was observed at 163.6 and 162.5 eV corresponding to S 2p_{1/2} and S 2p_{3/2} orbitals of divalent sulfide ions, which is in good agreement with the binding energy of S²⁻ ions in 2H-MoS₂.^[27] Raman spectroscopy, shown in Figure 3.1e, further confirmed the 2H-phase structure of the as-prepared MoS₂ precursor by the appearance of two distinct peaks at 380 cm⁻¹ and 406 cm⁻¹, which correspond to the in-plane vibration (E_{2g}¹) and out-of-plane mode (A_{1g}), respectively.^[28] These results indicate that highly pure and highly crystalline 2H-phase MoS₂

crystals with lateral sizes in the nanoscale can be successfully synthesized through the facile thermal decomposition of $(\text{NH}_4)_2\text{MoS}_4$. Furthermore, the 2H-phase of WS_2 crystals can also be successfully synthesized (Figure 3.2).



3.3.2 The exfoliation mechanism

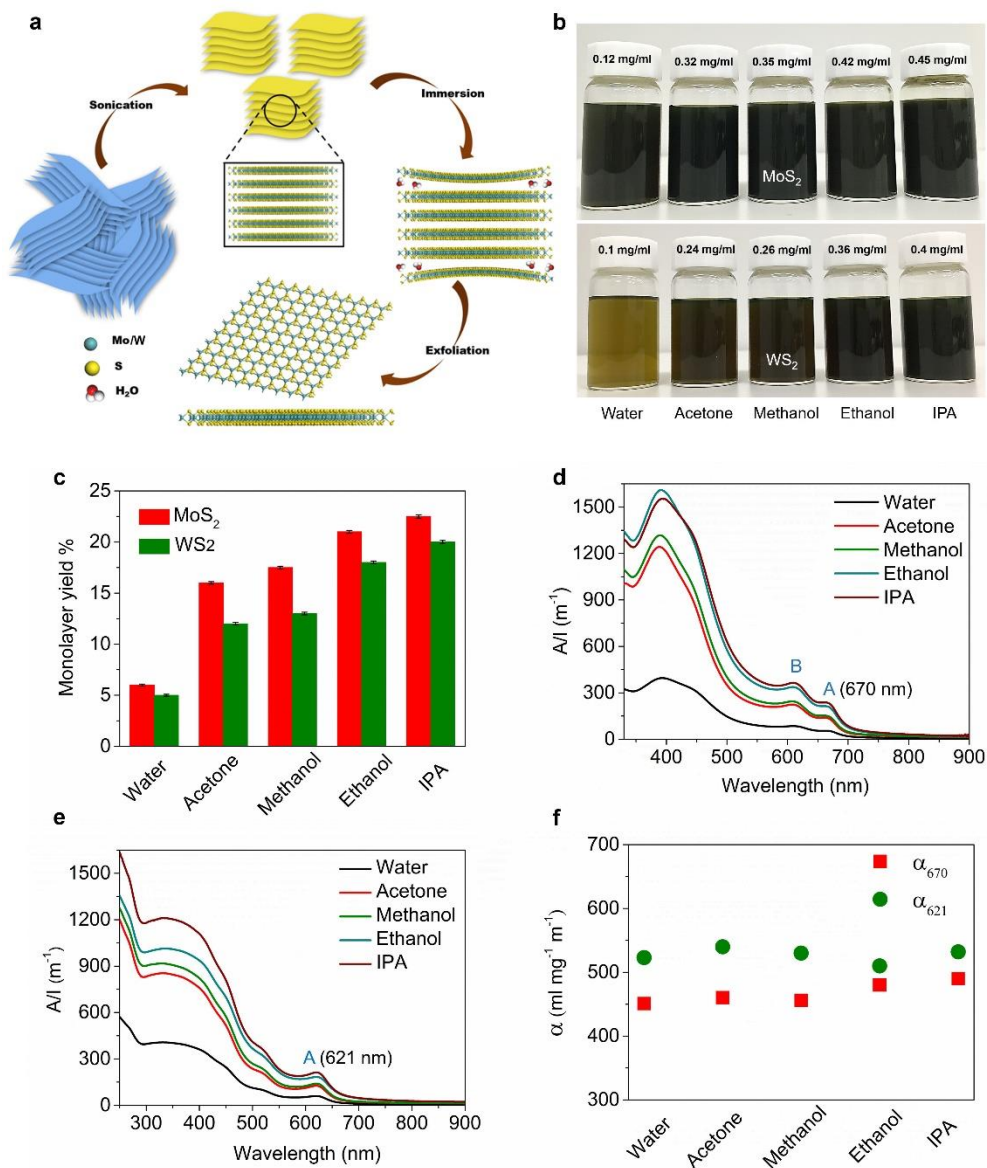


Figure 3.3 (a) Proposed mechanism of the liquid exfoliation process. (b) Photographs of obtained MoS₂ and WS₂ dispersions. (c) Monolayer yield. (d) Absorption spectra of MoS₂ dispersions. The positions of A- and B-excitons are marked. (e) Absorption spectra of WS₂ dispersions. The position of the A-exciton is marked. (f) Absorption coefficients at the A-exciton.

In an ideal liquid exfoliation, sufficient liquid intercalation into the layered crystal is the most effective and straightforward method to reduce the strength of the interlayer van der Waals attractions.^[29] Upon interaction with ultrasonic waves, the generated cavitation bubbles inside of the crystals collapse into high-energy liquid jets, breaking up the layered crystallites and producing exfoliated ultrathin nanosheets.^[23] However, the mismatch in surface tension between common polar micromolecular solvents, such as water, and MoS₂ (WS₂) crystals will hamper the intercalation of solvent into the layered crystals.^[20] High-energy liquid jets can only be generated at the interlayer edges rather than in the inner layers. For commercial MoS₂ and WS₂ crystals with lateral dimensions in the microscale, the resulting hydrodynamic forces around the crystal edge are insufficient to overcome the strong van der Waals attraction between the large adjacent layers, making direct exfoliation difficult. When the lateral size of the MoS₂ (WS₂) crystals is reduced from the microscale to the nanoscale, the ratio of hydrodynamic forces to interlayer van der Waals forces will be improved. Thus, for as-prepared MoS₂ and WS₂ crystals with lateral sizes on the nanoscale, the resulting hydrodynamic forces from high-energy liquid jets at the edge sites are enough to overcome the interlayer van der Waals attraction, allowing for ready exfoliation in polar micromolecular solvents, even in pure water, without the use of any surfactant. Herein, the following process is proposed for the successful exfoliation of the as-prepared MoS₂ and WS₂ precursors for producing monolayer nanosheets (Figure 3.3a). Upon sonication, the nanoflakes composed of MoS₂ and WS₂ precursors are first decomposed into individual nanoflakes (Figure 3.4). Next, the surrounding polar micromolecular solvents intercalate into the edges of the crystal interlayers. Then, the generated high-energy jets around the crystal edges overcome the interlayer van der Waals attraction, leading to the exfoliation and shearing of nanoflakes into monolayer nanosheets. After exfoliation, the exfoliated monolayer nanosheets can stably disperse in the polar micromolecular solvent.

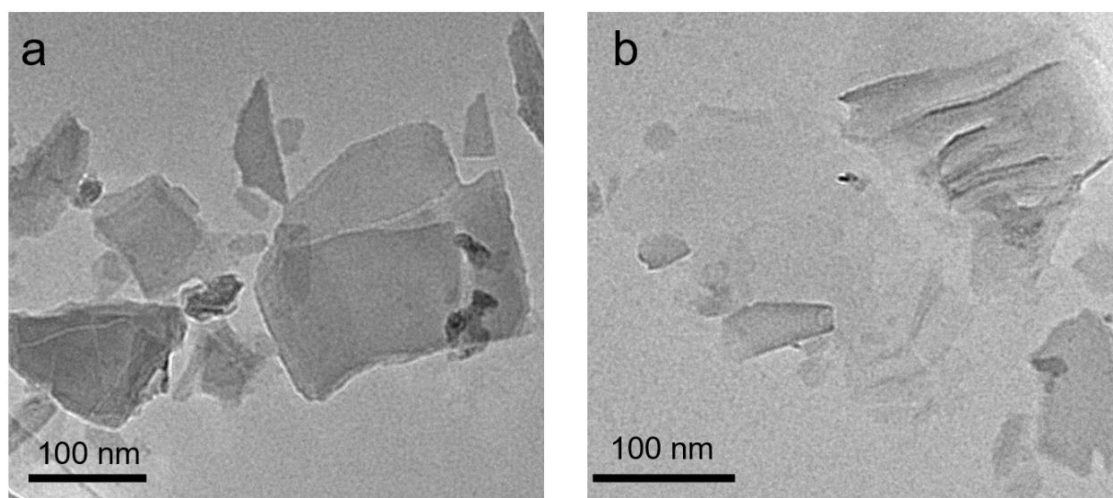


Figure 3.4 TEM images of the exfoliated nanosheets at the beginning (a) and with further sonication (b). The bulk crystals are first decomposed into individual thick nanoflakes. Then, these thick nanoflakes will be further exfoliated into thin nanosheets under continuous sonication.

To obtain purely monolayer, the sonicated suspensions of bulk MoS_2 or WS_2 were first centrifuged at 2000 rpm (RCF: 760 g) for 1 hour then at 4000 rpm (RCF: 3020 g) for another 1 hour to remove non-exfoliated precipitate. Figure 3.3b shows photographs of the obtained pure monolayer MoS_2 and WS_2 nanosheets in different polar micromolecular solvents, which were stable for over 100 days. Optimization of the exfoliation and dispersion procedure gave monolayer concentrations as high as 0.12 mg/ml (in water), 0.32 mg/ml (in acetone), 0.35 mg/ml (in methanol), 0.42 mg/ml (in ethanol), 0.45 mg/ml (in IPA) for MoS_2 , and as high as 0.10 mg/ml (in water), 0.24 mg/ml (in acetone), 0.26 mg/ml (in methanol), 0.36 mg/ml (in ethanol), 0.40 mg/ml (in IPA) for WS_2 . The initial concentration of the bulk crystal was 2 mg/ml, and the corresponding monolayer yield (Figure 3.3c) was calculated to be as high as 21% for MoS_2 and 18% for WS_2 in ethanol. Even in pure water, a monolayer yield of 6% for MoS_2 and 5% for WS_2 can be achieved. It is worth noting that the dispersions were obtained by high-speed centrifugation

over long periods of time, which inevitably results in many the exfoliated monolayer nanosheets reaggregating or adsorbing on the large sediments and being removed from the suspension.

Optical absorption spectra (Figure 3.3d) of the resulting dispersions show features expected for 2H-MoS₂.^[30] The distinct two peaks located at 615 (B-exciton) and 670 nm (A-exciton) are assigned to the direct excitonic transitions of MoS₂ at the K point of the Brillouin zone.^[31, 32] I determined the position of the A-exciton and B-exciton using the second derivative of the absorption spectra to exclude the contribution from the size-dependent scattering background.^[33] To simplify the tedious weighting process for determining nanosheet concentration, the concentration can be simply estimated using the optical absorption spectrum and the Beer-Lambert law, which relates the measured absorbance at a given wavelength to the concentration of the dispersion by the formula $A/l = \alpha C$, where A is the absorbance, l is the optical path length, α is the absorption coefficient, and C is the concentration.^[20] A/l scaled linearly with C (Figure 3.5) for all the dispersions, allowing for the calculation of α values. The obtained absorption coefficients of monolayer MoS₂ nanosheets range from 450 to 490 ml mg⁻¹ m⁻¹ (Figure 3.3f), which are much smaller than those previously published (~3000 ml mg⁻¹ m⁻¹).^[20, 23] This small α value may be attributed to the higher monolayer ratio and smaller lateral size. Figure 3.3e shows the optical absorption spectra of WS₂ dispersions exfoliated in different polar micromolecular solvents. A/l also scaled linearly with C (Figure 3.6). The obtained absorption coefficients of monolayer WS₂ nanosheets were calculated in the range of 510 to 532 ml mg⁻¹ m⁻¹ (Figure 3.3f), which are also much smaller than those previously published (~2500 ml mg⁻¹ m⁻¹).^[20,23]

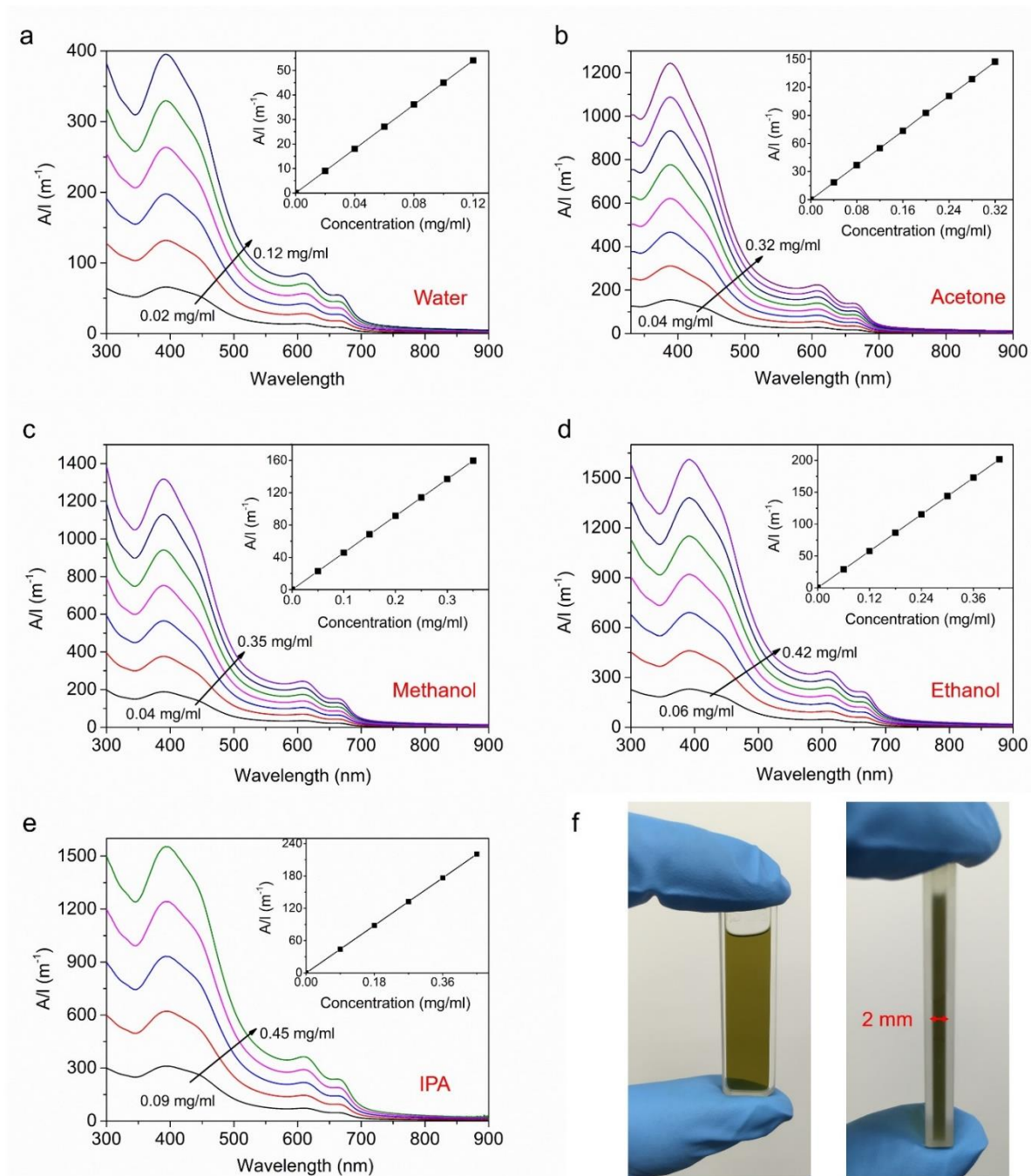


Figure 3.5 (a-e) Optical absorption spectra versus concentration of MoS₂ dispersions in different polar micromolecular solvents, insets are the absorption at A-exciton with the change of concentration. The absorption intensity at A-exciton scaled linearly with concentration for all solvents. (f) Photographs of dispersions in quartz cuvettes with a pathlength of 2 mm.

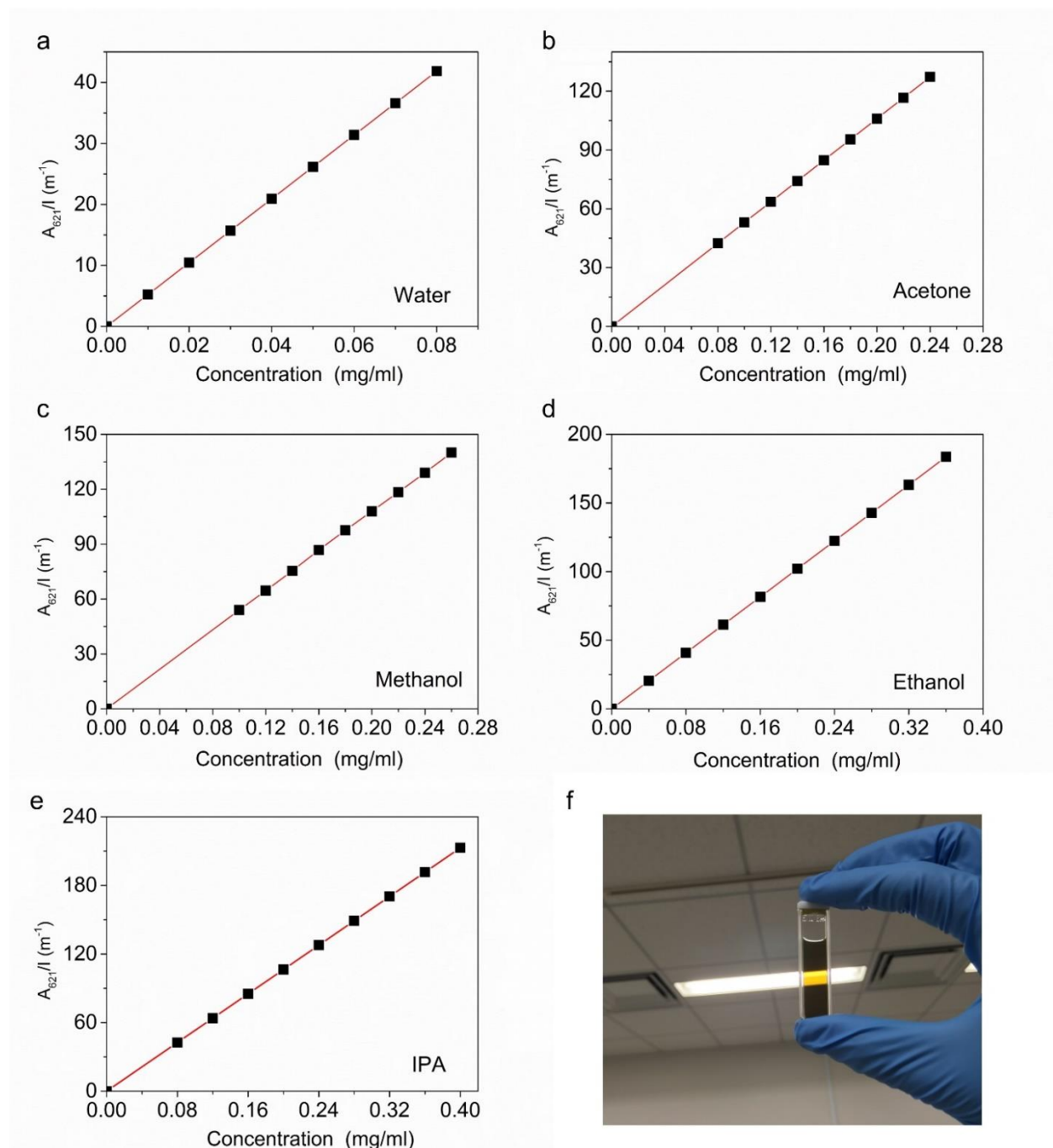


Figure 3.6 (a-e) Absorption at A-exciton versus concentration of WS_2 dispersions in different micromolecular solvents. The absorption at A-exciton also scaled linearly with concentration for all solvents. (f) Photograph of dispersions in quartz cuvette under the illumination of incandescent.

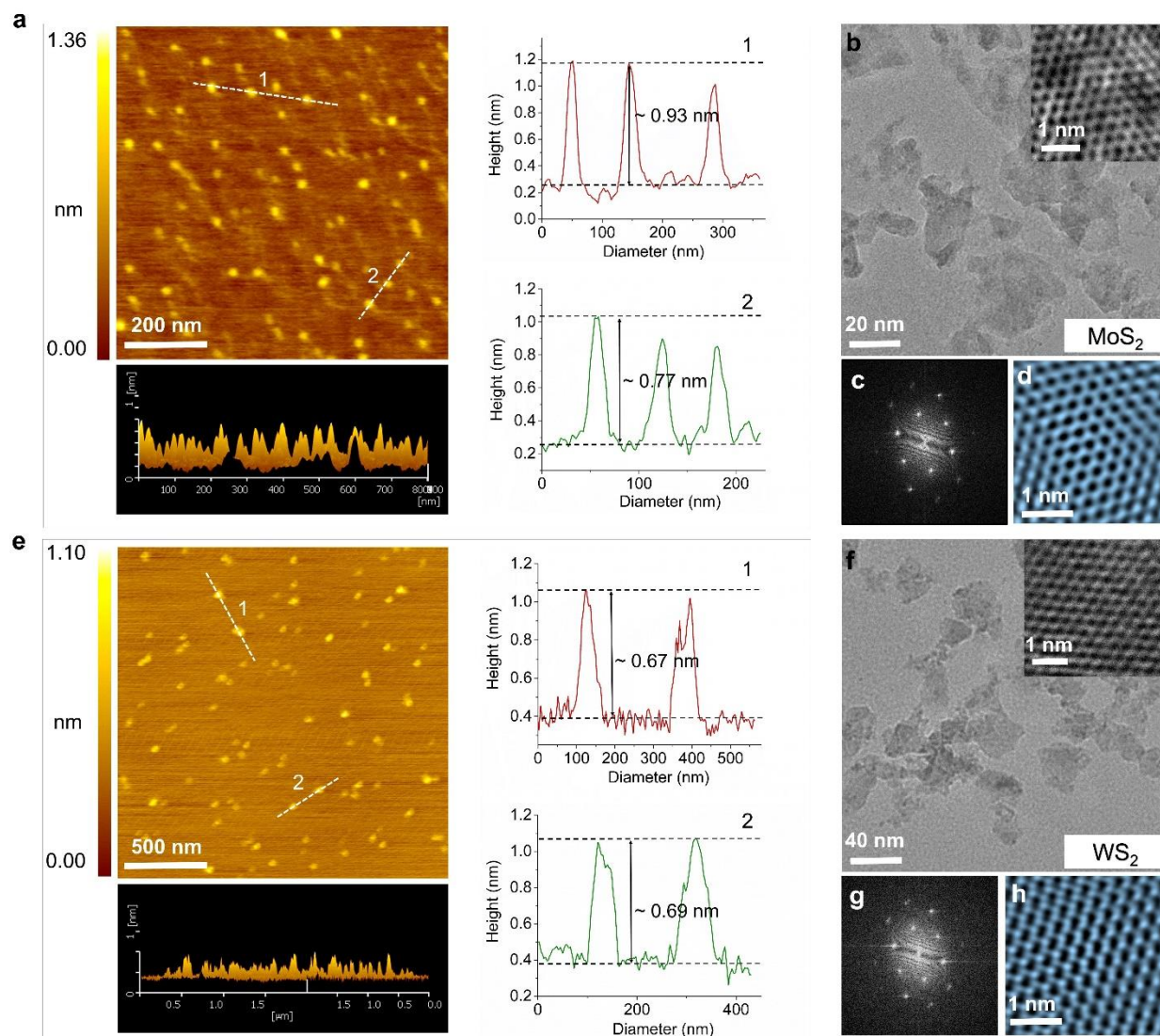
3.3.3 Characterization of exfoliated MoS₂ and WS₂ monolayers

Figure 3.7 (a) AFM image, 3D AFM image (bottom) and height profile of exfoliated monolayer MoS₂ nanosheets. (b) TEM image of monolayer MoS₂ nanosheets. Inset is the high-resolution TEM image of the selected region. (c, d) FFT pattern and FFT-filtered atomic resolution image of MoS₂. (e) AFM image, 3D AFM image (bottom) and height profile of exfoliated monolayer WS₂ nanosheets. (f) TEM image of monolayer WS₂ nanosheets. Inset is the high-resolution TEM image of the selected region. (g, h) FFT pattern and FFT-filtered atomic resolution image of WS₂.

The thickness of the exfoliated nanosheets was investigated by atomic force microscopy (AFM). I deposited dispersions on mica substrates by pipette and let them dry naturally. The high fluidity and volatility of these solvents allow the dispersed nanosheets to quickly and uniformly deposit on the mica substrates. The height profile of the two selected regions in the AFM images shows a height of ~ 0.8 nm (± 0.2 nm) for MoS₂ (Figure 3.7a and Figure 3.8) and ~ 0.7 nm (± 0.1 nm) for WS₂ (Figure 3.7e and Figure 3.9), which are close to the theoretical thickness of monolayer MoS₂ and WS₂ (~ 0.65 nm).^[34] This discrepancy is caused by surface corrugation due to distortions. The corresponding 3D images show that the dispersed nanosheets are all thinner than 1 nm, indicating that all the dispersed nanosheets have monolayer structures. To examine another typical characteristic for monolayer MoS₂ and WS₂, their photoluminescence (PL) spectra were also investigated to compare with bulk and partial monolayer dispersions (Figure 3.10). In agreement with other reports,^[21,33] the PL intensity of the A-exciton of the entirely monolayer MoS₂ (WS₂) dispersions was much stronger than their corresponding bulk and partial monolayer dispersions with the same concentration (Figure 3.11). Low-resolution TEM images (Figure 3.7b and 3.7f) indicate that the lateral size of the MoS₂ and WS₂ monolayers is approximately 40 nm. To further accurately measure the average sheet size, I employed particle size distribution analysis. The average lateral size was measured to be 46.5 nm for MoS₂ and 48.2 nm for WS₂, which are in good accordance with the results determined by the TEM images. The high-resolution TEM image of MoS₂ (inset of Figure 3.7b) and WS₂ (inset of Figure 3.7f) and associated Fourier transforms (Figure 3.7g and 3.7h) from the center of the nanosheets illustrate the hexagonally symmetric structure. The hexagonal widths of 3.8 Å for MoS₂ (Figure 3.7d) and 4.0 Å for WS₂ (Figure 3.7h) were determined after performing fast Fourier transform filtering of the high-resolution TEM images. These results indicate that the crystal structures obtained for the monolayer MoS₂ and WS₂ nanosheets were not damaged during water-bath sonication and retained their single crystalline nature.^[35,36]

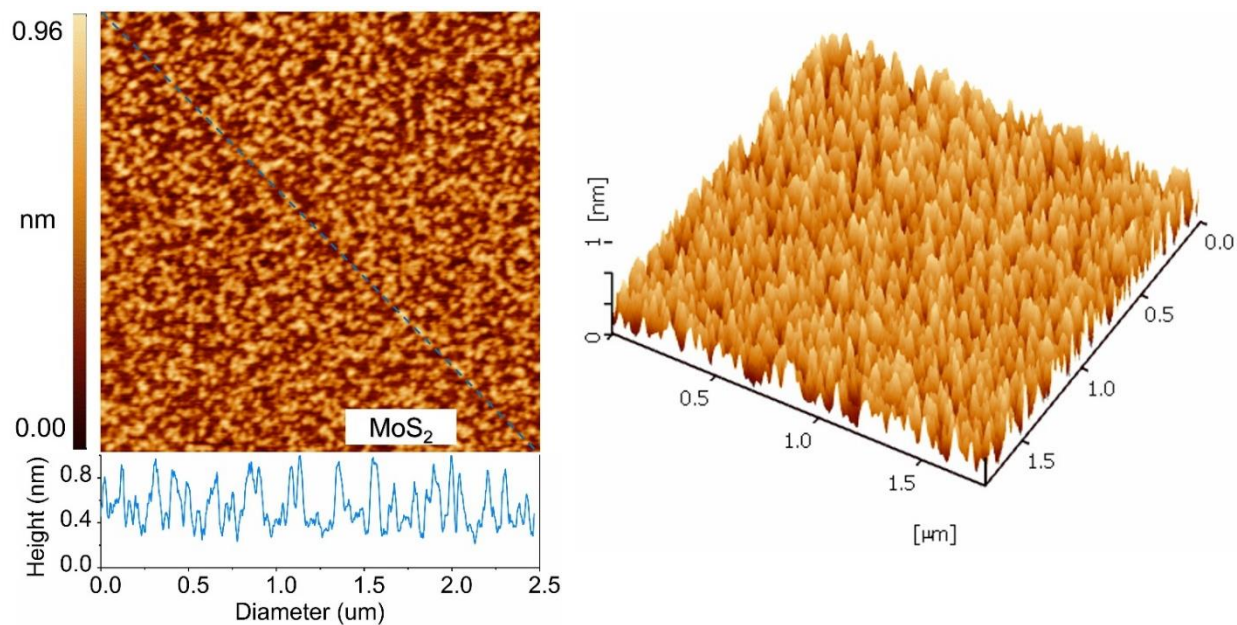


Figure 3.8 AFM images of obtained monolayer MoS₂ nanosheets.

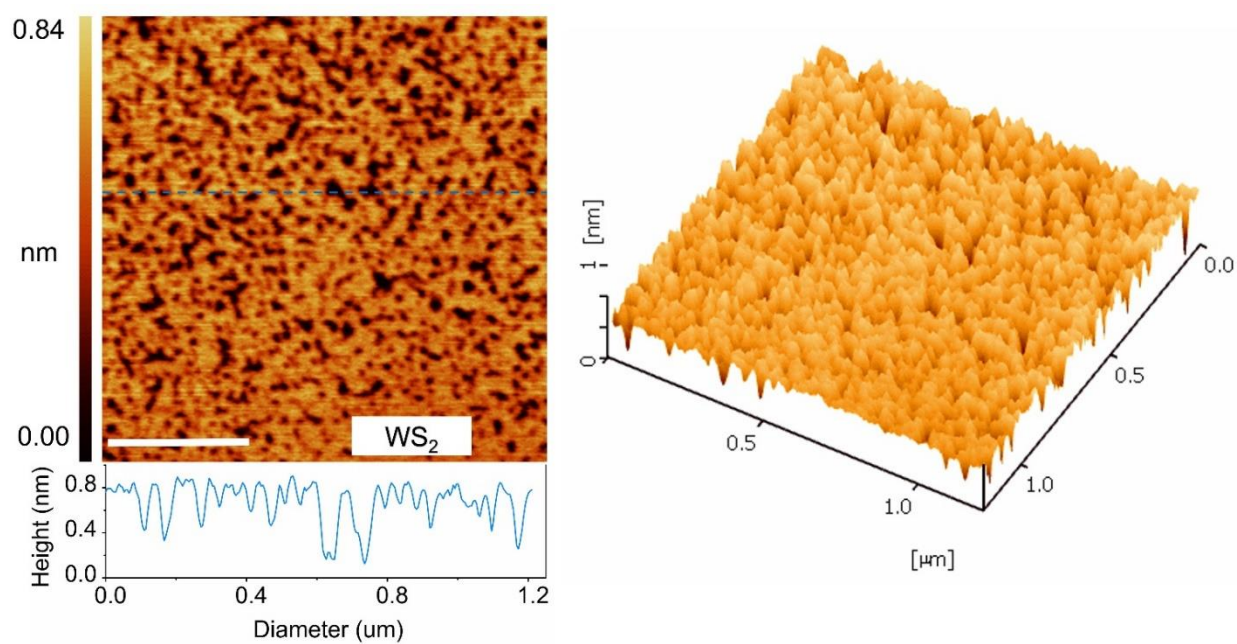


Figure 3.9 AFM images of obtained monolayer WS₂ nanosheets.

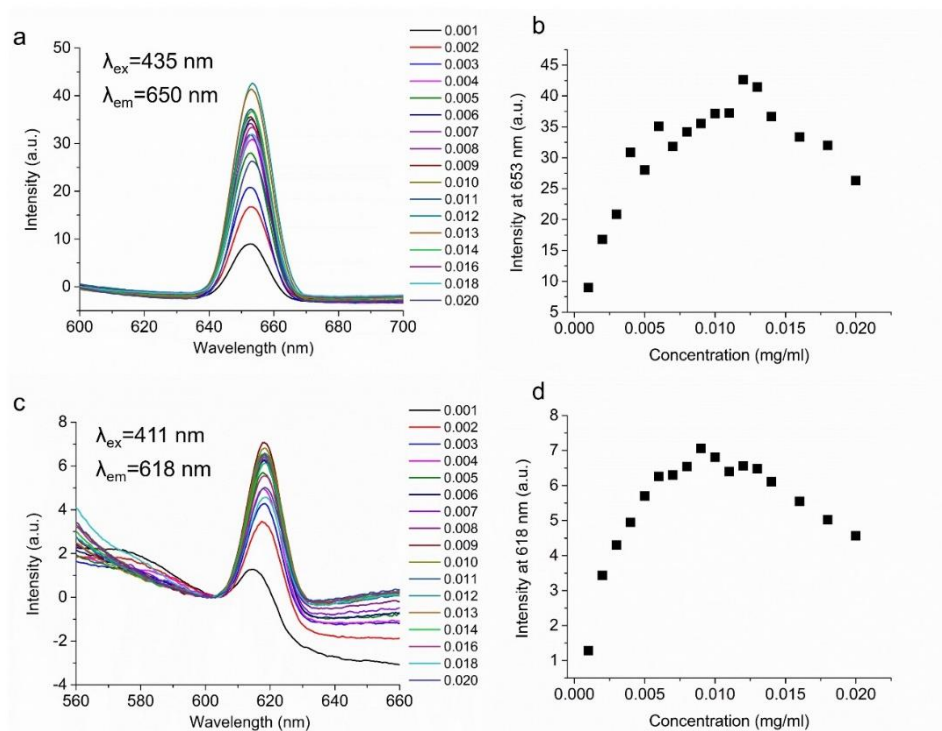


Figure 3.10 Concentration dependent photoluminescence spectra of (a) monolayer MoS₂ dispersion and (c) monolayer WS₂ dispersion. PL intensity of the A-exciton as a function of concentration for (b) MoS₂ monolayer and (d) WS₂ monolayer.

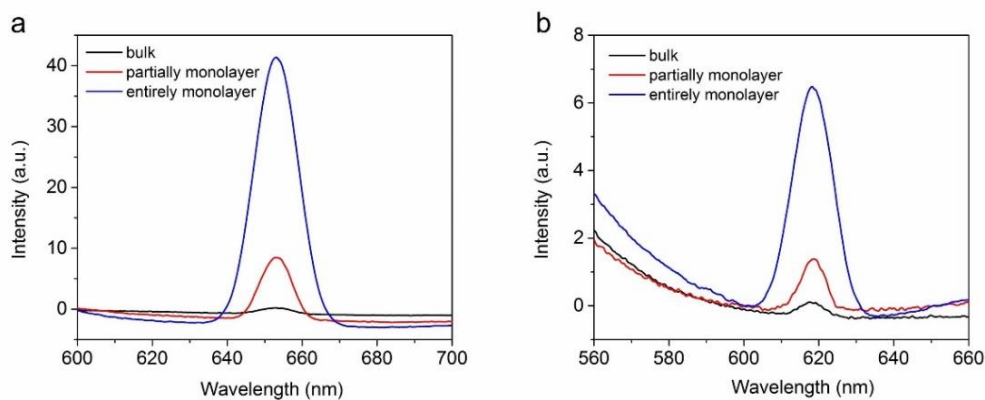


Figure 3.11 PL spectra of bulk, partial monolayer and entire monolayer dispersions with the same concentration for (a) MoS₂ with a concentration of 0.012 mg/mL and (b) WS₂ with a concentration of 0.013 mg/mL.

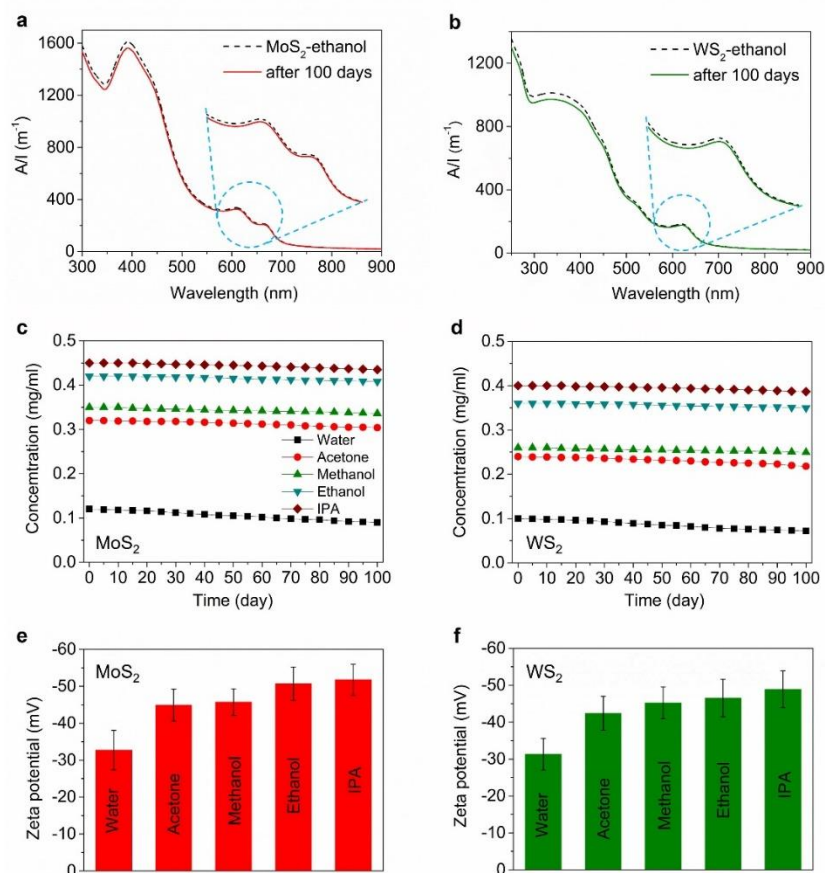


Figure 3.12 (a, b) Absorption spectra of MoS₂ and WS₂ monolayers dispersed in ethanol before and after storage for 100 days. (c, d) Concentration retention of MoS₂ and WS₂ as a function of time. (e, f) Zeta potential of MoS₂ and WS₂ dispersions.

Generally, the exfoliated monolayer MoS₂ and WS₂ nanosheets are easily aggregated and restacked due to the weak van der Waals force. It is important to examine the stability of the dispersions after centrifugation. Optical absorption spectra of MoS₂ (Figure 3.12a) and WS₂ (Figure 3.12b) dispersions in ethanol indicate that there is little attenuation after 100 days, suggesting the high stability of the monolayer dispersions in ethanol. The dispersion stability was tested by monitoring the change in the optical absorption spectra as a function of time (Figure 3.13). Concentration retention versus time can be

easily calculated from changes in the optical absorption spectra. These data are shown for MoS₂ (Figure 3.12a) and WS₂ (Figure 3.12b) dispersions. I

found that all of the MoS₂ and WS₂ dispersions, except those in water, are extremely stable, with more than 90% concentration retention after 100 days. Monolayer MoS₂ and WS₂ nanosheets dispersed in water are less stable, with 75% concentration retention for MoS₂ and 72% concentration retention for WS₂. The stability can also be reflected by performing zeta-potential tests, because nanomaterial solution stability is closely related to electrical double layers on the nanomaterial surface.^[37] In general, dispersed nanomaterials are stable with zeta-potential values of less than -30 mV.^[38,39] Each dispersion was tested three times, and the average value is reported (Figure 3.14). The measured zeta-potential values of the MoS₂ (Figure 3.12c) and WS₂ dispersions (Figure 3.12d) are all less than -30 mV, suggesting their good stability is irrespective of the solvent. Moreover, the exfoliated monolayer MoS₂ and WS₂ nanosheets are extremely stable when dispersed in acetone, methanol, ethanol and IPA, with zeta-potential values of less than -40 mV.

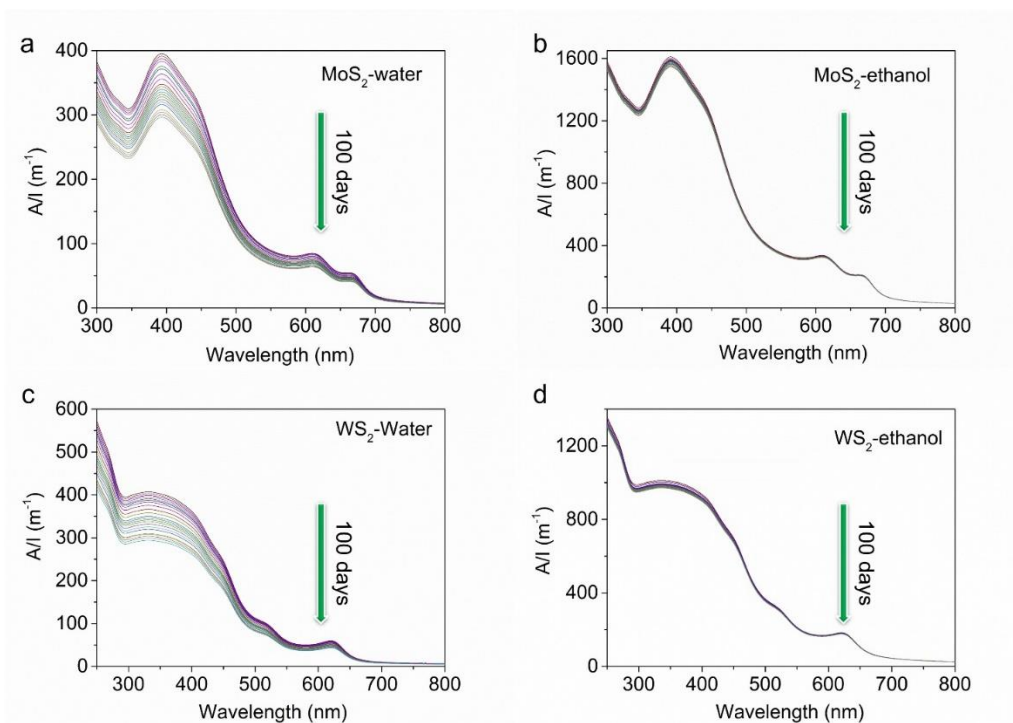


Figure 3.13 Absorption spectra of dispersions versus standing days. (a) MoS₂ monolayers dispersed in water. (b) MoS₂ monolayers dispersed in ethanol. (c) WS₂ monolayers dispersed in water. (d) WS₂ monolayers dispersed in ethanol.

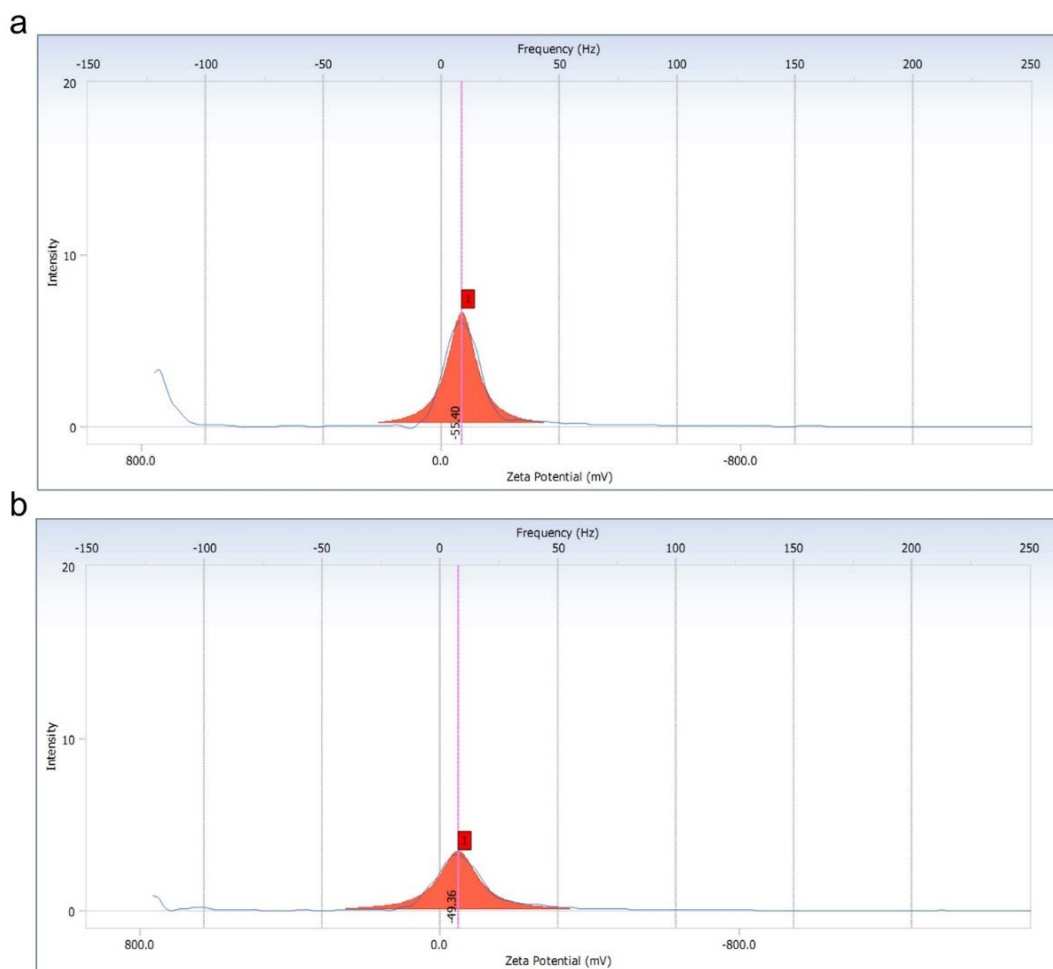


Figure 3.14 Zeta potential measurement of (a) MoS₂ and (b) WS₂ dispersions in ethanol with a concentration of 0.1 mg/mL.

3.3.4 Cocatalytic performance of exfoliated MoS₂ and WS₂ monolayers

As MoS₂ (WS₂) nanosheets are reported as potential electrocatalysts and cocatalysts to replace Pt in HER,^[40-42] I evaluated their HER performance by loading them on commercial CdS to be used as

cocatalysts for photocatalytic hydrogen evolution. These monolayer MoS₂ and WS₂ nanosheets can be easily and uniformly adsorbed on the surface of CdS due to their soft and small size features. Considering that the ΔG_{H}^* of MoS₂ (WS₂) active sites is slightly more than zero, the rate determining step in HER is the adsorption step.^[14] Although an acidic environment with an appropriate amount of H⁺ favors HER performance, the photoharvester CdS is not stable in a strongly acidic environment. Thus, the effect of pH value on the photocatalytic H₂ activity of the MoS₂/CdS composite was investigated (3.15).

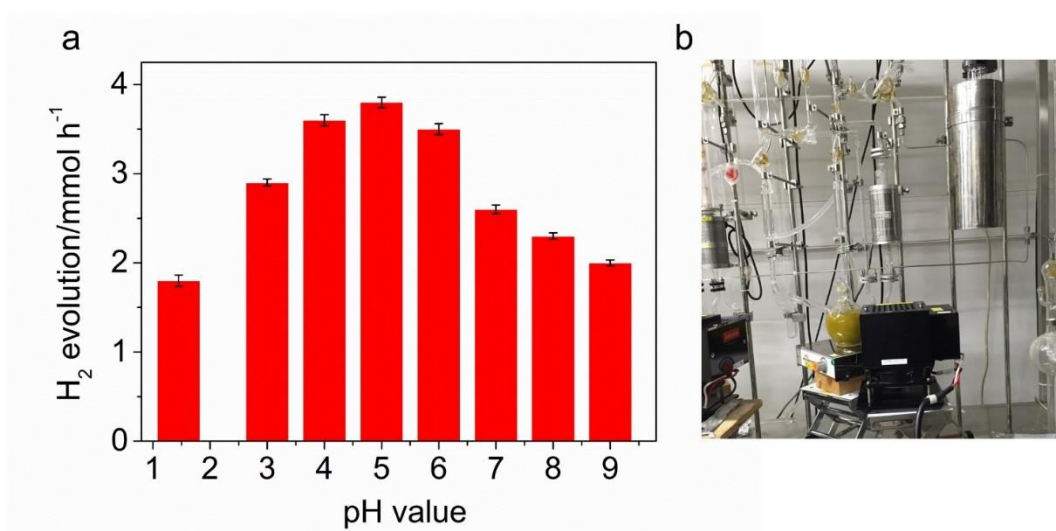


Figure 3.15 (a) Catalytic hydrogen activities of MoS₂ monolayers versus pH value. I evaluated the catalytic hydrogen activities of MoS₂ monolayers by loaded them on CdS for photocatalytic hydrogen production. Light source: 300-W Xe lamp with a L42 cut-off, $\lambda > 420$ nm; Reaction solution: 300 mL lactic acid solution (30 vol.%, pH=1.45), pH value was adjusted by NaOH; Catalyst: 200 mg, cocatalyst: 1.5wt %. (b) Photocatalytic hydrogen evolution system.

A series of MoS₂/CdS and WS₂/CdS composites with different amounts of cocatalyst were examined to investigate the effect of cocatalyst loading on the photocatalytic H₂ activity (Figure 3.16a). All of the composites were annealed in an Ar atmosphere at 400°C for 4 hours before testing.^[11] It was found that the composites show the highest H₂ evolution activities of 4.28 mmol h⁻¹ for MoS₂/CdS with 2 wt%

cocatalyst, and 5.5 mmol h^{-1} for WS_2/CdS with 3 wt % cocatalyst (Figure 3.17). Irradiated light will be blocked by the excess of MoS_2 (WS_2) monolayers upon further increasing the amount of cocatalyst, leading to a decrease in the H_2 evolution activity. The higher cocatalytic performance of WS_2 may be related to its stronger metallic properties.^[17] In addition to their remarkable photocatalytic activities, these materials also exhibit high stability, and no noticeable loss of activity for photocatalytic H_2 production can be observed after five cycles (Figure 3.16b). The wavelength dependence of H_2 evolution was then further investigated to prove that the reaction was driven by incident light. The UV-vis absorption spectrum of the CdS photoharvester along with the apparent quantum efficiency (AQE) of MoS_2/CdS and WS_2/CdS composites as a function of incident light wavelength are shown in Figure 3.16c. The AQE decreased as the wavelength of the monochromatic light increased, which was found to coincide well with the absorption edge of the CdS semiconductor. Under visible light irradiation at 420 nm, the AQE was calculated to be as high as 57.2% for MoS_2/CdS and 71.3% for WS_2/CdS . Figure 3.16d displays the H_2 production activities of MoS_2/CdS and WS_2/CdS composites under simulated sunlight using an Air Mass (AM) 1.5 solar simulator with a light intensity of 100 mW cm^{-2} . It can be seen that even under an irradiation of AM 1.5, the average hydrogen production of the WS_2/CdS composite can reach $\sim 500.0 \text{ } \mu\text{mol h}^{-1}$, which is higher than that of MoS_2/CdS ($\sim 397.2 \text{ } \mu\text{mol h}^{-1}$).

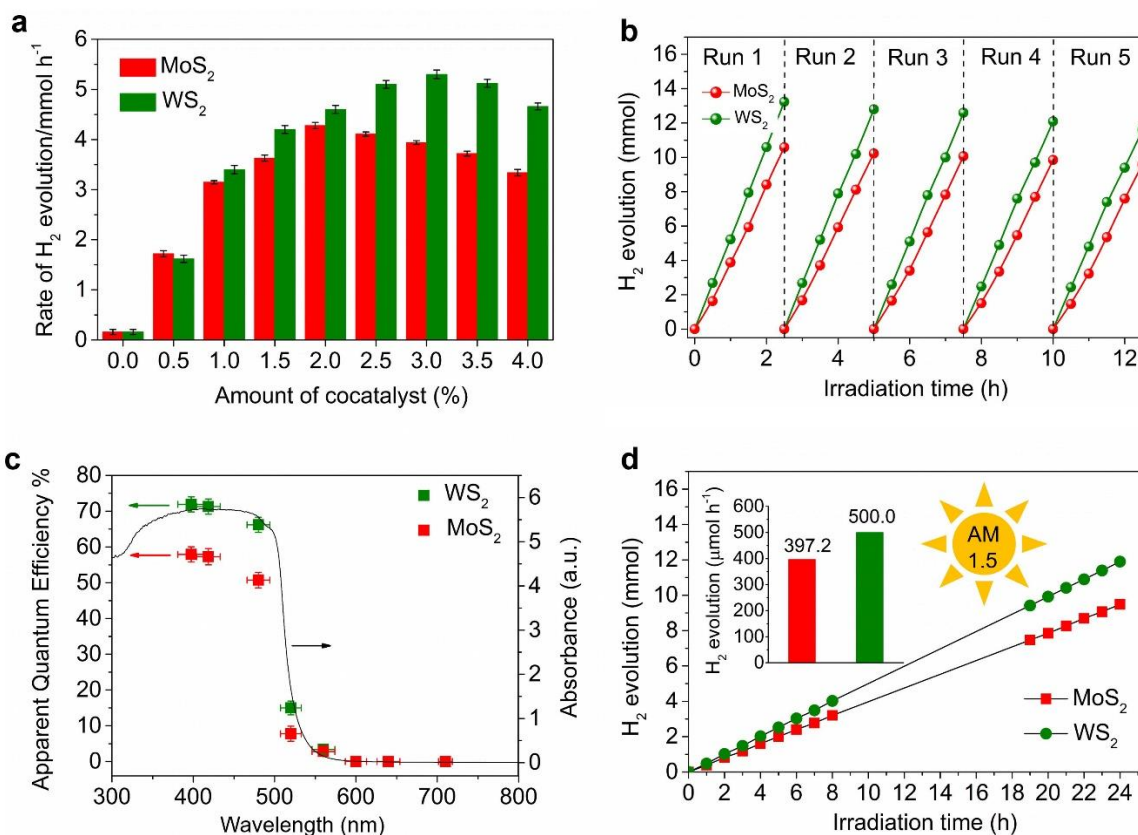


Figure 3.16 (a) Optimized content of cocatalysts over CdS. (b) Cycling test and (c) wavelength-dependent apparent quantum efficiency of H₂ evolution from MoS₂/CdS with 2 wt% cocatalyst and WS₂/CdS with 3 wt% cocatalyst. Light source: 300-W Xe lamp with a L42 cut-off, $\lambda > 420$ nm; Reaction solution: 300 mL sodium lactate solution (30 vol.% lactic acid adjusted by NaOH, pH~5.0); Catalyst: 200 mg. (d) Photocatalytic H₂ production activities of MoS₂/CdS and WS₂/CdS under the irradiation of AM 1.5 with a light intensity of 100 mW cm⁻². The inset shows the average rate of H₂ evolution.

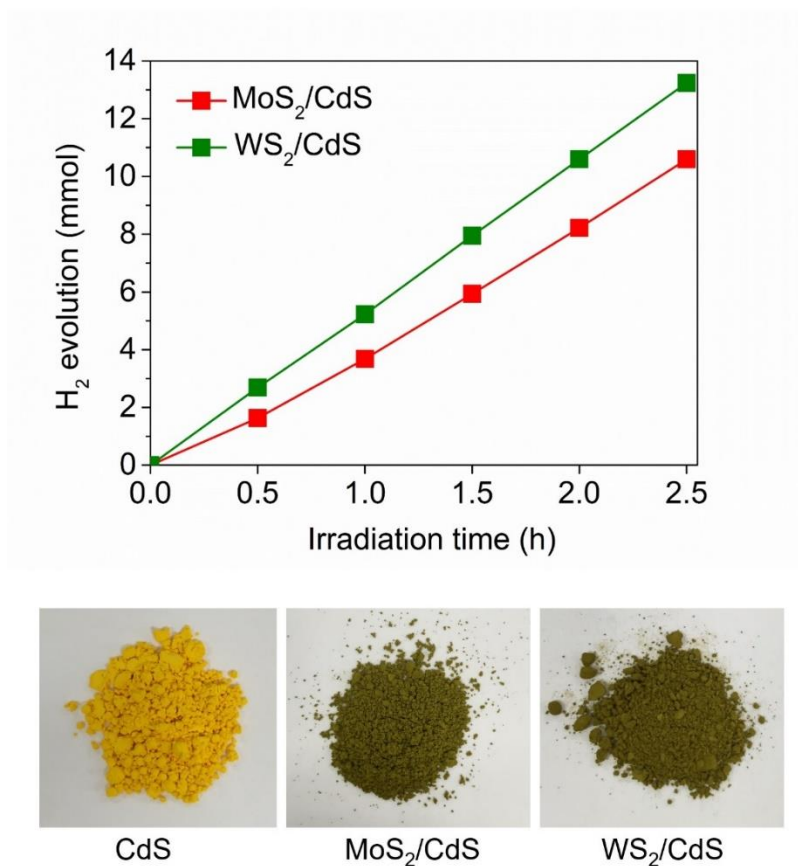


Figure 3.17 Photocatalytic H₂ evolution activities of MoS₂/CdS and WS₂/CdS under visible light irradiation. Light source: 300-W Xe lamp with a L42 cut-off, $\lambda > 420$ nm; Reaction solution: 300 mL sodium lactate solution (30 vol. % lactic acid adjusted by NaOH, pH=5.0); Catalyst: 200 mg; MoS₂/CdS with 2 wt% cocatalyst and WS₂/CdS with 3 wt% cocatalyst. Bottom: the photographs of MoS₂/CdS and WS₂/CdS composites.

During the photocatalytic HER process, the facile recombination of photoexcited electron-hole pairs before migrating to the surface to take part in the chemical reaction severely restricted the photo-conversion efficiency.^[43] Noble metals are often selected as cocatalysts to load on the surface of semiconductors to enhance the separation of photoexcited electrons and holes.^[17] Pt possesses the highest ability for trapping electrons because of its lowest Fermi level, giving it optimal cocatalytic performance in photocatalytic H₂ evolution.^[44] In this work, I compared the cocatalytic performance of the exfoliated monolayer MoS₂ and WS₂ nanosheets with Pt. It was found that the H₂ evolution activity of the MoS₂/CdS (4.28 mmol h⁻¹) composite is close to that of Pt/CdS (4.6 mmol h⁻¹), and the monolayer WS₂ (5.5 mmol h⁻¹) nanosheets exhibit an unexpectedly higher cocatalytic performance than Pt. The superior cocatalytic performances of the MoS₂ and WS₂ monolayers are attributed to the following two aspects. First, the monolayer MoS₂ and WS₂ nanosheets with lateral sizes in the tens of nanometers have more active edge sites for HER.^[45] The DFT-calculated free energy of atomic hydrogen bonding to MoS₂ edge sites is slightly positive at +0.08 eV.^[16] Chorkendorff and co-workers also experimentally determined that the active sites for HER are the MoS₂ edge-site S atoms.^[14] Compared with MoS₂ and WS₂ monolayers obtained from commercial bulk crystals (average lateral size > 200 nm), our exfoliated monolayer nanosheets (average lateral size < 50 nm) have a higher fraction of edges, which provides more exposed active sites for HER. Because of the strong dependence on the layers, the cocatalytic performance of the MoS₂ nanosheets increased with reducing layer number, where monolayer MoS₂ showed the best cocatalytic performance for photocatalytic hydrogen production.^[11] The obtained monolayer MoS₂ and WS₂ nanosheets can be uniformly adsorbed on CdS surfaces to avoid aggregation, as seen in the SEM images (Figure 3.18) and optical absorption spectra of the composites (Figure 3.19). Second, chemical bonding at the interface of the monolayer nanosheets with CdS is more favorable for interfacial charge transfer, which can efficiently suppress the recombination of photoexcited electron-hole pairs.^[46-48] The photocatalytic H₂ activities of MoS₂/CdS and WS₂/CdS composites with different annealing temperatures are shown in Figure 3.20. It can be seen that the activity gradually increased with increasing temperature and reached a plateau at 400°C. For the freshly made, mechanically mixed composites, their weak

physical adsorption severely lowered their photocatalytic HER activities, and the composites were greatly strengthened after annealing at 400°C through the creation of chemical bond. This result indicates that the chemically bonded interface of WS₂/CdS plays an important role in separating photoexcited electron-hole pairs, leading to a higher cocatalytic performance than Pt.

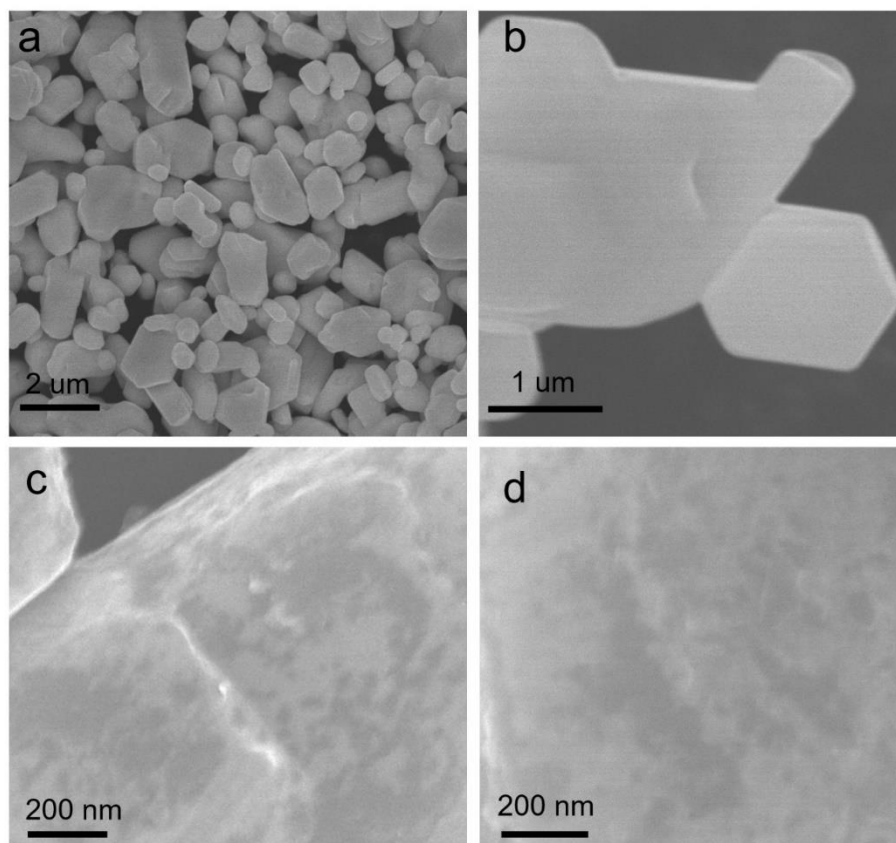


Figure 3.18 SEM images of pure CdS (a,b), MoS₂/CdS (c) and WS₂/CdS (d). Pure CdS surface is very smooth, the MoS₂ and WS₂ monolayers can be easily and uniformly adsorbed on the surface of CdS due to their soft and small size features.

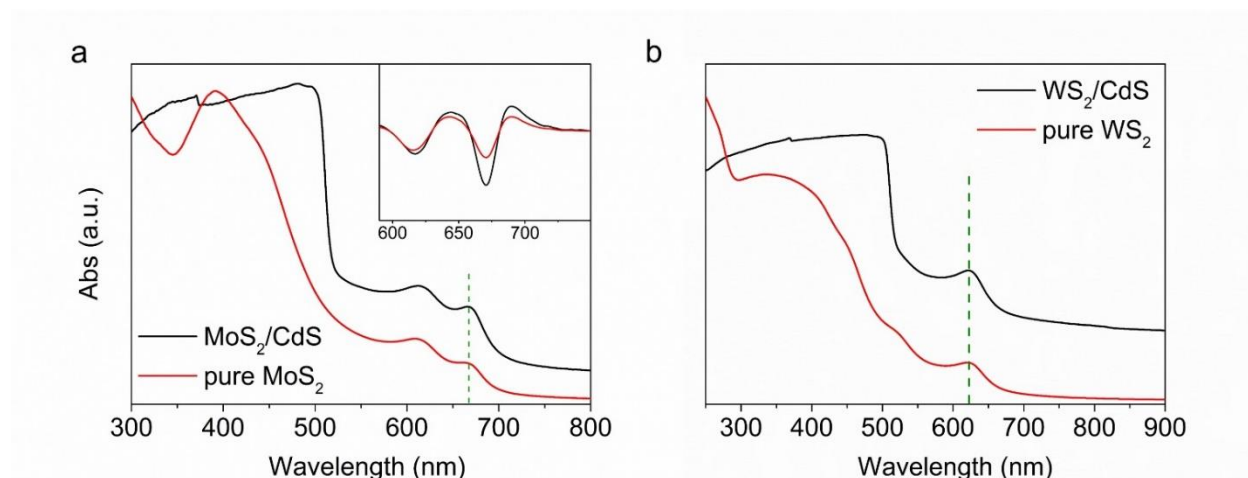


Figure 3.19 Comparison of absorption spectra of MoS₂ dispersions and MoS₂/CdS (a), WS₂ dispersions and WS₂/CdS (b). Inset of (a) is the second derivative of the absorption spectra. Peak position of the A-exciton is closely related to the nanosheets thickness, it will be red-shifted with the increase of nanosheets thickness. After loaded on CdS, peak positions of the A-exciton of MoS₂ and WS₂ do not have any movement compared with MoS₂ and WS₂ dispersions. This result indicates that MoS₂ and WS₂ monolayers are individually absorbed on the surface of CdS, and avoid restacking.

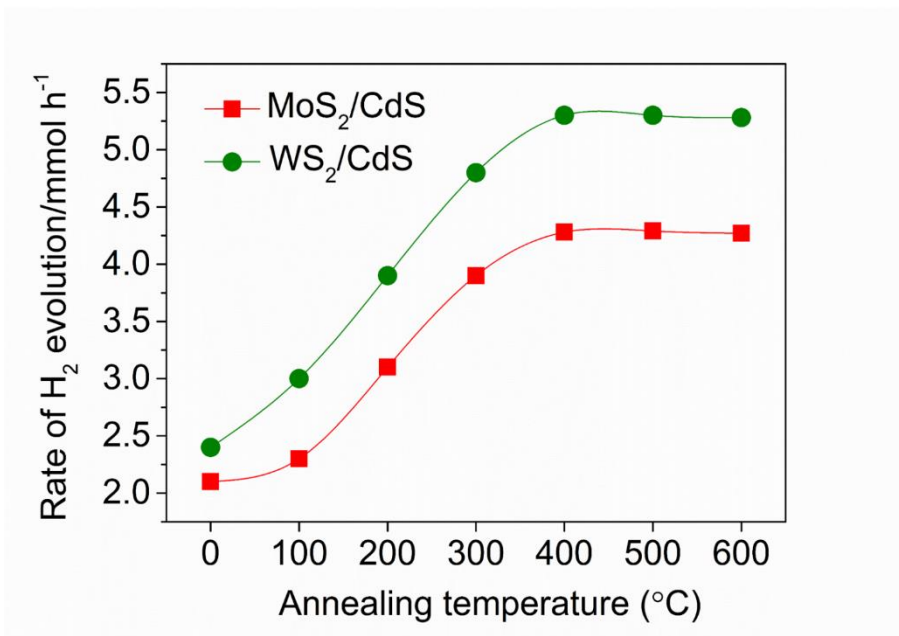


Figure 3.20 Photocatalytic H₂ evolution activities of MoS₂/CdS and WS₂/CdS composites with different annealing temperature. Light source: 300-W Xe lamp with a L42 cut-off, $\lambda > 420$ nm; Reaction solution: 300 mL sodium lactate solution (30 vol.% lactic acid adjusted by NaOH, pH=5.0); Catalyst: 200 mg; MoS₂/CdS with 2 wt% cocatalyst and WS₂/CdS with 3 wt% cocatalyst.

3.4 Conclusion

In summary, I have introduced a facile method to synthesize highly crystalline bulk MoS₂ (WS₂) precursors with a lateral size in the nanoscale, which can be readily exfoliated in polar micromolecular solvents, even in pure water, to produce MoS₂ (WS₂) monolayers without the use of any surfactant. Compared to commercial MoS₂ (WS₂), the successful exfoliation of the as-prepared MoS₂ (WS₂) crystals is attributed to their increased fraction of edges, which can improve the ratio of hydrodynamic forces on the edges to van der Waals forces between the adjacent layers. The exfoliation yield of monolayers was measured to be as high as 21% for MoS₂ and 18% for WS₂ in ethanol. Even in pure water, a monolayer yield of 6% for MoS₂ and 5% for WS₂ can be achieved. By reducing the lateral size of the layered crystals

to the nanoscale, the edge concentration is drastically increased and can provide sufficient hydrodynamic force to overcome the interlayer van der Waals attraction to delaminate the layered crystals in solution, providing a new strategy for the large-scale production of TMDC monolayers by liquid exfoliation. In addition to demonstrating successful exfoliation, the exfoliated MoS₂ and WS₂ monolayers also exhibit excellent catalytic hydrogen activities, particularly for monolayer WS₂, which has a cocatalytic performance that is even higher than that of Pt.

Reference

- [1] Novoselov, K. S.; Geim, A. K.; Morozov, S. V.; Jiang, D.; Zhang, Y.; Dubonos, S. V.; Grigorieva, I. V.; Firsov, A. A. *Science* 2004, 306, 666-669.
- [2] Fan, X. B.; Xu, P. T.; Li, Y. G.; Zhou, D. K.; Sun, Y. F.; Nguyen, M. A. T.; Terrones, M.; Mallouk, T. E. J. *Am. Chem. Soc.* 2016, 138, 5143-5149.
- [3] Novoselov, K. S.; Jiang, D.; Schedin, F.; Booth, T. J.; Khotkevich, V. V.; Morozov, S. V.; Geim, A. K. *Proc. Natl. Acad. Sci. U.S.A.* 2005, 102, 10451-10453.
- [4] Zeng, H.; Dai, J.; Yao, W.; Xiao, D.; Cui, X. *Nature Nanotech.* 2012, 7, 490-493.
- [5] Wang, Q. H.; Kalantar-Zadeh, K.; Kis, A.; Coleman, J. N.; Strano, M. S. *Nature Nanotech.* 2012, 7, 699-712.
- [6] Radisavljevic, B.; Radenovic, A.; Brivio, J.; Giacometti, V.; Kis, A. *Nature Nanotech.* 2011, 6, 147-150.
- [7] Li, T.; Galli, G. J. *Phys. Chem. C.* 2007, 111, 16192-16196.
- [8] Splendiani, A.; Sun, L.; Zhang, Y. B.; Li, T. S.; Kim, J.; Chim, C. Y.; Galli, G.; Wang, F. *Nano Lett.* 2010, 10, 1271-1275.
- [9] Lopez-Sanchez, O.; Lembke, D.; Kayci, M.; Radenovic, A.; Kis, A. *Nature Nanotech.* 2013, 8, 497-501.

- [10] Lee, C.-H.; Lee, G.-H.; van der Zande, A. M.; Chen, W.; Li, Y.; Han, M.; Cui, X.; Arefe, G.; Nuckolls, C.; Heinz, T. F.; Guo, J.; Hone, J.; Kim, P. *Nature Nanotech.* 2014, 9, 676-681.
- [11] Chang, K.; Li, M.; Wang, T.; Ouyang, S. X.; Li, P.; Liu, L. Q.; Ye, J. H. *Adv. Energy. Mater.* 2015, 5, 1402279.
- [12] Huang, X.; Zeng, Z. Y.; Zhang, H. *Chem. Soc. Rev.* 2013, 42, 1934-1946.
- [13] Zhang, H. *ACS Nano* 2015, 9, 9451-9469.
- [14] Jaramillo, T. F.; Jørgensen, K. P.; Bonde, J.; Nielsen, J. H.; Horch, S.; Chorkendorff, I. *Science* 2007, 317, 100-102.
- [15] Kibsgaard J.; Chen Z. B.; Reinecke B. N.; Jaramillo T. F. *Nat. Mater.* 2012, 11, 963-969.
- [16] Hinnemann, B.; Moses, P. G.; Bonde, J.; Jørgensen, K. P.; Nielsen, J. H.; Horch, S.; Chorkendorff, I.; Nørskov, J. K. *J. Am. Chem. Soc.* 2005, 127, 5308-5309.
- [17] Chang, K.; Hai, X.; Ye, J. *Adv. Energy Mater.* 2016, 6, 1502555-1502575.
- [18] Li, H.; Tsai, C.; Koh, A. L.; Cai, L. L.; Contryman, A. W.; Fragapane, A. H.; Zhao, J. H.; Han, H. S.; Manoharan, H. C.; Abild-Pedersen, F.; Nørskov, J. K.; Zheng, X. L. *Nat. Mater.* 2016, 15, 48-53.
- [19] Nicolosi, V.; Chhowalla, M.; Kanatzidis, M. G.; Strano, M. S.; Coleman, J. N. *Science* 2013, 340, 6139.
- [20] Coleman, J. N.; Lotya, M.; O'Neill, A.; Bergin, S. D.; King, P. J.; Khan, U.; Young, K.; Gaucher, A.; De, S.; Smith, R. J.; Shvets, I. V.; Arora, S. K.; Stanton, G.; Kim, H. Y.; Lee, K.; Kim, G. T.; Duesberg, G. S.; Hallam, T.; Boland, J. J.; Wang, J. J.; Donegan, J. F.; Grunlan, J. C.; Moriarty, G.; Shmeliov, A.; Nicholls, R. J.; Perkins, J. M.; Grievson, E. M.; Theuwissen, K.; McComb, D. W.; Nellist, P. D.; Nicolosi, V. *Science* 2011, 331, 568.
- [21] Backes, C.; Szydłowska, B. M.; Harvey, A.; Yuan, S.; Vega-Mayoral, V.; Davies, B. R.; Zhao, P.-l.; Hanlon, D.; Santos, E. J. G.; Katsnelson, M. I.; Blau, W. J.; Gabermaier, C.; Coleman, J. N. *ACS Nano* 2016, 10, 1589–1601.

- [22] Smith, R. J.; King, P. J.; Lotya, M.; Wirtz, C.; Khan, U.; De, S.; O'Neill, A.; Duesberg, G. S.; Grunlan, J. C.; Moriarty, G.; Chen, J.; Wang, J.; Minett, A. I.; Nicolosi, V.; Coleman, J. N. *Adv. Mater.* 2011, 23, 3944-3948.
- [23] Shen, J.; He, Y.; Wu, J.; Gao, C.; Keyshar, K.; Zhang, X.; Yang, Y.; Ye, M.; Vajtai, R.; Lou, J.; Ajayan, P. M. *Nano Lett.* 2015, 15, 5449-5454.
- [24] Kim, J.; Kwon, S.; Cho, D.-H.; Kang, B.; Kwon, H.; Kim, Y.; Park, S. O.; Jung, G. Y.; Shin, E.; Kim, W.-G.; Lee, H.; Ryu, G. H.; Choi, M.; Kim, T. H.; Oh, J.; Park, S.; Kwak, S. K.; Yoon, S. W.; Byun, D.; Lee, Z.; Lee, C. *Nat. Commun.* 2015, 6, 8294-8302.
- [25] Liang, K. S.; Chianelli, R. R.; Chien, F. Z.; Moss, S. C. *J. Non-Cryst. Solids.* 1986, 79, 251-273.
- [26] Chhowalla, M.; Amaratunga, G. A. *J. Nature* 2000, 407, 164-167.
- [27] Oakes, L.; Carter, R.; Hanken, T.; Cohn, A. P.; Share, K.; Schmidt, B.; Pint, C. L. *Nat. Commun.* 2016, 7, 11796.
- [28] Lee, C.; Yan, H.; Brus, L. E.; Heinz, T. F.; Hone, J.; Ryu, S. *ACS Nano* 2010, 4, 2695-2700.
- [29] Halim, U.; Zheng, C. R.; Chen, Y.; Lin, Z.; Jiang, S.; Cheng, R.; Huang, Y.; Duan, X. *Nat. Commun.* 2013, 4, 2213.
- [30] Wilcoxon, J. P.; P. P. Newcomer.; G. A. Samara. *J. Appl. Phys.* 1997, 81, 7934-7944.
- [31] Guan, G.; Zhang, S.; Liu, S.; Cai, Y.; Low, M.; Teng, C. P.; Phang, I. Y.; Cheng, Y.; Duei, K. L.; Srinivasan, B. M.; Zheng, Y.; Zhang, Y. W.; Han, M. Y. *J. Am. Chem. Soc.* 2015, 137, 6152-6155.
- [32] Mak, K. F.; Lee, C.; Hone, J.; Shan, J.; Heinz, T. F. *Phys. Rev. Lett.* 2010, 105, 136805.
- [33] Backes, C.; Smith, R. J.; McEvoy, N.; Berner, N. C.; McCloskey, D.; Nerl, H. C.; O'Neill, A.; King, P. J.; Higgins, T.; Hanlon, D.; Scheuschner, N.; Maultzsch, J.; Houben, L.; Duesberg, G. S.; Donegan, J. F.; Nicolosi, V.; Coleman, J. N. *Nat. Commun.* 2014, 5, 4576.
- [34] Li, H.; Zhang, Q.; Yap, C. C. R.; Tay, B. K.; Edwin, T. H. T.; Olivier, A.; Baillargeat, D. *Adv. Funct. Mater.* 2012, 22, 1385-1390.
- [35] Chou, S. S.; De, M.; Kim, J.; Byun, S.; Dykstra, C.; Yu, J.; Huang, J.; Dravid, V. P. *J. Am. Chem. Soc.* 2013, 135, 4584-4587.

- [36] Wang, L.; Xu, Z.; Wang, W.; Bai, X. *J. Am. Chem. Soc.* 2014, 136, 6693-6697.
- [37] Oakes, L.; Zulkifli, D.; Azmi, H.; Share, K.; Hanken, T.; Carter, R.; Pint, C. L. *J. Electrochem. Soc.* 2015, 162, D3063–D3070.
- [38] Voiry, D.; Salehi, M.; Silva, R.; Fujita, T.; Chen, M.; Asefa, T.; Shenoy, V. B.; Eda, G.; Chhowalla, M. *Nano Lett.* 2013, 13, 6222-6227.
- [39] Hunter, R. J. *Zeta potential in colloid science: Principles and applications*; Academic Press: London, 1981.
- [40] Zou, X. X.; Zhang, Y. *Chem Soc Rev.* 2015, 44, 5148-5180.
- [41] Chen, J.; Wu, X.-J.; Yin, L.; Li, B.; Hong, X.; Fan, Z.; Chen, B.; Xue, C.; Zhang, H. *Angew. Chem., Int. Ed.* 2015, 54, 1210-1214.
- [42] Cheng, L.; Huang, W. J.; Gong, Q. G.; Liu, C. H.; Liu, Z.; Li, Y. G.; Dai, H. J. *Angew. Chem., Int. Ed.* 2014, 53, 7860-7863.
- [43] Tong, H.; Ouyang, S. X.; Bi, Y. P.; Umezawa, N.; Oshikiri, M.; Ye, J. H. *Adv. Mater.* 2012, 24, 229-251.
- [44] Yan, H.; Yang, J.; Ma, G.; Wu, G.; Zong, X.; Lei, Z.; Shi, J.; Li, C. *J. Catal.* 2009, 266, 165-168.
- [45] Mcateer, D.; Gholamvand, Z.; Mcevoy, N.; Harvey, A.; O'Malley, E.; Duesberg, G. S.; Coleman, J. N. *ACS Nano* 2016, 10, 672– 683.
- [46] Huang, Q.; Tian, S.; Zeng, D.; Wang, X.; Song, W.; Li, Y.; Xiao, W.; Xie, C. *ACS Catal.* 2013, 3, 1477-1485.
- [47] Woan, K.; Pyrgiotakis, G.; Sigmund, W. *Adv. Mater.* 2009, 21, 2233-2239.
- [48] Zhang, H.; Lv, X.; Li, Y.; Wang, Y.; Li, J. *ACS Nano* 2009, 4, 380-386.

Chapter 4 Engineering crystallinity of MoS₂ monolayers for enhanced cocatalytic activity

4.1 Introduction

Efficient hydrogen evolution through photocatalysis or electrocatalysis from water bears great promise as a sustainable way for producing clean energy.^[1-4] Platinum (Pt) is the most efficient and stable hydrogen evolution reaction (HER) catalyst except for its scarcity and valuableness. Replacing it with low cost, natural-abundant catalysts would be significantly beneficial for making the hydrogen production more economic and competitive.^[5] During the past decade, great advances have been achieved to identify non-precious catalysts for HER based on transition metals such as Ni, Co, Fe, Mo and W.^[6-10] Among them, Mo-based catalyst as one of the most promising alternative to Pt has been extensively studied. Particularly in recent years, crystalline molybdenum disulfide (MoS₂) and amorphous molybdenum sulfide (MoS_x) have received tremendous attention due to their unique molecular and electronic structure, delivering the attractive catalytic activities.^[11-13] For crystalline MoS₂, edge sites holding a slightly positive free energy of hydrogen adsorption (+0.08 eV) are responsible for the HER activity.^[14, 15] In the case of amorphous MoS_x, its activity can be attributed to the unsaturated Mo sites, which is more active than the crystalline MoS₂ edge sites.^[6] In addition, previous studies have confirmed that monolayer MoS₂ compared with few-layer or bulk ones presented higher catalytic hydrogen evolution activities.^[16] Thus, it is necessary to investigate the effect of crystallinity on HER performance of monolayer MoS₂, which is important but unexplored. However, the posed technological challenges for preparing crystallinity tunable MoS₂ monolayers hinders its further study.^[17]

Over the past years, tremendous achievements have been acquired for reliable preparation of monolayer 2H-MoS₂, which can be concluded into three representative strategies: physical exfoliation

(“tape” method),^[18] chemical vapor deposition (CVD),^[19, 20] and liquid phase exfoliation (LPE).^[21, 22] LPE, firstly utilized by Coleman and colleagues, has been extensively used to directly exfoliate layered bulk crystals in solvents via sonication, which is considered to be the most promising route for large-scale production of mono- and few-layer MoS₂.^[21] Inspired by this, the crystallinity of obtained monolayer MoS₂ can be easily controlled by regulating the corresponding bulk crystals crystallinity.

In this chapter, I report the successful synthesis of crystallinity-dependent MoS₂ monolayers through liquid exfoliation of the corresponding crystallinity-controllable bulk precursors. Excellent cocatalytic performances of the proposed MoS₂ monolayers for photocatalytic HER were achieved and determined by their crystallinity. An apparent quantum efficiency as high as 71.6% can be achieved for the lowest crystalline monolayer MoS₂ over cadmium sulfide under visible light irradiation at 420 nm. This work provides a facile way to synthesis crystallinity controllable MoS₂ monolayers and elucidates that the HER activity can be further enhanced through crystallinity engineering, providing the new strategy to enhance the HER activity of monolayer MoS₂.

4.2 Experimental section

4.2.1 Synthesis of differently crystalline MoS₂ monolayers

Crystallinity-controllable bulk MoS₂ precursors were synthesized by thermal decomposition of (NH₄)₂MoS₄ (Purity 99.5%, Wako) at different temperatures ranging from 400°C to 1100 °C in an Ar atmosphere. The temperature was raised at a rate of 5°C per minute and maintained for 5 hours, then the material was cooled to room temperature naturally. Typically, 100 mg of the proposed bulk MoS₂ precursor was added into a 100 ml glass vial. Then, 50 mL of ethanol was added as the exfoliation and dispersion solvent. The mixture was bath sonicated for 48 h using an FU-260-C at a frequency of 28 kHz. The resulting suspensions were first centrifuged using a TOMY LC-200 centrifuge at 2000 rpm (RCF: 760 g) for 1 hour, then the top 2/3 portions of the supernatants were carefully collected by pipette. The obtained supernatants were added into a new glass vial and sonicated again for another 4 h. Then, the

monolayer MoS₂ dispersions were collected by pipette, followed by another centrifugation of the supernatant at 4000 rpm (RCF: 3020 g) for 1 h. The obtained monolayer MoS₂ with annealing temperature at XXX°C were marked as XXX-MoS₂ (such as 400-MoS₂, 500-MoS₂, 600-MoS₂, 700-MoS₂, 800-MoS₂, 900-MoS₂, 1000-MoS₂, 1100-MoS₂). The quantification of MoS₂ concentration was carried out by measuring the weight change of 5 mL MoS₂ dispersions before and after the totally evaporation of ethanol.

4.2.2 Preparation of differently crystalline MoS₂ monolayers decorated CdS photocatalysts

Monolayer MoS₂ suspensions were mixed with commercial CdS (99%, Aldrich) in certain stoichiometric ratios, sonicated and stirred overnight until dry, then the composites were collected and annealed in an Ar atmosphere at 400°C for 4 hours marked as 400-MoS₂/CdS (as-prepared composite).

4.2.3 Characterization

The bulk material structures were determined using an X-ray diffractometer (X'pert powder, PANalytical B.V., Netherlands) with Cu-K α radiation. SEM was performed on a JEOL 6701F field-emission scanning electron microscope. TEM was performed on an FEI Tecnai G2 F30 microscope with a 300 kV accelerating voltage. AFM was carried out in tapping mode (Nanocute H, Japan). XPS data were collected using a PHI Quantera SXM (ULVAC-PHI, Japan). Raman spectroscopy was performed using a Horiba Jobin Yvon LabRAM system with a 532 nm excitation laser. UV-vis-NIR absorption spectra were measured using a Shimadzu UV-2500 spectrophotometer in quartz cuvettes with a pathlength of 2 mm. The zeta potential was tested using a Zeta-potential & Particle size Analyzer ELSZ-2000 series.

4.2.4 Photocatalytic H₂ evolution

The photocatalytic H₂ evolution was carried out with 0.2 g of the photocatalyst hybrid in 300 mL of solution (30 vol.% lactic acid adjusted by NaOH to achieve a pH~5.0) in a Pyrex glass reaction cell. The

reaction cell was connected to a closed gas system with a gas circulation pump. A 300 W Xenon lamp equipped with L42 cut-off filter was used as the visible light source ($\lambda > 420$ nm). H_2 evolution was measured with an on-line gas chromatograph (GC-8A, Shimadzu) equipped with a thermal conductivity detector according to the standard curve. The AQEs with various monochromatic lights were obtained by using a series of band-pass filters (Optical Coatings Japan). The light intensity was measured using a radiant power energy meter (Ushio spectroradiometer, USR-40, Japan).

4.2.5 DFT Theoretical calculation

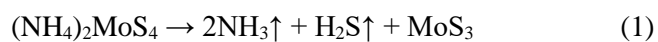
All calculations were performed with the Vienna ab-initio Simulation Package (VASP) based on the density functional theory (DFT). General gradient approximation was employed to evaluate the exchange-correlation energy. The number of k points and the cutoff energy were increased until the calculated total energy converged within an error of 1×10^{-5} eV/atom. Therefore, the cut-off energy of 500 eV with $11 \times 11 \times 1$ k points was set. The energy convergence tolerance was set to below 5×10^{-6} eV/atom. The lattice vectors and atomic coordinates were relaxed until the Hellmann-Feynman force was reduced to 0.01 eV/Å. To simulate the biaxial strain of MoS_2 , the relaxation of crystal with the lattice constants a fixed was performed. And the specified in-plane compression strain was defined as $= (a - a_0)/a_0$.

4.3 Results and discussion

4.3.1 Characterization of the crystalline-dependent MoS_2 crystals

The synthesis process for the crystallinity-dependent MoS_2 monolayers involves two steps. First, crystallinity-controllable bulk MoS_2 crystals were prepared by facile thermal decomposition of $(NH_4)_2MoS_4$ in the selection of temperature zone with $400 \sim 1100^\circ C$, where the incomplete decomposition to MoS_2 was below $400^\circ C$, and the impurity phase (Mo_2S_3) would present over $1200^\circ C$

(Figure 4.1). It is known that MoS_2 can be generated by thermal decomposition of $(\text{NH}_4)_2\text{MoS}_4$, which the salt decomposes in two distinct steps as following equations:



The first step (equation, eq. 1) involves the decomposition to the MoS_3 and the released NH_3 and H_2S gas, and the second step (eq. 2) the decomposition of the MoS_3 to the MoS_2 and elemental sulfur. It is known that the decomposition temperature of MoS_3 is over 335°C . Thus, our controllable experimental temperature is in the range from 400°C to 1100°C .

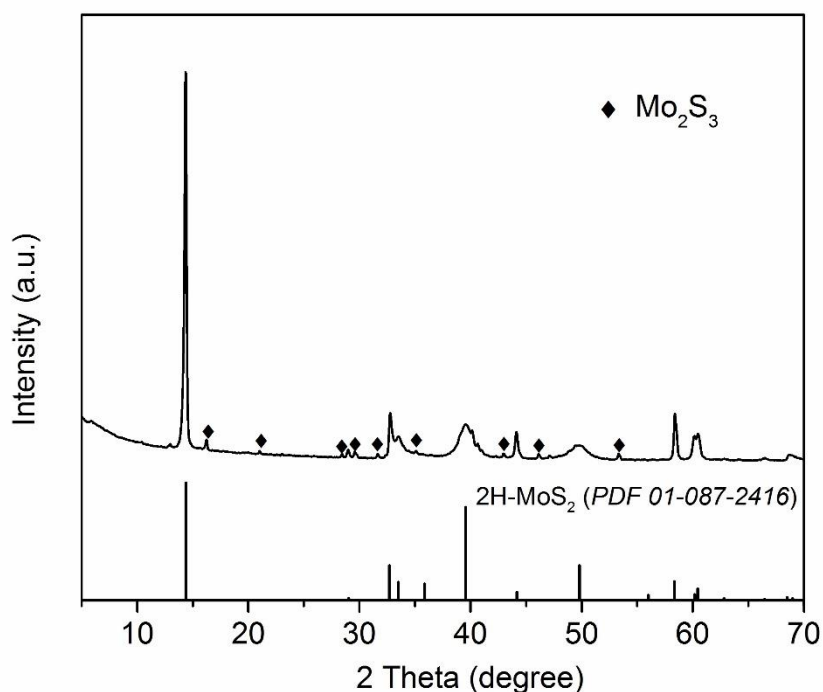


Figure 4.1 XRD pattern of the prepared bulk MoS_2 crystal with calcination temperature at 1200°C . There existed impurity phase (Mo_2S_3) when the calcination temperature reached as high as 1200°C .

Then, through liquid phase exfoliation, crystallinity-dependent monolayer MoS_2 dispersions can be obtained after high-speed centrifugation. Figure 4.2 shows the X-ray diffraction (XRD) patterns of the

differently crystalline bulk MoS₂ precursors, where all the observed diffraction peaks belong to pristine 2H-phase MoS₂ structure (PDF 01-087-2416). It is noteworthy that when the temperature is lower than 800°C, all of the peaks are significantly broadened with decreased calcination temperature, suggesting the drastically declined crystallinity.^[23] Detailed analysis of the XRD spectra shows that the (002) peak continuously shifts to a higher angle with increasing calcination temperature (Figure 4.3). By contrast, the (100) and (110) peaks first shift to a lower angle till 800°C and then level off, reaching a platform (Figure 4.4).

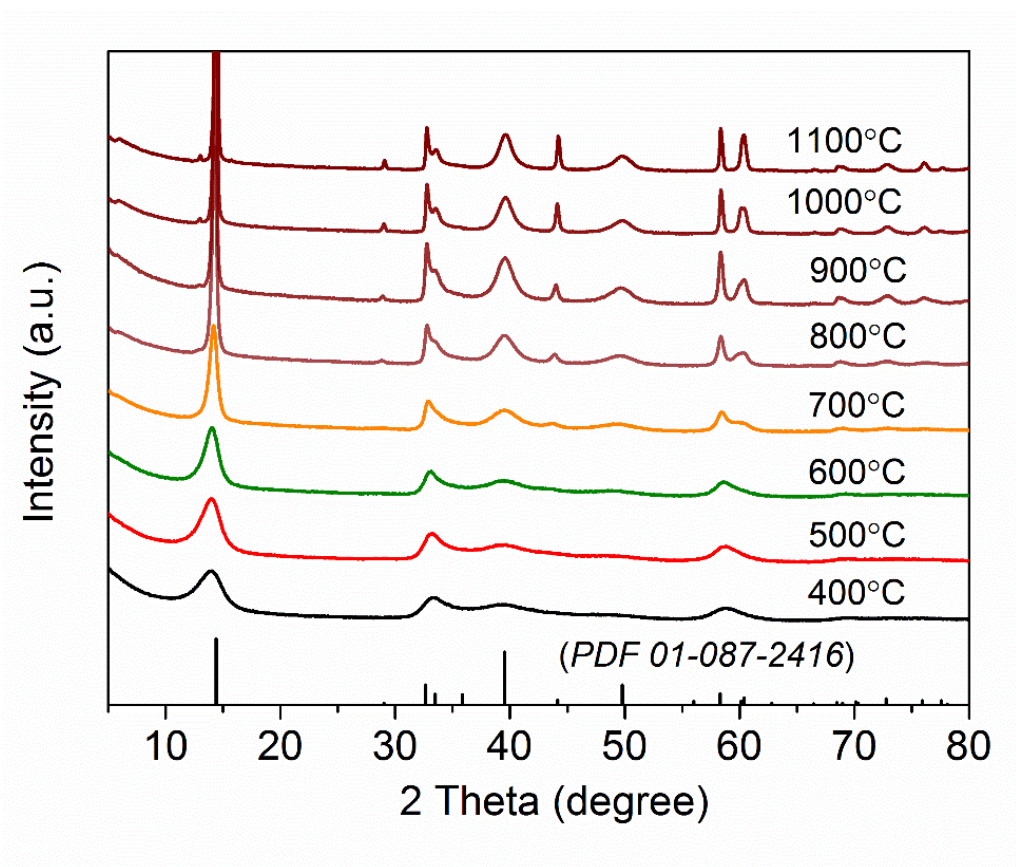


Figure 4.2 XRD patterns of the differently crystalline bulk MoS₂ crystals with calcination temperature in the range of 400°C to 1100°C. The standard diffraction peak position of 2H-MoS₂ is displayed at the bottom of the diagram.

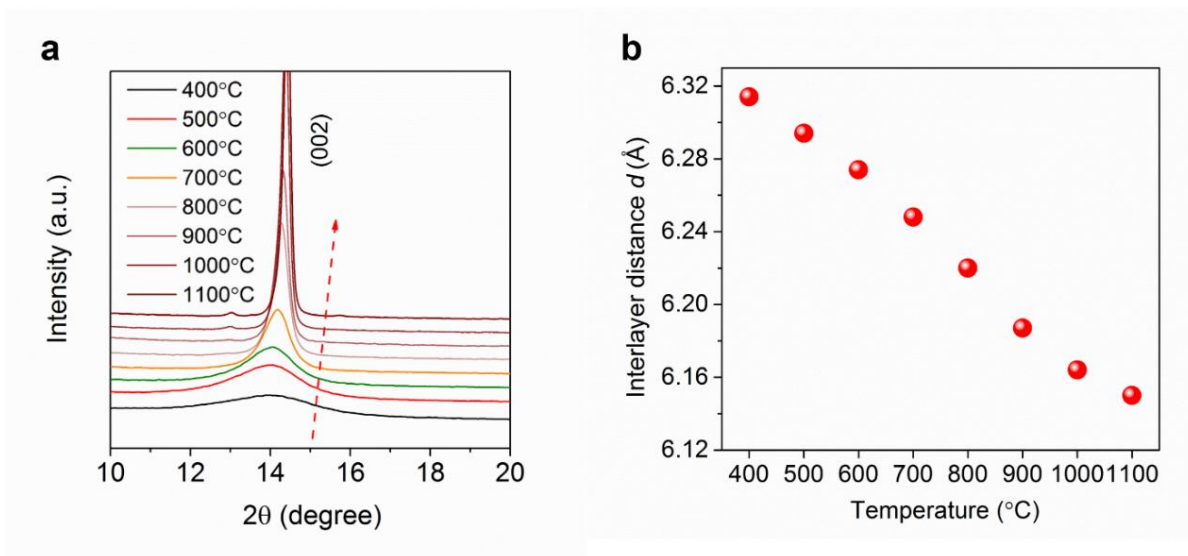


Figure 4.3 (a) Enlarged view of the (002) peak. The position of (002) peak monotonously shifts toward higher angle with the increase of calcination temperature. (b) The calculated interlayer distance from the position of (002) peak.

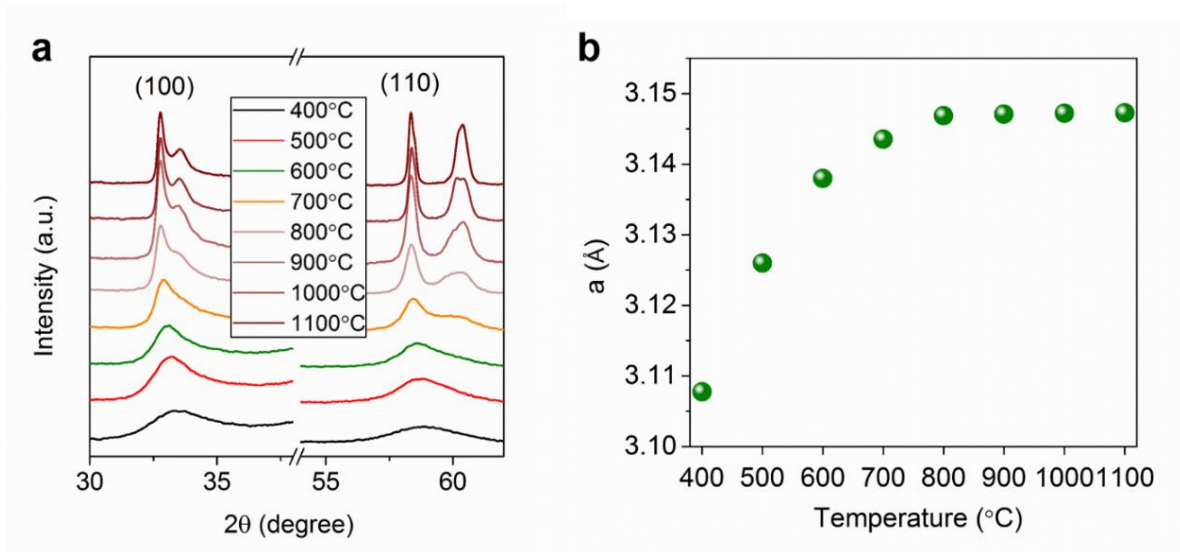


Figure 4.4 (a) Enlarged view of the (100) and (110) peaks. (b) The calculated in-plane lattice parameter from the position of (110) peak.

These structural data reveal that decreasing the calcination temperature (*i.e.*, crystallinity) can not only induce the structural disorder but also the shrinking of in-plane lattice (a) and the expansion of interlayer distance (d). The high-resolution transmission electron microscopy (TEM) images (Figure 4.5) further confirm the improved degree of atom ordering and a decreased interlayer space from 0.632 nm for 400-MoS₂ to 0.616 nm for 1000-MoS₂ with the increase of temperature, which is consistent with the results from the XRD analysis. Then, X-ray photoelectron spectroscopy (XPS) was performed on the as-prepared bulk MoS₂ crystals (Figure 4.6). For the lowly crystalline crystals with calcination temperature lower than 800°C, in addition to the expected 2H component of S 2p core level spectra, an additional component is observed besides the 2H component that can be identified to the disordered S.^[24,25] Moreover, the intensity of this additional component gradually increases with decreasing calcination temperature, showing the increased degree of structural disorder. Raman spectroscopy (Figure 4.7) further confirm the 2H-phase structure by the appearance of two distinct peaks at 380 cm⁻¹ and 406 cm⁻¹, which correspond to the in-plane vibration (E_{2g}^1) and out-of-plane mode (A_{1g}), respectively.^[26] These results indicate that crystallinity-controllable 2H-MoS₂ bulk crystals with different degree of structural disorder were successfully synthesized.

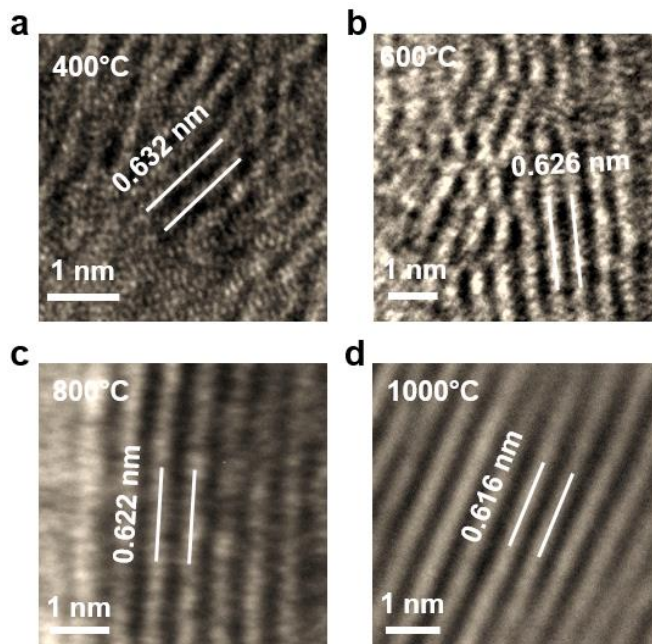


Figure 4.5 High-resolution TEM images of the as-prepared bulk MoS₂ crystals for 400°C, 600°C, 800°C and 1000°C, respectively.

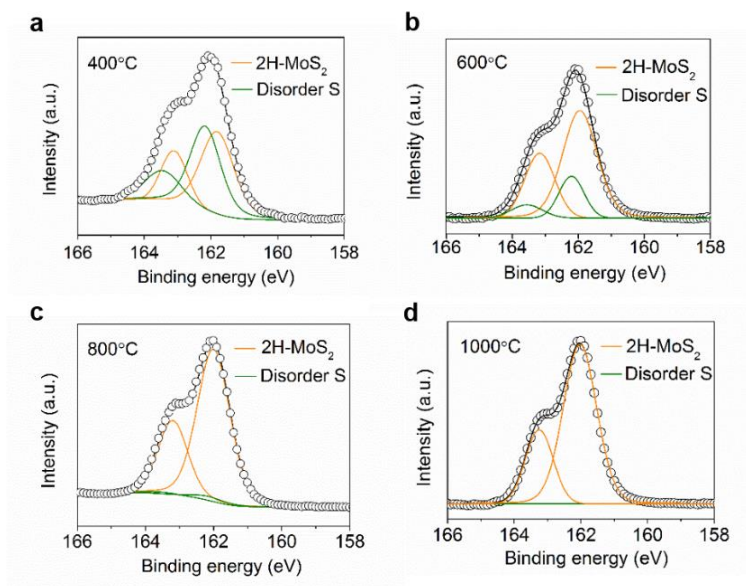


Figure 4.6 XPS spectra of the as-prepared bulk MoS₂ crystals for 400°C, 600°C, 800°C and 1000°C, respectively.

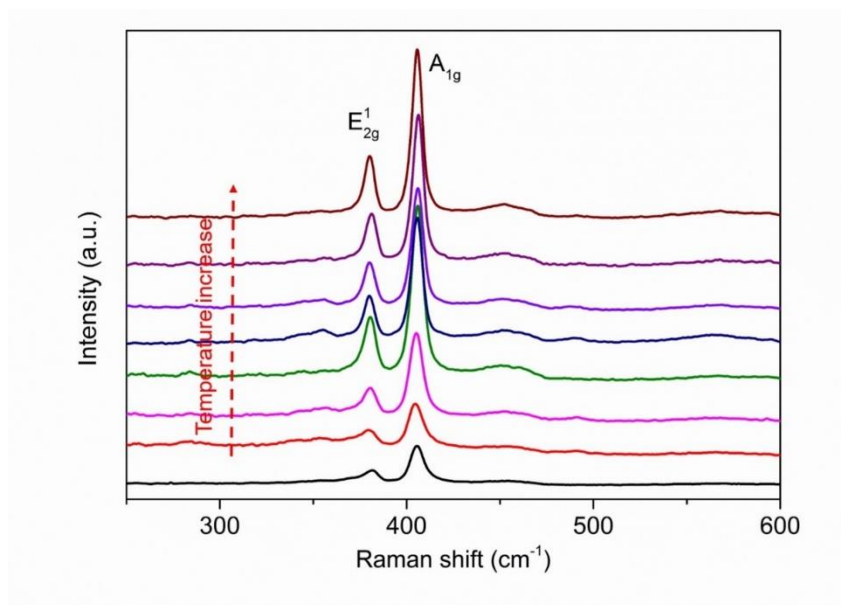


Figure 4.7 Raman spectra of the as-prepared differently crystalline bulk MoS₂ crystals. Raman spectra further confirmed the 2H-phase structure by the appearance of two distinct peaks at 380 cm⁻¹ and 406 cm⁻¹, which correspond to the in-plane vibration (E_{2g}¹) and out-of-plane mode (A_{1g}), respectively.

4.3.2 Characterization of the crystalline-dependent MoS₂ monolayers

The as-prepared bulk MoS₂ crystals are all composed of nanoflakes with a nanoscale lateral size (Figure 4.8). The accurate lateral sizes, estimated from the full-width at half-maximum of the (110) reflection in the XRD patterns, were found to be monotonously increased from 42 to 402 nm with increasing calcination temperature. In the liquid exfoliation process, the resulting hydrodynamic forces from high-energy liquid jets at the edge sites of the as-prepared bulk MoS₂ crystals are enough to overcome the interlayer van der Waals attraction, allowing for efficient exfoliation into monolayers.^[27] After optimizing the exfoliation conditions, highly concentrated monolayer MoS₂ dispersions can be obtained after sonication and following high-speed centrifugation. The measured concentration was summarized in Table 1. In detail, with the increase of calcination temperature, the concentration of the exfoliated monolayer nanosheets is first increased from 0.18 mg mL⁻¹ for 400-MoS₂ to 0.42 mg mL⁻¹ for 800-MoS₂ and achieves the highest value, showing the improved exfoliability with the enhancement of

crystallinity. Then, with further increasing temperature, the concentration is gradually dropped to 0.22 mg mL⁻¹ for 1100-MoS₂ due to the increased lateral size, making the exfoliation more difficult. Considering the initial concentration of bulk crystals was 2 mg mL⁻¹, the corresponding monolayer yield was calculated ranging from 9.0% for 400-MoS₂ to 21.0% for 800-MoS₂. Furthermore, with the enhancement of crystallinity, the stability of the dispersed monolayer MoS₂ nanosheets is gradually improved according to the decreased zeta potential values.^{28,29} In general, dispersed nanomaterials are stable with zeta-potential values of less than -30 mV. The lowly crystalline monolayer dispersion (400-MoS₂) with a zeta-potential value of -20.6 mV exhibited a less stability compared with the highly crystalline counterpart (800-MoS₂) with a zeta-potential value of -50.7 mV.

Table 1. Exfoliability and stability test of crystallinity-dependent MoS₂.

Temperature (°C)	Concentration (mg mL ⁻¹)	Monolayer yield	Zeta potential (mV)
400	0.18	9.0%	-20.6 ± 5.9
500	0.23	11.5%	-28.1 ± 4.6
600	0.31	15.5%	-35.8 ± 4.9
700	0.39	19.5%	-42.2 ± 4.6
800	0.42	21.0%	-50.7 ± 4.7
900	0.36	18.0%	-52.3 ± 4.0
1000	0.27	13.5%	-53.1 ± 3.6
1100	0.22	11.0%	-53.3 ± 4.1

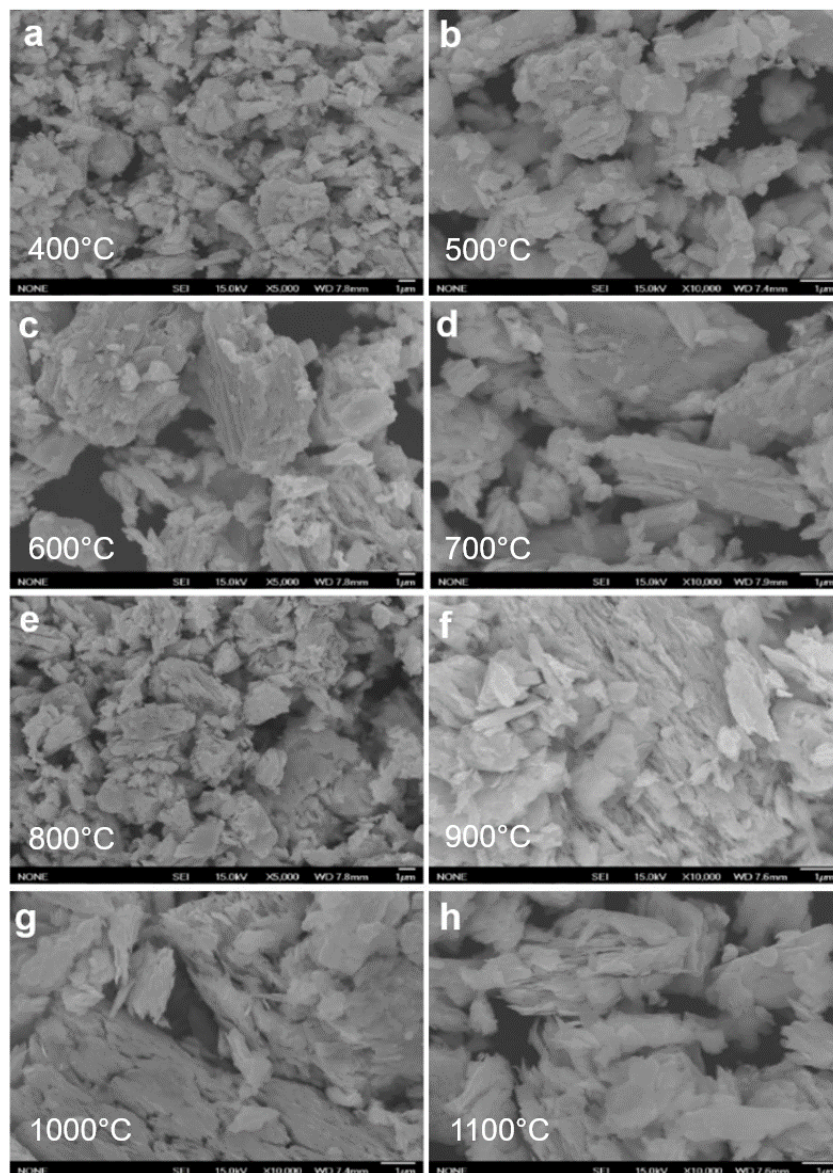


Figure 4.8 (a-h) SEM images of differently crystalline bulk MoS₂ crystals in the range of 400°C to 1100°C with per 100°C.

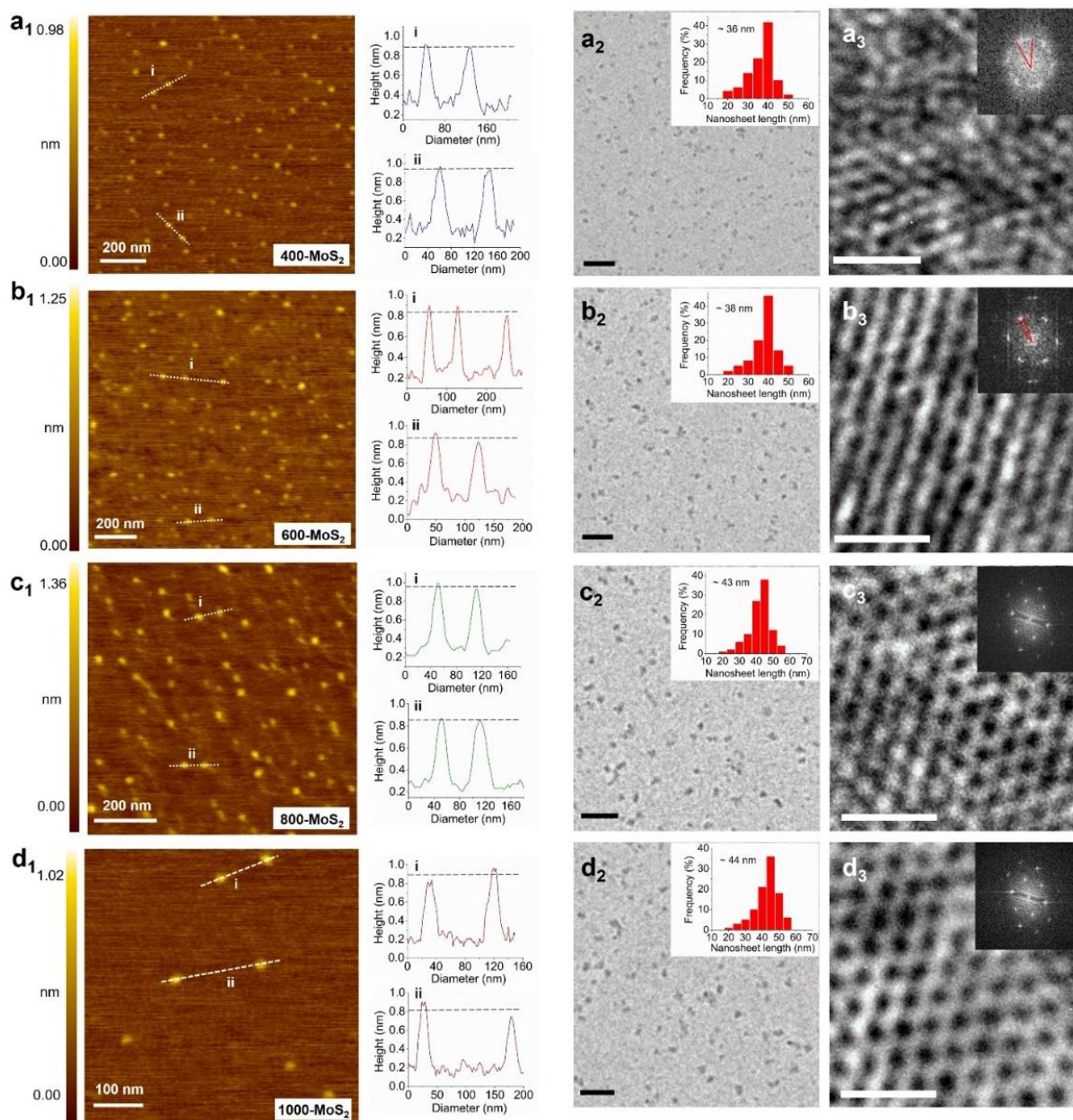


Figure 4.9 AFM (a₁-d₁), statistical analysis of size distribution from low-resolution TEM images (a₂-d₂) and high-resolution TEM images (a₃-d₃) of the obtained MoS₂ monolayers, where a-d represent for 400°C, 600°C, 800°C and 1000°C, respectively. Scale bar in a₂-d₂ and a₃-d₃ represent 200 nm and 1 nm, respectively.

Figure 4.9 gives general information about the thickness, size, and crystal structure of the exfoliated 400-MoS₂, 600-MoS₂, 800-MoS₂ and 1000-MoS₂ nanosheets. The thickness of the exfoliated nanosheets was investigated by atomic force microscopy (AFM). It can be seen that the height profile of the selected regions in the AFM images (Figure 4.9a₁-d₁) all show a height of ~0.7 nm (\pm 0.1 nm), confirming the single-layer structure of these exfoliated nanosheets.^[30,31] The TEM images in Figure 4.9a₂-d₂ reveal that the samples are distributed uniformly without obvious aggregation. I can conclude that all the samples exhibit a similar average lateral size of around 40 nm from the size statistics in the inset of Figure 4.9a₂-d₂. Moreover, their high-resolution TEM images (Figure 4.9a₃-d₃) and the fast Fourier transform (FFT) clearly show the improved order of atomic arranging with the increase of temperature.^[23] Generally, the degree of disorder can be assessed by the angle determined by two end points of a diffraction arc and the central spot.^[32] That is, the larger angle represents higher degree of structural disorder, while 0° represents perfect single crystal structure without disordering. For 400-MoS₂, the atomic arranging manners on the basal plane are strongly disordered with exhibiting six long diffraction arcs. The obviously shorted diffraction arcs for 600-MoS₂ shows an improved structural order. When the temperature reaches 800°C, the diffraction arcs become to hexagonal diffraction spots, representing highly crystalline single crystal structure without in-plane disorder.^[33]

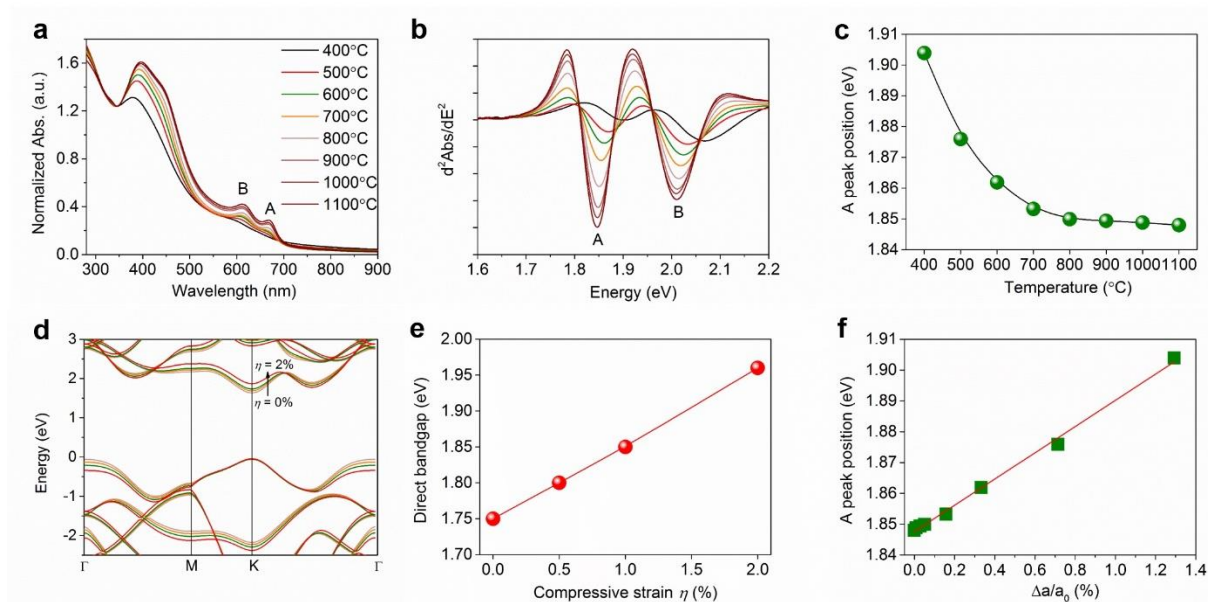


Figure 4.10 (a) Optical absorption spectra of the obtained differently crystalline monolayer MoS₂ dispersions normalized to the local minimum at 345 nm. (b) Second derivative of the normalized absorption spectra. (c) Peak position of the A-exciton as a function of temperature. (d) Electronic DFT band structure of monolayer MoS₂ under different biaxial compression strains from 0% to 2%. (e) Direct bandgaps under different biaxial compression strains calculated using DFT. (f) A peak position versus the change of in-plane lattice ($\Delta a/a_0$, a_0 represents the in-plane lattice parameter at 1100°C, Δa represents the decreased in-plane lattice parameter of a lower temperature compared to a_0).

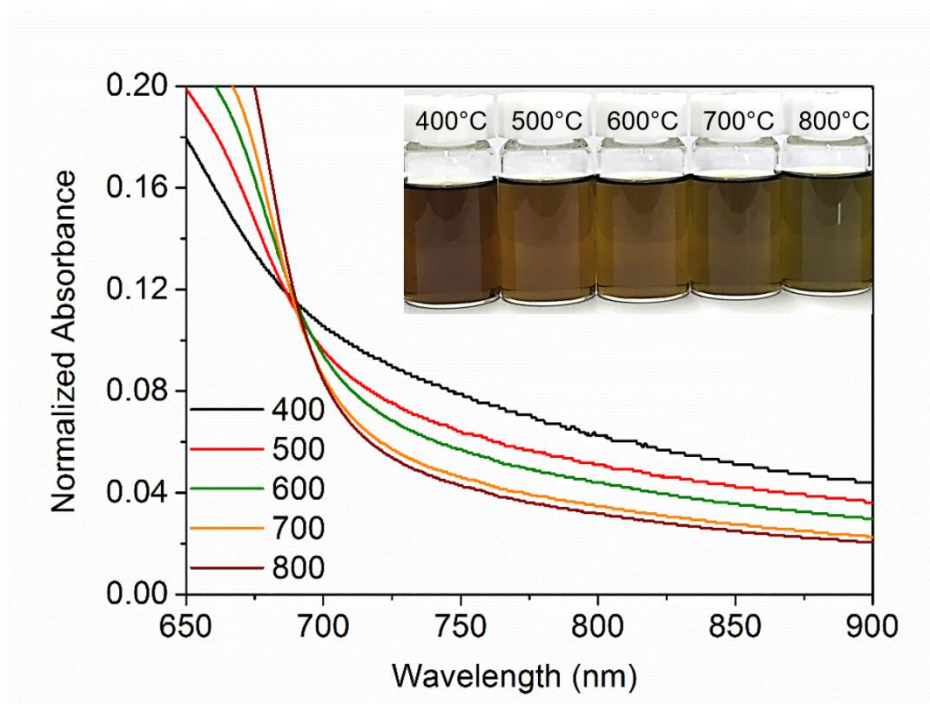


Figure 4.11 Tail absorption of the differently crystalline monolayer MoS₂ dispersions, inset is the corresponding photograph.

Evolution of crystallinity was further studied by measuring the optical absorption spectra of monolayer MoS₂ dispersions as a function of temperature (Figure 4.10a). The lowest crystalline 400-MoS₂ monolayer exhibits no clear feature peaks of standard 2H-MoS₂, where two characteristic peaks (A-exciton and B-exciton) located between 600 and 700 nm arising from the K point of the Brillouin zone.^[34, 35] As expected, the excitonic features become clear and sharp with increasing temperature, revealing an enhanced 2H-phase structure. In addition to the obvious spectral changes, detailed analysis of the absorption spectra shows that the position of A-exciton also slightly varied with the increase of temperature. I found the position of the A-exciton using the second derivative of the absorption spectra to exclude the contribution from the size-dependent scattering background (Figure 4.10b).^[36] The derived peak position is plotted in Figure 4.10c, showing a clear trend versus temperature. With the increase of temperature, A peak position was first decreased from 1.90 eV for 400-MoS₂ to 1.85 eV for 800-MoS₂ and then leveled off, reaching a plateau. This tendency is similar to the change of in-plane lattice, such

behavior indicates the potential intrinsic relationship between the A peak position and the in-plane lattice. First-principles density functional theory (DFT) calculations show that the direct bandgap increase monotonously with applying biaxial compression strain (Figure 4.10d,e). Correspondingly, the A peak position is linearly increased with the change of in-plane lattice at a rate of 40 meV/% $\Delta a/a_0$ (Figure 4.10f), reflecting the intrinsic effect of low-crystallization induced structural disorder on the electric structure, density of states and hence optical absorption. Furthermore, the structural disorder can also induce a gradually increased tail absorption in the near-IR region, leading to a slight colour change of monolayer MoS₂ dispersions (Figure 4.11).

4.3.3 Evaluation of cocatalytic performance of crystallinity-dependent MoS₂ monolayers

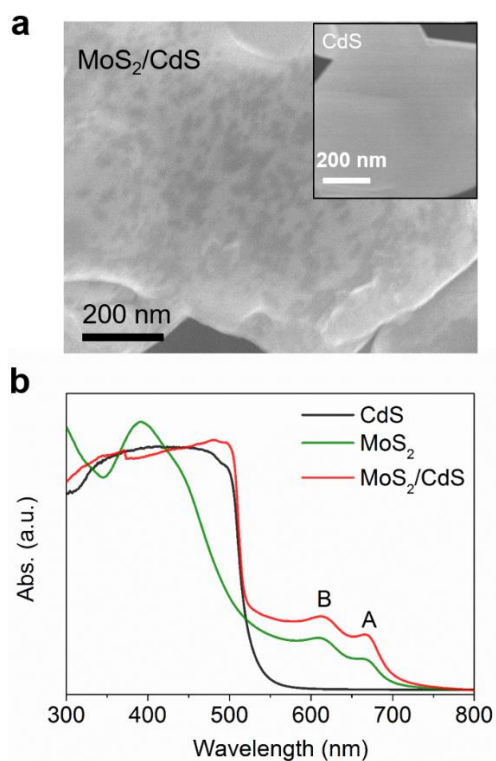


Figure 4.12 (a) SEM image of CdS after loading monolayer MoS₂ nanosheets. Inset shows the SEM image of bare CdS. (b) UV-vis absorption spectra of pure CdS, monolayer MoS₂ dispersion and MoS₂/CdS composite, respectively.

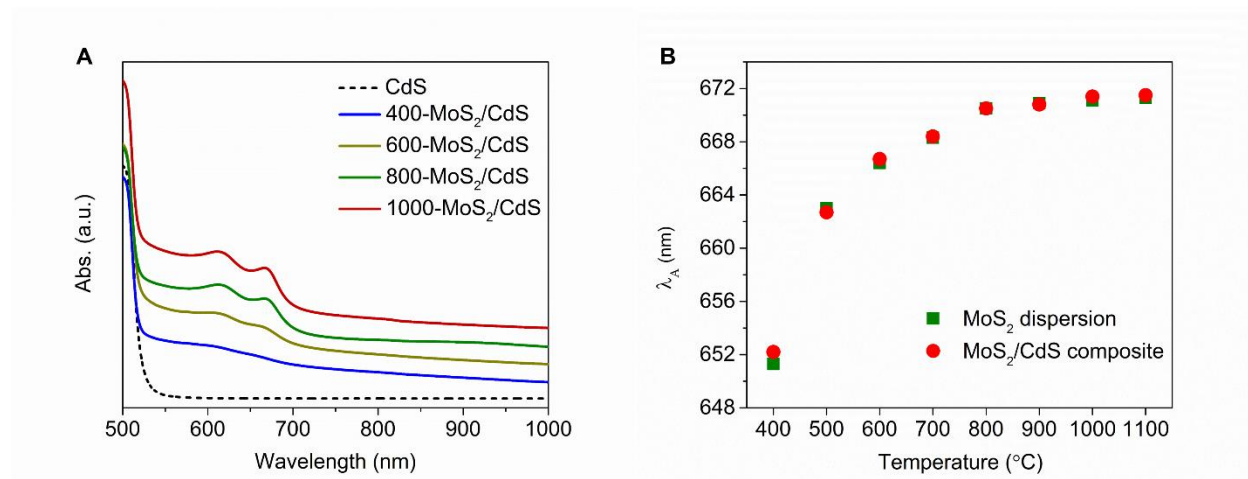


Figure 4.13 (a) UV-vis-NIR absorption spectra of pure CdS and the corresponding MoS₂/CdS composites. Fortunately, the absorption near A-exciton of MoS₂ is not affected due to the suitable band structure of CdS, leading to an accurate access of the absorption information regarding peak A. (b) Comparison of λ_A derived from absorption spectra of the MoS₂/CdS composites and monolayer MoS₂ dispersions.

One important application of MoS₂ monolayer is their potential for catalytic hydrogen evolution due to low cost, earth-abundance and high catalytic activity. In order to keep their monolayer characteristic, the HER activity of the obtained MoS₂ monolayers were evaluated by loading on CdS as cocatalyst for photocatalytic hydrogen evolution.^[16] As expected, these monolayer MoS₂ nanosheets can be uniformly adsorbed on the surface of CdS due to their soft and small size features (Figure 4.12a). According to the recent study by Coleman and co-workers, the average layer number of MoS₂ nanosheets can be estimated from an empirical equation based on the peak position of A-exciton, which red-shifts with the increase of layer number.^[36] Fortunately, the absorption near A-exciton of MoS₂ is not affected due to the suitable band structure of CdS, leading to an accurate access of the absorption information regarding peak A (Figure 4.12b). The obtained λ_A from the absorption spectra of MoS₂/CdS composites are almost overlapped the values derived from monolayer MoS₂ dispersions (Figure 4.13). This result further confirmed that the MoS₂ monolayers were monodispersed on the surface of CdS and restacking was avoided.

Under optimized reaction conditions, the MoS₂/CdS composites show extremely high photocatalytic HER activities (Figure 4.14a). Pure monolayer MoS₂ shows negligible visible light H₂ evolution activity of only 2 μmol h⁻¹. Besides the high cocatalytic performance, the monolayer MoS₂ also has a strong crystallinity dependent behavior for HER. Specifically, with the decrease of crystallinity, the photocatalytic HER activity of the corresponding MoS₂/CdS composite is gradually improved from 4.1 mmol h⁻¹ of 1100-MoS₂/CdS to 5.5 mmol h⁻¹ of 400-MoS₂/CdS. Notably, the cocatalytic performance of these lowly crystalline MoS₂ monolayers with annealing temperature lower than 800°C were even higher than that of Pt (Figure 4.15), which represented the state-of-the-art activity for HER. Furthermore, the wavelength dependence of H₂ evolution was then investigated to prove that the reaction was driven by incident light (Figure 4.14b). The apparent quantum efficiency (AQE) was calculated to be as high as 71.6% for the 400-MoS₂/CdS composite under visible light irradiation at 420 nm, which is the highest catalytic hydrogen activity for MoS₂-based cocatalysts to our best knowledge. Besides, the remarkable photocatalytic activity also exhibits a high stability, where little noticeable loss of activity can be observed after five cycles (Figure 4.14c). The superior photocatalytic performances of the MoS₂/CdS composites can be attributed to the following two aspects: first, the loaded monolayer MoS₂ nanosheets with average lateral sizes in the tens of nanometers can provide more active edge sites for HER.^[16] The bare CdS cannot offer active sites for catalytic hydrogen evolution, leading to the facile recombination of photo-excited electron-hole pairs before migration to the surface for reactions, and therefore it shows a poor photocatalytic hydrogen evolution activity of around 0.15 mmol h⁻¹; second, the heterojunction (Figure 4.14d) between CdS and the surface loaded monolayer MoS₂ is more favorable for interfacial charge transfer, which can efficiently suppress the recombination of photo-excited electron-hole pairs.^[37-39] For the freshly made, mechanically mixed composites, their weak physical adsorption severely attenuated their photocatalytic HER activities and the composites were greatly strengthened after annealing at 400°C through the creation of fine contacted heterojunction (Figure 4.16).

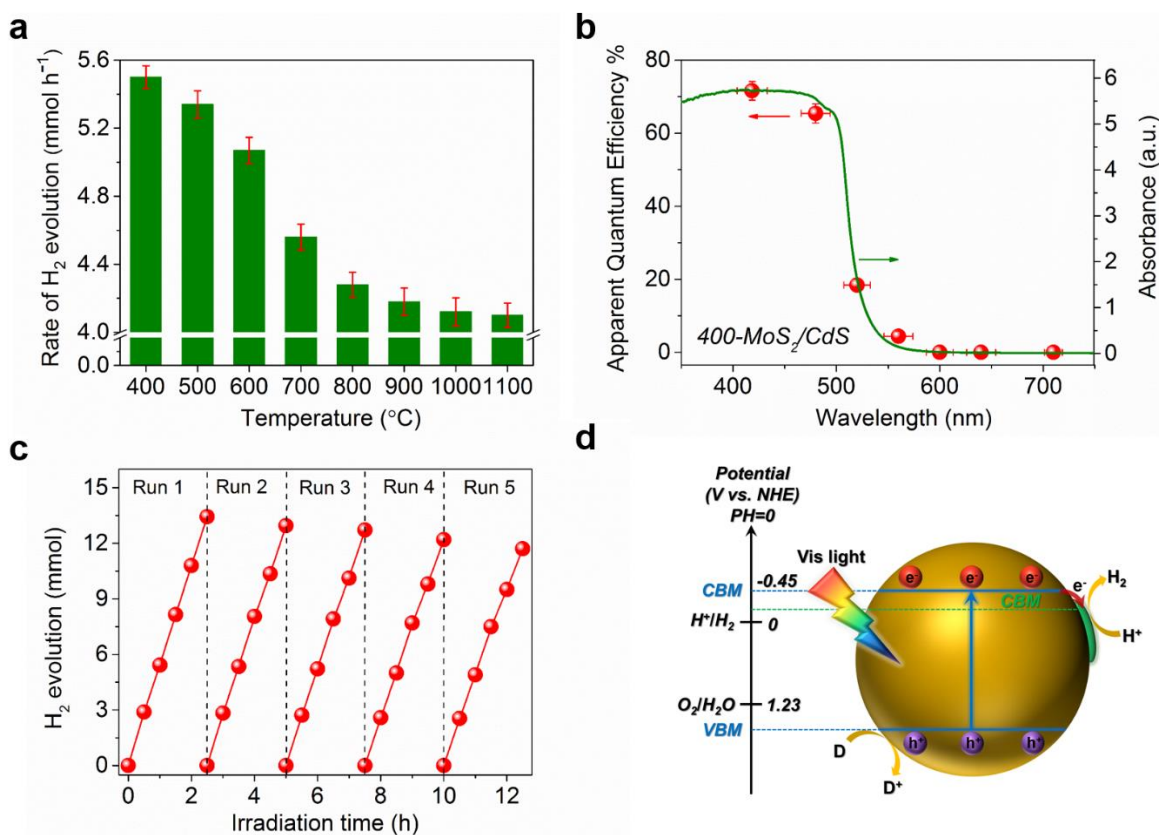


Figure 4.14 (a) Photocatalytic H₂ evolution activities of the differently crystalline MoS₂ monolayers over CdS under the optimized conditions. (b) Wavelength-dependent apparent quantum efficiency of H₂ evolution from the 400-MoS₂/CdS composite. (c) Cycling test of the 400-MoS₂/CdS composite. Light source: 300-W Xe lamp with a L42 cut-off, $\lambda > 420$ nm; Reaction solution: 300 mL sodium lactate solution (30 vol. % lactic acid adjusted by NaOH, pH~5.0); Catalyst: 200 mg; Cocatalyst: 2wt%. (d) Schematic illustration of the heterojunction between MoS₂ and CdS for photocatalytic hydrogen evolution.

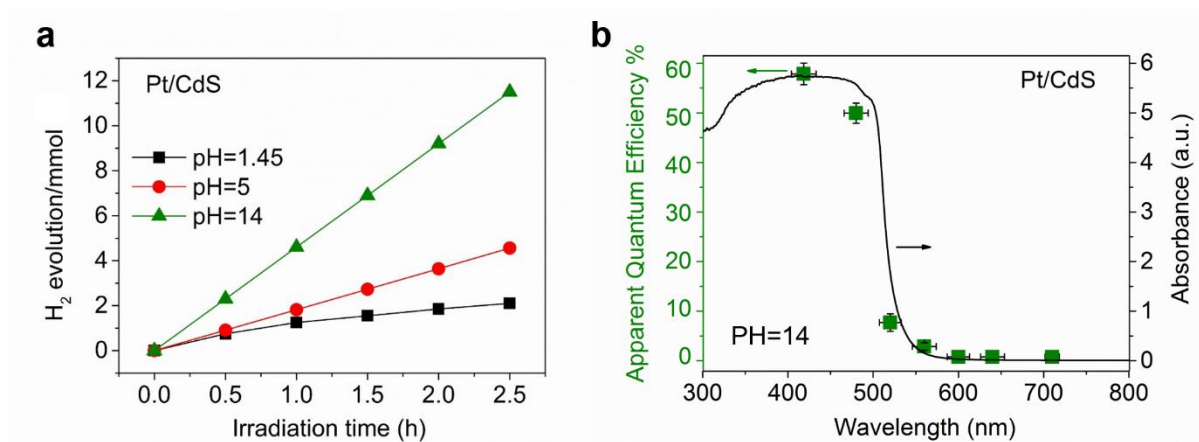


Figure 4.15 (a) Photocatalytic H₂ evolution activities of Pt/CdS under visible light irradiation. Light source: 300-W Xe lamp with a L42 cut-off, $\lambda > 420$ nm; Reaction solution: 300 mL lactic acid solution (30 vol. %, pH=1.45), 300 mL sodium lactate solution (30 vol. % lactic acid adjusted by NaOH, pH=5.0), 300 mL Na₂S-Na₂SO₃ solution (pH=14); Catalyst: 200 mg; cocatalyst: 0.65 wt%. (b) Wavelength-dependent apparent quantum efficiency of H₂ evolution from the Pt/CdS composite in 300 mL Na₂S-Na₂SO₃ solution.

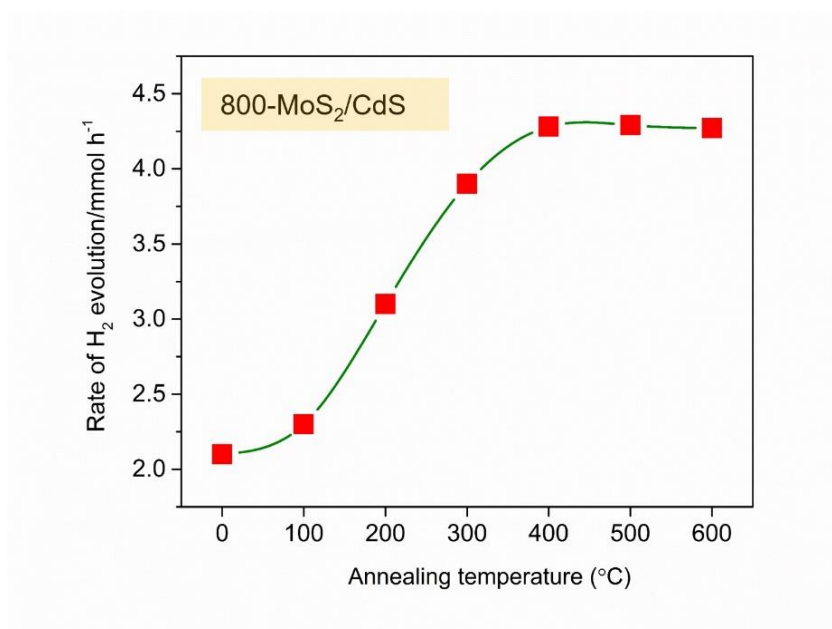


Figure 4.16 Photocatalytic H₂ evolution activities of the 800-MoS₂/CdS composite with different heat treatment temperature.

4.3.4 The role of crystallinity for enhanced cocatalytic performance

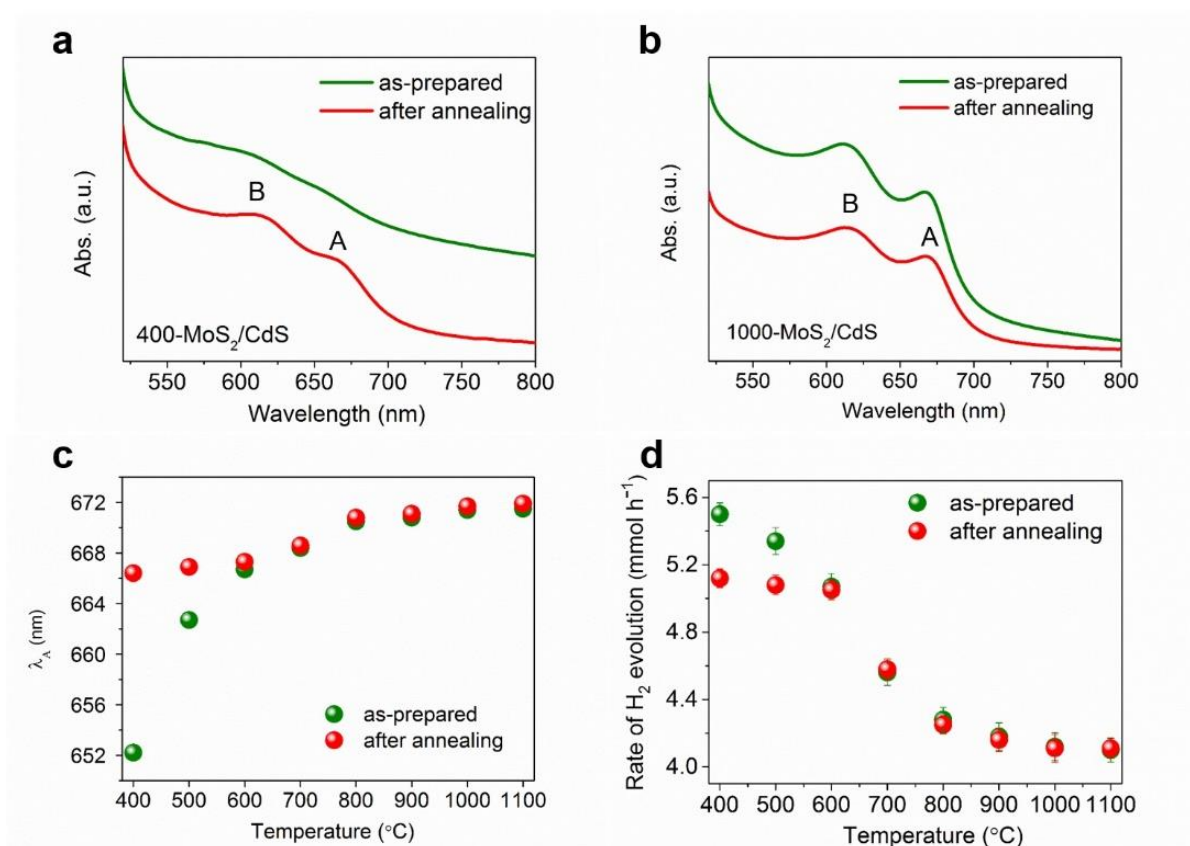


Figure 4.17 UV-vis absorption spectra of the as-prepared (a) 400-MoS₂/CdS and (b) 1000-MoS₂/CdS composites before and after annealing at 600°C. Comparison of (c) λ_A derived from absorption spectra and (d) photocatalytic H₂ evolution activities of the differently crystalline MoS₂/CdS composites before and after annealing at 600°C.

It has been known that the disordered structure in ultrathin MoS₂ nanosheets can offer abundant unsaturated sulfur atoms as active sites for HER.^[23] Furthermore, the higher activity of amorphous MoS_x compared to its crystalline counterpart suggests the structural disorder in MoS₂ should be beneficial to HER. Accordingly, I propose that the increased HER activity for lowly crystalline 2H-MoS₂ monolayers could be ascribed to the low-crystallization induced structural disorder, which can supply more active sites for HER. To confirm the increased cocatalytic activity of lowly crystalline MoS₂ monolayers is

attributed to structural disorder rather than the effect of lateral size, I annealed the 400-MoS₂/CdS composite at 600°C to in-situ enhance the crystallinity of loaded monolayer MoS₂ nanosheets and monitored the photocatalytic hydrogen activities. From the UV-vis absorption spectra of the 400-MoS₂/CdS composite before and after annealing at 600°C (Figure 4.17), it can be seen that the two characteristic peaks of 400-MoS₂ monolayers become clear and sharp towards a higher crystalline state after annealing. Simultaneously, a distinctly redshift of λ_A is also observed from the second derivative of the absorption spectra (Figure 4.18), revealing that the crystallinity of the loaded 400-MoS₂ monolayers was successfully improved by annealing at a higher temperature. The corresponding photocatalytic hydrogen activity also decreases from 5.5 mmol h⁻¹ to 5.12 mmol h⁻¹, which is similar to the 600-MoS₂/CdS composite (5.07 mmol h⁻¹). The highly crystalline 1000-MoS₂ shows negligible change in shape (Figure 4.17b) and λ_A (Figure 4.19) of the absorption spectra after annealing, suggesting the annealing treatment cannot make the loaded MoS₂ monolayers restack. Specifically, for the MoS₂ monolayers with synthesis temperature higher than 600°C, little change can be found of λ_A (Figure 4.17c) and photocatalytic HER activities (Figure 4.17d) after annealing. By contrast, for 400- and 500-MoS₂, both their λ_A and the corresponding photocatalytic HER activities move to the values approaching 600-MoS₂/CdS. These results reveal that the changes of optical absorption caused by structural disorder for the lowly crystalline MoS₂ monolayers can be restored through in-situ enhancing their crystallinity. Accordingly, their improved cocatalytic performance also reduced at the same time, excluding the effect of lateral size on the enhanced activity. Thus, I concluded that the improved HER activity for the lowly crystalline MoS₂ monolayers compared to the highly crystalline counterpart is exclusively attributed to the structural disorder.

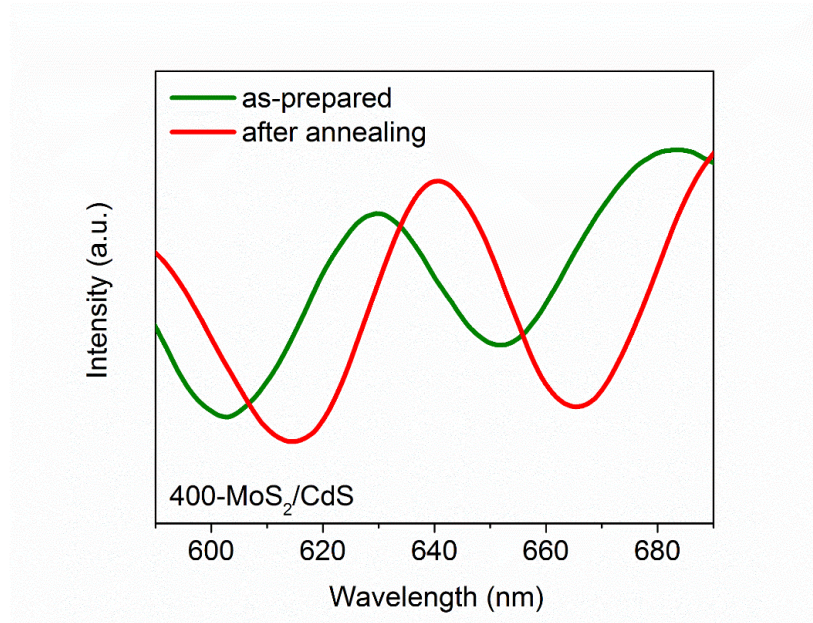


Figure 4.18 Second derivative of the absorption spectra for 400-MoS₂/CdS composite before and after annealing at 600 °C.

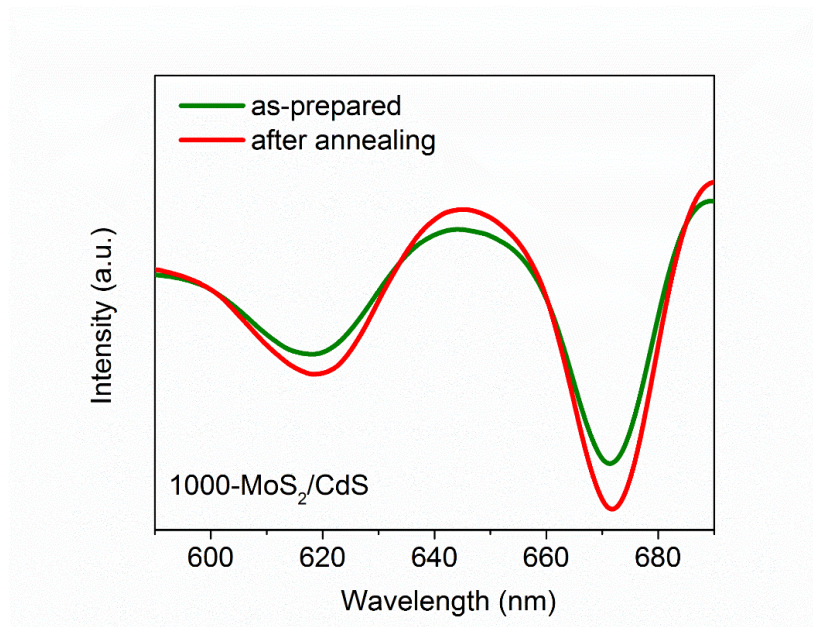


Figure 4.19 Second derivative of the absorption spectra for 1000-MoS₂/CdS composite before and after annealing at 600 °C.

4.4 Conclusion

In conclusion, I have successfully synthesized crystallinity-dependent MoS₂ monolayers by liquid exfoliation from their bulk counterparts for the first time. Excellent cocatalytic performances of the proposed monolayer MoS₂ nanosheets for photocatalytic HER were achieved and determined by their crystallinity. The cocatalytic performance of the monolayer MoS₂ is gradually enhanced with reducing its crystallinity. Especially, the lowly crystalline MoS₂ monolayers with the calcination temperature below 800°C showed cocatalytic performances even higher than that of Pt, an AQE as high as 71.6% can be achieved for the 400-MoS₂/CdS composite under visible light irradiation at 420 nm. As compared to the highly crystalline monolayer 2H-MoS₂, the increased HER activity for the poorly crystalline monolayers is attributed to the low-crystallization induced structural disorder. Furthermore, the degree of disorder can be easily regulated by controlling the crystallinity of the bulk precursor.

Reference

- [1] J. A. Turner, *Science* 2004, 305, 972-974.
- [2] H. Tong, S. X. Ouyang, Y. P. Bi, N. Umezawa, M. Oshikiri, J. H. Ye, *Adv. Mater.* 2012, 24, 229-251.
- [3] A. Kudo, Y. Miseki, *Chem. Soc. Rev.* 2009, 38, 253.
- [4] X. Lu, S. Xie, H. Yang, Y. Tong, H. Ji, *Chem. Soc. Rev.* 2014, 43, 7581.
- [5] J. Greeley, T. F. Jaramillo, J. Bonde, I. B. Chorkendorff, J. K. Norskov, *Nat. Mater.* 2006, 5, 909-913.
- [6] P. D. Tran, T. V. Tran, M. Orio, S. Torelli, Q. D. Truong, K. Nayuki, Y. Sasaki, S. Y. Chiam, R. Yi, I. Honma, J. Barber, V. Artero, *Nat. Mater.* 2016, 15, 640-646.
- [7] Z. Huang, W. Luo, L. Ma, M. Yu, X. Ren, M. He, S. Polen, K. Click, B. Garrett, J. Lu, K. Amine, C. Hadad, W. Chen, A. Asthagiri, Y. Wu, *Angew. Chem. Int. Ed.* 2015, 54, 15181–15185.
- [8] D. Voiry, H. Yamaguchi, J. Li, R. Silva, D. C. B. Alves, T. Fujita, M. Chen, T. Asefa, V. B.

- Shenoy, G. Eda, M. Chhowalla, *Nat. Mater.* 2013, 12, 850–855.
- [9] J. Kibsgaard, T. F. Jaramillo, F. Besenbacher, *Nat. Chem.* 2014, 6, 248–253.
- [10] E. S. Andreiadis, P. Jacques, P. D. Tran, A. Leyris, M. Chavarot-Kerlidou, B. Jousset, M. Matheron, J. Pécaut, S. Palacin, M. Fontecave, V. Artero, *Nat. Chem.* 2013, 5, 48–53.
- [11] J. Kibsgaard, Z. B. Chen, B. N. Reinecke, T. F. Jaramillo, *Nat. Mater.* 2012, 11, 963–969.
- [12] M. A. Lukowski, A. S. Daniel, F. Meng, A. Forticaux, L. S. Li, S. Jin, *J. Am. Chem. Soc.* 2013, 135, 10274–10277.
- [13] R. Lv, J. A. Robinson, R. E. Schaak, D. Sun, Y. F. Sun, T. E. Mallouk, M. Terrones, *Acc. Chem. Res.* 2015, 48, 56–64.
- [14] T. F. Jaramillo, K. P. Jorgensen, J. Bonde, J. H. Nielsen, S. Horch, I. Chorkendorff, *Science* 2007, 317, 100–102.
- [15] B. Hinnemann, P. G. Moses, J. Bonde, K. P. Jorgensen, J. H. Nielsen, S. Horch, I. Chorkendorff, J. K. Nørskov, *J. Am. Chem. Soc.* 2005, 127, 5308–5309.
- [16] K. Chang, M. Li, T. Wang, S. X. Ouyang, P. Li, L. Q. Liu, J. H. Ye, *Adv. Energy. Mater.* 2015, 5, 1402279.
- [17] H. Zhang, *ACS nano* 2015, 9, 9451–9469.
- [18] K. S. Novoselov, D. Jiang, F. Schedin, T. J. Booth, V. V. Khotkevich, S. V. Morozov, A. K. Geim, *Proc. Natl. Acad. Sci. U.S.A.* 2005, 102, 10451–10453.
- [19] Y. H. Lee, X. Q. Zhang, W. J. Zhang, M. T. Chang, C. T. Lin, K. D. Chang, Y. C. Yu, J. T. W. Wang, C. S. Chang, L. J. Li, T. W. Lin, *Adv. Mater.* 2012, 24, 2320–2325.
- [20] X. S. Wang, H. B. Feng, Y. M. Wu, L. Y. Jiao, *J. Am. Chem. Soc.* 2013, 135, 5304–5307.
- [21] J. N. Coleman, M. Lotya, A. O’Neill, S. D. Bergin, P. J. King, U. Khan, K. Young, A. Gaucher, S. De, R. J. Smith, I. V. Shvets, S. K. Arora, G. Stanton, H.-Y. Kim, K. Lee, G. T. Kim, G. S. Duesberg, T. Hallam, J. J. Boland, J. J. Wang, J. F. Donegan, J. C. Grunlan, G. Moriarty, A. Shmeliov, R. J. Nicholls, J. M. Perkins, E. M. Grievson, K. Theuwissen, D. W. McComb, P. D. Nellist, V. Nicolosi, *Science* 2011, 331, 568–571.

- [22] M. Chhowalla, H. S. Shin, G. Eda, L. J. Li, K. P. Loh, H. Zhang, *Nat Chem* 2013, 5, 263-275.
- [23] J. Xie, J. Zhang, S. Li, F. Grote, X. Zhang, H. Zhang, R. Wang, Y. Lei, B. Pan, Y. Xie, *J. Am. Chem. Soc.* 2013, 135, 17881–17888.
- [24] L. Oakes, R. Carter, T. Hanken, A. P. Cohn, K. Share, B. Schmidt, C. L. Pint, *Nat. Commun.* 2016, 7, 11796.
- [25] H. W. Wang, P. Skeldon, G. E. Thompson, *Surf. Coat. Technol.* 1997, 91, 200.
- [26] C. Lee, H. Yan, L. E. Brus, T. F. Heinz, J. Hone, S. Ryu, *ACS Nano* 2010, 4, 2695–2700.
- [27] X. Hai, K. Chang, H. Pang, M. Li, P. Li, H. M. Liu, L. Shi, J. H. Ye, *J. Am. Chem. Soc.* 2016, 138, 14962–14969.
- [28] J. Kim, S. Kwon, D.-H. Cho, B. Kang, H. Kwon, Y. Kim, S. O. Park, G. Y. Jung, E. Shin, W.-G. Kim, H. Lee, G. H. Ryu, M. Choi, T. H. Kim, J. Oh, S. Park, S. K. Kwak, S. W. Yoon, D. Byun, Z. Lee, C. Lee, *Nat. Commun.* 2015, 6, 8294-8302.
- [29] M. Acerce, D. Voiry, M. Chhowalla, *Nat. Nanotechnol.* 2015, 10, 313.
- [30] H. Li, Q. Zhang, C. C. R. Yap, B. K. Tay, T. H. T. Edwin, A. Olivier, D. Baillargeat, *Adv. Funct. Mater.* 2012, 22, 1385-1390.
- [31] B. Radisavljevic, A. Radenovic, J. Brivio, V. Giacometti, A. Kis, *Nature Nanotech* 2011, 6, 147–150; c) A. Splendiani, L. Sun, Y. Zhang, T. Li, J. Kim, C. Y. Chim, G. Galli, F. Wang, *Nano Lett.* 2010, 10, 1271–1275.
- [32] J. Xie, H. Zhang, S. Li, R. Wang, X. Sun, M. Zhou, J. Zhou, X. Lou, Y. Xie, *Adv. Mater.* 2013, 25, 5807.
- [33] G. Guan, S. Zhang, S. Liu, Y. Cai, M. Low, C. P. Teng, I. Y. Phang, Y. Cheng, K. L. Duei, B. M. Srinivasan, Y. Zheng, Y. W. Zhang, M. Y. Han, *J. Am. Chem. Soc.* 2015, 137, 6152.
- [34] J. P. Wilcoxon, P. P. Newcomer, G. A. Samara, *J. Appl. Phys.* 1997, 81, 7934.
- [35] X. Chen, N. C. Berner, C. Backes, G. S. Duesberg, A. R. McDonald, *Angew. Chem., Int. Ed.* 2016, 55, 5803–5808.

- [36] C. Backes, R. J. Smith, N. McEvoy, N. C. Berner, D. McCloskey, H. C. Nerl, A. O'Neill, P. J. King, T. Higgins, D. Hanlon, N. Scheuschner, J. Maultzsch, L. Houben, G. S. Duesberg, J. F. Donegan, V. Nicolosi, J. N. Coleman, *Nat. Commun.* 2014, 5, 4576.
- [37] K. Chang, X. Hai, H. Pang, H. B. Zhang, L. Shi, G. G. Liu, H. M. Liu, G. X. Zhao, M. Li, J. H. Ye, *Adv. Mater.* 2016, 28, 10033-10041.
- [38] K. Woan, G. Pyrgiotakis, W. Sigmund, *Adv. Mater.* 2009, 21, 2233.
- [39] K. Chang, X. Hai and J. H. Ye, *Adv. Energy. Mater.* 2016, 6, 1502555-1502575.

Chapter 5 Maximizing synergistic cocatalytic activity of MoS₂ monolayers combining crystallinity engineering and cobalt substitution

5.1 Introduction

The evolution of hydrogen from water splitting bears great promise as a sustainable way for energy storage, which stores electrical or solar energy in the form of hydrogen that can be delivered at will and consumed without pollution to the environment.^[1-6] Up to now, platinum-based precious metals are the most effective and stable catalysts for hydrogen evolution reaction (HER) except for their scarcity and high cost.^[7] The development of earth-abundant and inexpensive catalysts is essential for the implementation of this technology into application more economic and competitive.^[8] In the past few decades, substantial work has been devoted to explore and identify non-precious catalysts for HER based on transition metals such as Ni, Co, Fe, Mo and W.^[9-13] Among them, molybdenum disulfide (MoS₂) as one of the most promising alternative has received tremendous attention due to its layered crystal and unique electronic structure, showing an attractive hydrogen evolution performance in acidic media with high stability.^[14-16] As suggested from the theoretical calculation and experimentally proved, the HER activity of semiconducting MoS₂ mainly arises from the edge active sites, which possess favorable hydrogen adsorption free energy ($\Delta G_{\text{H}} \sim 0.08$ eV) that can be comparable to Pt.^[17] However, thermodynamics favors the presence of the relatively inactive basal plane and impedes the formation of highly energetic and atomically undercoordinated edge sites, limiting the number of active sites at the surface.^[2]

In order to exploit the catalytic performance of 2H-MoS₂, considerable efforts have been made during the past few years. One strategy focuses on engineering higher densities or enhancing the intrinsic activity of edge sites through morphology control or atomic-scale modifications such as controllable disorder engineering;^[18-23] another strategy strives to activate and make use of the basal plane normally through phase transformation to metallic metastable 1T phase, or introducing sulfur vacancies assisted with either strain to optimize ΔG_H or low resistance contact to facilitate electron injection.^[24-30] Despite the fact that the mentioned approaches can activate the basal plane of 2H-MoS₂ for HER, special supports must be used for the formation of tensile strain or low-resistance contact.^[29, 30] In addition, chemical doping is usually utilized to improve the intrinsic properties of the material and recent works suggest that through either cation or anion doping can decrease the ΔG_H of 2H-MoS₂ basal plane, which provides another potential way for activation of the basal plane, but still not satisfied for triggering an efficient HER.^[31, 32] Although it has been demonstrated that monolayer MoS₂ comparing with few-layer or bulk ones presents a much higher hydrogen evolution activity due to its unique electronic structure and superior conductivity,^[33, 34] until now, for freestanding and thermodynamically stable monolayer 2H-MoS₂, which is favorable and has a great potential for large-scale hydrogen production, it still lacks of an effective strategy to active the inert basal plane.^[35]

In this chapter, I explored a generalizable method to combine exposing more active sites and activating inert basal plane through crystallinity engineering and cobalt substitution to maximize synergistic activity of freestanding 2H-MoS₂ monolayers for HER. Reducing the crystallinity of MoS₂ monolayers can bring in defects on the basal plane that act as new active sites, leading to a significant enhanced HER activity compared to the highly crystalline counterpart. Furthermore, the HER activity for the lowly crystalline MoS₂ monolayers can be further much enhanced after introducing cobalt substitution. Our density function theory (DFT) calculations show that through cobalt substitution in collaboration with the low crystallization induced in-plane lattice contraction in monolayer 2H-MoS₂, the ΔG_H of cobalt-bonded sulfurs on the basal plane can be reduced and optimized to a suitable value that is responsible for the further enhanced HER activity. This study provides unique opportunity to combine the

function of more active sites and making use of the basal plane of monolayer 2H-MoS₂, which allow to achieve a superior HER performance and may pave the way for the further design and improvement of MoS₂-based catalysts for HER.

5.2 Experimental section

5.2.1 Synthesis of MoS₂ precursors with crystallinity engineering and cobalt substitution

For the preparation of pure MoS₂ precursors, 10 mmol (NH₄)₂MoS₄ (Purity 99.5%, Wako) was dissolved in 200 mL deionized water under Ar flow and stirring for 2 hours. Then 20 mL 1 M HCl solution was added slowly to the (NH₄)₂MoS₄ solution and the resultant black product was centrifuged and washed with deionized water, dried in a vacuum oven at 60°C overnight. The dried powder was annealed at 500°C and 1000°C for 5 hours under Ar atmosphere to obtain lowly crystalline MoS₂ (L-MoS₂) and highly crystalline MoS₂ (H-MoS₂) precursors, respectively. For the preparation of 5% cobalt doped MoS₂ precursors, 9.5 mmol (NH₄)₂MoS₄ (Purity 99.5%, Wako) was dissolved in 200 mL deionized water under Ar flow and stirring for 2 hours. Then 0.5 mmol CoCl₂·6H₂O dissolved in 18 mL 1 M HCl solution, added slowly to the (NH₄)₂MoS₄ solution and the resultant black product was centrifuged and washed with deionized water, dried in a vacuum oven at 60°C overnight. The dried powder was annealed at 500°C and 1000°C for 5 hours under Ar atmosphere to obtain lowly crystalline 5% cobalt doped MoS₂ (L-Co/MoS₂) and highly crystalline 5% cobalt doped MoS₂ (H-Co/MoS₂) precursors, respectively.

5.2.2 Exfoliation of bulk precursors to monolayers

Typically, 100 mg of the as-prepared bulk precursor was added into a 100 ml glass vial. Then, 50 mL ethanol was added as the exfoliation and dispersion solvent. The mixture was bath sonicated for 24 hours using an FU-260-C at a frequency of 28 kHz. The resulting suspensions were first centrifuged using a TOMY LC-200 centrifuge at 2000 rpm (RCF 760 g) for 1 hour, then the top 2/3 portions of the

supernatants were carefully collected by pipette. The obtained supernatants were added into a new glass vial and sonicated again for another 4 hours. Then, the monolayer dispersions were collected by pipette, followed by another centrifugation of the supernatant at 4000 rpm (RCF 3020 g) for 1 hour.

5.2.3 Characterization

The bulk material structures were determined using an X-ray diffractometer (X'pert powder, PANalytical B.V., Netherlands) with Cu-K α radiation. SEM was performed on a JEOL 6701F field-emission scanning electron microscope. TEM was performed on an FEI Tecnai G2 F30 microscope with a 300 kV accelerating voltage. AFM was carried out in tapping mode (Nanocute H, Japan). XPS data were collected using a PHI Quantera SXM (ULVAC-PHI, Japan). Raman spectroscopy was performed using a Horiba Jobin Yvon LabRAM system with a 532 nm excitation laser. UV-vis absorption spectra were measured using a Shimadzu UV-2500 spectrophotometer in quartz cuvettes with a pathlength of 2 mm. PL spectra excited at 435 nm were recorded on a Spex Fluorolog-3 spectrofluorometer. The zeta potential was tested using a Zeta-potential & Particle size Analyzer ELSZ-2000 series. ESR spectra were recorded on a JES-FA200 electron spin resonance spectrometer operating at about 9.0 GHz at room temperature.

5.2.4 Electrode preparation and electrochemical measurements

Electrochemical measurements were performed in a standard three-electrode system using a CHI650A instrument. A graphite rod, Ag/AgCl (saturated KCl), and a glassy carbon electrode were used as counter, reference, and working electrodes, respectively. The catalysts were ultrasonically dispersed in a water-ethanol solution (v/v 3:1) containing 0.1 wt% Nafion, and a drop of the catalyst (5 μ L, 2.0 mg/mL) was then transferred onto the glassy carbon electrode to obtain the catalyst loading of 0.14 mg cm⁻². All the measurements were performed in 0.5 M H₂SO₄ aqueous solution under continuous purging with N₂ at room temperature and 2000 rpm, with a sweep rate of 10 mV s⁻¹. Cyclic voltammograms at various scan rates (20, 40, 60, 80, 100, 120, 140, 160, and 180 mV/s) were collected in the 0.1-0.2 V vs RHE range and used to estimate the double-layer capacitance. The electrochemical

impedance spectroscopy (EIS) measurements were carried out at 250 mV overpotential with the frequency ranging from 10^6 to 0.1 Hz. The impedance data were fitted to a simplified Randles circuit to determine the system resistance and capacitance.

5.2.5 Preparation of MoS₂/CdS photocatalysts

Monolayer MoS₂ suspensions were mixed with commercial CdS (99%, Aldrich) in certain stoichiometric ratio, sonicated and stirred overnight until dry, then the composites were collected and annealed in an Ar atmosphere at 400°C for 4 hours.

5.2.6 Photocatalytic hydrogen evolution

The photocatalytic H₂ evolution was carried out with 0.2 g of the photocatalyst hybrid in 300 mL of solution in a Pyrex glass reaction cell. The optimized reaction solution is 30 vol. % lactic acid adjusted by NaOH to achieve a pH ~5.0. The reaction cell was connected to a closed gas system with a gas circulation pump. A 300 W Xenon lamp equipped with L42 cut-off filter was used as the visible light source ($\lambda > 420$ nm). H₂ evolution was measured with an on-line gas chromatograph (GC-8A, Shimadzu) equipped with a thermal conductivity detector according to the standard curve. The AQEs with various monochromatic lights were obtained by using a series of band-pass filters (Optical Coatings Japan). The light intensity was measured using a radiant power energy meter (Ushio spectroradiometer, USR-40, Japan). The AQE was calculated using the following equation:

$$\begin{aligned} \text{AQE} &= \frac{\text{Number of reacted electrons}}{\text{Number of incident photons}} = \frac{\text{Number of evolved H}_2 \text{ molecules} \times 2}{\text{Number of incident photons}} \\ &= \frac{M \times N_A \times 2}{\frac{I \times A \times t}{E_g \times J}} \end{aligned}$$

where M represents the amount of H₂ generation, N_A represents Avogadro's constant, I is the light intensity, A is the light incident area, t is light incident time, E_g and J are fixed constants.

5.2.7 DFT calculations

All calculations were performed with the Vienna ab-initio Simulation Package (VASP) based on the density functional theory (DFT).^[36] General gradient approximation was employed to evaluate the exchange-correlation energy.^[37] The number of k points and the cutoff energy were increased until the calculated total energy converged within an error of 1×10^{-5} eV/atom. Therefore, the cut-off energy of 500 eV with $11 \times 11 \times 1$ k points was set. The energy convergence tolerance was set to below 5×10^{-6} eV/atom. The lattice vectors and atomic coordinates were relaxed until the Hellmann-Feynman force was reduced to 0.01 eV/Å. To simulate the biaxial strain of MoS₂, the relaxation of crystal with the lattice constants a fixed was performed. And the specified in-plane compression strain was defined as $= (a - a_0) / a_0$.

5.3 Results and discussion

5.3.1 Characterization of rational designed MoS₂ precursors

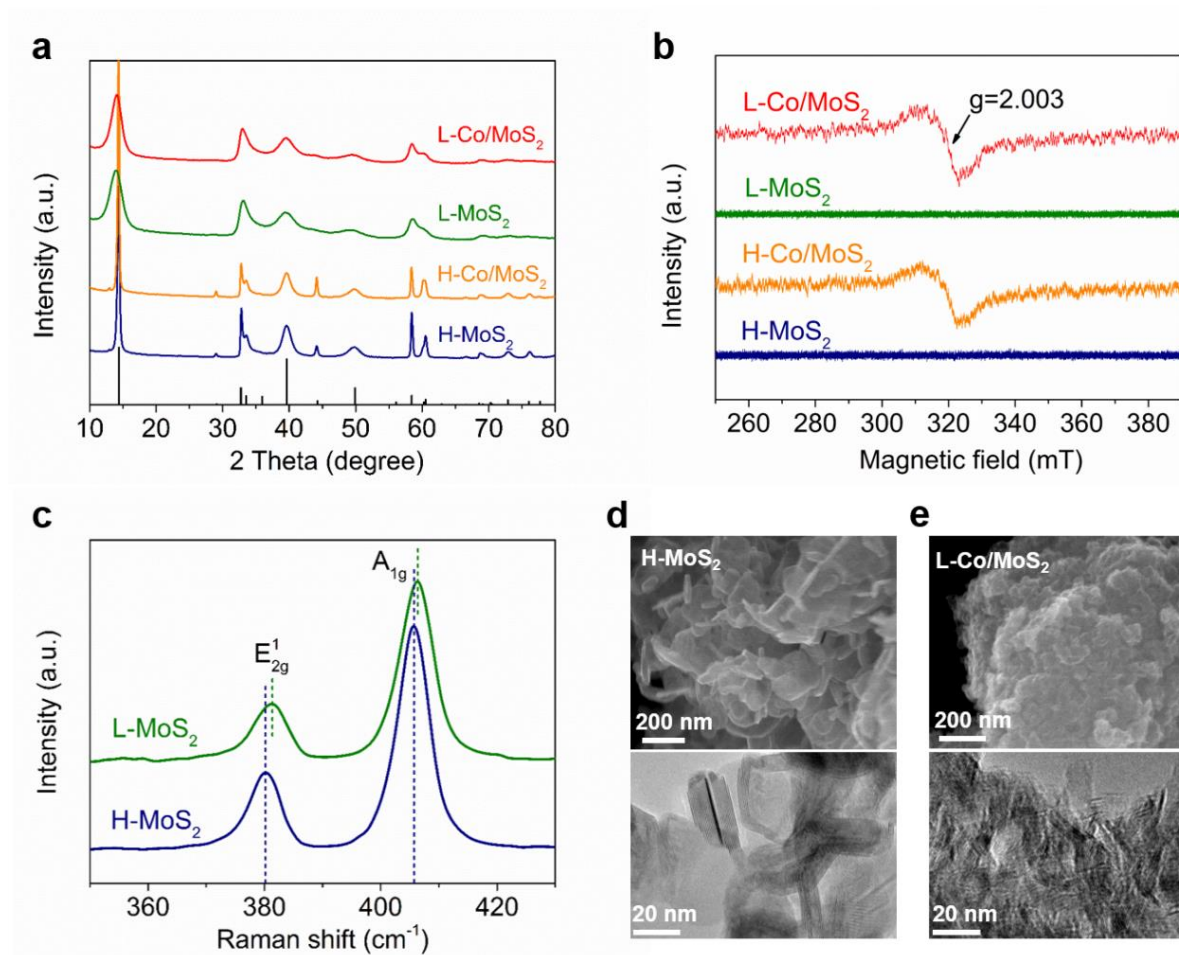


Figure 5.1 (a) XRD patterns and (b) EPR spectra of the as-prepared H-MoS₂, H-Co/MoS₂, L-MoS₂, and L-Co/MoS₂ bulk precursors. (c) Raman spectra of the as-prepared H-MoS₂ and L-MoS₂ bulk precursors. SEM (top) and TEM (down) images of (d) H-MoS₂ and (e) L-Co/MoS₂ bulk precursors.

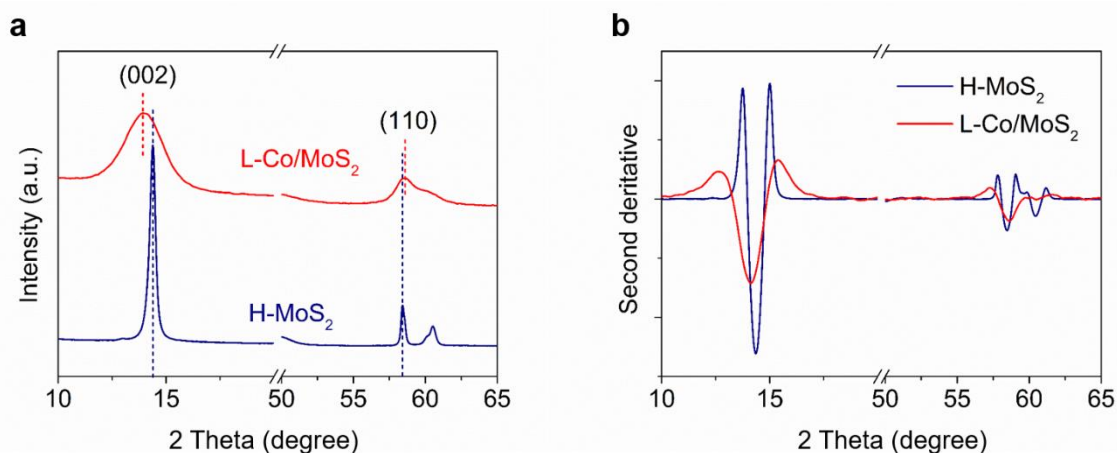


Figure 5.2 (a) Enlarged XRD patterns of H-MoS₂ and L-Co/MoS₂ bulk crystals. (b) Second derivative of the corresponding XRD plots.

I have demonstrated that edge-engineered bulk MoS₂ crystal can be directly exfoliated into monolayer nanosheets in polar micromolecular solvents such as ethanol, providing a facile way to prepare elemental doping and crystallinity controllable monolayer MoS₂ through direct liquid exfoliation from their corresponding bulk counterparts.^[38] Highly crystalline (H-MoS₂), 5% cobalt-substituted highly crystalline (H-Co/MoS₂), lowly crystalline (L-MoS₂), and 5% cobalt-substituted lowly crystalline (L-Co/MoS₂) bulk precursors with nanoscale lateral size were first prepared. Figure 5.1a shows the X-ray diffraction (XRD) patterns of the as-prepared bulk precursors, where all the observed diffraction peaks belong to pristine 2H-phase MoS₂ structure (PDF 01-087-2416) and no other impurity phase existed. For crystallinity engineering, the significantly broadened peaks of L-MoS₂ and L-Co/MoS₂ suggest the drastically declined crystallinity.^[39] For cobalt substitution, the broad resonances at $g = 2.003$ in electron paramagnetic resonance (EPR) spectra of H-Co/MoS₂ and L-Co/MoS₂ are featured for Co²⁺ (Figure 5.1b).^[40] Detailed analysis of the XRD spectra shows that the 002 peak shifts to a lower angle while the 100 and 110 peaks shift to a higher angle with crystallinity engineering (Figure 5.2), indicating a contraction of in-plane lattice for the lowly crystalline MoS₂ crystals.^[41] This in-plane lattice contraction was further confirmed by the blue shift of the two dominant peaks E_{2g}¹ and A_{1g} of 2H-MoS₂ in their Raman spectra (Figure

5.1c).^[42, 43] Their morphology and crystal structure are further examined by scanning electron microscopy (SEM) and high-resolution transmission electron microscopy (TEM), as shown in Figure 5.1d and 5.1e. Both the H-MoS₂ and L-Co/MoS₂ crystals have a nanoscale lateral size and the L-Co/MoS₂ shows reduced lattice order, which are consistent well with the results from the XRD analysis.

5.3.2 Characterization of rational designed MoS₂ monolayers

Next, the monolayer H-MoS₂, H-Co/MoS₂, L-MoS₂, and L-Co/MoS₂ nanosheets were produced by direct liquid exfoliation from their bulk counterparts as depicted in Figure 5.3 a. As demonstrated by our previous work, in the liquid exfoliation process, the resulting hydrodynamic forces from high-energy liquid jets at the edge sites of the as-prepared bulk crystals are enough to overcome the interlayer van der Waals attraction, allowing for efficient exfoliation into monolayers.^[38] Their general information about the size, crystal structure, thickness and chemical states were investigated by TEM, AFM and XPS. The low-resolution TEM image of the exfoliated monolayer L-Co/MoS₂ nanosheets shows a uniform distribution without aggregation and an average lateral size around of 40 nm (Figure 5.3b). Comparing with H-MoS₂ monolayers (Figure 5.4), its HRTEM image and the fast Fourier transform pattern show a weak hexagonal lattice structure which exhibiting six diffraction arcs and obvious defects in the basal plane as marked by the red ring (Figure 5.3c).^[20] This indicates that crystallinity engineering is an effective way to form defect enriched MoS₂ that would benefit its HER performance. Their thickness was evaluated by tapping-mode AFM (Figure 5.3d), where the line profiles of the two selected regions show a topographic height of ~0.6 nm (± 0.1 nm), confirming the single-layer structure of the exfoliated MoS₂ nanosheets.^[44, 45] Then, high-resolution XPS measurement was performed to check its chemical state of the exfoliated L-Co/MoS₂ monolayers. The banding energies of Mo and S are consistent with the previously reported values of 2H-MoS₂ (Figure 5.3e,f).^[46] The Co 2p spectrum (Figure 5.3g) shows two weak peaks at 779.3 and 795.1 eV that are corresponding to Co 2p_{3/2} and Co 2p_{1/2} respectively, implying the existence but small amount of Co²⁺ in the L-Co/MoS₂ monolayers.^[47]

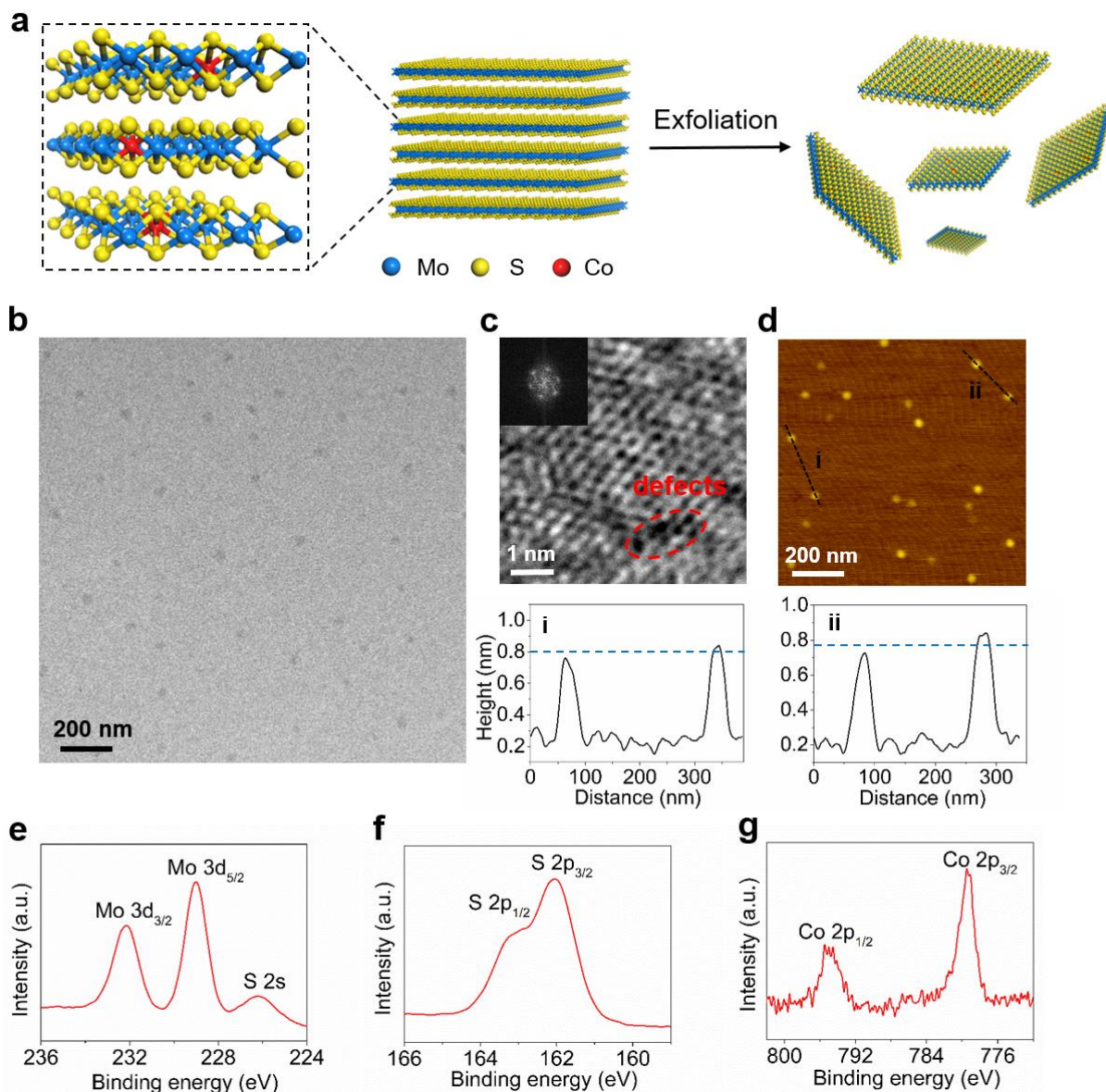


Figure 5.3 Structural analysis of monolayer L-Co/MoS₂ nanosheets. (a) Schematic illustration of the exfoliation process from bulk crystals to monolayer nanosheets. (b) Low-resolution TEM image of monolayer L-Co/MoS₂ nanosheets, and (c) HRTEM image of a monolayer L-Co/MoS₂ nanosheet. Inst show its FFT pattern and the defects as denoted by the red ring. (d) AFM image of the exfoliated height of ~0.6 nm. The measured height of ~0.6 nm from the line profiles well-matches the theoretical thickness of monolayer MoS₂. XPS spectra of (e) Mo_{3d}, (f) S_{2p} and (g) Co_{2p} of monolayer L-Co/MoS₂ nanosheets.

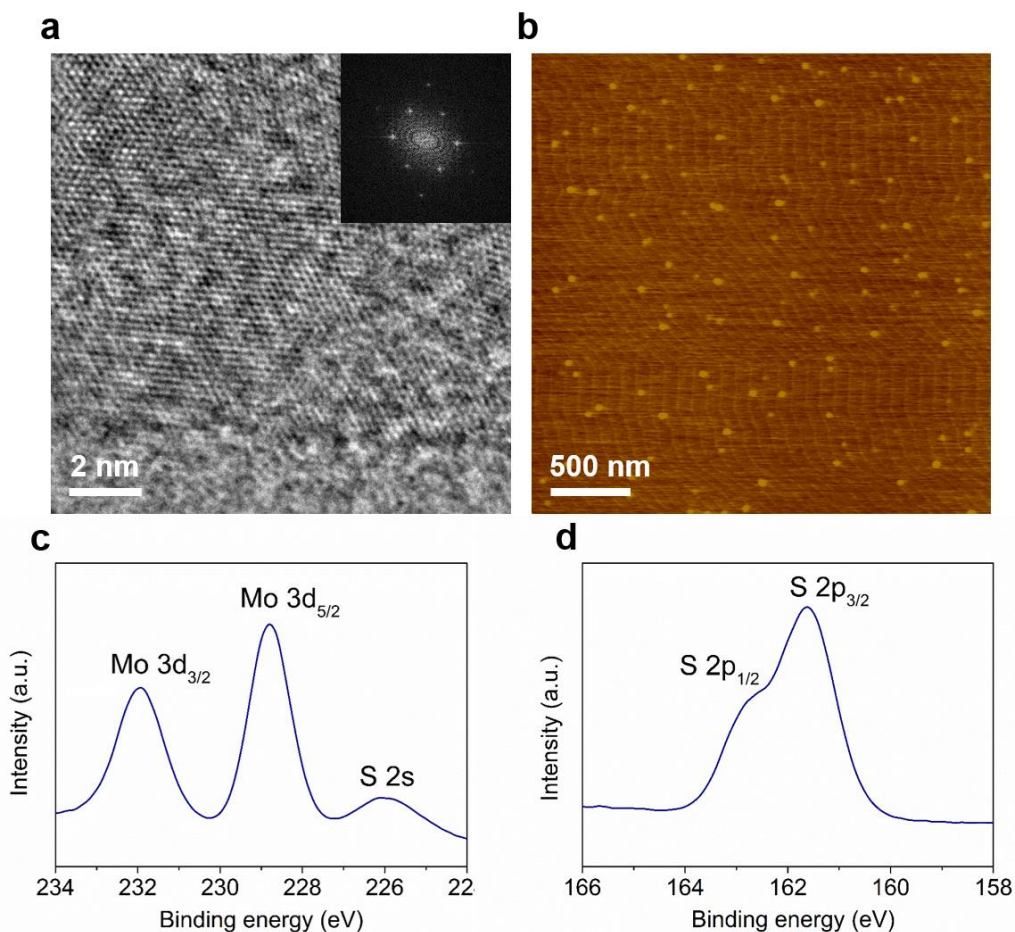


Figure 5.4 (a) HRTEM image of monolayer H-MoS₂. Inset shows the corresponding FFT pattern. (b) AFM image of monolayer H-MoS₂ nanosheets. XPS spectra of (c) Mo_{3d} and (d) S_{2p} of monolayer H-MoS₂ nanosheets.

Their UV-vis absorption and photoluminescence (PL) spectra were also investigated to track the influence of crystallinity and cobalt doping on the optical properties of monolayer 2H-MoS₂. Figure 5.5a shows the optical absorption spectra of the resulting dispersions, all exhibiting feature peaks of standard 2H-MoS₂, where two characteristic peaks (A-exciton and B-exciton) located between 600 and 700 nm arising from the K point of the Brillouin zone.^[48, 49] As expected, for L-MoS₂ monolayers, the two excitonic peaks become much weaker and broader compared to H-MoS₂ monolayers due to the reduced 2H-MoS₂ crystal symmetry. The more weakened peaks after cobalt substitution in L-Co/MoS₂ suggests

the cobalt substitute for Mo in lattice, which will further lower the MoS₂ crystal symmetry. Correspondingly, the reduced crystal symmetry caused by crystallinity engineering and cobalt substitution would also decrease the PL intensity (Figure 5.5b) and stability of monolayer 2H-MoS₂ dispersions. These results indicate that the monolayer H-MoS₂, H-Co/MoS₂, L-MoS₂, and L-Co/MoS₂ nanosheets were successfully produced by liquid exfoliation from their bulk counterparts.

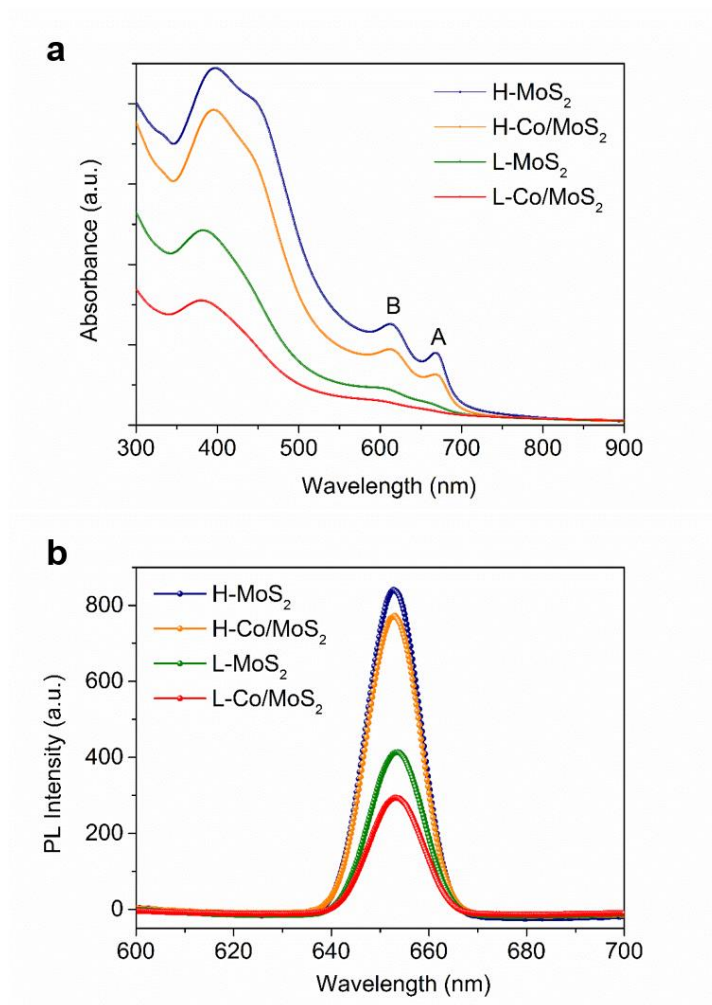


Figure 5.5 (a) Optical absorption spectra and (b) PL spectra of monolayer H-MoS₂, H-Co/MoS₂, L-MoS₂, and L-Co/MoS₂ nanosheets dispersed in ethanol.

5.3.3 Theoretical study of the rational designed MoS₂ monolayers for H₂ evolution

Recent theoretical studies show that some foreign elements doping in 2H-MoS₂ can decrease the ΔG_H of basal plane, providing the opportunity to activate the inert basal plane, in particular of freestanding

MoS₂ monolayers for HER.^[31, 32] On basis of the DFT calculations, I evaluate the HER performances of the basal plane sulfurs of 2H-MoS₂ with introducing cobalt substitution and in-plane lattice contraction, where the hydrogen adsorption free energy ΔG_H was employed as a descriptor to evaluate the activity.^[29] Generally, the optimal value of ΔG_H is 0 eV, where hydrogen is bound neither too strongly nor too weakly to facilitate both the hydrogen adsorption and desorption.^[17] For the ideal basal plane of 2H-MoS₂ without any defects, ΔG_H is 2.1 eV uphill, indicating that the basal plane is catalytic inert (Figure 5.6).^[50] When 6.25 % cobalt substitution is introduced, the ΔG_H drastically decreases to -0.24 eV, which, however, may be too strong for the hydrogen desorption from the surface.^[31] ΔG_H continues to decrease with increasing densities of cobalt, showing a negative trend for HER. Therefore, in the next, additional biaxial compressive strains were applied on 6.25% cobalt substituted monolayer MoS₂ to examine the synergistic effect of cobalt substitution and the crystallinity engineering induced in-plane lattice contraction, as illustrated in Figure 5.7a. It can be seen that the ΔG_H gradually improves from -0.24 eV with 0% compressive strain to -0.07 eV under 8% compressive strain (Figure 5.7b), which is very close to the ideal value and can be comparable to the highly active Mo-terminated edge sites ($\Delta G_H \sim 0.08$ eV). The trend of ΔG_H versus compressive strain as a guide suggests that the hydrogen adsorption energy of cobalt-connected sulfurs on the basal plane of monolayer 2H-MoS₂ could be optimized in favor of HER through combining crystallinity engineering and cobalt substitution.

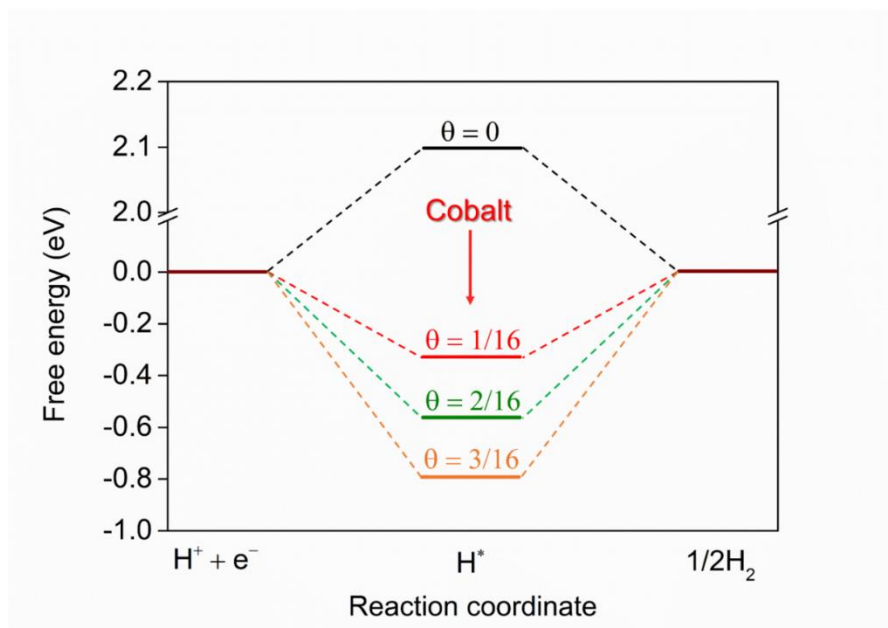


Figure 5.6 Hydrogen adsorption free energy versus the reaction coordinate of HER for the cobalt doping range of 0-18.75%.

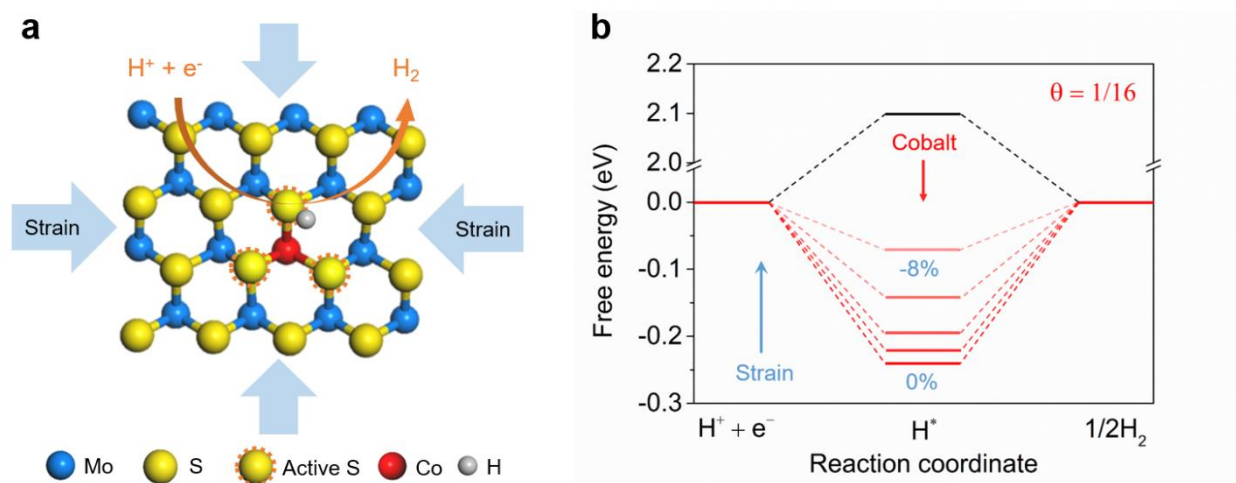


Figure 5.7 Theoretical calculations for the effects of crystallinity engineering and cobalt substitution on the HER activity of MoS₂. (a) Schematic of the top views of monolayer with biaxial compressive strain and cobalt substitution on the basal plane, where cobalt-connected S serve as the active sites for hydrogen evolution and applied strain further tunes the HER activity. (b) Hydrogen adsorption free energy versus the reaction coordinate of HER for the compressive strain range of 0-8%.

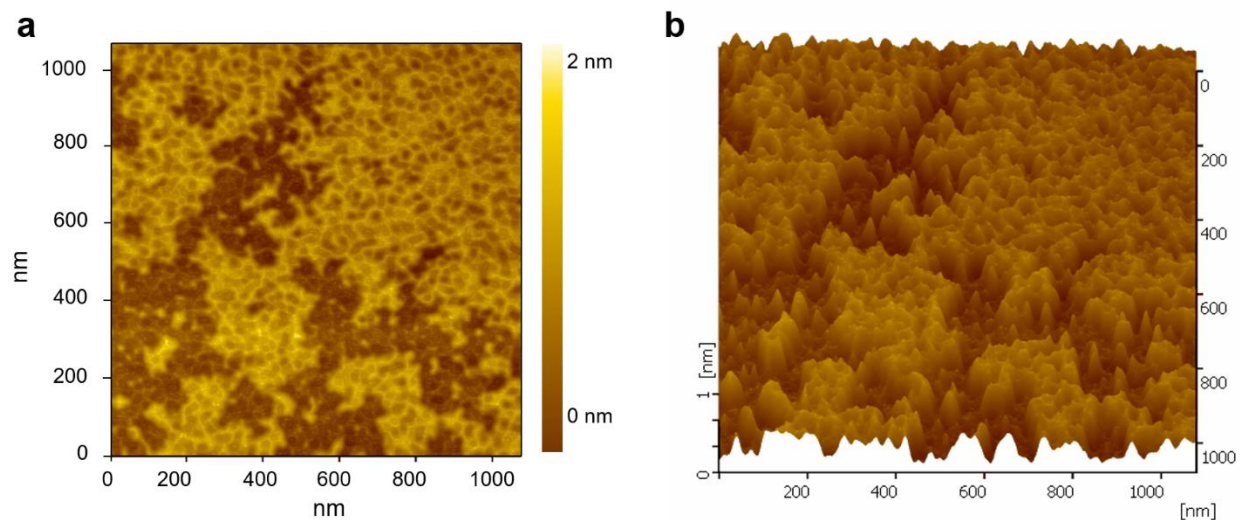
5.3.4 Electrochemical H₂ evolution

Figure 5.8 (a) AFM and (b) 3D AFM images of L-Co/MoS₂ monolayers deposited on mica.

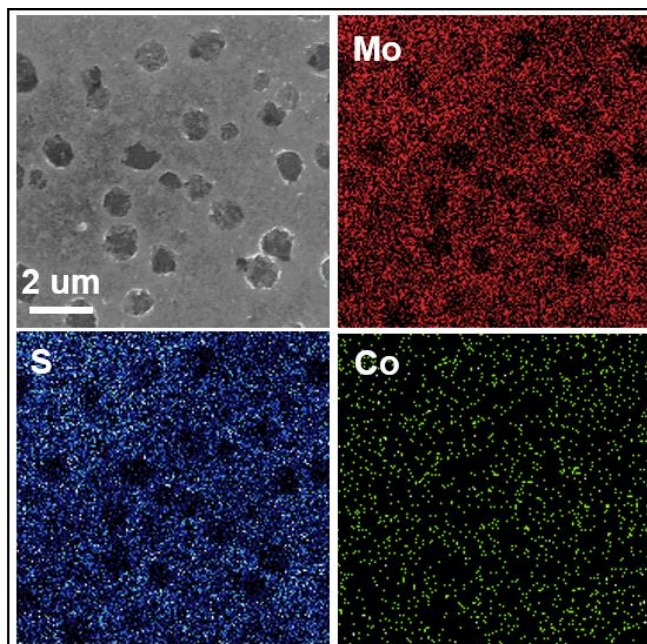


Figure 5.9 SEM and the corresponding element mapping images of L-Co/MoS₂ monolayers deposited on wafer.

Table 1. Summary of the electrocatalytic parameters of MoS₂ monolayers with the independent and combined effects of cobalt substitution and crystallinity engineering.

samples	η (mV vs RHE) for $j = -10 \text{ mA cm}^{-2}$	Tafel slope (mV dec ⁻¹)	Double-layer capacitance (C_{dl} , mF cm ⁻²)	Charge-transfer resistance (R_{ct} , Ω)	exchange current density (j_0 , $\mu\text{A cm}^{-2}$)
H-MoS ₂	283	86	4.3	263	5.2
H-Co/MoS ₂	260	81	6.9	195	6.9
L-MoS ₂	231	70	11.2	132	9.3
L-Co/MoS ₂	156	58	30.2	68	13.8

In order to verify our expectation, the separate and combined effects of cobalt substitution and crystallinity engineering on the catalytic HER activity of monolayer 2H-MoS₂ nanosheets were examined using a three-electrode configuration, with graphite rod as the counter-electrode, Ag/AgCl electrode as the reference electrode, and glassy carbon electrode drop-casted of monolayer nanosheets as the working electrode. As we know, good contact between active materials and the work electrode can facilitate interfacial electron injection and transfer are important in designing an efficient electrochemical reaction system.^[30] Fortunately, due to their soft and small size features, these monolayer nanosheets can be densely dispersed on the surface of support with a tough contact checked by AFM (Figure 5.8) and SEM (Figure 5.9). Then, all measurements were carried out at the same loading weight of 0.14 mg cm⁻² and the obtained key electrochemical results were listed in Table 1. Figure 5.10a shows the representative linear sweep voltammograms (LSV) for the monolayer H-MoS₂, H-Co/MoS₂, L-MoS₂, and L-Co/MoS₂ nanosheets, where they can achieve a geometric catalytic current density of 10 mA cm⁻² at overpotentials (η) of 283, 260, 231, and 156 mV, respectively (Table 1). We can see that cobalt substitution alone only slightly increases the HER activity, whereas crystallinity engineering alone can significantly increase the HER activity owing to the more exposed active sites. More importantly, the combination of cobalt substitution and crystallinity engineering leads to a drastically enhanced HER performance, which even

can be comparable to most of the reported metallic 1T-MoS₂ monolayers.^[24, 25, 27] The corresponding Tafel plots (Figure 5.10b) from the extrapolation of the linear region of overpotential (η) versus $\log j$ show that cobalt substitution decreases the Tafel slope from 86 to 81 mV dec⁻¹ whereas crystallinity engineering reduce the Tafel slope from 86 to 70 mV dec⁻¹. When combining cobalt substitution and crystallinity engineering, the Tafel slope drastically decreases from 86 to 58 mV dec⁻¹, strongly suggesting the synergistic effect of cobalt substitution and crystallinity engineering in promoting the HER. Then, from the intercept of the linear region of the Tafel plots, exchange current density (j_0) of 5.2, 6.9, 9.3, and 13.8 $\mu\text{A cm}^{-2}$ were obtained for H-MoS₂, H-Co/MoS₂, L-MoS₂, and L-Co/MoS₂ monolayers, respectively (Table 1). This remarkable j_0 value again reveals the excellent HER activity of L-Co/MoS₂ monolayers.

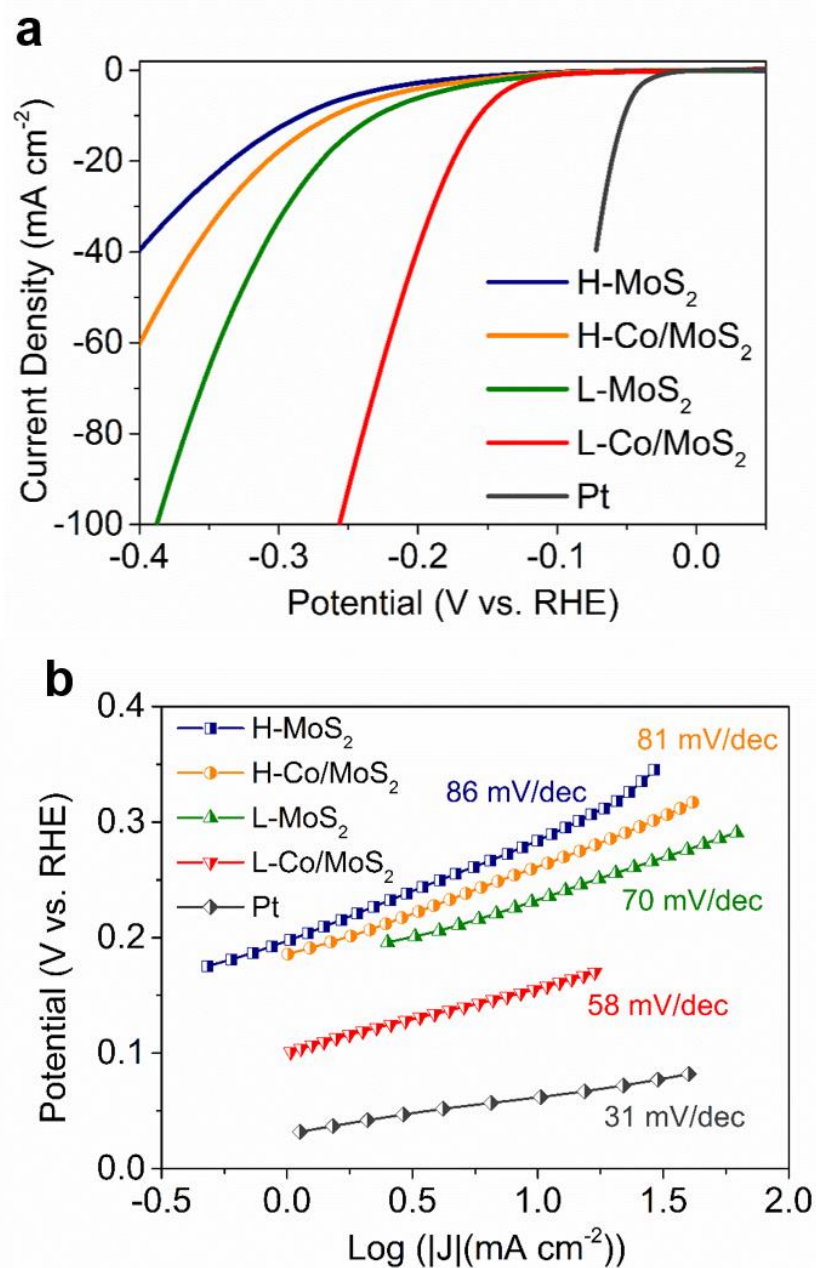


Figure 5.10 (a) Polarization curves and (b) corresponding Tafel plots of monolayer H-MoS₂, H-Co/MoS₂, L-MoS₂, and L-Co/MoS₂.

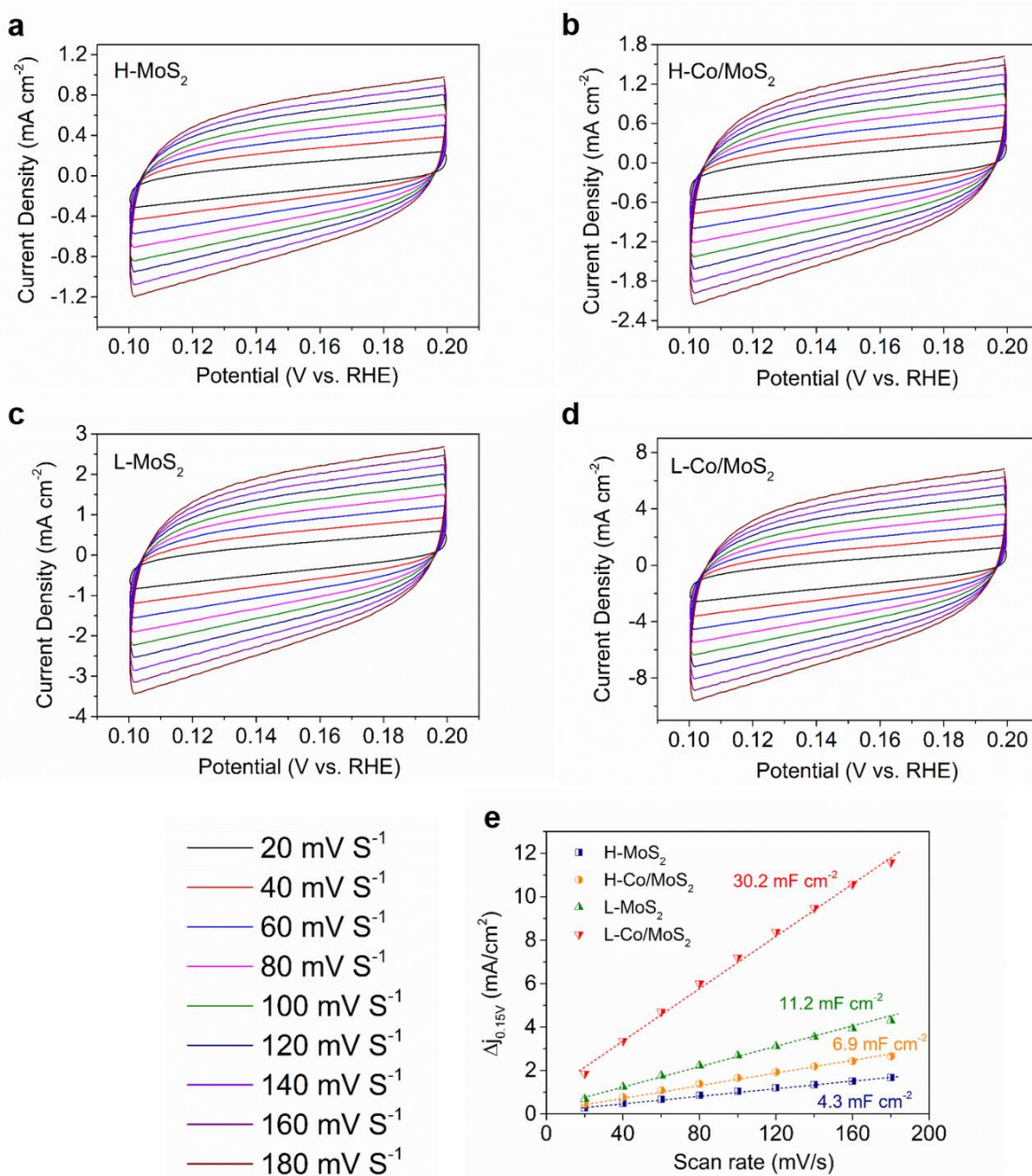


Figure 5.11 (a-d) Cyclic voltammetry curves of monolayer H-MoS₂, H-Co/MoS₂, L-MoS₂, and L-Co/MoS₂ nanosheets under different scan rates, in the region of 0.1-0.2 V vs. RHE. (e) The extracted C_{dl} from Cyclic voltammetry curves.

Furthermore, the double-layer capacitances (C_{dl}) derived from the cyclic voltammogram measurement results (Figure 5.11), which are proportional to the efficient electrochemically active surface area, are measured to evaluate the effective surface area after separate and combined effects of cobalt substitution and crystallinity engineering. As shown in Table 1, the calculated C_{dl} values were 4.3, 6.9, 11.2, and 30.2 mF cm^{-2} for H-MoS₂, H-Co/MoS₂, L-MoS₂, and L-Co/MoS₂ monolayers, respectively. Similar to the HER activities, cobalt substitution alone only slightly increases the catalytically active sites whereas crystallinity engineering alone can significantly increase the catalytically active sites. The combination of cobalt substitution and crystallinity engineering leads to a drastic increase of catalytically active sites more than seven times compared to the pristine monolayer 2H-MoS₂.

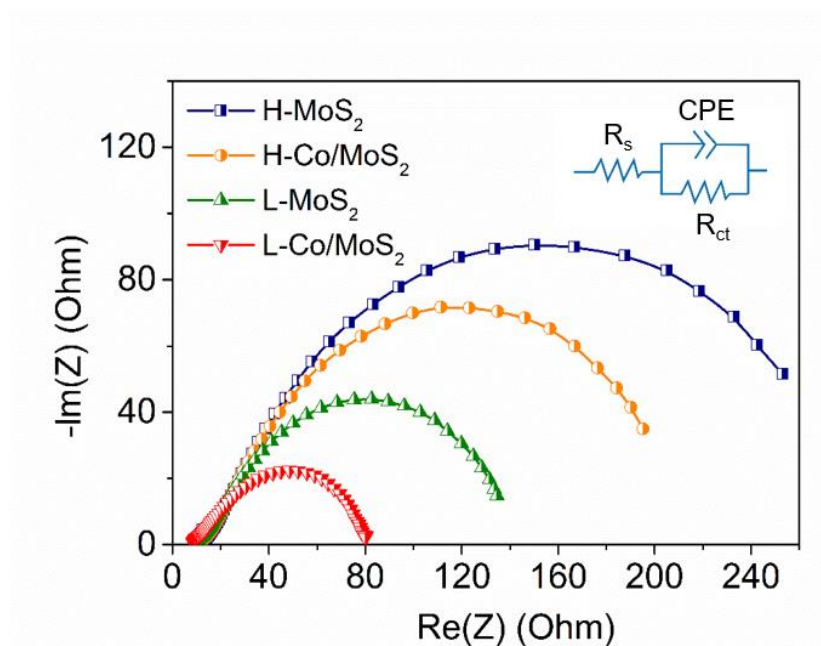


Figure 5.12 Electrochemical impedance spectroscopy Nyquist plots for monolayer H-MoS₂, H-Co/MoS₂, L-MoS₂ and L-Co/MoS₂. The data was fit to the simplified Randles equivalent circuit shown in the inset.

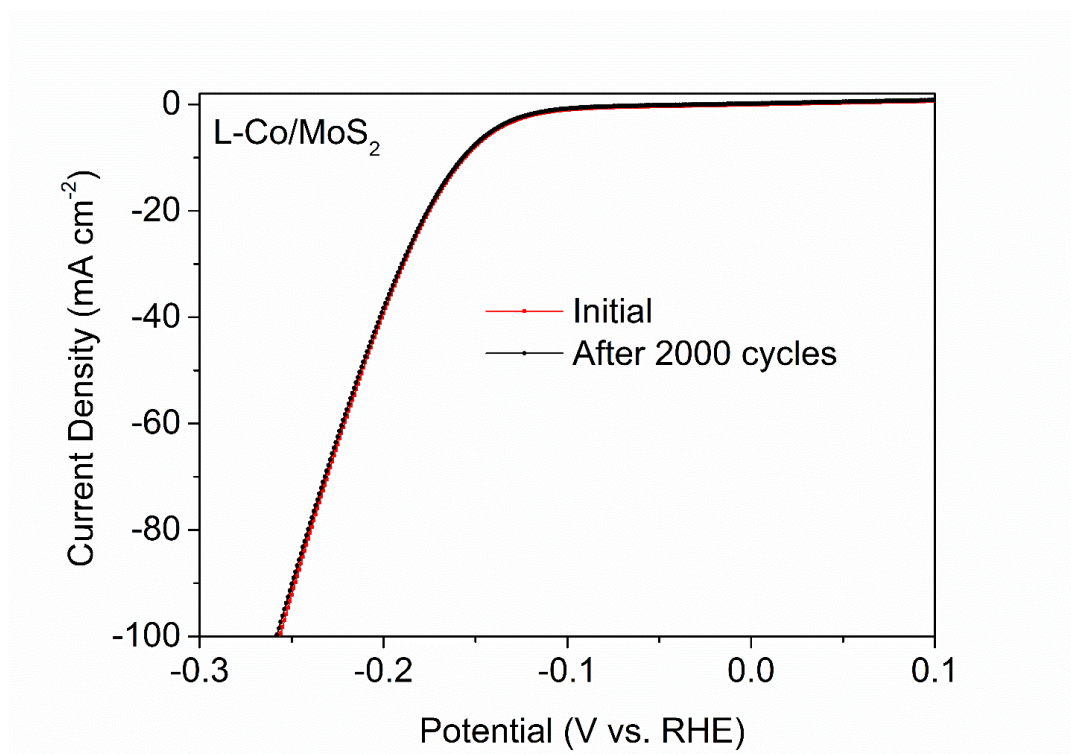


Figure 5.13 Durability test of monolayer L-Co/MoS₂ demonstrating negligible current loss even after 2000 cycles.

The electrochemical impedance spectroscopy (EIS) is further performed to investigate the electrode kinetic during HER process. The Nyquist plots (Figure 5.12) were fitted using an equivalent circuit (inset of Figure 5.12) to extract the charge transfer resistance (R_{ct}) of 263, 195, 132, and 68 Ω for H-MoS₂, H-Co/MoS₂, L-MoS₂, and L-Co/MoS₂ monolayers, respectively (Table 1). This remarkable decreased R_{ct} suggests a fast Faradaic process and thus superior HER kinetic after combining cobalt substitution and crystallinity engineering. The electrochemical stability of the L-Co/MoS₂ monolayers is also investigated by performing continuous cyclic voltammetry for 2000 cycles. As displayed in Figure 5.13, negligible decline can be observed between the curves measured at the initial cycle and after 2000 CV cycles, suggesting the excellent durability of L-Co/MoS₂ monolayers during long-term cycling. On the basis of the systematic electrochemical measurements, the integrated superior catalytic parameters of monolayer L-Co/MoS₂ nanosheets (low overpotential, small Tafel slop, large exchange current density, large double-

layer capacitance) undoubtedly confirm that combining cobalt substitution and crystallinity engineering is an effective way to improve the HER performance of monolayer 2H-MoS₂ both in thermodynamics and dynamics. Although the modified monolayer L-Co/MoS₂ can acquire a superior HER activity, but it still has a gap with the state-of-the-art catalyst Pt. It is worth noting that besides the different intrinsic catalytic properties, the unavoidable restacking and aggregation of the monolayer L-Co/MoS₂ nanosheets after deposition on the electrode is a critical issue that would seriously hinder the role of their unique monolayer features.

5.3.5 Photocatalytic H₂ evolution

As we know, MoS₂ also serves as an excellent cocatalyst when associated with a suitable photoharvester for solar hydrogen evolution.^[49-51] Thus, in order to fully take advantage of their monolayer features, the obtained monolayer H-MoS₂, H-Co/MoS₂, L-MoS₂ and L-Co/MoS₂ nanosheets were loaded on commercial CdS to evaluate their cocatalytic performances for photocatalytic hydrogen evolution. As expected, these monolayer MoS₂ nanosheets can be uniformly adsorbed on the surface of CdS due to their soft and small size features and still keep their monolayer structure (inset of Figure 5.14a).^[38] The obtained A-exciton peak position from the absorption spectra of L-Co/MoS₂-CdS composite (Figure 5.14a) is almost overlapped the value derived from monolayer L-Co/MoS₂ dispersion, further confirming that the monolayer nanosheets are monodispersed on the surface of CdS and restacking is avoided.^[54] The bare CdS cannot offer active sites for catalytic hydrogen evolution, leading to the facile recombination of photo-excited electron-hole pairs, and therefore it shows a poor photocatalytic hydrogen evolution activity of around 0.15 mmol h⁻¹. While after loading H-MoS₂, H-Co/MoS₂, L-MoS₂, and L-Co/MoS₂ monolayers as cocatalysts, the CdS can achieve photocatalytic HER activities as high as 4.2, 4.4, 5.1, and 6.2 mmol h⁻¹, respectively (Figure 5.14b). The atomic contact and heterojunction bonding between CdS and MoS₂ monolayers are favorable for the photogenerated electrons from CdS injecting into the surface loaded MoS₂ monolayers to drive the reduction reaction, leading to the superior photocatalytic performances of MoS₂/CdS composites. Notably, the cocatalytic performance of L-

Co/MoS₂ monolayers is even higher than that of Pt (4.6 mmol h⁻¹, Figure 5.15), which represented the state-of-the-art activity for HER. The corresponding apparent quantum efficiency (AQE) was calculated to be 80.2% for the L-Co/MoS₂-CdS composite under visible light irradiation at 420 nm (Figure 5.14c), which is the highest catalytic hydrogen activity for MoS₂-based cocatalysts to the best of our knowledge. Besides, the remarkable photocatalytic activity also exhibits a high stability, where only little loss of activity can be observed after five cycles (Figure 5.14d). More importantly, the even higher cocatalytic performance of L-Co/MoS₂ monolayers compared to H-MoS₂, H-Co/MoS₂, and L-MoS₂ monolayers, also demonstrates the maximizing synergistic HER activity of 2H-MoS₂ monolayers when combining cobalt substitution and crystallinity engineering.

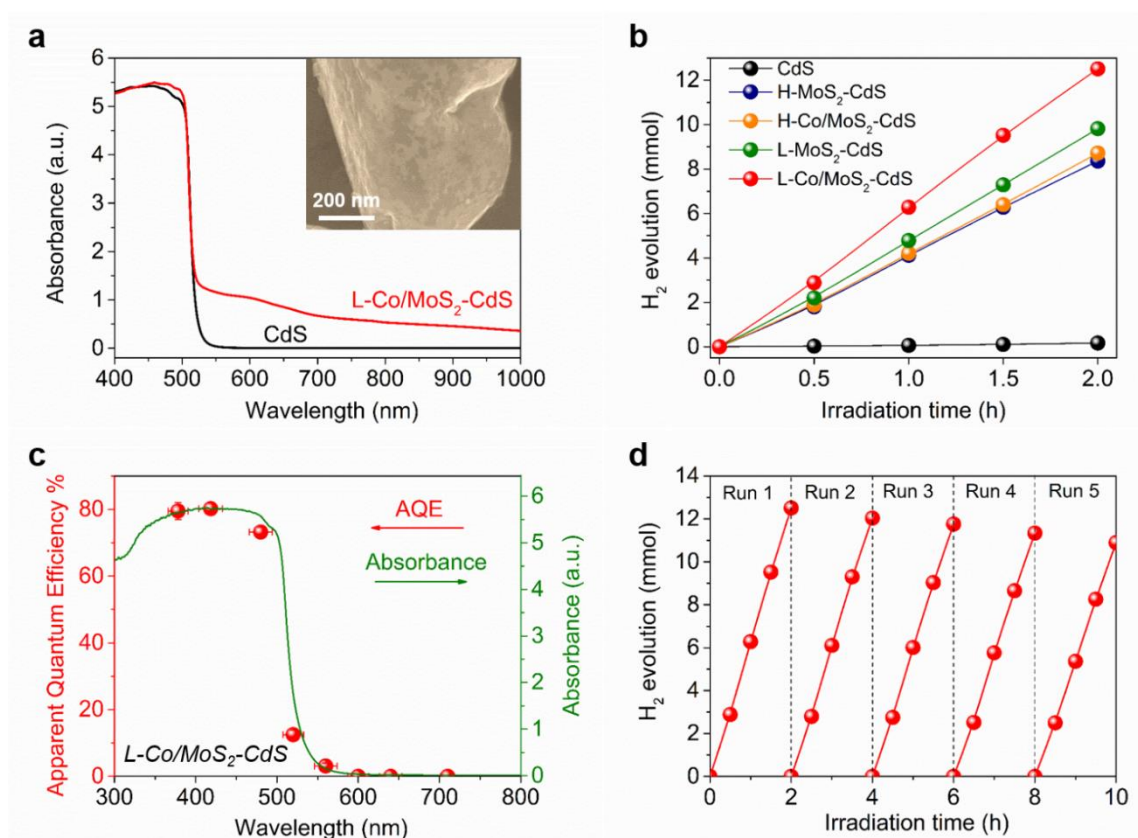


Figure 5.14 Cocatalytic characterization of monolayer H-MoS₂, H-Co/MoS₂, L-MoS₂, and L-Co/MoS₂ over CdS for photocatalytic hydrogen evolution. (a) UV-vis absorption spectra of pure CdS and L-Co/MoS₂-CdS composite. Inset shows the SEM image of the L-Co/MoS₂-CdS composite. (b) Hydrogen evolution of various MoS₂-CdS composites. (c) Wavelength-dependent apparent quantum efficiency of H₂

evolution from the L-Co/MoS₂-CdS composite. (e) Cycling test of the L-Co/MoS₂-CdS composite. Light source: 300-W Xe lamp with a L42 cut-off, $\lambda > 420$ nm; Reaction solution: 300 mL sodium lactate solution (30 vol. % lactic acid adjusted by NaOH, pH~5.0); Catalyst: 200 mg; Cocatalyst: 2wt%.

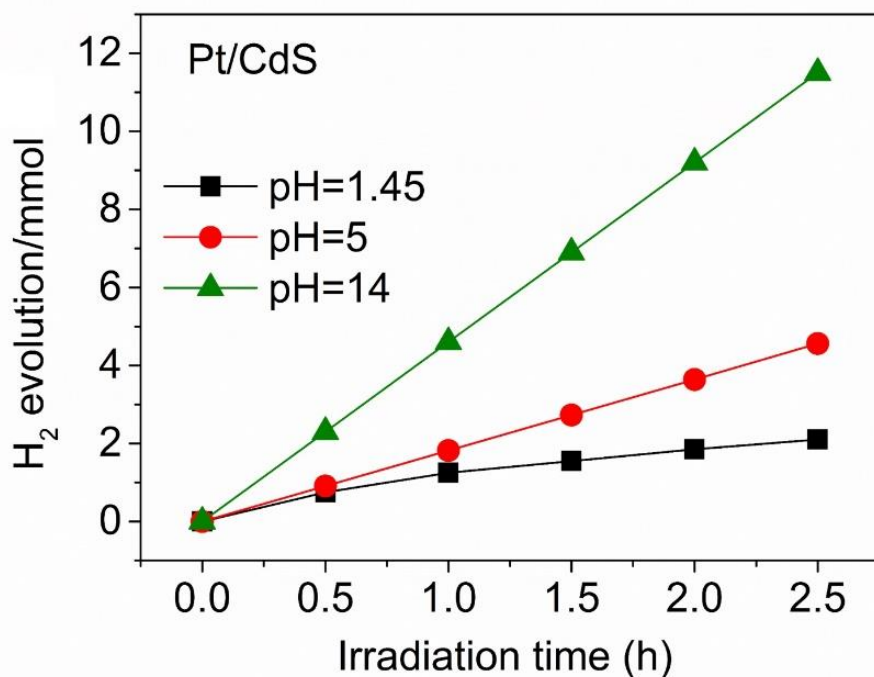


Figure 5.15 Photocatalytic H₂ evolution activities of Pt/CdS under visible light irradiation. Light source: 300-W Xe lamp with a L42 cut-off, $\lambda > 420$ nm; Reaction solution: 300 mL lactic acid solution (30 vol. %, pH=1.45), 300 mL sodium lactate solution (30 vol. % lactic acid adjusted by NaOH, pH=5.0), 300 mL Na₂S -Na₂SO₃ solution (pH=14); Catalyst: 200 mg; cocatalyst: 0.65 wt%.

The above theoretical and experimental results suggest that combining crystallinity engineering and cobalt substitution in freestanding 2H-MoS₂ monolayers is an efficient way to enhance its electrochemical and photocatalytic HER performance. The improved activity arises from the following two aspects: on the one hand, crystallinity engineering produced defects on the basal plane, as confirmed by the HRTEM analysis, can act as new active sites; on the other hand, crystallinity engineering induced in-plane lattice contraction in collaboration with cobalt substitution, which plays a key role in decreasing the hydrogen

adsorption energy, can activate and make use of the basal plane for HER, leading to a much higher synergistic activity compared to independent crystallinity engineering or cobalt substitution.

5.4. Conclusion

In summary, I have maximized the synergistic activity of freestanding 2H-MoS₂ monolayers for HER by combining strategies of exposing more active sites with activating basal plane through a facile crystallinity engineering in collaboration with cobalt substitution. The integrated superior electrocatalytic parameters (low overpotential of 156 mV at 10 mA cm⁻², small Tafel slop of 58 mV dec⁻¹, large exchange current density of 13.8 μA cm⁻², large double-layer capacitance of 30.2 mF cm⁻², and small charge-transfer resistance 68 Ω) and predominant cocatalytic performance even better than Pt undoubtedly confirm that combining cobalt substitution and crystallinity engineering efficiently improve the HER performance of 2H-MoS₂ not only in increasing number of active sites but also enhancing its intrinsic activity. This study provides new insights to maximize synergistic activity of freestanding 2H-MoS₂ monolayers for hydrogen evolution and promises further design and improvement of other layered materials in the application of catalysis and energy conversion.

Reference

- [1] Turner, J. A. *Science* 2004, 305, 972.
- [2] Kibsgaard, J.; Chen, Z.; Reinecke, B. N.; Jaramillo, T. F. *Nat. Mater.* 2012, 11, 963.
- [3] Voiry, D.; Yamaguchi, H.; Li, J.; Silva, R.; Alves, D. C. B.; Fujita, T.; Chen, M.; Asefa, T.; Shenoy, V. B.; Eda, G.; Chhowalla, M. *Nat. Mater.* 2013, 12, 850.
- [4] Jin, H. Y.; Wang, J.; Su, D. F.; Wei, Z. Z.; Pang, Z. F.; Wang, Y. J. *Am. Chem. Soc.* 2015, 137, 2688.

- [5] Hou, Y.; Abrams, B. L.; Vesborg, P. C. K.; Bjorketun, M. E.; Herbst, K.; Bech, L.; Setti, A. M.; Damsgaard, C. D.; Pedersen, T.; Hansen, O.; Rossmeyl, J.; Dahl, S.; Nørskov, J. K.; Chorkendorff, I. *Nat. Mater.* 2011, 10, 434.
- [6] Tong, H.; Ouyang, S. X.; Bi, Y. P.; Umezawa, N.; Oshikiri, M.; Ye, J. H. *Adv. Mater.* 2012, 24, 229.
- [7] Greeley, J.; Jaramillo, T. F.; Bonde, J.; Chorkendorff, I.; Nørskov, J. K. *Nat. Mater.* 2006, 5, 909.
- [8] Casado-Rivera, E.; Volpe, D. J.; Alden, L.; Lind, C.; Downie, C.; Vazquez-Alvarez, T.; Angelo, A. C. D.; DiSalvo, F. J.; Abruna, H. D. J. *Am. Chem. Soc.* 2004, 126, 4043.
- [9] Le Goff, A.; Artero, V.; Jusselme, B.; Tran, P. D.; Guillet, N.; Métayé, R.; Fihri, A.; Palacin, S.; Fontecave, M. *Science* 2009, 326, 1384.
- [10] Tran, P. D.; Tran, T. V.; Orio, M.; Torelli, S.; Truong, Q. D.; Nayuki, K.; Sasaki, Y.; Chiam, S. Y.; Yi, R.; Honma, I.; Barber, J.; Artero, V. *Nat. Mater.* 2016, 15, 640.
- [11] Huang, Z.; Luo, W.; Ma, L.; Yu, M.; Ren, X.; He, M.; Polen, S.; Click, K.; Garrett, B.; Lu, J.; Amine, K.; Hadad, C.; Chen, W.; Asthagiri, A.; Wu, Y. *Angew. Chem. Int. Ed.* 2015, 54, 15181.
- [12] Kibsgaard, J.; Jaramillo, T. F.; Besenbacher, F. *Nat. Chem.* 2014, 6, 248.
- [13] McKone, J. R.; Marinescu, S. C.; Brunshwig, B. S.; Winkler, J. R.; Gray, H. B. *Chem. Sci.* 2014, 5, 865.
- [14] Yu, X. Y.; Feng, Y.; Jeon, Y.; Guan, B.; Lou, X. W.; Paik, U. *Adv. Mater.* 2016, 28, 9006.
- [15] Kiriya, D.; Lobaccaro, P.; Nyein, H. Y. Y.; Taheri, P.; Hettick, M.; Shiraki, H.; Sutter-Fella, C. M.; Zhao, P.; Gao, W.; Maboudian, R.; Ager, J. W.; Javey, A. *Nano Lett.* 2016, 16, 4047.
- [16] Jaramillo, T. F.; Jorgensen, K. P.; Bonde, J.; Nielsen, J. H.; Horch, S.; Chorkendorff, I. *Science* 2007, 317, 100.
- [17] Hinnemann, B.; Moses, P. G.; Bonde, J.; Jorgensen, K. P.; Nielsen, J. H.; Horch, S.; Chorkendorff, I.; Nørskov, J. K. *J. Am. Chem. Soc.* 2005, 127, 5308.
- [18] Wang, H.; Tsai, C.; Kong, D.; Chan, K.; Abild-Pedersen, F.; Nørskov, J. K.; Cui, Y. *Nano Res.*

2015, 8, 566.

[19] Gao, M. R.; Chan, M. K. Y.; Sun, Y. G. *Nat. Commun.* 2015, 6, 78932.

[20] Xie, J.; Zhang, J.; Li, S.; Grote, F.; Zhang, X.; Zhang, H.; Wang, R.; Lei, Y.; Pan, B.; Xie, Y. J. *Am. Chem. Soc.* 2013, 135, 17881.

[21] Kong, D.; Wang, H.; Cha, J. J.; Pasta, M.; Koski, K. J.; Yao, J.; Cui, Y. *Nano Lett.* 2013, 13, 1341.

[22] Shi, J. P.; Ma, D. L.; Han, G. F.; Zhang, Y.; Ji, Q. Q.; Gao, T.; Sun, J. Y.; Song, X. J.; Li, C.; Zhang, Y. S.; Lang, X. Y.; Zhang, Y. F.; Liu, Z. F. *ACS Nano* 2014, 8, 10196.

[23] Ye, G. L.; Gong, Y. J.; Lin, J. H.; Li, B.; He, Y. M.; Pantelides, S. T.; Zhou, W.; Vajtai, R.; Ajayan, P. M. *Nano Lett.* 2016, 16, 1097.

[24] Voiry, D.; Salehi, M.; Silva, R.; Fujita, T.; Chen, M.; Asefa, T.; Shenoy, V. B.; Eda, G.; Chhowalla, M. *Nano Lett.* 2013, 13, 6222.

[25] Lukowski, M. A.; Daniel, A. S.; Meng, F.; Forticaux, A.; Li, L.; Jin, S. J. *Am. Chem. Soc.* 2013, 135, 10274.

[26] Ding, Q.; Meng, F.; English, C. R.; Caban-Acevedo, M.; Shearer, M. J.; Liang, D.; Daniel, A. S.; Hamers, R. J.; Jin, S. J. *Am. Chem. Soc.* 2014, 136, 8504.

[27] Yin, Y.; Han, J.; Zhang, Y.; Zhang, X.; Xu, P.; Yuan, Q.; Samad, L.; Wang, X.; Wang, Y.; Zhang, Z.; Zhang, P.; Cao, X.; Song, B.; Jin, S. J. *Am. Chem. Soc.* 2016, 138, 7965.

[28] Li, G.; Zhang, D.; Qiao, Q.; Yu, Y.; Peterson, D.; Zafar, A.; Kumar, R.; Curtarolo, S.; Hunte, F.; Shannon, S.; Zhu, Y.; Yang, W.; Cao, L. *J. Am. Chem. Soc.* 2016, 138, 16632.

[29] Li, H.; Tsai, C.; Koh, A. L.; Cai, L.; Contryman, A. W.; Fragapane, A. H.; Zhao, J.; Han, H. S.; Manoharan, H. C.; Abild-Pedersen, F.; Norskov, J. K.; Zheng, X. *Nat. Mater.* 2016, 15, 48.

[30] Voiry, D.; Fullon, R.; Yang, J.; de Varvalho Castro e Silva, C.; Kappera, R.; Bozkurt, I.; Lagos, M. J.; Batson, P. E.; Gupta, G.; Mohite, A. D.; Dong, L.; Er, D.; Shenoy, V. B.; Asefa, T.; Chhowalla, M.

Nat. Mater. 2016, 15, 1003.

[31] Voiry, D.; Yang, J.; Chhowalla, M. *Adv. Mater.* 2016, 28, 6197.

(32) Gao, G.; Sun, Q.; Du, A. *J. Phys. Chem. C.* 2016, 120, 16761.

[32] Lv, R.; Robinson, J. A.; Schaak, R. E.; Sun, D.; Sun, Y.; Mallouk, T. E.; Terrones, M. *Acc. Chem. Res.* 2015, 48, 56.

[33] Chang, K.; Li, M.; Wang, T.; Ouyang, S. X.; Li, P.; Liu, L. Q.; Ye, J. H. *Adv. Energy. Mater.* 2015, 5, 1402279.

[34] Yu, Y.; Huang, S.-Y.; Li, Y.; Steinmann, S. N.; Yang, W.; Cao, L. *Nano Lett.* 2014, 14, 553.

[35] Kresse, G.; Furthmuller, J. *Phys. Rev. B: Condens. Matter Mater. Phys.* 1996, 54, 11169.

[36] Perdew, J. P.; Burke, K.; Ernzerhof, M. *Phys. Rev. Lett.* 1996, 77, 3865.

[37] Hai, X.; Chang, K.; Pang, H.; Li, M.; Li, P.; Liu, H.; Shi, L.; Ye, J. *J. Am. Chem. Soc.* 2016, 138, 14962.

[38] Xie, J.; Zhang, H.; Li, S.; Wang, R.; Sun, X.; Zhou, M.; Zhou, J.; Lou, X. W.; Xie, Y. *Adv. Mater.* 2013, 25, 5807.

[39] Muruganandam, S.; Anbalagan, G.; Murugadoss, G. *Appl Nanosci.* 2015, 5, 245.

[40] Zhang, J. Y.; Wang, X. Y.; Xiao, M.; Qu, L.; Peng, X. *Appl. Phys. Lett.* 2002, 81, 2076.

[41] Lee, C.; Yan, H.; Brus, L. E.; Heinz, T. F.; Hone, J.; Ryu, S. *ACS Nano* 2010, 4, 2695.

[42] Li, H.; Contryman, A. W.; Qian, X.; Ardakani, S. M.; Gong, Y.; Wang, X.; Weisse, J. M.; Lee, C. H.; Zhao, J.; Ajayan, P. M.; Li, J.; Manoharan, H. C.; Zheng, X. *Nat. Commun.* 2015, 6, 7381.

[43] Li, H.; Zhang, Q.; Yap, C. C. R.; Tay, B. K.; Edwin, T. H. T.; Olivier, A.; Baillargeat, D. *Adv. Funct. Mater.* 2012, 22, 1385-1390.

[44] Radisavljevic, B.; Radenovic, A.; Brivio, J.; Giacometti, V.; Kis, A. *Nature. Nanotechnol.* 2011, 6, 147.

[45] Oakes, L.; Carter, R.; Hanken, T.; Cohn, A. P.; Share, K.; Schmidt, B.; Pint, C. L. *Nat. Commun.* 2016, 7, 11796.

- [46] Faber, M. S.; Dziejic, R.; Lukowski, M. A.; Kaiser, N. S.; Ding, Q.; Jin, S. J. *Am. Chem. Soc.* 2014, 136, 10053.
- [47] Guan, G.; Zhang, S.; Liu, S.; Cai, Y.; Low, M.; Teng, C. P.; Phang, I. Y.; Cheng, Y.; Duei, K. L.; Srinivasan, B. M.; Zheng, Y.; Zhang, Y. W.; Han, M. Y. *J. Am. Chem. Soc.* 2015, 137, 6152.
- [48] Mak, K. F.; Lee, C.; Hone, J.; Shan, J.; Heinz, T. F. *Phys. Rev. Lett.* 2010, 105, 136805.
- [49] Tsai, C.; Chan, K.; Abild-Pedersen, F.; Norskov, J. K. *Surf. Sci.* 2015, 640, 133
- [50] Zong, X.; Yan, H. J.; Wu, G. P.; Ma, G. J.; Wen, F. Y.; Wang, L.; Li, C. J. *Am. Chem. Soc.* 2008, 130, 7176.
- [51] Chang, K.; Hai, X.; Ye, J. *Adv. Energy Mater.* 2016, 6, 1502555.
- [52] Chang, K.; Mei, Z.; Wang, T.; Kang, Q.; Ouyang, S.; Ye, J. *ACS Nano* 2014, 8, 7078.
- [53] Backes, C.; Smith, R. J.; McEvoy, N.; Berner, N. C.; McCloskey, D.; Nerl, H. C.; O'Neill, A.; King, P. J.; Higgins, T.; Hanlon, D.; Scheuschner, N.; Maultzsch, J.; Houben, L.; Duesberg, G. S.; Donegan, J. F.; Nicolosi, V.; Coleman, J. N. *Nat. Commun.* 2014, 5, 4576.

Chapter 6 General conclusion and future prospects

6.1 General conclusion

In this thesis, the main work is to explore generalizable methods for targeted synthesis of TMDs monolayers with various phases, lateral sizes, crystallinities, and atomic structures to create more exposed active sites, in particular reactivate the inert basal plane towards superior cocatalytic performance for photocatalytic HER. The detailed study could be concluded in the following parts.

1. Targeted synthesis of 2H- and 1T-phase MoS₂ monolayers for catalytic hydrogen evolution.

A facile and effective lithium molten salt assisted method was first developed to synthesize a series of MoS₂ precursors by simply controlling the calcination temperature. These precursors can be easily and accurately exfoliated into 2H- and 1T-phase MoS₂ monolayers by subsequent hydrolysis process. During the synthesis process, lithium molten salt not only acts as the fluxing medium, but also controls the MoS₂ phases switching between 1T and 2H. Through matching with different photo-harvesters, the cocatalytic performance of different phased MoS₂ monolayers was comprehensively studied. Due to metallic characteristics, the 1T-MoS₂ monolayers show significantly higher cocatalytic activities than the 2H-MoS₂ monolayers over TiO₂ for photocatalytic H₂ evolution.

2. Engineering the edges of transition metal disulfides for direct exfoliation into monolayers in polar micromolecular solvents and their cocatalytic performances.

A novel strategy through engineering lateral size of TMDs (MoS₂ and WS₂) was explored for direct exfoliation in polar micromolecular solvents, even pure water, to produce monolayer MoS₂ and WS₂ nanosheets in high yield. The exfoliation yield of monolayers was measured to be as high as 21% for MoS₂ and 18% for WS₂ in ethanol. Even in pure water, a monolayer yield of 6% for MoS₂ and 5% for WS₂ can be achieved. By reducing the lateral size of the layered crystals to the nanoscale, the edge concentration is drastically increased and can provide sufficient hydrodynamic force to overcome the interlayer van der Waals attraction to delaminate the layered crystals in solution, allowing for ready

exfoliation in polar micromolecular solvents. These exfoliated monolayer TMDs nanosheets exhibit excellent catalytic hydrogen activities, particularly for monolayer WS₂, which has a cocatalytic performance that is even higher than that of Pt.

3. Engineering crystallinity of MoS₂ monolayers for enhanced cocatalytic activity.

In view of the lack of active edge sites in MoS₂ monolayers for HER, crystallinity engineering was adopted to create more active sites to enhance its cocatalytic performance. It was found that the cocatalytic performance of the monolayer MoS₂ is gradually enhanced with reduced crystallinity, and an apparent quantum efficiency as high as 71.6% can be achieved for the lowest crystalline monolayer MoS₂ over CdS under visible light irradiation at 420 nm. As compared to the highly crystalline monolayer MoS₂, the increased cocatalytic activity for the poorly crystalline monolayers is attributed to the low-crystallization induced structural disorder, which contains abundant unsaturated sulfur atoms as additional active sites for HER.

4. Maximizing synergistic cocatalytic activity of MoS₂ monolayers combining crystallinity engineering and cobalt substitution.

For the activation of inert basal plane of MoS₂ monolayers to further enhance its cocatalytic performance, cobalt doping was then introduced on the basis of crystallinity engineering. The density functional theory calculations and experimental results show that the combination of crystallinity engineering and cobalt substitution in monolayer MoS₂ can not only introduce massive defects and structural disorder that act as additional active sites, but also activate and reuse of the basal plane, leading to a much enhanced cocatalytic activities with an apparent quantum efficiency of 80.2% over CdS under visible light irradiation at 420 nm.

6.2 Future prospects

Although some achievements have been made in developing TMDs as Pt-alternative co-catalysts, research on them is still at the primary stage, and there are many challenges towards significant

improvement of photocatalytic HER and overall water splitting efficiency *via* modification with TMD co-catalysts. Some issues as listed below are worthy of special attention:

(i) Defined control of phase transformation

Current studies indicated that 1T phase TMDs show higher HER activities than 2H phase due to their high conductivity which is beneficial for the rapid charge transport. However, two issues of 1T phase TMDs as co-catalysts are worth to be noted: one is their stability. It is known that 1T phase TMDs are metastable states with distorted crystal structure. The transformation from 1T phase to 2H phase is a downhill reaction. Under the specific conditions, the metastable 1T phase can change into the stable 2H phase. In addition, it is usually seen that 1T and 2H were co-existed in the exfoliated 1T phase TMDs, or in other words, an incomplete phase transformation was accompanied by this procedure. Thus, how to precisely control the 1T phase TMDs as co-catalysts is important, particularly during the loading procedure. The other thing need to be considered is the size control of 1T phase TMDs. Current synthesis of 1T phase TMD often shows a large sheets or plates. When used as the co-catalysts, it is difficult to composite with the photoharvester, especially for the most of high-activity metal oxides with nanosized structures. The synthesis of nanosized (< 20 nm) and stable 1T phase TMDs as co-catalysts is therefore significant in the following research.

(ii) Application in overall water splitting

Current studies on non-precious metal co-catalysts are still focused on the hydrogen evolution half-reaction, i.e., in the presence of sacrificial electron donors. Although the photocatalytic H₂ production rate of TMDs based catalysts could approach or even exceed that of commonly used Pt-based photocatalysts, the utilization of high-cost and non-renewable sacrificial agents disobey the advocated sustainable development in present research. Further explorations and investigations for non-precious metal co-catalysts including TMDs should be studied and applied in the overall water splitting process, such as one-step water splitting system, the Z-scheme water splitting system. The final goal to explore high efficient noble-metal-alternative co-catalysts is after all, to realize the overall water splitting only by using solar energy.

Acknowledgement

I would like to express my deep and sincere gratitude to my supervisor, Prof. Jinhua Ye for the continuous support of my PH. D study and related research, for her patience, motivation, and immense knowledge. Her understanding, encouraging and personal guidance helped me in all the time and provided a good basis for the present thesis.

Besides my supervisor, I would like to thank the rest of my thesis committee: Prof. Kei Murakoshi, Prof. Masako Kato, Prof. Shin Mukai, and Prof. Kazunari Yamaura for their insightful comments and encouragement, but also for the hard questions which incited me to widen my research from various perspectives.

I am also very grateful to Dr. Kun Chang, who enlightened me the first glance of research and gave me a lot of detailed and constructive suggestions based on his abundant knowledge of photocatalysis. Without his kind help it would be difficult for me to finish the thesis.

I would like to thank my fellow labmates in Photocatalytic Materials Group in NIMS for the stimulating discussions, for the deep nights we were working together, and for all the fun we have had in the last three years.

I appreciate the financial support from the State Scholarship Fund by China Scholarship Council (CSC).

Last but not the least, I would like to thank my parents for supporting me spiritually throughout writing this thesis and my life in general.